Hybrid Perovskite Nanocrystals: Synthesis, Optoelectronic Properties and Applications

THESIS SUBMITTED TO ACADEMY OF SCIENTIFIC AND INNOVATIVE
RESEARCH (**AcSIR**) FOR THE AWARD OF THE DEGREE OF
DOCTOR OF PHILOSOPHY IN CHEMISTRY
UNDER THE FACULTY OF SCIENCE

By
CHINNADURAI M.
Enrollment No: 10CC14J39016

Under the Supervision of
Dr. Vijayakumar C.

PHOTOSCIENCES AND PHOTONICS SECTION
CHEMICAL SCIENCES AND TECHNOLOGY DIVISION
CSIR-NATIONAL INSTITUTE FOR INTERDISCIPLINARY
SCIENCE AND TECHNOLOGY (CSIR-NIIST)
THIRUVANANTHAPURAM - 695019, KERALA

MARCH 2020

DECLARATION

I hereby declare that the matter embodied in the Ph.D. thesis entitled: "**Hybrid Perovskite Nanocrystals: Synthesis, Optoelectronic Properties and Applications**" is the result of an independent work carried out by me at the Photosciences and Photonics Section, Chemical Sciences and Technology Division of the CSIR-National Institute for Interdisciplinary Science and Technology (CSIR-NIIST), Thiruvananthapuram, under the supervision of Dr. Vijayakumar C. and the same has not been submitted elsewhere for any other degree or diploma.

In keeping with the general practice of reporting scientific observations, research materials obtained from other investigations has been duly cited and acknowledged in the thesis.

M. Chinnadurai
Chinnadurai M. 23/03/20

Thiruvananthapuram
March 23, 2020

National Institute for Interdisciplinary Science and Technology (NIIST)
Council of Scientific and Industrial Research, Thiruvananthapuram – 695 019, INDIA
Dr. Vijayakumar C., PhD
Senior Scientist, Photosciences and Photonics Section, CSTD
Tel: +91-471-2515-484; E-mail: cvijayakumar@niist.res.in

March 23, 2020

CERTIFICATE

This is to certify that the work embodied in the thesis entitled: "**Hybrid Perovskite Nanocrystals: Synthesis, Optoelectronic Properties and Applications**" has been carried out by Mr. Chinnadurai M. under my supervision and guidance at the Photosciences and Photonics Section, Chemical Sciences and Technology Division of the CSIR-National Institute for Interdisciplinary Science and Technology (CSIR-NIIST), Thiruvananthapuram and the same has not been submitted elsewhere for a degree.

23/03/2020
Dr. Vijayakumar C.

(Thesis Supervisor)

M. Chinnadurai 23/03/20
Chinnadurai M.

ACKNOWLEDGEMENTS

I have great pleasure in placing on record my deep sense of gratitude to Dr. Vijayakumar C., my thesis supervisor, for suggesting the research problem and for his guidance, immense knowledge, endearing care, constant support, and motivation, leading to the successful completion of this work.

I would like to express my sincere thanks to Professor M. V. George for his constant help and encouragement during my stay at CSIR-NIIST.

I wish to thank Dr. A. Ajayaghosh, Director and Dr. Gangan Pratap and Dr. Suresh Das, former Directors of the CSIR-National Institute for Interdisciplinary Science and Technology for providing me the necessary facilities for carrying out the work.

I sincerely thank Prof. Vasudevanpillai Biju for all the experiments conducted at Hokkaido University, Japan. I also sincerely thank Dr. K. B. Jinesh for memory device fabrication at Indian Institute of Space Science and Technolgy (IIST), Thiruvananthapuram.

I sincerely acknowledge Dr. C. H. Suresh, AcSIR coordinator and Dr. Mangalam S. Nair and Dr. R. Luxmi Varma, former AcSIR coordinators for their help in the successful completion of the course work.

I am very much thankful to Dr. Joshy Joseph, Dr. K. Yoosaf and Dr. K. N. Narayanan Unni, my Doctoral Advisory Committee members for their valuable comments and suggestions to improve the quality of my work.

I would also like to thank Dr. K. N. Narayanan Unni, Photosciences and Photonics Section head for all the help and support extended to me.

I would like to thank Dr. K. R. Gopidas, Dr. Sujatha Devi P., Dr. J. D. Sudha, Dr. V. Karunakaran, Dr. V. K. Praveen, Dr. Suraj Soman, Dr. Bijitha Balan, Dr. Sreejith

Sankar, Dr. Rakhi B., Dr. Animesh Samantha and all other scientists of the Photosciences and Photonics Section, Chemical Sciences and Technology Division, for all the help and support extended to me.

I would like to thank Mr. Robert Philip and Mr. Kiran Mohan for general help and TEM analysis and Mrs. Saumini Mathew, Mr. Saran and Mr. Shyam for NMR analysis and Mrs. Viji, and Ms. Athira for HRMS data, Dr. Vedhanarayanan and Mr. Vibhu Darshan for AFM analysis. I would also like to thank Dr. Padma Ishwarya, Ms. Anaga Nair, and Mr. Billu Abraham for their help during my thesis writing.

I express my sincere thanks to my labmates Mr. Naeem K.C., Dr. Tanwista Ghosh, Dr. Jayanthy S. Panicker, Mr. Johnpaul K. P., Ms. Neethi Raveendran, Ms. Susanna Poulose, Dr. Suresh Kumar, Ms. Nayana Krishna, Ms. Neethu M., Ms. Anuja Vijayan, Mr. Arjun P., Dr. Vishnu Vijayakumar, Ms. Reshma P., Ms. Parvathy P. R., Dr. Devika S., Mr. Abhijith S. Kumar and Mr. Maneesh Mohan for their valuable help and support. I also thank all M. Sc. project students who have worked with me.

Words are inadequate to express my gratitude to my dear friends at photosciences for their care, love, support, and encouragement, which made my life in NIIST memorable. I also thank all the present and former members of the Photosciences and Photonics and other Divisions of CSIR-NIIST for their help and cooperation.

I am deeply indebted to my mother and sister, family members and friends for their support and encouragement. I would also like to extend my thanks and appreciation to all my teachers for their help and blessings.

Finally, I sincerely thank the Counsil of Scientic and Industrial Research (CSIR) for financial assistance.

Chinnadurai M.

CONTENTS

Chapter 2 Energy Transfer Properties of Perovskite Nanocrystals

Chapter 3 Electron Transfer Properties of Perovskite Nanocrystals

Chapter 4 Perovskite Nanocrystal/Squaraine Dye Conjugate: Development of Visibly Opaque and NIR Transmitting Material

Chapter 5 Perovskite Nanocrystals based Memristor Devices: Chemically Induced Control of Operational Parameters

PREFACE

Luminescent perovskite nanocrystals (PNCs) are receiving great scientific attention in recent years due to their narrow emission with exceptionally high photoluminescence quantum yields and facile tunability of optical band gap over the entire visible region. In addition to photoluminescence, they exhibit fascinating properties such as defect tolerance, tunable morphologies, multiple exciton generation, charge generation and amplified stimulated emission. However, addressing fundamental photophysical properties of PNCs in combination with other materials calls for exploration, and is expected to further the applications of PNCs in various optoelectronic devices such as solar cells, LEDs etc. The current thesis makes an effort to study in detail the synthesis, photophysical and optoelectronic properties and applications of PNCs.

The thesis is organized into six Chapters. The first Chapter provides an overview of PNCs and the recent developments in this area. This chapter highlights the history, structure, general synthesis, photophysical properties and optoelectronic applications of PNCs. In the second Chapter, we have studied in detail the energy transfer and accepting properties of PNCs. The light-harvesting antenna property of luminescent nanocrystals was studied using rhodamine B and rhodamine 101 dyes as energy acceptors. The energy transfer efficiency was highly dependent on the number of anchoring groups and binding ability of the dyes to the surface of the nanocrystals. The energy accepting property of PNCs was also studied using polyfluorene (PF) as an energy donor. The halogen exchange of yellow emitting mixed halide PNCs was completely arrested in the gel state due to the surface passivation of nanocrystals with PF polymers. As a result, a stable white emitting gel was produced from PNCs composite via energy transfer from PF donors to PNCs acceptor.

The third Chapter deals with the electron transfer property of PNCs and its application in sensing. The excitation energy migration and electron transfer properties of PNCs were studied comprehensively. The closely packed PNCs film showed extended fluorescence lifetime compared to isolated PNCs in colloidal state due to hopping or migration of photogenerated excitons among PNCs in the film. The fluorescence quantum efficiency and lifetime was decreased in films doped with fullerene (C_{60}), which was attributed to channelling of excitons migration into electron transfer to C_{60}. Next, PNCs were used for the sensing of picric acid. The sensing mechanism was found to be an efficient electron transfer from PNCs to picric acid molecules.

The fourth chapter deals with the phase retention behaviour of α-$HC(NH_2)_2PbI_3$ PNCs and their application in NIR imaging. The size of PNCs was gradually increased followed by the introduction of a NIR absorbing squaraine dye onto the surface of nanocrystals to obtain visibly opaque NIR transmitting properties. The acid group presents in squarine dye molecules strongly interacted with the surface of nanocrystals leading to improved stability of nanocrystals. The filters obtained from PNC/SQ composite were used for the security and NIR photography applications.

The fifth chapter describes the synthesis of hybrid lead halide PNCs for high performance, air-stable, non-volatile memory devices through low-cost solution processing techniques at ambient conditions. The write-erase voltages of the devices reduced from 2 V to 0.5 V by replacing bromide with chloride ions in the basic structure of $CH_3NH_3PbBr_3$ nanocrystals. Though the on/off voltage dropped, the on/off ratio, retention, and endurance of the devices were enhanced on chloride doping.

The last chapter deals with the phase effect of $FAPbI_3$ PNCs on the memristor characteristics. The ReRAM devices fabricated from a thin layer of α-$FAPbI_3$ PNCs as active layer showed a remarkable switching property which is in contrast to the bulk α-$FAPbI_3$ perovskite. The bulk perovskite is not capable of exhibiting resistive switching due to the difficulty in rupturing filaments formed by iodide vacancies. The presence of capping ligands in PNCs reduces the interaction energy between the iodide vacancies. As a result, the filaments formed by the iodide vacancies in PNC film were easy to rupture during the reset process. Interestingly, memristors fabricated from δ-$FAPbI_3$ nanorods (NRs) showed 4-fold enhanced on/off ratio compared to that of α-form. The δ-$FAPbI_3$ NRs formed from the self-assembly of individual hexagonal nanocrystals were in parallel orientation towards the FTO substrate and also they are zero-dimensional material. As a result, the intrinsic conductivity (off current) of δ-$FAPbI_3$ NRs decreased and hence high on/off ratio for δ-$FAPbI_3$ PNCs.

LIST OF ABBREVIATIONS

1. A - Acceptor
2. AFM - Atomic force microscopy
3. Ag - Silver
4. Al - Aluminum
5. Au - Gold
6. CBM - Conduction band minimum
7. $CH_3NH_3PbI_3$ - Methylammonium lead iodide
8. CIE - Commission Internationale de I'Elcairage
9. C_{60} - Fullerene
10. D - Donor
11. DFT - Density functional theory
12. DMF - *N,N*-Dimethyl formamide
13. DNT - Dinitro toluene
14. DPP - Diketopyrrolopyrrole
15. DRAM - Dynamic random access memory
16. °C - Degree Celsius
17. EDX - Energy dispersive X-ray
18. ET - Electron transfer
19. *et al.* - *Et allii/alia*
20. *etc*. - Et cetera
21. eV - Electron volt
22. $FAPbBr_3$ - Formamidinium lead bromide
23. $FAPbI_3$ - Formamidinium lead iodide

24. FET - Field-effect transistor
25. FRET - Fluorescence resonance energy transfer
26. FTIR - Fourier-transform infrared spectroscopy
27. FTO - Fluorine tin oxide
28. FWHM - Full width at half maximum
29. g - Gram
30. h - Hour
31. HBr - Hydrobromic acid
32. HDD - Hard disk drive
33. HRS - High resistance state
34. I - Current
35. InP - Indium phosphide
36. IT - Information technology
37. LARP - Ligand assisted reprecipitation method
38. LRS - Low resistance state
39. μM - Micromolar
40. μs - Microseconds
41. mg - Milligram
42. mL - Milliliter
43. mmol - Millimole
44. ms - Millisecond
45. Ni - Nickel
46. NIR - Near infrared
47. nm - Nanometer

48. NMR - Nuclear magnetic resonance
49. NP - Nanoparticle
50. NR - Nile red
51. ns - Nanosecond
52. OA - Oleic acid
53. ODE - 1-Octadecene
54. OLA - Oleylamine
55. OLED - Organic light emitting diode
56. $PbBr_2$ - Lead bromide
57. $PbCl_2$ - Lead chloride
58. PbI_2 - Lead iodide
59. PC - Personal computer
60. PDI - Perylene tetracarboxylic diimide
61. PET - Photo induced electron transfer
62. PF - Polyfluorene
63. PNC - Perovskite nanocrystal
64. PLQY - Photoluminescence quantum yield
65. QDs - Quantum dots
66. Φ_F - Quantum yields of fluorescence
67. RAM - Random access memory
68. ReRAM - Resistive random access memory
69. RhB - Rhodamine B
70. Rh101 - Rhodamine 101
71. rpm - Rotation per minute

72. RS - Resistive switching

73. SEM - Scanning electron microscopy

74. Si - Silicon

75. SQ - Squaraine

76. TEM - Tunneling electron microscopy

77. TNP - Trinitro phenol

78. TNT - Trinitro toluene

79. UV - Ultraviolet

80. V - Voltage

81. VBM - Valence band maximum

82. V_I - Iodide vacancy

83. V_{Reset} - Reset voltage

84. V_{Set} - Set voltage

85. λ_{max} - Wavelength maximum

86. XPS - X-ray photoelectron spectroscopy

87. XRD - X-ray diffraction

Chapter 1

Hybrid Perovskite Nanocrystals: An Overview

1.1. Abstract

Organic-inorganic hybrid perovskite materials have gained significant attention from researchers in recent years due to their unique properties including but not limited to strong absorption coefficient, long charge carriers diffusion length, small exciton binding energy, and tunable bandgap. These outstanding intrinsic properties render these materials as highly promising for various optoelectronic applications such as solar cells, light-emitting diodes, photodetectors, transistors, memories, capacitors, and so forth. The great success of bulk perovskites has led to research on perovskite nanocrystals (PNCs). The PNCs possess excellent photoluminescence quantum yield and size/morphology tunable optoelectronic properties besides the properties similar to that of the corresponding bulk materials. Unlike bulk perovskites, PNCs are very stable due to the presence of hydrophobic capping ligands on their surface. The PNCs are found to be a promising candidate for various optoelectronic device applications similar to that of bulk perovskite materials. This chapter provides an overview of PNCs and the recent developments in this area.

1.2. Introduction

1.2.1. History of metal halide perovskites

The study of perovskites started with the discovery of calcium titanate ($CaTiO_3$), an inorganic rock oxide mineral, by the German mineralogist, Gustav Rose in 1839. The name ‘perovskite’ is applied to any material which adopts a similar structure of $CaTiO_3$ to honor the Russian mineralogist Lev A. Perovski, who characterized the mineral structure of $CaTiO_3$.[1] The first all-inorganic perovskite material, $CsPbX_3$ (X represents halide ions) was synthesized by Möller in 1958.[2] He varied the halogen compositions in the perovskite structure and studied their photoconductive properties. Later in 1978, Weber and Naturforsch prepared the first organic-inorganic hybrid perovskite (or halide perovskite) material, $CH_3NH_3PbX_3$.[3] In the 90s, Mitzi and coworkers carried out studies on layered hybrid perovskites for applications in thin film transistors and light-emitting diodes.[1] The first use of hybrid perovskites in photovoltaics was demonstrated by Miyasaka in 2006 using $CH_3NH_3PbBr_3$ as the sensitizer in mesoporous TiO_2 based dye-sensitized solar cell.[4] He obtained a power conversion efficiency (PCE) of 2.2% which was further improved to 3.8% in 2009 by replacing bromide with iodide ions.[5] In 2011, Park and coworkers introduced PNCs onto the mesoporous TiO_2 resulting in 6.5 % PCE, which was attributed to the high surface area of PNCs.[6] These devices had a very short lifetime because the perovskite materials underwent rapid degradation in the presence of liquid electrolytes. A major break-through in perovskites based photovoltaics happened in 2012 when Park and

Grätzel used solid spiro-OMeTAD as the hole transport material instead of liquid electrolytes. They used a device architecture consisting of FTO/mesoporous $TiO_2/CH_3NH_3PbI_3$/spiro-OMeTAD/Au. The photograph and the cross-sectional SEM image of the device are shown in **Figure 1.1**. The device showed an excellent photoconversion efficiency (9.7%) and environmental stability.[7] Subsequently, various remarkable developments have been made in perovskite photovoltaics via device engineering and materials designing. Recent reports suggested that the certified PCE of perovskite based photovoltaics is reached upto 25.2%.[8]

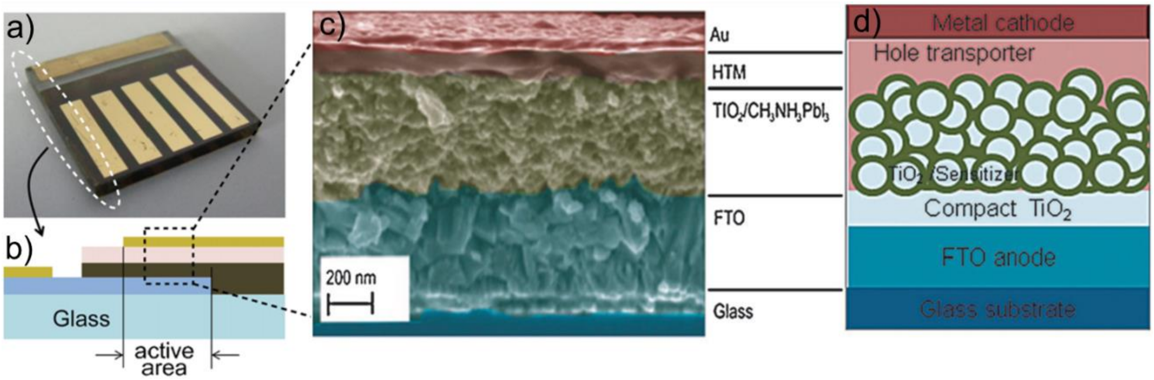

Figure 1.1. a) Photograph of a $CH_3NH_3PbI_3$ perovskite based solar cell device and b) The schematic representation of the corresponding cross-sectional structure. c) Cross-sectional SEM image of the solar cell device. d) Schematic representation of the active layer-underlayer-FTO interfacial junction structure (*Adapted from reference* 7).

Hybrid perovskites have the potential for other optoelectronic devices also such as light-emitting diodes (LEDs), lasers, photodetectors, memories, field-effect transistors, and sensors. The diverse applications of these materials are owing to their excellent optoelectronic properties such as direct bandgap, strong light absorption coefficient, tunable bandgap, ambipolar transport, long and balanced charge carriers diffusion lengths, high charge carriers mobilities, small exciton binding energy, and low carrier trap density.[9-14] Importantly, perovskites could be prepared from low-cost precursors using simple synthetic procedures, which make them highly attractive.

1.2.2. Structure of perovskites

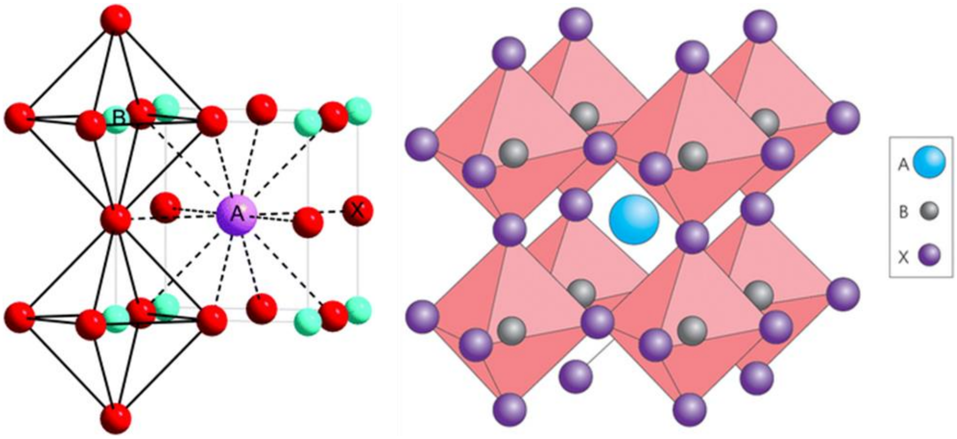

Figure 1.2. Structure of AMX_3 type 3-dimensional perovskite (*Adapted from reference 15*).

Perovskites are represented by the general formula of AMX_3 where 'A' and 'M' represent the cations of dissimilar sizes and 'X' represents halide ions or pseudo halogens.[1] In the perovskite structure, the metal ion 'M' (Pb^{2+}, Sn^{2+}, Ge^{2+}, Co^{2+}, Fe^{2+}, Cu^{2+}, Mn^{2+}, Pd^{2+}, Cd^{2+}, Eu^{2+}, Yb^{2+}, Bi^{3+}, Sb^{3+} etc.) is surrounded by six halide ions (Cl^-, Br^- and I^-) or pseudo halogens (SCN^-, BF_4^-, PF_6^- *etc.*) to form an octahedra. Subsequently, several of these octahedras are joined together via corner sharing in all the directions to form a three dimensional structure (**Figure 1.2**). The voids formed by the joining of eight octahedra will be occupied by the cation 'A'. The 'A' cation provides a positive charge to the structure thus stabilizing the material. In the case of inorganic rock-solid perovskites, A is also a metal cation such as Ca^{2+}, Ba^{2+}, Pb^{2+}, Pd^{2+}, Bi^{3+}, Sb^{3+}, *etc*. On the other hand, organic cations such as $CH_3NH_3^+$ (MA^+) and $H_2NCHNH_2^+$ (FA^+) are being used in hybrid perovskites and Cs^+ ion is used as the 'A' part in all inorganic, synthetic halide perovskites. The 'A' cation fits onto the voids via hydrogen bonding or electrostatic interaction with the halide ions.

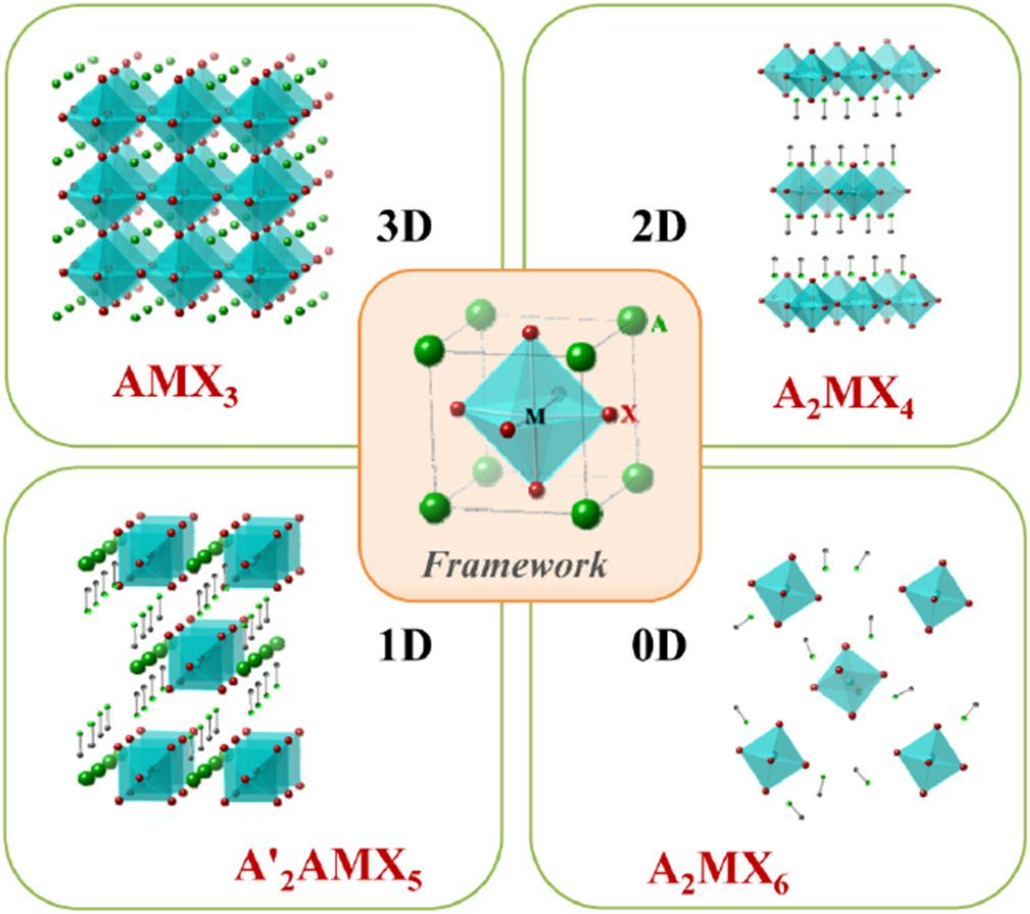

Figure 1.3. Schematic representation of different dimensional (3D, 2D, 1D & 0D) perovskite material (*Adapted from reference 16*).

The different dimensionalities of perovskite materials are schematically represented in **Figure 1.3**. The dimensionality of perovskites could be reduced from 3D to 0D by using different ‘A’ cations.[16] In the 3D perovskite material, the smaller sized A cations (MA^+, FA^+, Cs^+) exactly fit onto the voids formed by PbX_6^{4-} octahedra. When the cation size is large, the 3D network structure changes to 2D, 1D or 0D. In the 0D structure, the PbX_6^{4-} octahedras are isolated, while in the 1D, the PbX_6^{4-} octahedras are connected to form a chain and in the 2D perovskites, the PbX_6^{4-} octahedras are connected to form layered sheets. The dimension of inorganic framework (PbX_6^{4-} octahedras) changes the stoichiometry of perovskite materials. The 3D, 2D, 1D, and 0D perovskite materials possess the stoichiometry of AMX_3, A_2MX_4, A'_2AMX_5, and A_2MX_6, respectively.

1.2.3. Tolerance factor

The stability of perovskite crystal structure could be explained using Goldschmidt tolerance factor (t), which can be calculated using the following relation.[17,18]

$$(R_A + R_X) = t\sqrt{2(R_M + R_X)}$$

where R_A, R_M, and R_X represent the ionic radii of organic cation, metal ion, and halide ion, respectively. The tolerance factor equal to one is considered as an ideal close-packing system with a perfect cubic structure. The value of $t = 0.9 - 1$ is the empirical stability range for 3D perovskite materials. The t value for the most studied $CH_3NH_3PbI_3$ perovskite is found to be 0.92. The t values of $CsPbBr_3$ and $CsPbI_3$

perovskites are 0.9 and 0.89, respectively, which indicate the borderline stability for $CsPbI_3$.[17] The *t* value of $FAPbI_3$ was found to be 1.03 which could be brought down to the stability window by mixing Cs and FA cations in a suitable ratio into the perovskite structure.[19,20]

1.2.4. Electronic structure

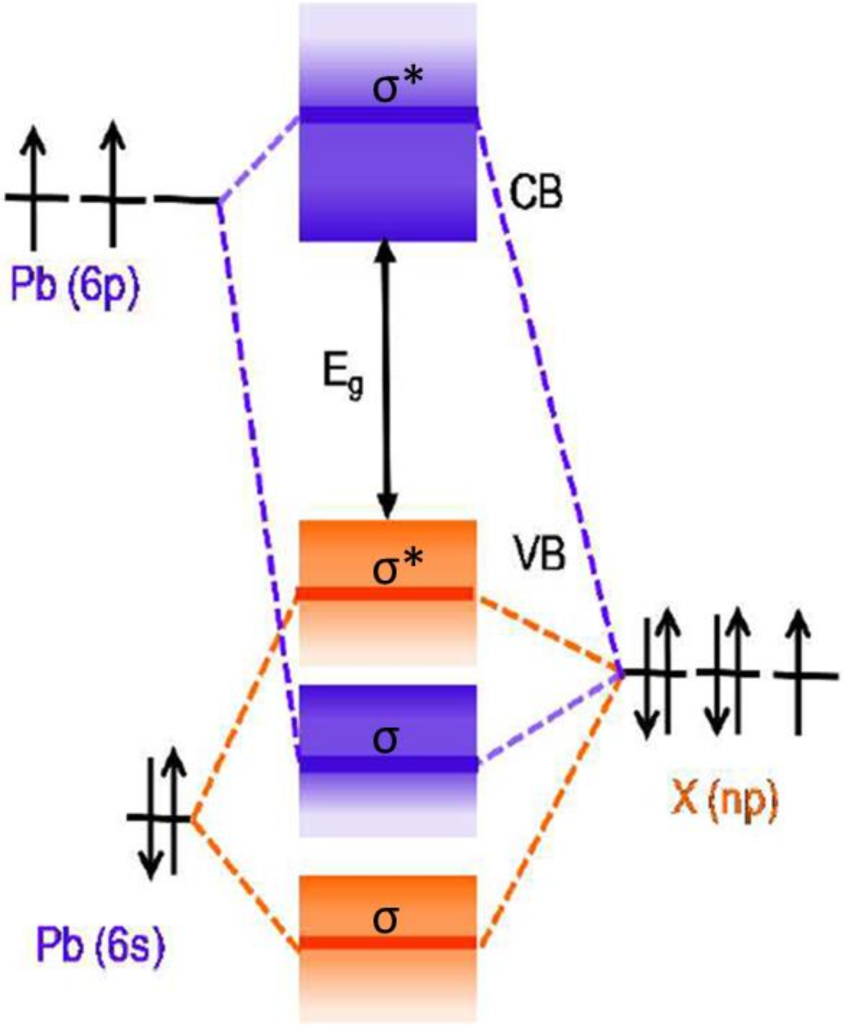

Figure 1.4. Schematic representation of bonding (σ) and antibonding (σ*) orbitals of perovskite materials showing the formation of valence and conduction band (*Adapted from reference 21)*.

The formation of valance band (VB) and conduction band (CB) in perovskite material could be explained through a schematic diagram shown in **Figure 1.4**. The valance band maximum (VBM) consists of antibonding hybrid states formed by the overlapping of s orbital of metal ions and p orbitals of halide ions. The antibonding hybrid states between p orbitals of metal ion and p orbitals of halide ion form the conduction band minimum (CBM). The CBM is mainly dominated by the p orbitals contribution of metal ions and is further stabilized by a spin-orbit splitting of metal ions p states, which bring the CBM below the metal ions p orbitals. In $MAPbBr_3$ perovskite, VBM originates from the Pb(6s)-Br(4p) antibonding interactions and CBM originates from the less hybridized Pb(6p)-Br(4p) antibonding interactions. The CBM is mainly dominated by the Pb 6p orbitals contribution and is further stabilized by a spin-orbit splitting of Pb 6p states. Generally, the organic cation 'A' has no direct effect on the electronic properties of perovskites due to its weak interaction and negligible orbital overlap with inorganic octahedras.[22,23] However, organic cations indirectly affect the electronic properties by the means of their different sizes that distort the geometry of the perovskite structure.[24-26] For example, the change of organic cation from MA^+ to FA^+ exerts a trivial impact on the electronic properties due to the size change. On the other hand, halogens play a key role in determining the electronic bandgap, as different p orbitals (3p for Cl, 4p for Br and 5p for I) are contributing to VBM.[27] The bandgap of perovskites could be easily reduced by varying the halogen from chloride to bromide to iodide in the perovskite structure.[28]

As evidenced from the cyclic voltametric studies, there is a significant increase in the energy of VBM by 0.80 eV, when the halide ion was changed from Cl^- to Br^- and Br^- to I^-. Contrastingly, CBM showed a trivial shift in energy which was only about 0.19 eV. Metal ions also play a key role in deciding the bandgap of perovskites due to the difference in their orbitals involved in bonding.[29]

1.3. Metal halide perovskite nanocrystals

The great success of bulk perovskites has led to the synthesis and study of PNCs for various optoelectronic applications.[30-35] The PNCs possess high photoluminescence quantum yield (PLQY) with a narrow full width at half maximum (FWHM) of emission. Excellent PLQY of these materials could be attributed to their high exciton binding energy and lower exciton recombination lifetime. The luminescence wavelengths of these materials are tunable in the whole visible region by simply varying the halogen composition in the perovskite structure. The optoelectronic properties of PNCs could also be controlled by the modulation of quantum confinement effect by changing their size or dimensionality (nanorods, nanocubes, nanoplatelets, *etc*.) or chemical composition or via doping. It was also established that the incorporation of hydrophobic longer alkyl chains as a capping agent can provide significant moisture and colloidal stability to the PNCs.

1.3.1. Defect tolerance

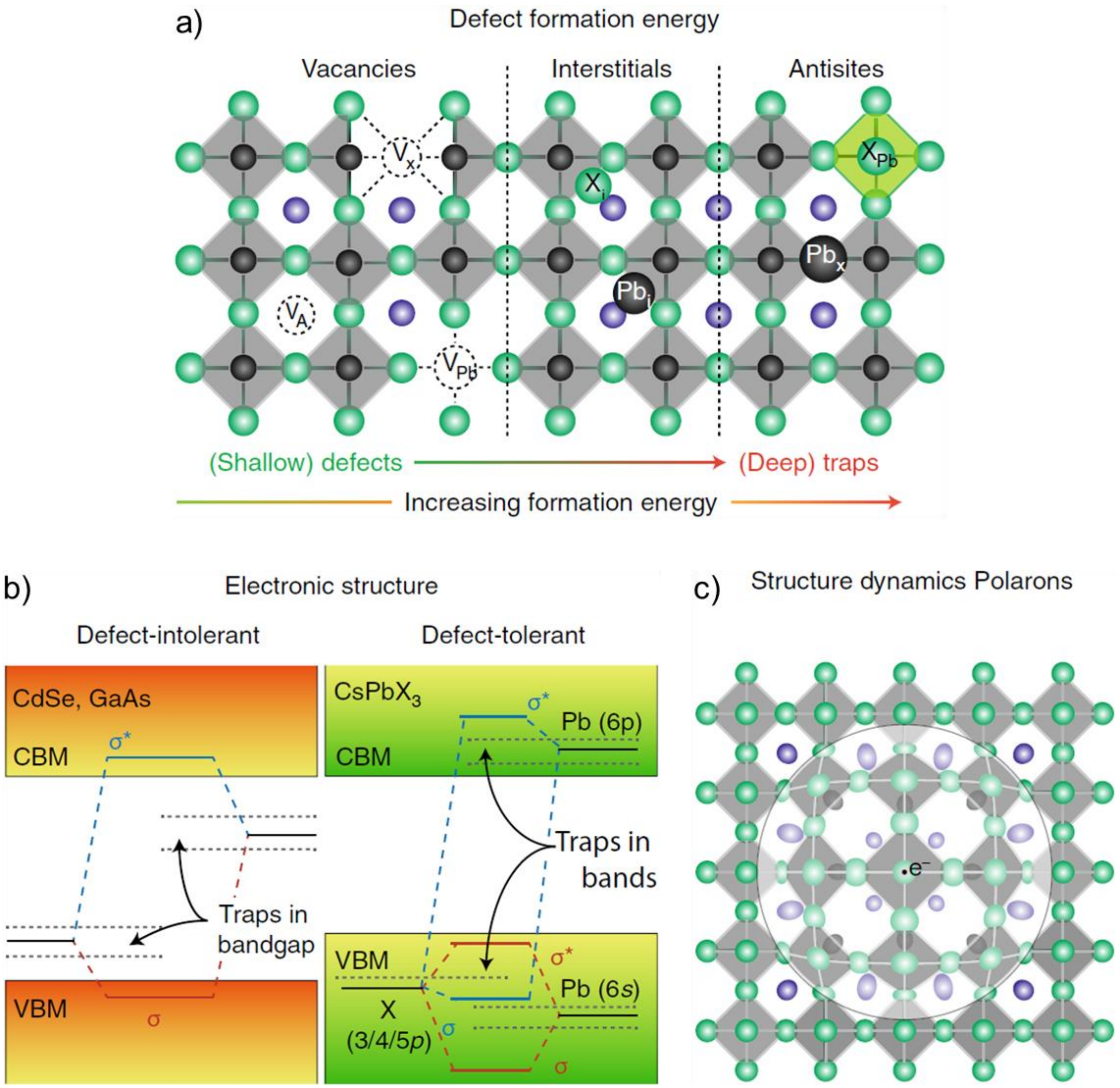

Figure 1.5. a) Possible point defects such as vacancies, interstitial and antisite atoms in perovskite materials. b) Schematic representation of the electronic band structure of typical defect-intolerant semiconductors and defect-tolerant perovskite materials. c) Illustration of local structural deformation of the Pb–X framework that, combined with a charge carrier (electron or hole), forms a polaron (*Adapted from reference 30*).

Defect tolerance refers to the condition in which the intrinsic defects do not function as electronic trap states that are activated by the unique electronic band structure. The defect tolerance of perovskite materials could be explained through three phenomena: i) The possible point defects present in perovskite materials are vacancies and the deep trap states formed by interstitial and antisite defects are almost absent due to their high formation energy (**Figure 1.5a**).[30] ii) The VBM formed from the hybridization of M s and X p orbitals are antibonding in nature (**Figure 1.5b**) whereas, in metal-chalcogenide semiconducting materials, the VBM is formed by bonding orbitals (**Figure 1.5b**). The strong spin-orbit coupling effect in lead halide perovskite materials lowers the CBM down to Pb 6p atomic orbitals (**Figure 1.5b**). Therefore, the energy states related to vacancies (trap states) are buried inside the valance and conduction bands. iii) The local deformation of lead halide framework combined with the charge carriers (electrons/holes) form polarons (**Figure 1.5c**) which help to screen the coulombic potential and reduce trapping and carrier scattering.[36,37] The 'A' site molecular cation present in perovskite material helps to screen the hot carriers resulting in efficient in photoconversion efficiency or hot-carrier photoluminescence.[36,37]

The conventional semiconductors such as Si, CdTe, and GaAs require ultralow concentrations of impurities and crystalline defects (ppb levels) for better performance in optoelectronic devices as their defect states are in between VBM and CBM. On the other hand, lead halide perovskite materials show high photoconversion efficiency even though their defect densities are higher than 2% because their defect states are lying within VBM and CBM. In PNCs, the creation of dangling bonds by removing some of the surface atoms/capping molecules does not introduce any trap states.[38,39] Therefore, PNCs show bright luminescence without any surface passivation. This indicates that the electronic properties of perovskite materials are highly tolerant of their defects and surfaces.[35]

1.3.2. Synthesis of perovskite nanocrystals

The concept of ionicity is one of the most important exponents in lattice dynamics, chemical bonds and so on. J. C. Phillips, an American physicist invented the exact theory of the ionicity of chemical bonding in insulators and semiconductors.[40] He divided the chemical bond in insulators and semiconductors into a covalent part (E_h) and an ionic part (E_c). Phillips ionic character is defined as $f = E_c^2/(E_g^2 + E_h^2)$. The Phillips ionic character equal to one is considered as a purely ionic bond, whereas, zero implies a pure covalent bond. The formation energies for ionic bonds are lower compared to that of covalent bonds. The Philips iconicity value of hybrid perovskite material is in the range of 0.7-0.8, indicating an ionic character.[41] Due to the significant ionic bonding character, the synthesis of PNCs is simpler compared to the synthesis of other traditional semiconducting QDs (Phillips iconicities for GaAs, CdTe, and CdS are 0.31, 0.67 and 0.69 respectively). The PNCs are considered as the arrested co-precipitation of all ions in apolar media in the presence of long chain capping ligands.[41] The synthesis of PNCs has been inspired by the protocols used for the preparation of conventional metal chalcogenide nanocrystals. Perovskite materials are highly crystalline in nature and hence they can form crystalline nanocrystals even at room temperature.[30] The PNCs are generally prepared via template or non-template method which is explained in the following section.

1.3.2.1. Template method

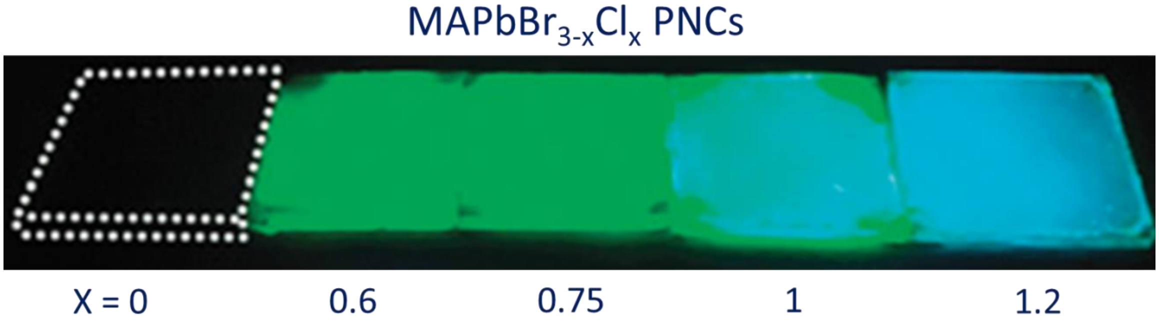

Figure 1.6. Photoluminescence of $CH_3NH_3PbBr_{3-x}Cl_x$ PNCs film after irradiation with UV light (*Adapted from reference 42*).

In this method, mesoporous inorganic oxide nanoparticles such as Al_2O_3, TiO_2, and ZrO_2 are used as templates for the synthesis of PNCs. The size and shape of the nanocrystals are decided by the shape and porosity of the template. In this method, the precursors required for the synthesis of PNCs are dissolved in a suitable solvent such as *N,N*-Dimethyl formamide (DMF). Then, the precursor solution is spin coated onto the mesoporous substrate followed by annealing to form PNCs.[16] Miyasaka *et al*. prepared 2-3 nm sized $CH_3NH_3PbBr_3$ and $CH_3NH_3PbI_3$ nanocrystals using TiO_2 as a scaffold for DSSC application.[5] The nanocrystals interacted with the surface of TiO_2 due to their high surface area. Wang and his team prepared highly luminescent mixed halide $CH_3NH_3PbBr_{3-x}Cl_x$ PNCs (x = 0-1.2) using 50 nm sized mesoporous Al_2O_3 as a scaffold and tuned their emission in the range of 484-530 nm by varying the halogen composition (Br/Cl) in the PNCs structure (**Figure 1.6**).[42] The emission intensity of $CH_3NH_3PbBr_3$ nanocrystals was almost negligible compared to mixed halide PNCs. The excellent photoluminescence intensity of mixed halide PNCs was attributed to their high semiconducting quality and low defect density.

1.3.2.2. Non-template method

In this method, longer alkyl chain capping ligands are used to control the growth and size of PNCs. The capping ligands also provide better colloidal stability to the nanocrystals in different non-polar solvents. In 2014, Prof. J. Pérez-Prieto and coworkers reported for the first time the synthesis of luminescent green emitting $CH_3NH_3PbBr_3$ PNCs via non-template method.[43] The synthesis method was as follows: lead bromide and CH_3NH_3Br precursors were added into a non-coordinated solvent system, 1-octadecence combined with oleic acid and octylamine, at a moderate temperature of 80 °C. The yellow coloured PNCs were formed after the addition of acetone. Then the nanocrystals were precipitated by centrifugation at 7000 rpm followed by washing with acetone. The photoluminescence quantum yield of the nanocrystals was found to be 17% which was further improved to 85% by varying the concentration of organic cations and capping ligands.[44]

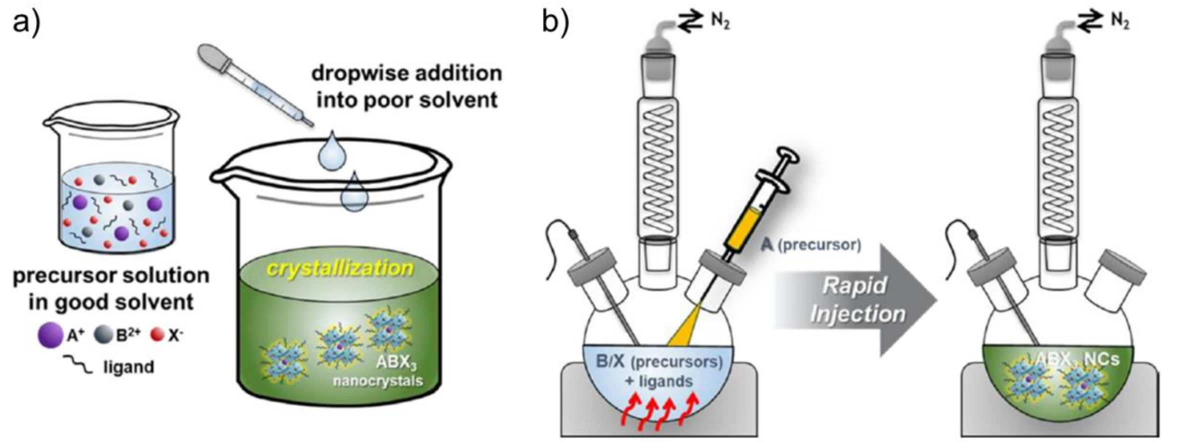

Figure 1.7. Schematic representation of the synthesis of PNCs through a) reprecipitation method and b) hot-injection method (*Adapted from reference 45*).

Though various methods have been adopted for the synthesis of PNCs, ligand assisted reprecipitation (LARP) and hot injection methods are the two methods widely being used. LARP is a room temperature synthetic method developed by Zhang and coworkers which is based on supersaturation induced recrystallization.[46] This method was introduced to avoid the poor solubility of precursors in 1-octadecene. Other advantages of this method are room temperature synthesis, free from the inert atmosphere and injection condition. A schematic representation of the LARP method is shown in **Figure 1.7a**. In this method, the precursors along with capping agents (oleylamine and oleic acid) were dissolved in a polar solvent such as DMF was dropwise added into the non-polar solvent like hexane/toluene/acetone resulting in the formation of PNCs. The non-polar solvent act as a poor solvent for organic cation, metal ions, halide ions and capping ligands. Therefore, the recrystallization process takes place upon liquid transfer and finally, the nanocrystals started to grow rapidly due to supersaturated states of all ions.

Kovalenko *et al.* have developed the synthesis of highly luminescent PNCs by hot injection method.[47] A schematic illustration of the method is shown in **Figure 1.7b**. In this method, a powder of the metal halide salt (PbX_2/SnX_2) is dissolved in a hot solvent such as 1-octadecene containing oleylamine and oleic acid as the surfactants. The nanocrystals are subsequently formed after injecting the organic cation precursor (formamidinium oleate/Cs-oleate) solution into the hot solvent. Then the nanocrystals were separated via centrifugation followed by purification with suitable solvents. The same group has synthesized the first all-inorganic halide PNCs ($CsPbX_3$) using a hot injection method in which Cs-oleate precursor solution was injected into the hot solution containing lead halide, oleic acid and oleylamine in 1-octadecene.[47]

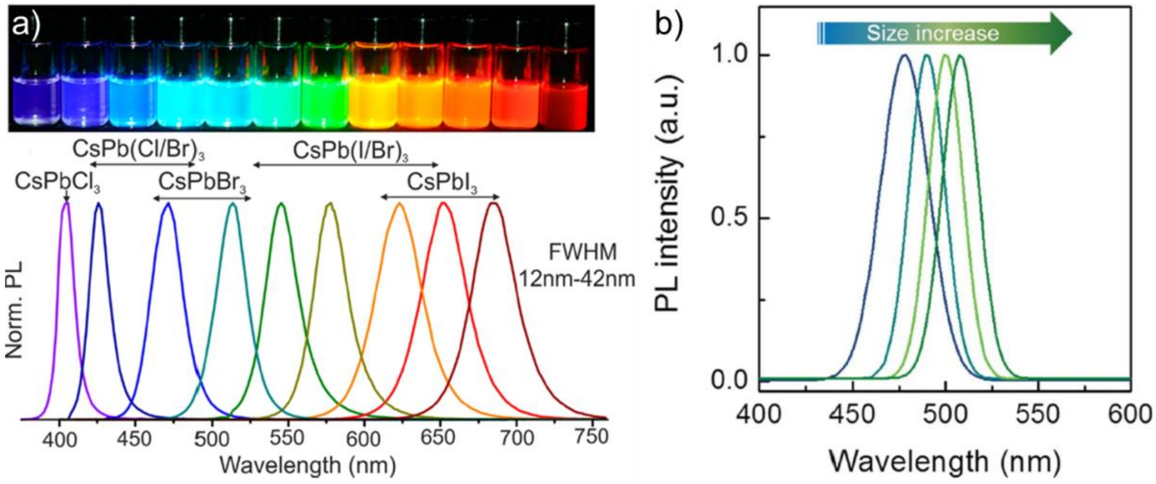

Figure 1.8. a) Tunable bandgap emission of PNCs by varying the halogen composition in their structure. b) The effect of size on the emission bandgap of PNCs (*Adapted from reference 47*).

They also tuned the emission bandgap of these NCs in the entire visible region by varying the halogen composition in the perovskite structure (**Figure 1.8a**). The reaction temperature, reaction time and precursor concentration were also found to play a key role in deciding the size of nanocrystals. The emission bandgap of $CsPbBr_3$ PNCs can be tuned by varying the reaction temperature of solvent between 140-200 °C.[47] High temperature (200 °C) lead to reduce the size of nanocrystals resulting in a blue shift in the emission maximum of nanocrystals compared to that prepared at 140 °C (**Figure 1.8b**).

1.3.2.3. Post synthetic reaction

Apart from direct synthesis, desired perovskite materials could also be obtained through post synthetic reactions such as phase transformation, anion and cation exchange.[48-52] The halide ions in PNCs can be replaced partially or completely with other halide anions or other halide PNCs.[50-52] In the halogen exchange method, the bandgap of PNCs could be varied in the entire visible region without any change in the PLQY indicating the lack of trap states. The rapid anion exchange process is a combined result of ionic properties of perovskite and low activation energy for the formation and diffusion of halide vacancies. The different possibilities of halogen exchange in $CsPbX_3$ PNCs are schematically represented in **Figure 1.9**.

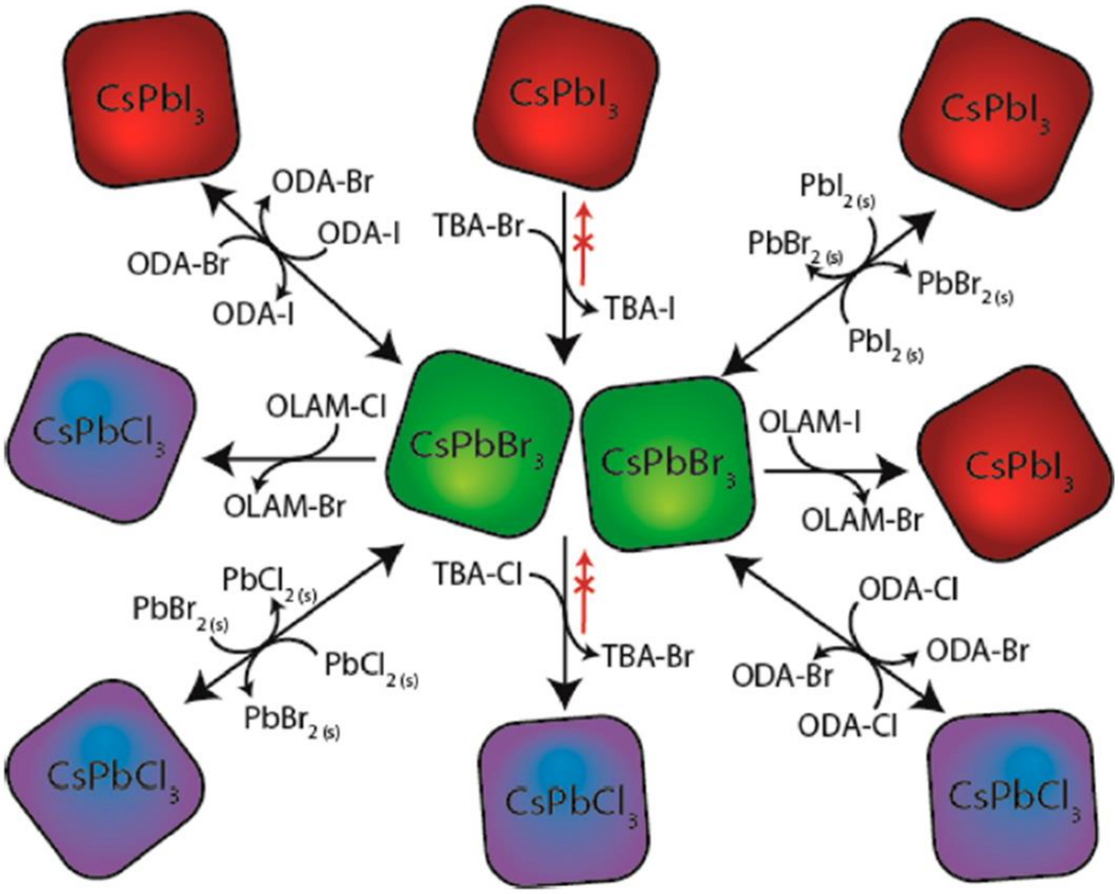

Figure 1.9. Overview of the different routes adopted for the anion exchange reactions in $CsPbX_3$ PNCs (*Adapted from reference 48*).

Dong and coworkers reported the bandgap tuning of $CH_3NH_3PbX_3$ nanocrystals in the whole visible region by the halogen exchange method.[46] They tuned the bandgap of PNCs in the entire visible region by mixing $CH_3NH_3PbBr_3$ PNCs with a suitable concentration of organic cations, CH_3NH_3Cl/CH_3NH_3I. Cation (M^{2+} ion) exchange is more challenging compared to halogen exchange in perovskites due to the high activation energy for cation vacancy formation or interstitial diffusion. Early attempts led to the decomposition of parent PNCs. Later, cation exchange was achieved by incorporating divalent metal cations such as Sn^{2+}, $Cd^{2+,}$ and Zn^{2+} ions into $CsPbBr_3$ based nanocrystals without changing the shape of nanocrystals.[49] In addition to the exchange reactions, the phase transition is also a powerful strategy to tailor the synthesis of PNCs. For, example 0D Cs_4PbBr_6 can be converted into 3D $CsPbBr_3$ by reacting with $PbBr_2$.[51]

1.3.2.4. Capping ligands engineering

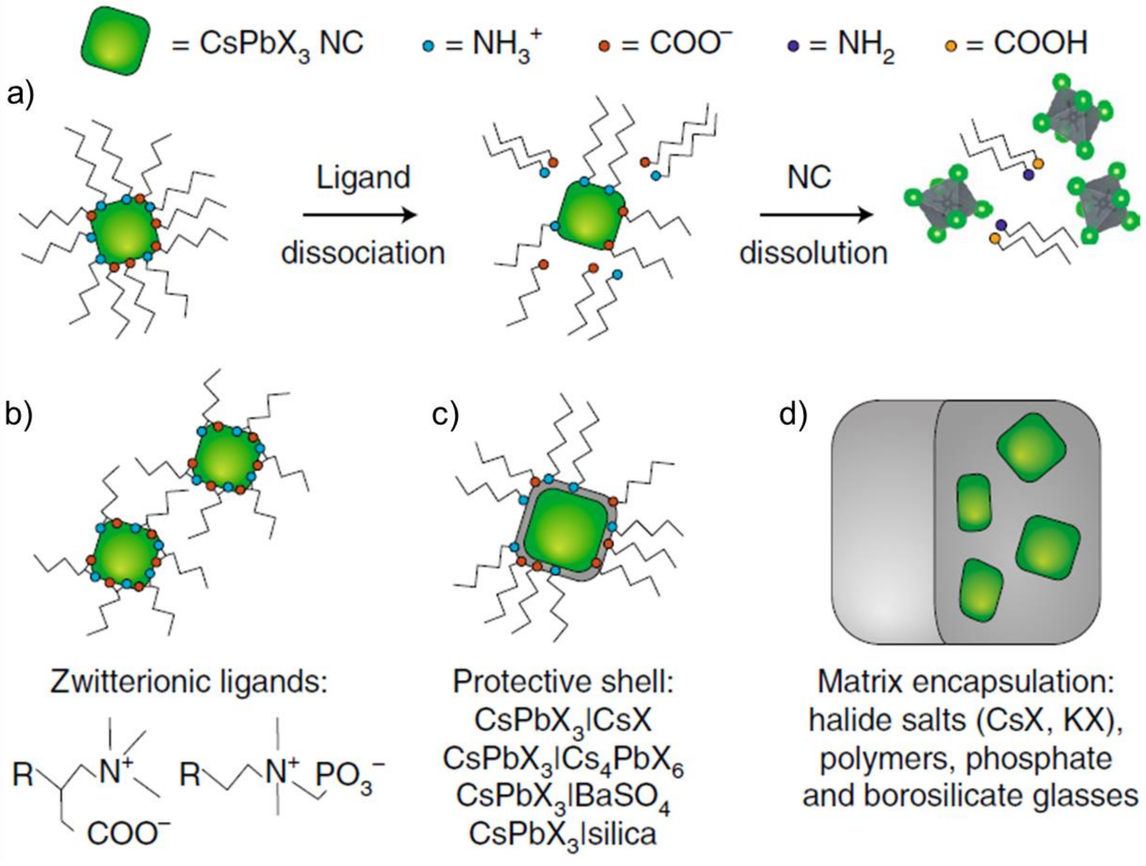

Figure 1.10. Structural lability of PNCs. a) Loss of colloidal stability and structural integrity of PNCs owing to the detachment of weakly bounded capping ligands. b-d) Various approaches adopted for achieving stability of the surface coverage of PNCs via ligands (*Adapted from reference 30*).

Ligands play a key role in the formation and stabilization of PNCs. Larger alkyl chain capping ligands such as oleic acid, oleylamine, and octylamine are commonly used for the synthesis of PNCs. During the synthesis, the capping ligands inhibit the crystal growth, passivate the surface defects and provide colloidal stability to the nanocrystals in a variety of solvents. The PNCs are terminated by oleylammonium bromide alone or in combination with oleylammonium carboxylate. The capping agents coordinate with the surface of nanocrystals as an ionic pair; ammonium groups replace a surface A-site cation, whereas, carboxylates (bromides) act as surface anions. These ligands tend to quickly desorb from the surface of PNCs (**Figure 1.10a**) and hence it is difficult to isolate and purify the PNCs using standard methods (repetitive precipitation with a non-polar solvent followed by redispersion in a pure solvent) reported for traditional QDs.[53] Later, ligands with multiple anchoring groups like zwitter ionic molecules containing both quaternary ammonium and carboxylate/sulphonate/phosphonate groups (**Figure 1.10b**) were introduced to enhance their coordination with the surface of PNCs.[54] Oligomeric capping ligands with a large number of binding sites and long alkyl chains were also introduced to increase their interactions with the surface of PNCs.[30] Although the traditional long chain capping ligands well passivate the surface of PNCs, the fluorescence of PNCs would quench when exposed to polar solvents. Therefore, different passivation strategies have been developed to improve the stability of NCs via ligand engineering. The bulky tail ligands prohibit the formation of a flat surface due to large Van der

Waals repulsion between each other. Compared to straight chain ligands, the branched ligands offer great control over the particle size and uniformity. PNCs with branched ligands (3-aminopropyl) triethoxysilane (APTES) and polyhedral oligomeric silsesquioxane (POSS) were found to show improved stability in protic solvents.[55] The PNCs are highly soluble in water due to the ionic bonding character and low crystal lattice energy. This problem could be solved by coating the surface of nanocrystals with silica/titania/alumina as shown in **Figure 1.10c**. The encapsulation of nanocrystals with polymers/phosphate/borosilicate glasses has also been achieved to improve their stability in water (**Figure 1.10d**). The conducting ligands such as benzylamine, cinnamylamine, and melamine were introduced to improve the charge transport between the PNCs.[56]

Deng and co-workers controlled the shape of NCs by altering the concentration of ligands such as octylamine, dodecylamine, hexanoic acid, and oleic acid.[57] The ligands passivate a particular crystal phase of PNCs, which is similar to the mechanism governing the formation of 2D perovskite layers. The kinetics of these reactions is faster than that of traditional QDs and hence the mechanisms of the reactions are yet to be clarified. New precursors to gain control over the reaction conditions are under investigation, which is essential to stabilize the desirable phases and to control the metal-halide stoichiometry for optimizing their performance in optoelectronics.

1.3.3. Photoluminescence properties

Like bulk perovskite materials, PNCs exhibit strong absorption at energies larger than their bandgap. The bandgap emission of PNCs could be varied in the range of 410-950 nm.[16] The emission spectra of PNCs have a narrow FWHM value with the PLQY upto 100% and the emission from trap states is not yet reported in PNCs. The radiative recombination rate in PNCs is 20 times faster compared to traditional QDs at room temperature. The lowest energy transition in PNCs is allowed transition due to p-orbital characters of both VBM and CBM. The excitions formed by this transition have high exciton binding energy which leads to an increase in the rate of radiative recombination. In addition to the linear properties, multiphoton absorption and emission properties have also been reported in PNCs film.[58]

The excellent PLQY of PNCs led to the investigation of charge carrier dynamics in these nanocrystals. Like other nanoparticles, hybrid and inorganic PNCs films show intermittency in fluorescence (blinking). In general, upon photoexcitation, the light-induced charging/ionization and discharging of the colloidal NCs or trapping of surface electrons can lead to blinking. The neutral semiconducting NCs show a bright emission upon the recombination of photoexcited electron-hole pairs. Nevertheless, charging of NCs promotes Augur recombination and the trap states present in nanocrystals can bind the charge carriers preventing their recombination, which also contributes to photoluminescence blinking.[30-34] Several studies show that blinking in PNCs increases with increasing excitation intensity.[58] Tian *et al*. reported PL blinking of perovskite rods, which was attributed to the photo-induced activation and de-activation of PL quenching sites present at the end of the perovskite rods.[59] The blinking observed in single $MAPbBr_3$ PNCs was ascribed to the occurrence of charge trapping states.[60] Blinking was also observed in all-inorganic $CsPbX_3$ PNCs.[61] Preventing the blinking in PNCs is central to promote their utility in LEDs and biosystems. The ionization could be suppressed by growing a thick semiconductor shell on the NC surface. Yet, there are no reports on the complete arresting of the blinking property in PNCs. However, some results show that blinking of PNCs could be reduced at low temperatures.[62]

1.3.3.1. Quantum confinement effects in PNCs

The optical properties of PNCs do not only depend on the metal and halide ions but also have a strong dependence on their size and dimensionality. A quasi-2D (having thickness of more than one unit cell) and 2D perovskite nanoplatelets having a thickness of one unit cell (**Figure 1.11a**) can be obtained by continuously reducing the lateral dimension of PNC structure through altering the proportions of the two organic cations ($CH_3NH_3^+$ and oleylammonium cations).[63] By this method, the thickness of $MAPbBr_3$ nanoplates was varied between 1-7 units. The exciton binding energy of nanocrystals was increased by reducing the number of inorganic layers due to the quantum confinement effect. The bandgap of 2D perovskite nanoplatelets was decreased as the number of inorganic layers was gradually increasing due to the quantum confinement effect (**Figure 1.11b**).

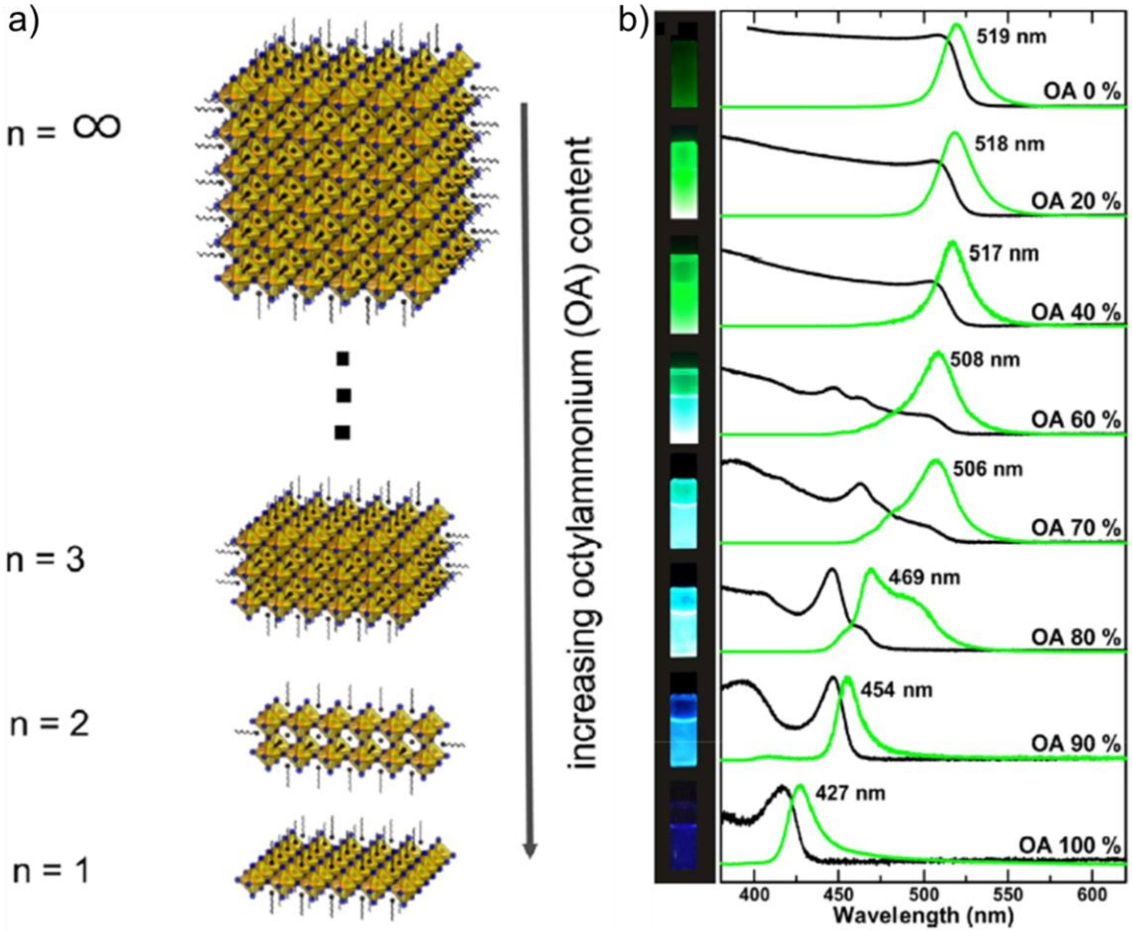

Figure 1.11. a) Schematic representation of $CH_3NH_3PbBr_3$ nanoplatelets with a different number of inorganic layers (n=1,2,3 and ∞). b) The corresponding UV-visible absorption and PL emission spectra of $CH_3NH_3PbBr_3$ perovskite nanoplates showing their bandgap tunable property (*Adapted from reference 63*).

1.3.4. Comparison of PNCs with traditional quantum dots

The PNCs are found to be superior compared to traditional QDs in several aspects.[16,30,64] The traditional QDs require a longer time, high temperature and inert atmosphere for their synthesis, whereas, PNCs can be prepared by a simple synthetic procedure under ambient conditions. The presence of mid trap states in traditional QDs reduces the PLQY and hence a core-shell structure is required to passivate the surface for improving their PLQY. Such surface passivation is not required in the case of PNCs due to their defect tolerant nature and hence they show PLQY of almost 100% without any surface passivation. The solution processable compositional engineering (exchange of organic cation, metal ion, and halide ions) is possible in all three lattice sites (organic cation, metal ion, and halide ion) of PNCs. For example, the phase segregation like $CH_3NH_3PbBr_3$ and $CH_3NH_3PbI_3$ is absent in mixed halide $CH_3NH_3PbBr_{3-x}I_x$ perovskite material. The atomistic homogeneity with high optoelectronic quality is difficult to achieve in traditional QDs. Typically, for the tetrahedrally coordinated compounds, disorder and inhomogeneities are enhanced in the nanocrystal state. The traditional QDs show bright luminescence only when their size is reduced to below Bohr exciton radius (5.6 nm) and a small difference in the size during synthesis leads to the broadening of PL spectra. The smaller sized QDs also lead to self-absorption and FRET due to their size distribution. The preparation of several batches of traditional QDs with similar PL peaks within an error of 5% is challenging. The weak confinement of charge carriers in PNCs is sufficient to show high PLQY. An equal degree of confinement is observed for both electron and hole in PNCs due to their same effective mass. Therefore, the overlapping probability between electrons and holes is high which leads to enhanced radiative recombination (high PLQY). Further, the weakly confined charge carriers (holes and electrons) in PNCs doesn’t affect the batch-batch reproducibility and the narrow FWHM of an ensemble (No change in absorption and emission maximum of PNCs by slightly changing their size). Though PNCs with high PLQY and size independent optical properties are advantageous, the weak confinement of charge carriers in PNCs could affect the tuning of optical properties. This problem could be solved by varying the halogen composition in the PNCs structure. The narrow PL linewidth can effectively suppress the detrimental reabsorption process and interparticle FRET in the PNCs ensemble system. The traditional QDs bandgaps are highly sensitive to temperature, which could change the chromaticity of a LED under operational temperature. But, the optical bandgap of PNCs is generally not affected in the temperature range of 25 °C - 100 °C due to their electronic structure. The optical band of PNCs results from the transition of 6s to 6p transition of Pb^{2+} with less influence of halide ions. Therefore, the thermal expansion could reduce the cation-anion interaction and not the optical bandgap. The photoluminescence in the range of 410-530 nm is easy to obtain in the case of PNCs by a facile single step method, whereas, traditional QDs require a very smaller size (below 5 nm) to emit in this region.

1.4. Applications of perovskite nanocrystals

The research interest in the study of optoelectric properties and potential applications of metal halide perovskites was started in 1958.[2] Moller and his team studied in detail the photoconductivity of $CsPbX_3$ (X = Cl, Br and I) perovskites. Era *et al*. demonstrated the first hybrid perovskite based light emitting device in 1994.[65] They used 2D phenylethylammonium lead iodide, $(C_6H_5C_2H_4NH_3)_2PbI_4$ (PEPI), as the active light emitting layer. The device architecture was ITO/PEPI emitter/oxadiazole derivative/Mg-Ag, similar to standard OLEDs. The electroluminescence spectrum of the device was similar to the photoluminescence spectrum of the PEPI film (emission maximum at 520 nm and FWHM = 10 nm). Mitzi and his team used 2D phenylethylammonium tin iodide, $(C_6H_5C_2H_4NH_3)_2SnI_4$, as channel layers in thin-film transistors.[66] The 2D layered perovskites formed a p-channel transistor which also provided high field-effect mobilities of 0.55-0.62 $cm^2/V \cdot s$ and current modulations greater than 10^4. In 2006, Miyasaka *et al*. introduced 3D hybrid $CH_3NH_3PbBr_3$ perovskites as the sensitizer in the dye-sensitized solar cell. Since 2012, perovskite materials were found to be promising for several other optoelectronic devices. The PNCs are also widely used in various optoelectronic applications such as LEDs, lasers, solar cells, photodetectors, sensors and memory devices due to their unique properties which are mentioned in the previous sections.

1.4.1. Light-emitting diodes

The PNCs are highly suitable for LED applications due to their excellent PLQY, tunable bandgap emission, and narrow FWHM. Perez-Pritto *et al.*[43] used $MAPbBr_3$ PNCs as the active layer in the electroluminescent device, followed by Coasta and coworkers with $MAPbBr_3$ and $FAPbBr_3$ PNCs.[67] Song *et al*. fabricated three different emissive (blue, green and red) $CsPbX_3$ (X = Cl, Br and I) PNCs based LEDs by varying the halogen compositions in PNCs basic structure.[68] Rogach *et al*. introduced a new interfacial perfluorinated ionomer layer to improve the charge carriers injection in the PNCs active layer for intense emission and low operation voltage.[69] Tan and co-workers introduced a trimethylaluminum based cross-linking layer for highly efficient PNCs-LEDs.[70] The cross-layer was not only soluble in the used solvent but also provided more contact with adjacent layers resulting in improved luminescence intensity (2,000 cd/m^2) with higher EQE (5.7%).

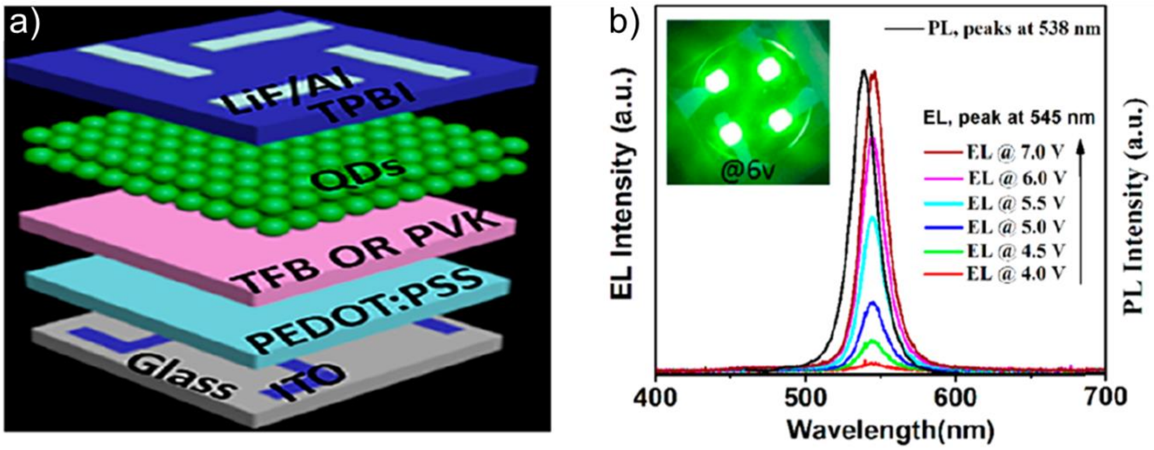

Figure 1.12. a) Schematic representation of a LED device consisting of FAPbBr$_3$ PNCs as the active layer. b) The electroluminescence spectra of the corresponding device with increasing voltage. The device showed bright green colour electroluminescence as shown in the inset of figure 1.12b (*Adapted from reference* 72).

Recently, Sun *et al*. fabricated highly luminescent FAPbBr$_3$ PNCs based LEDs.[71] The schematic representation of the device shown in **Figure 1.12a**. The PNCs active layer showed a very bright green electroluminescence maximum at 545 nm with high colour purity (FWHM ~20 nm) upon increasing the voltage (**Figure 1.12b**). The electroluminescence maximum of the device was slightly red shifted compared to the photoluminescence of nanocrystals dispersed in a solvent. The device showed excellent luminance of 33993 cd m^{-2}, the current efficiency of 20.3 cd A^{-1} and external quantum efficiency of 4.07%. Later, various developments have been made in the PNCs based LEDs for improving their performance as a result of which an EQE of upto 24% has been achieved recently.[72]

The PNCs are also used for the white light generation via the light down conversion method. Snaith and coworkers fabricated $MAPbX_3$ (X = Br, I) quantum dots/polystyrene composites based LEDs for the generation of white light.[73] The white light was also produced from the direct mixing of green and red-emitting $CsPbX_3$ PNCs without using any polymer.[74] This was done by X-ray treatment to prevent the halogen exchange among different halide PNCs. Huang *et al*. coated water-resistant polyhedral oligomeric silsesquioxane (POSS) over PNCs surface not only to arrest the halogen exchange but also to produce stable white light emission.[75]

The well studied semiconducting nanocrystals such as CdSe and InP possess the required properties such as tunable narrow bandgap emission, high PLQY, shorter PL lifetime, chemical processability and durability for the utilization in backlighting. Though InP QDs are non-toxic, their photoluminescence FWHM is 1.5-2 times higher than the PNCs, which is the major drawback for lighting application.[30] Therefore, the use of PNCs in television technologies might be an alternative to InP QDs. However, appropriate aging tests are necessary to ensure a device's lifetime for more than

30,000 hours. Avantama Ltd., a Swiss based company is currently a leader in the development of PNCs based display applications. They have shown that the aging of PNCs based backlight films is more than 1000 hours at a temperature upto 90 °C under ambient conditions. The main advantage is that electronic surface passivation is not required in PNCs and hence the charge carriers injection in PNCs active layer must be easier than InP active layer.

1.4.2. Lasing application

The PNCs are being used in lasing applications due to their high absorption coefficient, optical gain, slow Augur recombination, size tunable optical properties and high PLQY with narrow FWHM (15-25 nm) emission.[31] The lasing performance of PNCs is associated with their carrier lifetime and non-radiative recombination rates. The PNCs showed low threshold lasing and stable wavelength tunable amplified spontaneous emission (ASE). The ASE using pulsed lasers has been demonstrated in densely packed PNCs films and low pumping threshold fluencies are observed in PNCs compared to conventional QDs. Unlike traditional QDs, PNCs exhibit an order of magnitude higher ASE threshold. Weakly confined $CsPbBr_3$ PNCs (~10 nm) exhibited ASE thresholds of about 10 μJ cm^{-2} and the appearance of ASE peak at lower energy side of PL peak suggests a biexcitonic mechanism in PNCs. Two types of lasing modes have been realized in densely packed PNCs films: whispering gallery mode (WGM) lasing in which silica microspheres as high-finest resonators are conformally coated with PNCs and random lasing in films of PNCs.[31,34]

1.4.3. Photodetector application

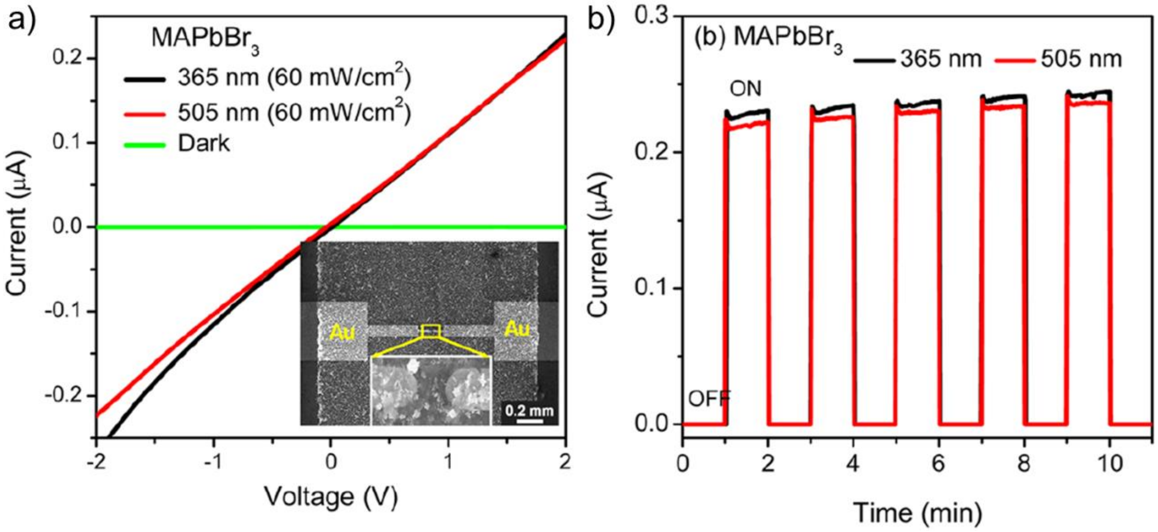

Figure 1.13. a) *I−V* characteristics of MAPbBr$_3$ film under 365 and 505 nm irradiation (60 mW/cm^2) and dark conditions. The SEM image shows the film deposited on Au electrodes with a 2-μm gap (inset). b) The current-time curve at a bias voltage of 2 V under chopped radiation (*Adapted from reference 46*).

The PNCs could be used in photodetector application due to their sensitivity towards visible light and high photovoltage generation, which are also the main parameters for the conversion of solar energy into electrical energy. Song *et al*. reported mixed halide PNCs (MAPbBr$_{3-x}$I$_x$ where, x = 0, 1 and 2) for photodetector application.[46] The devices were fabricated by spin coating the dispersed nanocrystals in toluene between two Au electrodes (on SiO$_x$ substrates) separated by a gap of 2 μm. The current-voltage (*I−V*) curves of a MAPbBr$_3$ PNCs based photodetector under dark and 365 nm/ 505 nm light is shown in **Figure 1.13a**. The inset of **Figure 1.13a** shows a scanning electron microscopy image of a photodetector device. The $I-V$ curves are almost linear within the measured range from -2 to 2 V and the dark current was found to be ~1 pA. The real-time (*I*-*t*) curves collected at a bias voltage of 2 V under a series of on-off cycles are shown in **Figure 1.13b**. A strong correlation was observed between the photocurrents and PL decay times of different halide PNCs. Among the mixed halide PNCs, I-rich alloy, $MAPbBrI_2$ PNCs exhibited the highest photocurrent due to their long PL decay time ascribed to its pure tetragonal phase nature. Wang *et al*. fabricated a photodetector using a bilayer consisting of mp-TiO_2 and $CsPbBr_3$ PNCs composite.[76] The device showed three times higher on/off ratio and 44 times better photoresponsivity compared to $CsPbBr_3$ PNCs alone based photodetector due to better charge carriers injections into the TiO_2 layer.

1.4.4. Solar cell application

The bulk hybrid perovskite materials based solar cells have recently reached an efficiency upto 25.2%.[8] But, the thin-film perovskite active layers undergo fast degradation in the presence of both heat and humidity. Recently, the PNCs have been used as light absorbing material in solar cell application to improve the environmental stability of solar cells. Luther and coworkers synthesized phase stable α-$CsPbI_3$ PNCs for the fabrication of photovoltaic devices.[77] The schematic representation and cross-sectional SEM image of the device are shown in **Figure 1.14**. The devices showed an open-circuit voltage of 1.23 V with the power conversion efficiency upto 10.77% (**Figure 1.14c**) which are the highest values compared to till now reported PNCs based solar cells.[77] Various other PNCs have also been used as the photon absorbing layer in the solar cell application.[31]

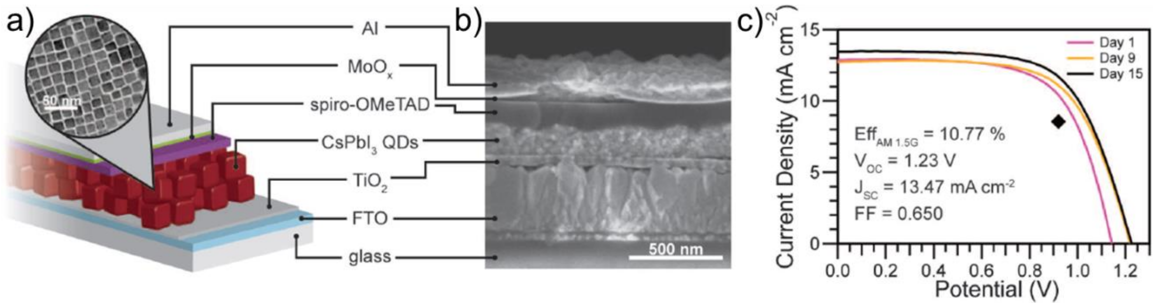

Figure 1.14. a) Schematic representation of α-$CsPbI_3$ PNCs based photovoltaic (PV) cell and TEM image of NCs. b) Cross-sectional SEM image of the PV cell. c) The characteristic *I-V* curve of a device measured at ambient condition over 15 days. The black diamond symbol indicates the stabilized power output of the device at 0.92 V (*Adapted from reference* 77).

1.4.5. Miscellaneous applications

Apart from the above mentioned applications, PNCs are also found to be a good catalytic reservoir in the Finkelstein exchange reaction, which is essential for different synthetic reactions and a colorimetric assay of free ions in solution.[78] Su *et al*. reported $CsPbBr_3$/graphene oxide composite for the photocatalytic reduction of CO_2 into solar fuels.[79] The tunable emission and lifetime properties of PNCs render this material more suitable for security applications.[80] The narrow and symmetric PL spectrum property of PNCs are difficult to reproduce with other materials. Theoretically, the number of achievable colour combinations in PNCs can be estimated as n^m where 'n' is the number of intensities and 'm' is the number of emission bands. Based on this 10,000 unique barcodes could be detected with conventional low-cost spectrometers. Piezoelectric properties of PNCs were demonstrated using $FAPbBr_3$ PNCs/polydimethylsiloxane polymer composite.[81] Fu *et al*. reported water resistant $CsPbX_3$ NCs (X = Cl, Br & I) @ polystyrene MHSs (MHSs-microhemispheres) for the multicolour luminescence probes in live cells.[82]

1.5. Objectives of the present investigation

Recent literature reports suggest that PNCs are promising candidates for various optoelectronic applications due to their unique properties. Inspired by the developments, we have synthesized a few hybrid PNCs to study their photophysical properties and optoelectronic applications. **In Chapter 2**, we have studied in detail, the fluorescence resonance energy transfer (FRET) and acceptor properties of PNCs using various energy acceptors and donors, respectively. The light-harvesting antenna property of luminescent $CH_3NH_3PbBr_3$ PNCs was studied using rhodamine B and rhodamine 101 dyes as energy acceptors. Subsequently, the energy acceptor properties of PNCs were studied using polyfluorene (PF) as an energy donor. Interestingly, a stable white emission was generated from PF/$CsPbBr_{1.5}Cl_{1.5}$ composite via energy transfer from PF donor to PNCs. **Chapter 3** deals with the electron transfer property of PNCs and its application in sensing. The excitation energy migration and electron transfer properties of $FAPbBr_3$ PNCs were studied comprehensively. The closely packed PNCs in a thin film showed extended fluorescence lifetime (ca. 4.2 μs), which is due to the hopping or migration of photogenerated excitons among PNCs. Both fluorescence quantum efficiency and lifetime decreased in films doped with fullerene (C_{60}), which was attributed to channeling of exciton migration into electron transfer to C_{60}. Then, $CH_3NH_3PbBr_3$ PNCs were used for the sensing of picric acid and the sensing mechanism was based on the fluorescence quenching of PNCs due to efficient electron transfer from PNCs to picric acid molecules. In **Chapter 4**, we have developed visibly opaque NIR transmitting filters from α-$FAPbI_3$ PNCs. This was achieved by passivating the surface of PNCs with squaraine (SQ) dye molecules. The α-$FAPbI_3$ PNCs/SQ composite can be used for the security and NIR photography applications. In **Chapter 5**, we described the use of hybrid lead halide PNCs for high performance, air-stable, nonvolatile memory devices through low-cost solution processing techniques at ambient conditions. The write-erase voltages of the devices reduced from 2 V to 0.5 V by replacing bromide with chloride ions in the basic structure of the nanocrystals ($CH_3NH_3PbBr_3$). Though the on/off voltage dropped, the on/off ratio, retention, and endurance of the devices were enhanced on chloride doping. In **Chapter 6**, we have studied in detail the phase effect on the memristor properties of α- and δ- $FAPbI_3$ PNCs. Unlike bulk α-$FAPbI_3$ perovskite material, its corresponding PNCs showed resistive switching which is due to the weak interactions between the iodide vacancies in nanocrystals. The δ-$FAPbI_3$ nanorods also showed memristor property with a better on/off ratio compared to α-$FAPbI_3$ PNCs.

1.6. References

1. D. B. Mitzi, Synthesis, structure, and properties of organic-inorganic perovskites and related materials in Progress in Inorganic Chemistry, John Wiley & Sons, Inc. **2007**, *48*, 1-121.
2. C. K. Moller, *Nature* **1958**, *182*, 1436.
3. D. Weber, Inst. Anorg. Chem. Univ. Stutt. **1978**, *33b*, 1443-1445.
4. A. Kojima, K. Teshima, T. Miyasaka, Y. Shirai, Proc. 210th ECS Meeting, ECS, **2006**.
5. A. Kojima, K. Teshima, Y. Shirai, T. Miyasaka, *J. Am. Chem.Soc*. **2009**, *131*, 6050-6051.
6. J.-H. Im, C.-R. Lee, J.-W. Lee, S.-W. Park, N.-G. Park, *Nanoscale* **2011**, *3*, 4088-4093.
7. H. S. Kim, C. R. Lee, J. H. Im, K. B. Lee, T. Moehl, A. Mar-chioro, S. J. Moon, R. Humphry-Baker, J. H. Yum, J. E. Moser, M. Gratzel, N. G. Park, *Sci. Rep.* **2012**, *2*, 591.
8. https://www.nrel.gov/pv/assets/pdfs/best-research-cell-efficiencies. (Dated on 15.03.2020).
9. W. Li, Z. Wang, F. Deschler, S. Gao, R. H. Friend, A. K. Cheetham, *Nat. Mater.* **2017**, *2*, 16099.
10. J. Huang, Y. Yuan, Y. Shao, Y. Yan, *Nat. Mater.* **2017**, *2*, 17042.
11. B. Saparov, D. B. Mitzi, *Chem. Rev.* **2016**, *116*, 4558-4596.
12. J. S. Manser, J. A. Christians, P. V. Kamat, *Chem. Rev.* **2016**, *21*, 12956-13008.
13. Y. Zhao, K, Zhu, *Chem. Soc. Rev.* **2016**, *45*, 655-689.

14. K. Chen, S. Schunemann, S. Song, H. Tuysuz, *Chem. Soc. Rev.* **2018**, *47*, 7045-7077.
15. P. You, G. Tang, F. Yan, *Mater. Today Energy* **2019**, *11*, 128-158.
16. S. Gonzalez-Carrero, R. E. Galian, J, Pérez-Prieto, *OPTICS EXPRESS A* **2016**, *24*, 285-301.
17. W. Travis, E. N. K. Glover, H. Bronstein, D. O. Scanlon, R. G. Palgrave, *Chem. Sci.* **2016**, *7*, 4548-4556.
18. G. Kieslich, S. Sun, A. K. Cheetham, *Chem. Sci*. **2015**, *6*, 3430-3433.
19. D. Chen, X. Chen, Z. Wan, G. Fang, *ACS Appl. Mater. Interfaces* **2017**, *9*, 20671-20678.
20. L. Protesescu, S. Yakunin, S. Kumar, J. Bär, F. Bertolotti, N. Masciocchi, A. Guagliardi, M. Grotevent, I. Shorubalko, M. I. Bodnarchuk, C.-J. Shih, M. V. Kovalenko, *ACS Nano* **2017**, *11*, 3119-3134.
21. V. K. Ravi, G. B. Markad, A. Nag, *ACS Energy Lett.* **2016**, *1*, 665-671.
22. I. Borriello, G. Cantele, D. Ninno, *Phys. Rev. B* **2008**, *77*, 235214.
23. Y. H. Chang, C. H. Park, *J. Korean Phys. Soc.* **2004**, *44*, 889-893.
24. S. Pang, H. Hu, J. Zhang, S. Lv, Y. Yu, F. Wei, T. Qin, H. Xu, Z.Liu, G. Cui, *Chem. Mater*. **2014**, *26*, 1485-1491.
25. G. E. Eperon, S. D. Stranks, C. Menelaou, M. B. Johnston, L. M. Herz, H. J. Snaith, *Energy Environ. Sci.* **2014**, *7*, 982-988.
26. S. Aharon, A. Dymshits, A. Rotem, L. Etgar, *J. Mater. Chem. A* **2015**, *3*, 9171-9178.
27. J. M. Frost, K. T. Butler, F. Brivio, C. H. Hendon, M. van Schilf-gaarde, A. Walsh, *Nano Lett.* **2014**, *14*, 2584-2590.
28. Y. Ogomi, A. Morita, S. Tsukamoto, T. Saitho, N. Fujikawa, Q. Shen, T. Toyoda, K. Yoshino, S. S. Pandey, T. Ma, S. Hayase, *J. Phys. Chem. Lett.* **2014**, *5*, 1004-1011.
29. S. P. R. D. Madan, *Mod. Inorg. Chem.* **1987**, 207-212.

30. Q. A. Akkerman, G. Rainò, M. V. Kovalenko, L. Manna, *Nat. Mater*. **2018**, *17*, 394-405.
31. H. Huang, L. Polavarapu, J. A Sichert, A. S. Susha, A. S. Urban, A. L. Rogach, *NPG Asia Mater*. **2016**, *8*, e328 (1-15).
32. M. V. Kovalenko, L. Protesescu, M. I. Bodnarchuk, *Science* **2017**, *358*, 745-750.
33. S. Bai, Z. Yuan, F. Gao, *J. Mater. Chem. C* **2016**, *4,* 3898-3904.
34. D. Amgar, S. Aharon, L. Etgar, *Adv. Funct. Mater.* **2016**, *26*, 8576-8593.
35. H. Huang, M. I. Bodnarchuk, S. V. Kershaw, M. V. Kovalenko, A. L. Rogach, *ACS Energy Lett*. **2017**, *2*, 2071-2083.
36. H. Zhu, K. Miyata, Y. Fu, J. Wang, P. P. Joshi, D. Niesner, K. W. Williams, S. Jin, X.-Y. Zhu, *Science* **2016**, *353*, 1409-1413.
37. A. A. Bakulin, O. Selig, H. J. Bakker, Y. L. A. Rezus, C. Müller, T. Glaser, R. Lovrincic, Z. Sun, Z. Chen, A. Walsh, J. M. Frost, T. L. C. Jansen, *J. Phys. Chem. Lett.* **2015**, *6*, 3663-3669.
38. S. ten Brinck, I. Infante, *ACS Energy Lett.* **2016**, *1*, 1266-1272.
39. G. R. Yettapu, D. Talukdar, S. Sarkar, A. Swarnkar, A. Nag, P. Ghosh, P. Mandal, *Nano Lett.* **2016**, *16*, 4838-4848.
40. J. C. Phillips, *Rev. Mod. Phys*. **1970**, *42,* 317-356.
41. M. V. Kovalenko, M. I. Bodnarchuk, *CHIMIA* **2017**, *71*, 461-470.
42. M. Zhang, H. Yu, M. Lyu, Q. Wang, J.-H. Yun, L. Wang, *Chem. Commun.* **2014**, *50*, 11727-11730.
43. L. C. Schmidt, A. Pertegás, S. González-Carrero, O. Malinkiewicz, S. Agouram, G. M. Espallargas, H. J. Bolink, R. E. Galian, J. Pérez-Prieto, *J. Am. Chem. Soc.* **2014**, *136,* 850-853.
44. S. Gonzalez-Carrero, R. E. Galian, J. P´erez-Prieto, *J. Mater. Chem. A* **2015**, *3,* 9187-9193.
45. J. Sun, J. H. Yang, J. I. Lee, J. H. Cho, M. S. Kang, *J. Phys. Chem. Lett*. **2018**, *9*, 1573-1583.

46. F. Zhang, H. Zhong, C. Chen, X.-G. Wu, X. Hu, H. Huang, J. Han, B. Zou, Y. Dong, *ACS Nano* **2015**, *9*, 4533-4542.
47. L. Protesescu, S. Yakunin, M. I. Bodnarchuk, F. Krieg, R. Caputo, C. H. Hendon, R. X. Yang, A. Walsh, M. V. Kovalenko, *Nano Lett.* **2015**, *15*, 3692-3696.
48. Q. A. Akkerman, V. D'Innocenzo, S. Accornero, A. Scarpellini, A. Petrozza, M. Prato, L. Manna, *J. Am. Chem. Soc.* **2015**, *137*, 10276-10281.
49. W. Stam, J. J. Geuchies, T. Altantzis, K. H. W. Bos, J. D. Meeldijk, S. V. Aert, S. Bals, D. Vanmaekelbergh, C. M. Donega, *J. Am. Chem. Soc.* **2017**, *139*, 4087-4097.
50. R. Begum, M. R. Parida, A. L. Abdelhady, B. Murali, N. M. Alyami, G. H. Ahmed, M. N. Hedhili, O. M. Bakr, O. F. Mohammed, *J. Am. Chem. Soc*. **2017**, *139*, 731-737.
51. T. Udayabhaskararao, L. Houben, H. Cohen, M. Menahem, I. Pinkas, L. Avram, T. Wolf, A. Teitelboim, M. Leskes, O. Yaffe, D. Oron, M. Kazes, *Chem. Mater.* **2018**, *30*, 184-193.
52. G. Nedelcu, L. Protesescu, S. Yakunin, M. I. Bodnarchuk, M. J. Grotevent, M. V. Kovalenko, *Nano Lett.* **2015**, *15*, 5635-5640.
53. J. D. Roo, M. Ibáñez, P. Geiregat, G. Nedelcu, W. Walravens, J. Maes, J. C. Martins, I. V. Driessche, M. V. Kovalenko, Z. Hens, *ACS Nano* **2016**, *10*, 2071-2081.
54. F. Krieg, S. T. Ochsenbein, S. Yakunin, S. Brinck, P. Aellen, A. Süess, B. Clerc, D. Guggisberg, O. Nazarenko, Y. Shynkarenko, S. Kumar, C.-J. Shih, I. Infante, M. V. Kovalenko**,** *ACS Energy Lett.* **2018**, *33*, 641-646.
55. B. Luo, Y.-C. Pu, S. A. Lindley, Y. Yang, L. Lu, Y. Li, X. Li, J. Z. Zhang, *Angew. Chem. Int. Ed.* **2016**, *55*, 8864-8868.
56. J. Dai, J. Xi, L. Li, J. F. Zhao, Y. Shi, W. Zhang, C. Ran, B. Jiao, X. Hou, X. Duan, Z. Wu, *Angew. Chem. Int. Ed*. **2018**, *57*, 5754-5758.
57. S. Sun, D. Yuan, Y. Xu, A. Wang, Z. Deng, *ACS Nano* **2016**, *10*, 3648-3657.

58. Y. Wang, H. Sun, *Small Methods* **2017**, *2*, 1700252 (1-27).
59. Y. Tian, A. Merdasa, M. Peter, M. Abdellah, K. Zheng, C. S. Jr Ponseca, T. Pullerits, A. Yartsev, V. Sundstrom, I. G. Scheblykin, *Nano Lett.* **2015**, *15*, 1603-1608.
60. T. Tachikawa, I. Karimata, Y. Kobori, *J. Phys. Chem.Lett.* **2015**, *6*, 3195-3201.
61. Y. S. Park, S. Guo, N. S. Makarov, V. I. Klimov, *ACS Nano* **2015**, *9*, 10386-10393.
62. G. Rainò, G. Nedelcu, L. Protesescu, M. I. Bodnarchuk, M. V. Kovalenko, R. F. Mahrt, T. Stöferle, *ACS Nano* **2016**, *10*, 2485-2490.
63. J. A. Sichert, Y. T. N. Mutz, M. Vollmer, S. Fischer, K. Z. Milowska, R. G. Cortadella, B. Nickel, C. Cardenas-Daw, J. K. Stolarczyk, A. S. Urban, J. Feldmann, *Nano Lett.* **2015**, *15*, 6521-6527.
64. A. Swarnkar, R. Chulliyil, V. K. Ravi, M. Irfanullah, A. Chowdhury, A. Nag, *Angew. Chem. Int. Ed.* **2015**, *54,* 15424-15428.
65. M. Era, S. Morimoto, T. Tsutsui, S. Saito, *Appl. Phys. Lett.* **1994**, *65*, 676-678.
66. C. R. Kagan, D. B. Mitzi, C. D. Dimitrakopoulos, *Science* **1999**, *286*, 945-947.
67. M. F. Aygüler, M. D. Weber, B. M. D. Puscher, D. D. Medina, P. Docampo, R. D. Costa, *J. Phys. Chem. C* **2015**, *119*, 12047-12054.
68. J. Song, J. Li, X. Li, L. Xu, Y. Dong, H. Zeng, *Adv. Mater.* **2015**, *27*, 7162-7167.
69. X. Zhang, H. Lin, H. Huang, C. Reckmeier, Y. Zhang, W. C. H. Choy, A. L. Rogach, *Nano Lett.* **2016**, *16*, 1415-1420.
70. G. Li, F. W. R. Rivarola, N. J. L. K. Davis, S. Bai, T. C. Jellicoe, F. Peña, S. Hou, C. Ducati, F. Gao, R. H. Friend, N. C. Greenham, Z.-K. Tan, *Adv. Mater.* **2016**, *28*, 3528-3534.
71. Q. Li, H. Li, H. Shen, F. Wang, F. Zhao, F. Li, X. Zhang, D. Li, X. Jin, W. Sun, *ACS Photonics* **2017**, *4*, 2504-2512.
72. T. Chiba1, Y. Hayashi, H. Ebe, K. Hoshi, J. Sato, S. Sato, Y.-J. Pu, S. Ohisa, J. Kido, *Nat. Photon.* **2018**, *12*, 681-687.

73. S. Pathak, N. Sakai, F. W. R. Rivarola, S. D. Stranks, J. Liu, G. E. Eperon, C. Ducati, K. Wojciechowski, J. T. Griffiths, A. A. Haghighirad, A. Pellaroque, R. H. Friend, H. J. Snaith, *Chem. Mater.* **2015**, *27*, 8066-8075.
74. F. Palazon, F. D. Stasio, Q. A. Akkerman, R. Krahne, M. Prato, L. Manna, *Chem. Mater*. **2016**, *28*, 2902-2906.
75. H. Huang, B. Chen, Z. Wang, T. F. Hung, A. S. Susha, H. Zhong, A. L. Rogach, *Chem. Sci*. **2016**, *7*, 5699-5703.
76. L. Zhoua, K. Yuaa, F. Yanga, J. Zhenga, Y. Zuo, C. Lia, B. Chenga, Q. Wang, *Dalton Trans*. **2017**, *46*, 1766-1769.
77. A. Swarnkar, A. R. Marshall, E. M. Sanehira, B. D. Chernomordik, D. T. Moore, J. A. Christians, T. Chakrabarti, J. M. Luther, *Science* **2016**, *354*, 92-95.
78. T. L. Doane, K. L. Ryan, L. Pathade, K. J. Cruz, H. Zang, M. Cotlet, M. M. Maye, *ACS Nano* **2016**, *10*, 5864-5872.
79. Y.-F. Xu, M.-Z. Yang, B.-X. Chen, X.-D. Wang, H.-Y. Chen, D.-B. Kuang, C.-Y. Su, *J. Am. Chem. Soc.* **2017**, *139*, 5660-5663.
80. H. Wang, H. Lin, X. Piao, P. Tian, M. Fang, X. An, C. Luo, R. Qi, Y. Chena, H. Peng, *J. Mater. Chem. C* **2017**, *5*, 12044-12049.
81. R. Ding, H. Liu, X. Zhang, J. Xiao, R. Kishor, H. Sun, B. Zhu, G. Chen, F. Gao, X. Feng, J. Chen, X. Chen, X. Sun, Y. Zheng, *Adv. Funct. Mater.* **2016**, *26*, 1-9.
82. H. Zhang, X. Wang, Q. Liao, Z. Xu, H. Li, L. Zheng, H. Fu, *Adv. Funct. Mater*. **2017**, *27*, 1604382 (1-8).

Chapter 2

Energy Transfer Properties of Perovskite Nanocrystals

2.1. Abstract

Though luminescent hybrid perovskite nanocrystals are suitable for most of the optoelectronic applications, their potential use as a light-harvesting antenna in artificial photosynthesis systems is not yet explored. In this chapter, the fluorescence resonance energy transfer (FRET) properties of PNCs were studied using suitable energy acceptors and donor. Use of luminescent $CH_3NH_3PbBr_3$ *nanocrystals as an energy donor and rhodamine B and rhodamine 101 dyes as energy acceptors revealed that efficient FRET occurs from the nanocrystals to the dyes. Further, the energy transfer efficiency was found to be dependent on the number of anchoring groups and binding ability of the dyes to the surface of the nanocrystals. The use of PNCs as an energy acceptor was also explored using polyfluorene (PF) as an energy donor. Interestingly, stable white light emission was generated from PF/PNC composite via energy transfer from PF to PNCs. These observations may have significant implications for perovskite-based light-harvesting devices and their possible use in artificial photosynthesis systems.*

2.2. Introduction

Photosynthesis is the process used by plants, algae, and certain bacteria to harness energy from sunlight and turn it into chemical energy. This is one of the most important and fundamental natural processes responsible for life on earth and has been subjected to numerous studies. In this process, the solar light energy is harvested via photon absorption and tunneled to reaction centers through energy and electron transfer processes for the conversion of carbon dioxide and water into sugar and oxygen. A schematic diagram illustrating the different processes involved in photosynthesis in plants is shown in **Figure 2.1**.

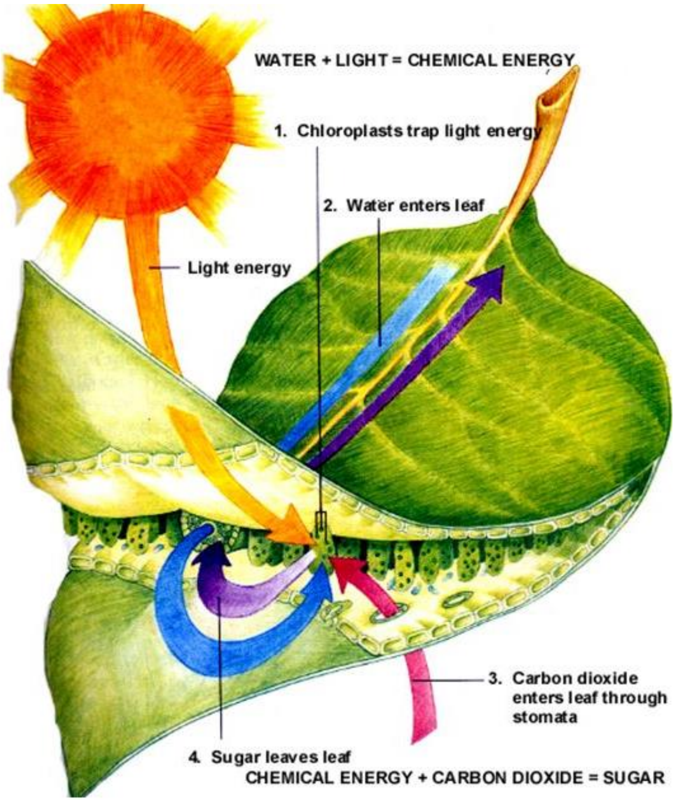

Figure 2.1. Schematic representation of natural photosynthesis in plants (*Adapted from reference 1*).

Inspired from the natural photosynthesis, chemists have been attempting to mimic such processes using various synthetic materials consisting of covalent or supramolecular systems.[2-5] Further interest in this area was evolved due to the research in advanced materials for optoelectronic devices, where energy and electron-transport processes at the nanoscale play important roles.[6,7] For instance, FRET along donor/acceptor arrays was found to be a successful strategy to improve the power conversion efficiency of photovoltaic devices.[8-11]

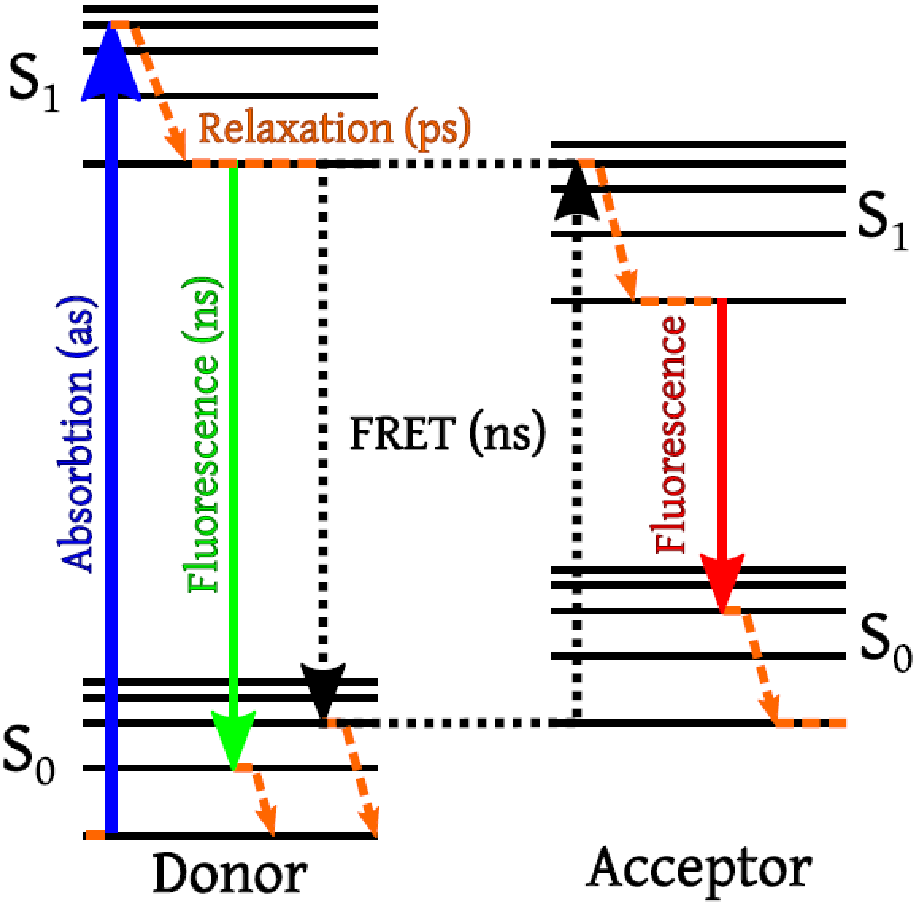

Figure 2.2. Schematic representation of FRET indicating non-radiative energy transfer from excited state donor to ground state acceptor (All non-radiative transitions are indicated by dotted lines) (*Adapted from reference 12*).

The dipole-dipole interactions between the excited state donor and ground state acceptor results in efficient FRET from an excited donor to a ground-state acceptor. A schematic diagram of the FRET process is shown in **Figure 2.2**. In this process, the donor absorbs light energy and goes to the excited state. Then, the excited state donor transfers its energy to the ground state acceptor through a non-radiative manner, which results in the fluorescence quenching of donor with the concomitant emission from the acceptor. The rate and efficiency of energy transfer process depends on different factors such as the extent of overlap between the donor emission and acceptor absorption, relative orientation between the dipoles of donor/acceptor pair, and the distance between them (10-100 Å).[13,14]

The use of conventional organic fluorophores for FRET has certain limitations. For example, the narrow excitation region and broad emission spectrum of organic molecules lead to self-absorption and direct excitation of the acceptor. On the other hand, semiconductor nanoparticles (NP) and quantum dots (QD) are found to be an alternative to conventional organic chromophoric systems due to their superior properties.[15-17] The selective excitation of NPs/QDs is possible due to its broad absorption spectra which restricts the direct excitation of acceptor molecules. The spectral overlap between the NPs/QDs and acceptors could be enhanced by tuning their bandgap emission. They also possess a high molar extinction coefficient (10^5-10^6 $M^{-1}cm^{-1}$), longer fluorescence lifetimes, and greater stability against photobleaching. Furthermore, the large number of binding sites present on the surface of NPs/QDs provides easy accessibility to multiple dye molecules enabling efficient FRET. The NPs/QDs based FRET systems are widely used in numerous applications such as sensing, bio labeling, luminescence tagging, imaging, medical diagnostics, multiplexing, and solar energy harvesting.[15-17]

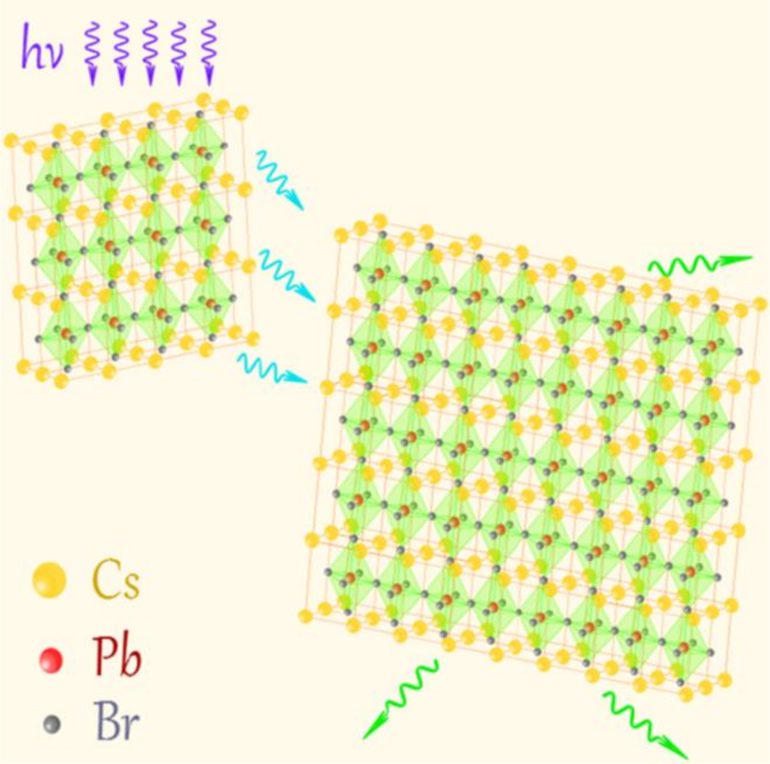

Figure 2.3. Schematic diagram representing the energy transfer process from smaller PNCs to the bigger one (*Adapted from reference 18*).

Though hybrid perovskite materials are found to be promising for different applications, the light-harvesting antenna property of these materials is not explored except two recent reports.[18,19] Gregorkiewicz *et al.* reported the energy transfer between $CsPbBr_3$ PNCs of dissimilar sizes.[18] A schematic diagram representing the energy transfer process from smaller $CsPbBr_3$ PNCs to bigger ones is shown in **Figure 2.3**. Efficient energy transfer was observed from 8.4 nm sized PNCs to 18.3 nm sized PNCs. As a result, the emission intensity corresponding to smaller sized nanocrystals was decreased with the concomitant emission of bigger sized nanocrystals. This energy transfer process was further confirmed from the time-resolved PL studies. Based on this, the authors suggested that a minimum of 35% energy transfer occurs from smaller to bigger PNCs.

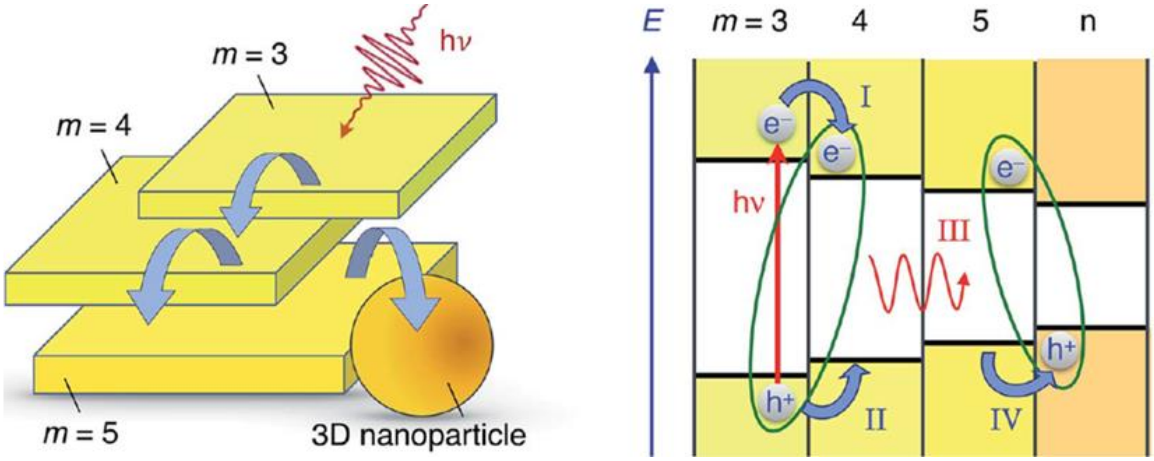

Figure 2.4. Schematic representation showing the energy/charge transfer processes from smaller to bigger sized quasi 2D $CH_3NH_3PbBr_3$ nanoplatelets. The numbers 3, 4 and 5 indicate the number of inorganic layers in 2D perovskite nanoplatlets (*Adapted from reference 19*).

Moser *et al.* studied in detail the cascade energy and charge transfer processes between different layered quasi-2D perovskite nanoplatelets along with 3D $CH_3NH_3PbBr_3$ PNCs using various analytical techniques.[19] They observed efficient energy and/or charge transfer cascade from low thickness quasi-2D perovskite nanoplatelets to high thickness nanoplatelets which were schematically represented by curved blue arrows as shown in the left side of **Figure 2.4a**. Various photophysical processes of cascade charge and energy transfer between different perovskite nanostructures were explained through a schematic diagram as shown in **Figure 2.4b**. In the process I, upon photoexcitation a thin quasi-2D (m=3) nanoplatelet donates its electron to the adjacent nanoplatelet (m=4). The electrostatic interaction between the transferred electron and hole in m=3 layered nanoplatelet forms charge transfer (CT) excitons (green ellipse). Subsequently, the hole is transferred from m=3 to m=4 thick quasi-2D nanoplatelet (process II). In process III, energy is transferred from m=4 to m=5 thick nanostructure via non-radiative recombination of hole and electron in m=4 thick nanostructure. In process IV, interfacial hole transfer finally enables the formation of new interfacial CT excitonic species (green ellipse).

2.3. Results and discussion

2.3.A. PNCs as energy donor

In order to use a material as a light-harvesting antenna, it has to display two capabilities; excellent light absorption and efficient energy transfer to the acceptors. In this context, luminescent PNCs are potential candidates as they exhibit intense light absorption and good fluorescence quantum yield due to quantum confinement effect.[20-22] Moreover, they possess a high surface area, which helps them interact effectively with suitable acceptor dyes through electrostatic forces. As a proof of concept, we investigated the light-harvesting antenna properties of PNCs as energy donor using rhodamine dyes as energy acceptors. Rhodamine dyes, characterized by excellent photophysical properties such as high extinction coefficients and good fluorescence quantum yields, are known to act as efficient energy acceptors for FRET studies.[23, 24] For the present study, rhodamine B (RhB) and rhodamine 101 (Rh101) were used. The chemical structures of the dyes are shown in **Scheme 2.1**.

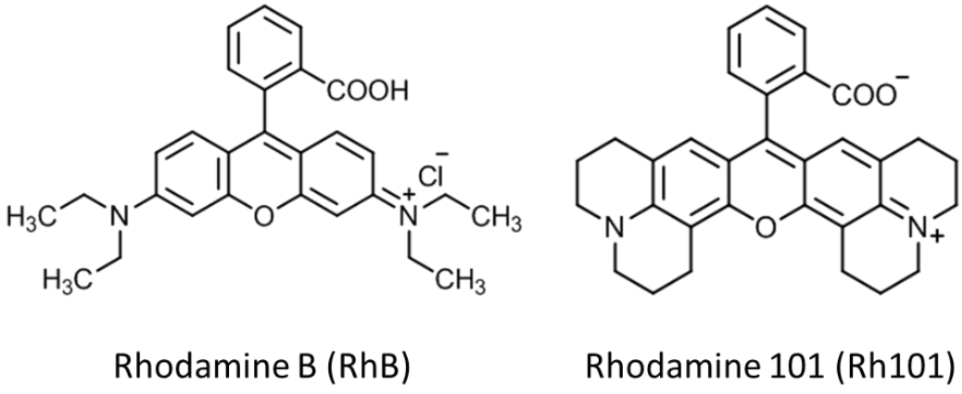

Scheme 2.1. Chemical structure of the acceptor dyes used for FRET studies.

2.3.A1. Synthesis and characterization of PNCs

Methylammonium lead bromide ($CH_3NH_3PbBr_3$) PNCs with octylammonium bromide as the capping agents were synthesized as a suspension in toluene.[25] Briefly, octylammonium bromide was dissolved in a mixture of oleic acid and octadecene at 80 °C, which was followed by the addition of methyl ammonium bromide and lead(II) bromide dissolved in *N*,*N*-dimethylformamide. The addition of acetone to the above reaction mixture precipitates out PNCs which were separated by ultracentrifugation followed by drying. PNCs in powder form were re-dispersed in chloroform and used for studies. Details of the preparation of PNCs and samples for various analysis are provided in the experimental section.

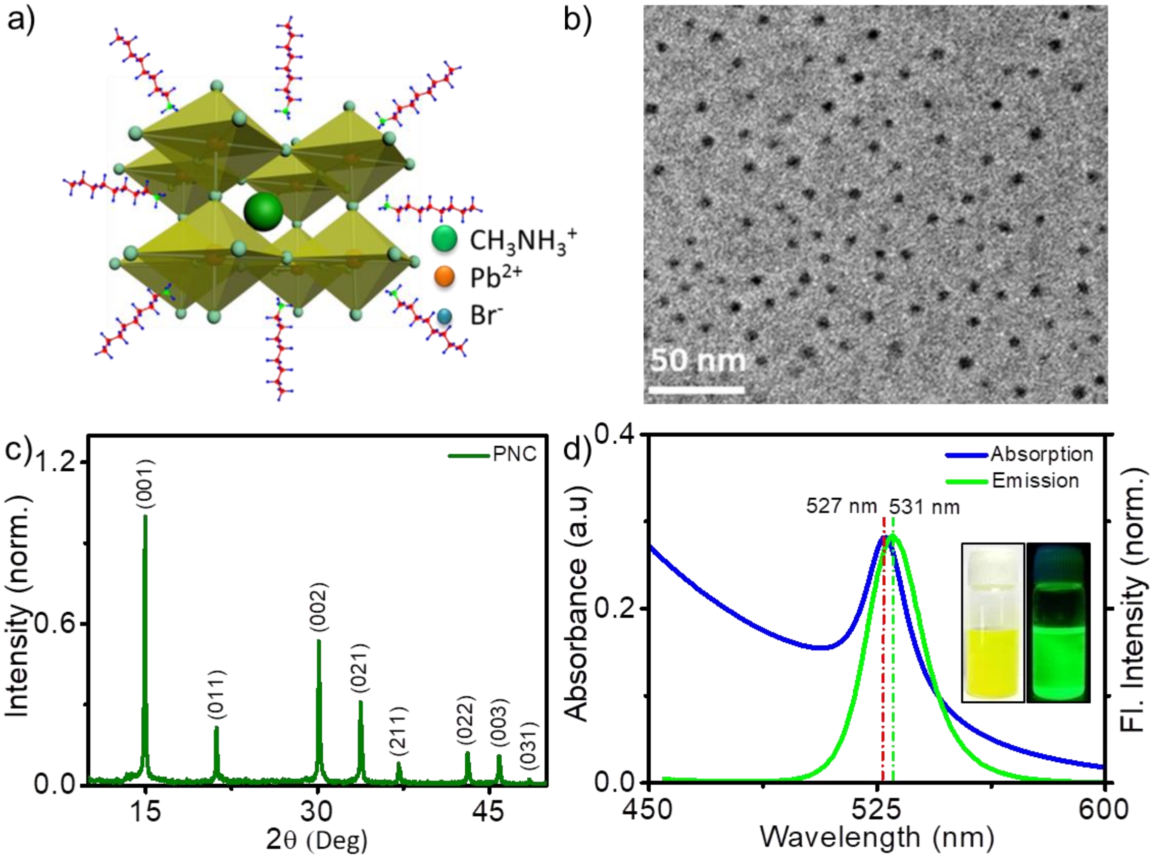

Figure 2.5. a) Simplified schematic representation of a $CH_3NH_3PbBr_3$ PNC. b) TEM image of PNCs obtained by drop casting a colloidal dispersion of nanocrystals in chloroform on a carbon-coated copper grid, c) XRD spectrum of PNCs film obtained by drop casting the chloroform dispersion on a glass substrate and d) UV/Vis absorption and emission spectra of the nanocrystals (λ_{ex} = 425 nm, l = 10 mm, solvent: chloroform).

The PNCs consist of lead ions surrounded by six bromide anions forming octahedra, of which several connected to form a three-dimensional structure. The voids formed between the connected octahedra are occupied by the organic cations

($CH_3NH_3^+$). The capping ligands present in the reaction mixture interact with the surface of the initially formed perovskite nanostructures through electrostatic forces. The interaction not only prevents the growth of the perovskite structures to restrict the size in nanometers but also provides colloidal stability to the nanocrystals. A simplified schematic representation of a PNC is shown in **Figure 2.5a**. The PNCs were characterized by transmission electron microscopy (TEM), X-ray diffraction (XRD), UV-vis absorption and fluorescence spectroscopy. For TEM measurements, the PNCs dispersed in chloroform were drop cast on a carbon coated copper grid and removed the solvent under vacuum. The TEM image revealed that the nanocrystals were spherical in shape with an average diameter of 6.1 nm (**Figure 2.5b**). The phase purity and crystallinity of PNCs were confirmed from XRD analysis (**Figure 2.5c**). For XRD measurement, the PNCs dispersed in chloroform were drop cast onto a glass substrate and removed the solvent at ambient condition. The observed diffraction patterns were corresponding to the cubic phase with a lattice constant of 5.93 Å. The absorption and emission spectra of PNCs were measured in chloroform (**Figure 2.5d**). An absorption maximum corresponding to the excitonic band was observed at 527 nm. The green emission was sharp (FWHM: 21nm) and intense with a maximum of 531 nm. The relatively smaller Stokes shift (4 nm) implies that the photoluminescence emission originates nearly completely from the direct exciton recombination due to the strong quantum confinement effect.[25,26] In chloroform, the PLQY of PNCs was found to be 72% by a comparative method using fluorescein dissolved in 0.1M NaOH as the standard dye (Φ_s=0.95). The quantum yield of the PNCs (Φ_u) was calculated using equation (2.1).

$$\Phi_u = \frac{A_S F_u n_u^2}{A_u F_S n_S^2} . \Phi_s \tag{2.1}$$

Where A_s and A_u are the absorbance of standard (dye) and unknown (PNC) respectively; F_s and F_u are the areas under the fluorescence spectrum of the standard and unknown; n_s and n_u are the refractive indices of the solvent used for standard and unknown, respectively.

2.3.A2. Energy transfer studies

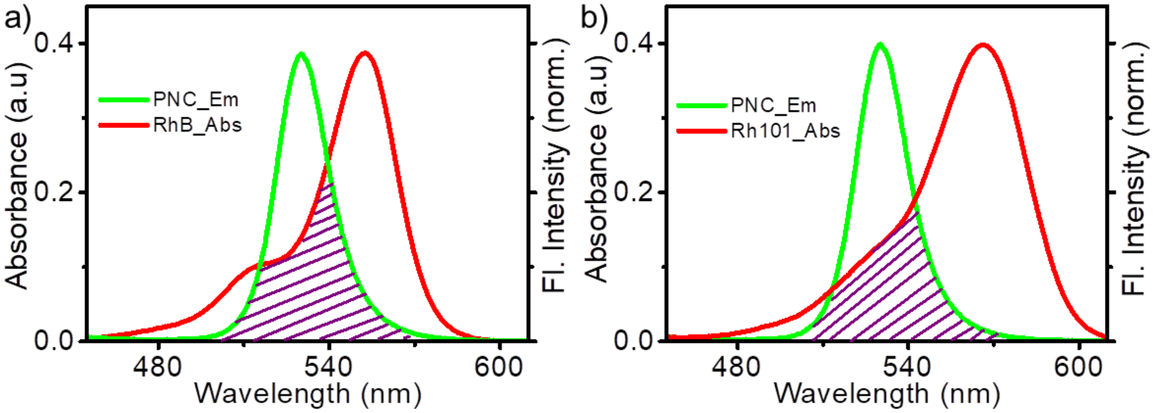

Figure 2.6. Spectral overlap (shaded portion) of the emission spectra of PNCs and absorption spectra of a) RhB and b) Rh101 dyes in chloroform (λ_{ex} = 425 nm, *l* =10 mm).

FRET studies were carried out using a chloroform suspension of the PNCs. One of the important criteria for donor/acceptor materials to be efficient FRET pairs is a good overlapping integral between donor emission and acceptor absorption. This implies the presence of matching excited energy levels in donor and acceptor species, which facilitates seamless energy transfer from the excited donor to the acceptor in the ground state. The emission spectrum of PNCs showed a significant overlap with the high energy side of the absorption band of rhodamine dyes (**Figure 2.6**). The overlapping integral that describes the degree of spectral overlap between the donor emission and acceptor absorption was calculated using the equation

$$J(\lambda) = \frac{\int_0^{\infty} F_D(\lambda)\varepsilon_A(\lambda)\lambda^4 d\lambda}{\int_0^{\infty} F_D(\lambda) d\lambda} \tag{2.2}$$

where $F_D(\lambda)$ is the fluorescence intensity of the PNCs in the wavelength range of λ to $d\lambda$ (dimensionless unit) and ε_A is the molar extinction coefficient of the dye molecules ($M^{-1}cm^{-1}$) at the wavelength λ. The spectral overlap was found to be almost similar for both PNC/RhB and PNC/Rh101 pairs with an overlap integral of 2.98×10^{15} and 2.53×10^{15} $M^{-1}cm^{-1}nm^4$, respectively. These values are comparable to several quantum dot/organic dye FRET pairs reported in literature.[27,28]

For the FRET studies, the concentration of the donor was kept constant (2 mg in 100 mL $CHCl_3$), and the concentration of the acceptor dyes was increased from 0 to 0.6 µM by the successive addition of 10 µL from a 15 µM stock solution of the dye to 3 mL of the donor solution. The absorption of PNCs and dye molecules (**Figure 2.7**) were measured to find out the appropriate excitation wavelength for the selective excitation of nanocrystals. Therefore, 425 nm was selected as the excitation wavelength as the dye's absorption was negligible at that wavelength.

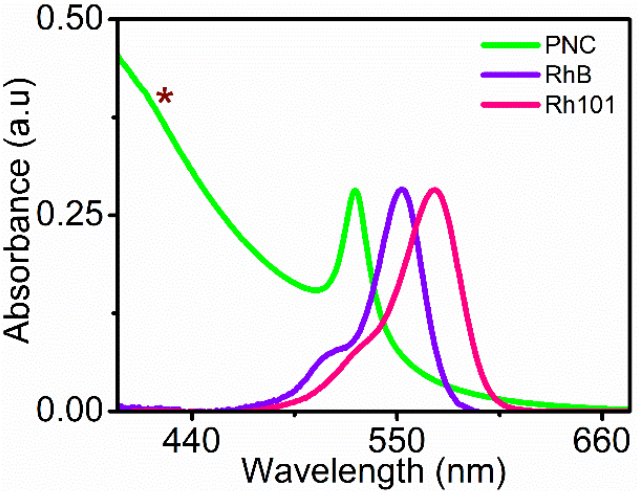

Figure 2.7. Absorption spectra of PNCs and the dye molecules. (The PNCs were excited at 425 nm for energy transfer studies, where the absorption of the dye molecule is negligible).

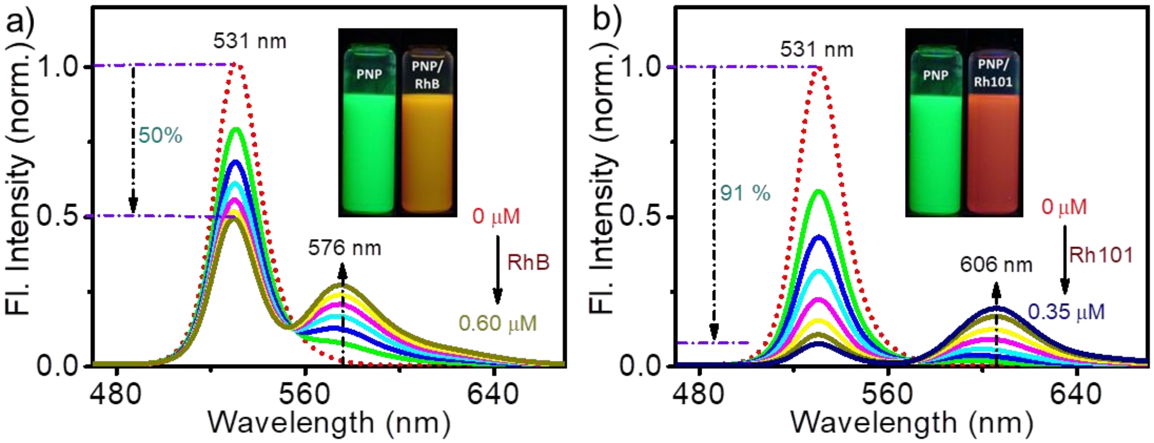

Figure 2.8. Steady-state emission spectral changes of the PNCs on addition of increasing amounts of a) RhB and b) Rh101 in chloroform (λ_{ex}=425 nm, l=10 mm).

In the absence of the acceptor dyes, PNCs exhibit intense green emission with an emission maximum at 531 nm on excitation at 425 nm. On addition of increasing amounts of RhB (0–0.6 µM), the donor emission at 531 nm decreased with a concomitant emission at 576 nm corresponding to the dye emission (**Figure 2.8a**).

Donor emission quenching reached a saturation point when the acceptor concentration was at 0.6 µM. At this concentration, the total quenching of the donor emission was 50%. On the other hand, the fluorescence quenching of PNCs was much more efficient in the presence of Rh101 dye (**Figure 2.8b**). About 40% of the PNC emission was quenched on the first addition (0.05 µM) of the dye. When the dye concentration reached 0.35 µM, 91% of the donor emission was quenched. No further change in the emission intensity was seen on increasing the acceptor content, indicating a saturation state.

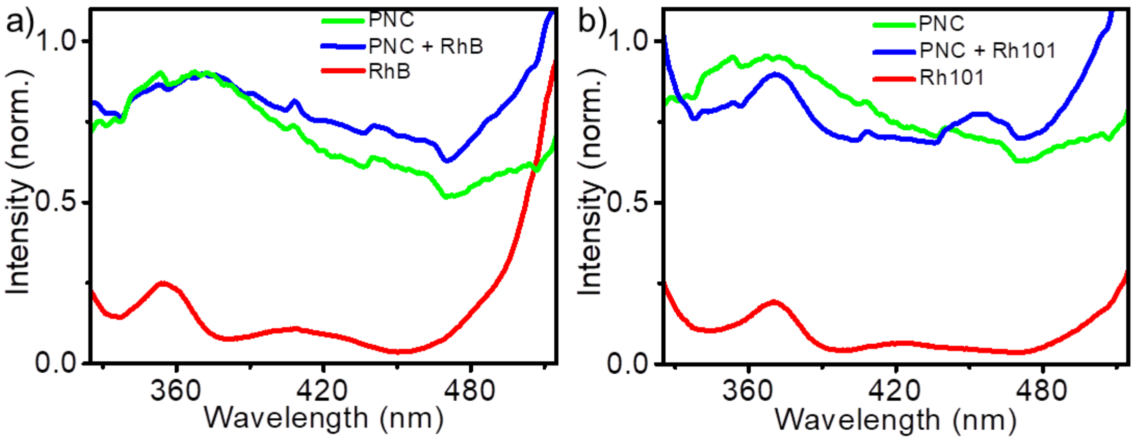

Figure 2.9. Excitation spectra of the PNCs in the presence and absence of a) RhB and b) Rh101 compared with that of respective dye alone (monitored at dye emission maximum). The observation of absorption corresponding to PNCs when monitored at the dye emission maximum confirms FRET from PNCs to the dye molecules.

The excitation spectrum is a powerful tool to confirm FRET from donor to acceptor molecules. It helps us to determine the wavelengths of light which are responsible for the emission maximum of acceptor molecules. Therefore, the excitation spectra of PNC/dye mixture was recorded at the dye emission maximum

(RhB: 576 nm; Rh101: 606 nm; **Figure 2.9**). The observation of the absorption features of the PNCs in the excitation spectra confirmed the FRET process from PNCs to the dyes in both cases.

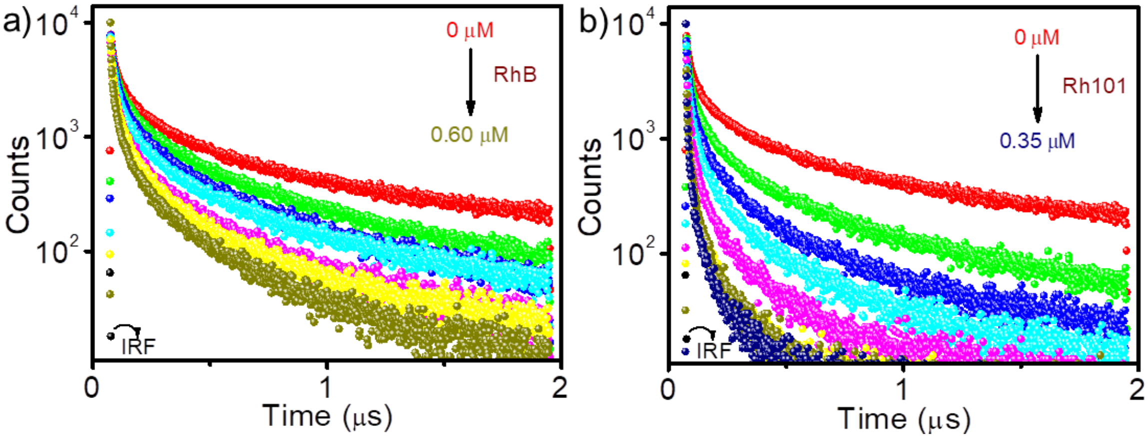

Figure 2.10. Fluorescence decay profiles of PNCs in the absence and presence of a) RhB (0-0.60 μM) and b) Rh101 (0-0.35 μM). The samples were excited with 410 nm laser and the emission decay was probed at 531 nm.

The non-radiative nature of the energy transfer process was confirmed by monitoring the fluorescence decay of PNCs in the absence and presence of the acceptor dyes (excited at 410 nm, probed at 531 nm). The PNCs exhibited multi-exponential fluorescence decay with an average lifetime of 614 ns. The decay becomes faster on the addition of increasing amounts of acceptor dyes. Such a shortening of the fluorescence lifetime in the presence of an acceptor indicates non-radiative energy transfer and rules out the possibility of a trivial radiative energy transfer mechanism, i.e., the emission-reabsorption process.[13] As in the case of fluorescence quenching, shortening of the lifetime of PNCs was distinctly different in the presence of RhB and Rh101. It was relatively slower on the addition of RhB (**Figure 2.10a**), and at the saturation point (i.e., in the presence 0.60 μM of RhB), the fluorescence lifetime of the donor was decreased to 303 ns. On the other hand, shortening of the donor lifetime was faster on addition of Rh101 (**Figure 2.10b**). It was decreased to 181 ns in the presence of 0.35 μM of Rh101.

Table 2.1. Fluorescence spectral decay components of PNCs in the presence of varying concentrations of RhB dye molecules.

Con (μM)	τ_1 (s)	τ_2 (s)	τ_3 (s)	τ_4 (s)	α_1	α_2	α_3	α_4	τ_{av} (ns)
0	1.44×10^{-7}	6.54×10^{-7}	3.30×10^{-8}	5.68×10^{-9}	22.53	65.04	9.75	2.67	614.04
0.1	1.20×10^{-7}	5.42×10^{-7}	2.53×10^{-8}	3.69×10^{-9}	29.25	52.14	14.67	3.94	489.91
0.2	1.05×10^{-7}	4.75×10^{-7}	2.26×10^{-8}	4.22×10^{-9}	30.06	45.00	17.71	7.24	420.25
0.3	0.99×10^{-7}	4.30×10^{-7}	1.99×10^{-8}	2.23×10^{-9}	31.86	44.05	17.81	6.28	376.80
0.4	0.78×10^{-7}	3.90×10^{-7}	1.59×10^{-8}	2.07×10^{-9}	32.07	40.23	19.02	8.68	341.63
0.5	0.76×10^{-7}	3.60×10^{-7}	1.52×10^{-8}	2.16×10^{-9}	30.10	40.32	19.43	10.14	315.81
0.6	0.72×10^{-7}	3.44×10^{-7}	1.45×10^{-8}	2.10×10^{-9}	28.89	41.12	18.99	10.01	303.20

Table 2.2. Fluorescence spectral decay components of PNCs in the presence of varying concentrations of Rh101 dye molecules.

Con (μM)	τ_1 (s)	τ_2 (s)	τ_3 (s)	τ_4 (s)	α_1	α_2	α_3	α_4	τ_{av} (ns)
0	1.44×10^{-7}	6.54×10^{-7}	3.30×10^{-8}	5.68×10^{-9}	22.53	65.04	9.75	2.67	614.04
0.05	1.06×10^{-7}	5.23×10^{-7}	2.06×10^{-8}	2.75×10^{-9}	29.27	51.51	14.82	4.39	475.37
0.1	0.99×10^{-7}	4.74×10^{-7}	1.98×10^{-8}	3.20×10^{-9}	32.66	39.12	19.94	8.29	411.12
0.15	0.86×10^{-7}	4.22×10^{-7}	1.77×10^{-8}	2.61×10^{-9}	31.03	32.59	24.41	11.67	357.67
0.20	0.84×10^{-7}	3.69×10^{-7}	2.06×10^{-8}	4.29×10^{-9}	28.23	24.23	28.63	18.92	292.00
0.25	0.67×10^{-7}	3.30×10^{-7}	1.38×10^{-8}	3.14×10^{-9}	26.37	14.70	29.59	29.34	242.30
0.30	0.27×10^{-7}	2.70×10^{-7}	0.99×10^{-8}	1.97×10^{-9}	30.14	12.74	21.39	35.73	211.64
0.35	0.38×10^{-7}	2.27×10^{-7}	0.75×10^{-8}	1.11×10^{-9}	17.69	12.71	22.66	46.95	180.77

The efficiency of the energy transfer was calculated from Equation (2.3).

$$E = 1 - \frac{\tau}{\tau_0} \tag{2.3}$$

Where τ and τ_0 are the fluorescence intensities of the donor in the presence and absence of the acceptor dyes. The energy transfer efficiency calculated from the lifetime data was found to be 50% for PNC/RhB, which is the same as that obtained from fluorescence quenching studies. On the other hand, in the case of PNC/Rh101 pair, the efficiency was found to be 71%, which was lower than the efficiency calculated from fluorescence quenching (91%).

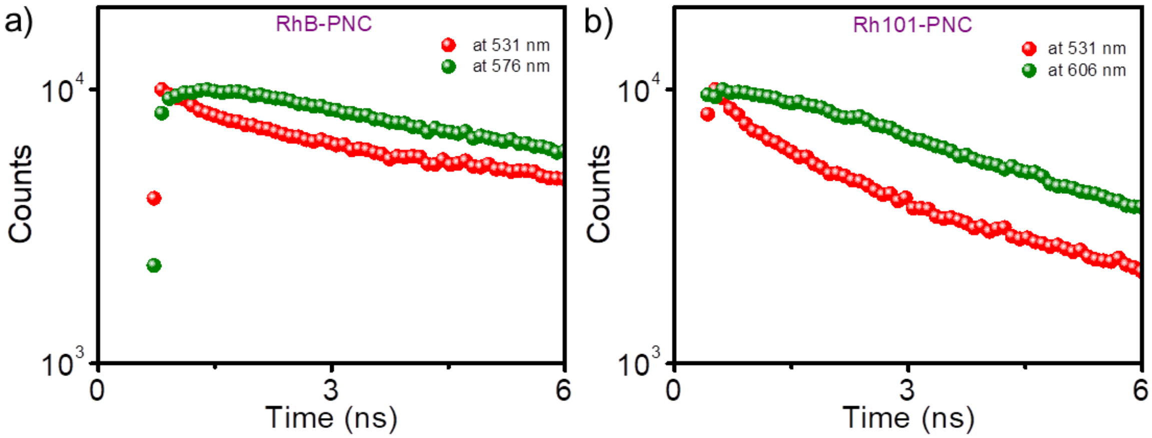

Figure 2.11. Time-resolved fluorescence decay of a) PNC/RhB and b) PNC/Rh101 monitored at the emission maximum of PNCs (red) and dye molecules (green).

FRET provides an additional de-excitation pathway for the donor in the presence of acceptor resulting in a shortening of fluorescence lifetime. This is always accompanied by an enhancement in the excited state lifetime of the acceptor for the emission monitored at its emission maximum in a shorter time scale (time window of

100 ns).[27,29] The fluorescence decay was monitored at the dye emission maximum (RhB: 576 nm; Rh101: 606 nm) on excitation of the PNCs at 410 nm (**Figure 2.11**). The presence of a fast rise component in the initial time-scale clearly suggests the formation of a dye-excited state through FRET from PNCs.

2.3.A3. Calculation of Stern-Volmer constant

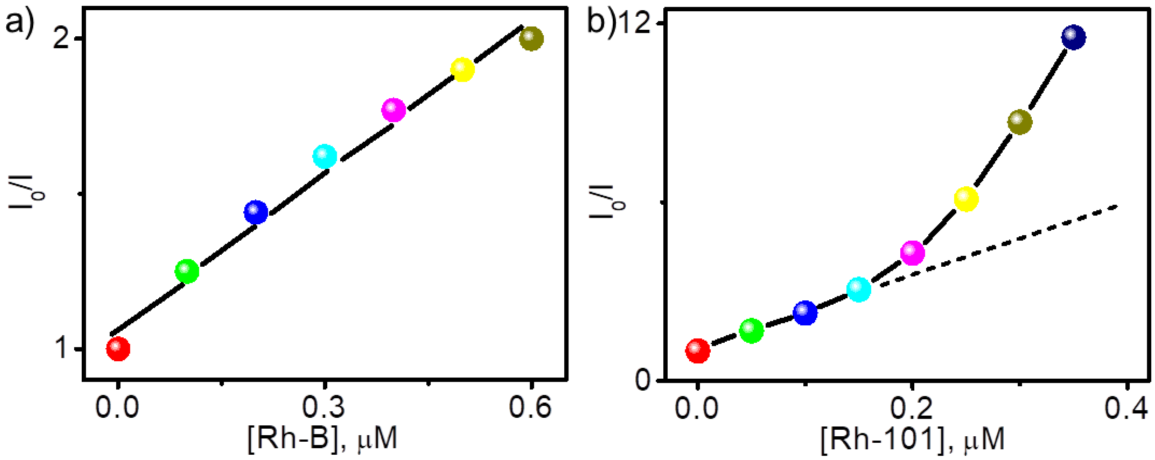

Figure 2.12. Relative changes in the emission intensity of PNCs as a function of the concentration of a) RhB and b) Rh101. (Solvent:chloroform, λ_{ex}=425 nm, l=10 mm).

In order to gain a better understanding about the nature of the quenching process, a Stern-Volmer (SV) plot was drawn by plotting the ratio of the emission intensity of the donor in absence and presence of the acceptor (I_0/I) against the concentration of the acceptor, [Q]. The linear behavior of the SV plot in the case of PNC/RhB (**Figure 2.12a**) indicated that the quenching process is dynamic in nature. The Stern-Volmer constant (K_{SV}) was determined using the following equation (2.4).

$$\frac{I_0}{I} = 1 + K_{SV}[Q] \tag{2.4}$$

From the slope of the plot, the K_{SV} was calculated as 1.83×10^6 M^{-1}. Interestingly, the SV plot of PNC/Rh101 showed a nonlinear behavior with an upward curvature (**Figure 2.12b**). The positive deviation from linearity implies the presence of both static and dynamic components in the fluorescence quenching process.[13,30,31]

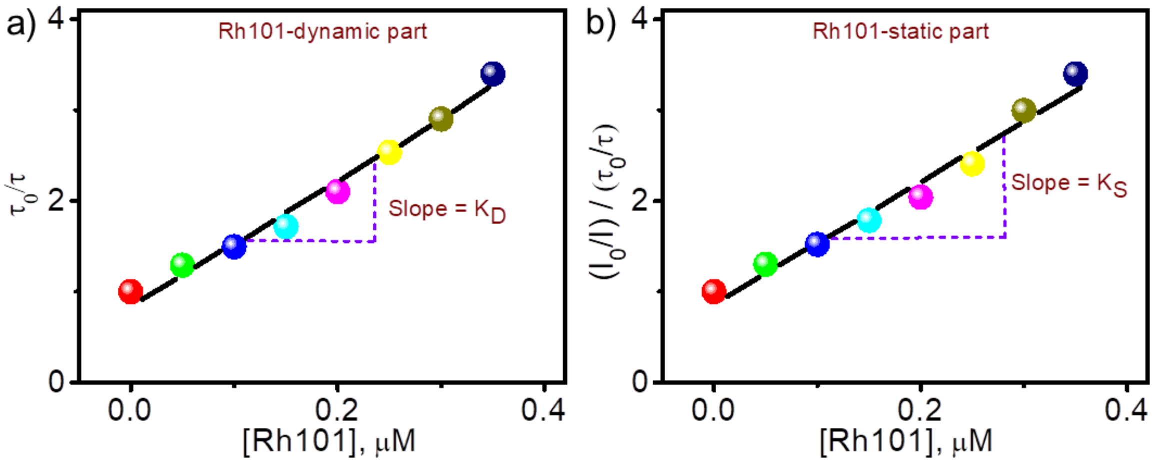

Figure 2.13. Stern-Volmer plot corresponding to the fluorescence quenching of PNC in the presence of Rh101 divided into a) dynamic part and b) static part.

The following adjusted Stern-Volmer equation (2.5) was used to separate the dynamic (K_D) and static (K_S) quenching components.

$$\frac{I_0}{I} = (1 + K_D[Q])(1 + K_S[Q]) \tag{2.5}$$

K_D and K_S were determined using the following equations (2.6 & 2.7)

$$\frac{\tau_0}{\tau} = 1 + K_D[Q] \tag{2.6}$$

$$\frac{(I_0/I)}{(\tau_0/\tau)} = 1 + K_S[Q] \tag{2.7}$$

where, τ and τ_0 are the lifetime of PNC in the presence and absence of the dyes, respectively. The corresponding plots are shown in **Figure 2.13**. The dynamic and static quenching constants were calculated as 7.30×10^6 M^{-1} and 6.57×10^6 M^{-1}, respectively. The presence of both components in the quenching process explains the discrepancy in energy transfer efficiency of the PNC/Rh101 pair obtained from fluorescence and lifetime studies. In static quenching, the lifetime of the donor does not decrease in the presence of the acceptor. However, the fluorescence intensity decreases due to the formation of a non-fluorescent complex in the ground state. Accordingly, the difference of 20% in the energy transfer efficiency could be attributed to the contribution of static quenching.

2.3.A4. Importance of anchoring groups

The above observations imply that the FRET efficiency of the PNCs is significantly higher in the presence of Rh101 than in the presence of RhB. It must be noted that the major difference between RhB and Rh101 is that the former has only one binding site, the quarternary ammonium group (the carboxylic acid group remains unionized in a relatively non-polar solvent like chloroform). On the other hand, the latter is a zwitter ion or an inner salt with two binding sites, the quarternary ammonium and carboxylate groups. As a result, it could be assumed that the electrostatic interaction between PNCs and RhB would be weak, whereas that of PNCs and Rh101 would be strong.

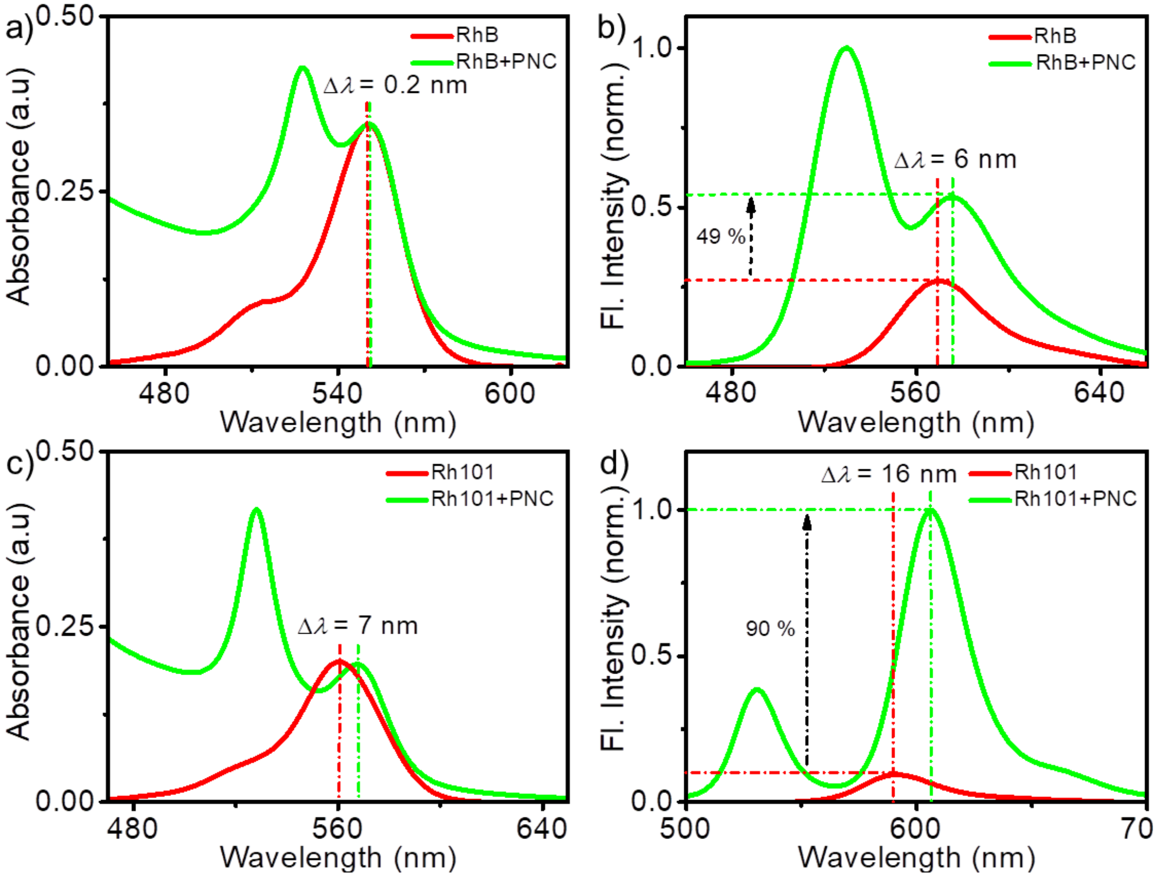

Figure 2.14. Absorption spectra of a) RhB, c) Rh101 and the emission spectra of b) RhB, d) Rh101 in the absence (red) and presence (green) of PNCs. (λ_{ex}=425 nm; [RhB]: 0.60 μM and [Rh101]: 0.35 μM).

To confirm this aspect, UV/Vis absorption and emission spectra of the mixtures were measured in chloroform. Interestingly, both dyes showed a red-shift in the absorption and emission maxima in the presence of PNCs. This indicates that the dye molecules are interacting with the PNC surface through electrostatic forces, which changes the electron distribution of the dyes resulting in the red-shift in the absorption and emission maxima.[13,27] However, the red-shift was marginal for RhB; only 0.2 nm in the absorption maximum (**Figure 2.14a**) and of 6 nm in the emission maximum (**Figure 2.14b**). On the other hand, a remarkable red-shift was observed for Rh-101; the absorption maximum shifted by 7 nm (**Figure 2.14c**) and the emission maximum shifted by 16 nm (**Figure 2.14d**). Such a shift in the absorption and emission maxima not only confirms a strong electrostatic interaction but also reiterates the contribution of the static component in the fluorescence quenching of PNCs due to the close proximity of Rh101. It must also be noted that about 49% enhancement was observed for RhB emission on by FRET when compared to that of the direct excitation of the dye, whereas this enhancement was about 90% for Rh101. This implies that FRET from PNCs is a more efficient pathway for the excitation of the dyes than that of direct excitation. Moreover, the improved enhancement for Rh101 reiterates that the FRET efficiency is higher in the PNC/Rh101 mixture.

Further evidence for the effect of binding groups was obtained from ^{1}H NMR and FT-IR spectroscopic studies of the dyes in the absence and presence of PNCs. The ^{1}H NMR spectra of aliphatic and aromatic regions of RhB and Rh101 dye molecules in the absence and presence of PNCs are shown in **Figures 2.15-2.18.** The ^{1}H NMR spectra revealed that the protons of RhB close to quaternary ammonium (δ = 1.3 - 3.6 ppm, **Figure 2.15**) and acid group (δ = 6.6 - 8.4 ppm**, Figure 2.16**) were negligibly shifted in the presence of PNCs, which indicates a weak interaction with PNCs. The acid group presents in RhB remains unionized and the quaternary ammonium group is steric hindered, which might be the reason for the weak interaction of RhB with the nanocrystals. On the other hand, Rh101 is in the zwitter ionic form which enables both quaternary ammonium and carboxyl group to strongly interact with PNCs. Therefore, the protons of Rh101 close to quaternary ammonium (δ = 1.9 - 3.4 ppm, **Figure 2.17**) and acid group (δ = 6.3 - 8.3 ppm, **Figure 2.18**) were significantly shifted in the presence of PNCs as observed in the ^{1}H NMR spectra. FT-IR analysis (**Figure 2.19**) reiterated this observation; the keto group in Rh101 was shifted by 17 cm^{-1}, whereas only a 6 cm^{-1} shift was seen in the case of RhB in the presence of PNCs.

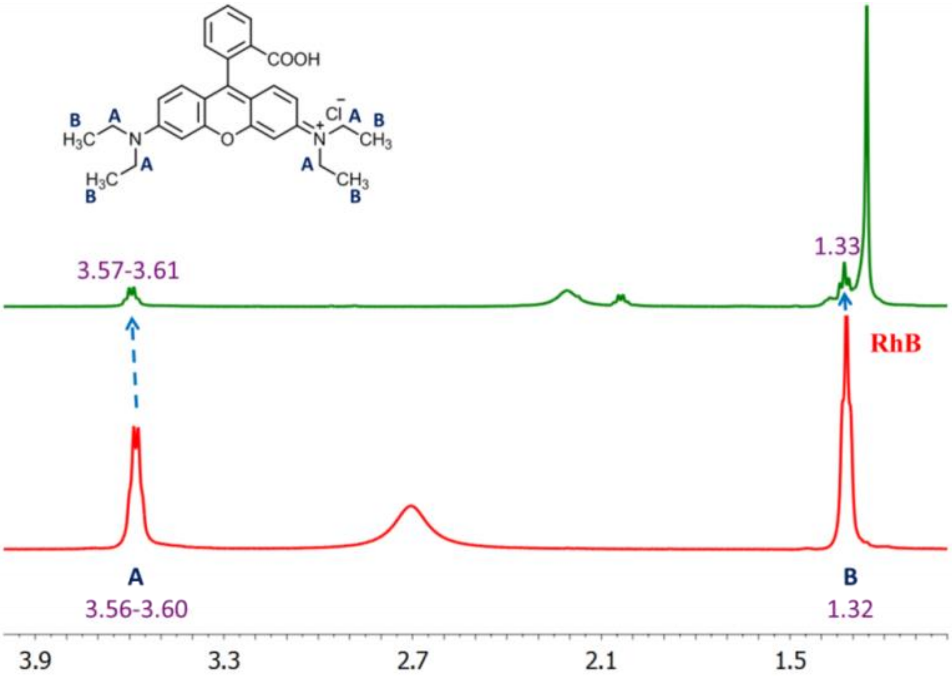

Figure 2.15. ^{1}H-NMR spectra of RhB dye molecules (0.1 mM) in chloroform in the absence and presence of PNCs (aliphatic region).

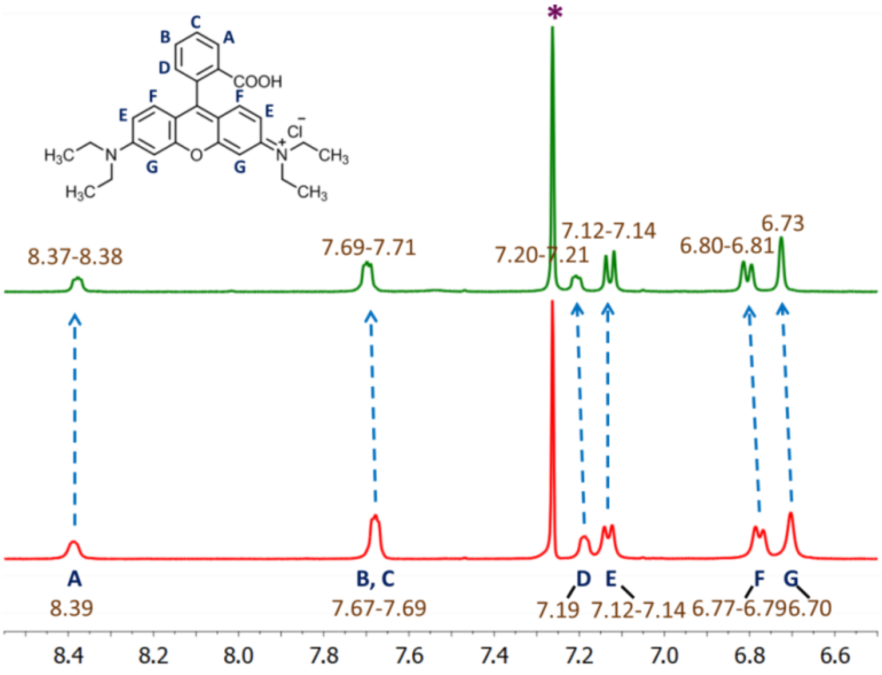

Figure 2.16. ^{1}H-NMR spectra of RhB dye molecules (0.1 mM) in chloroform in the absence and presence of PNCs (aromatic region).

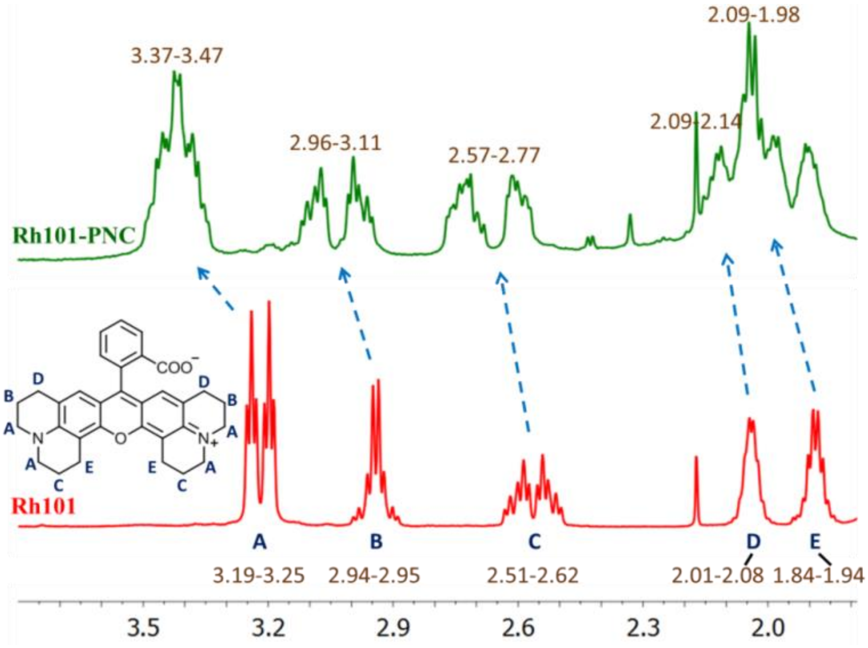

Figure 2.17. ^{1}H-NMR of Rh101 dye molecules (0.1 mM) in chloroform in the absence and presence of PNCs (aliphatic region).

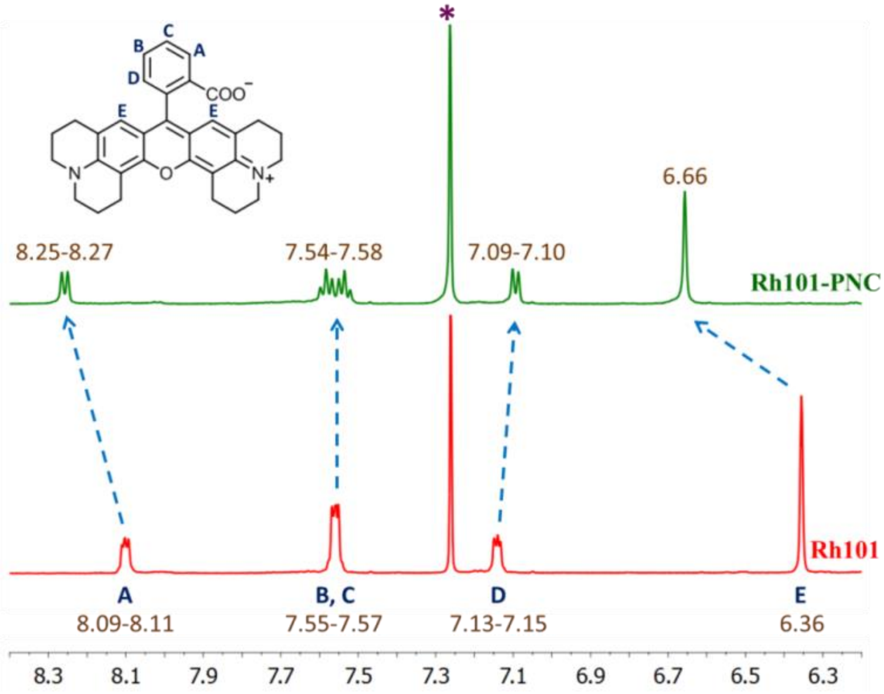

Figure 2.18. ^{1}H-NMR spectra of Rh101 dye molecules (0.1 mM) in chloroform in the absence and presence of PNCs (aromatic region).

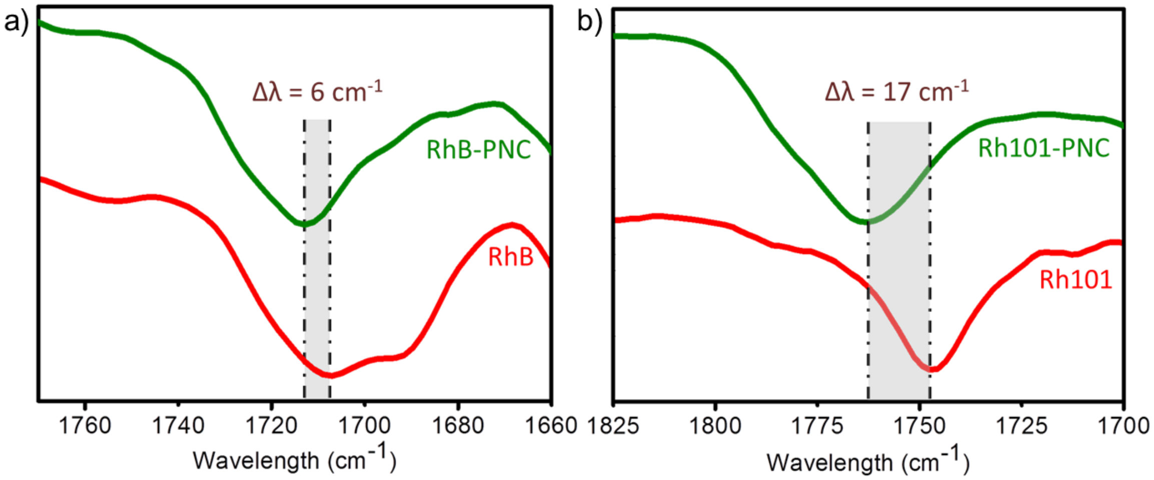

Figure 2.19. FT-IR spectra of dye molecules in the absence and presence of PNCs, a) RhB and b) Rh101.

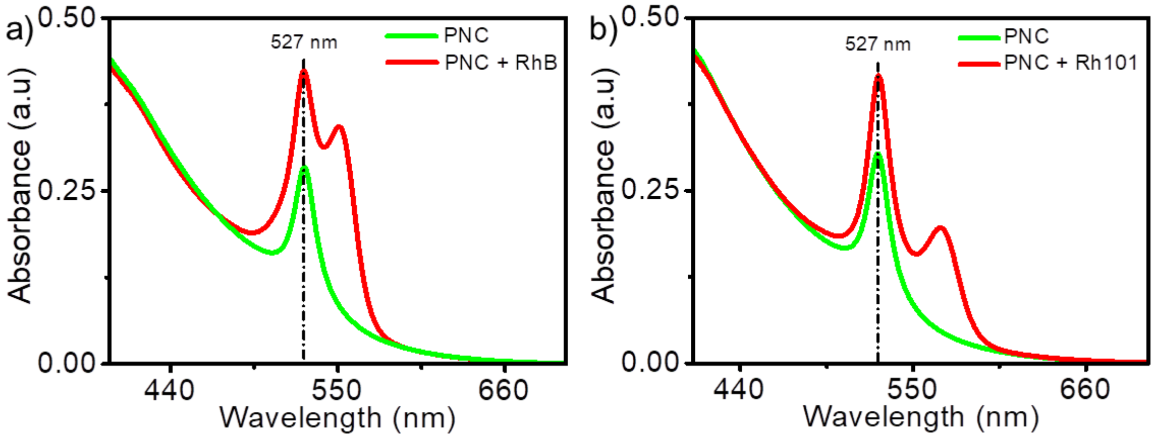

Figure 2.20. Absorption spectra of the PNCs in the presence of a) RhB and b) Rh-101 dyes.

No change in the absorption characteristics of PNCs was observed in the presence of dyes, indicating that the dye binding does not affect the electronic properties of the nanocrystals (**Figure 2.20**). The morphological features such as the size and shape of the PNCs were also not altered on dye binding, as observed from the TEM images of the mixed samples (**Figure 2.21**).

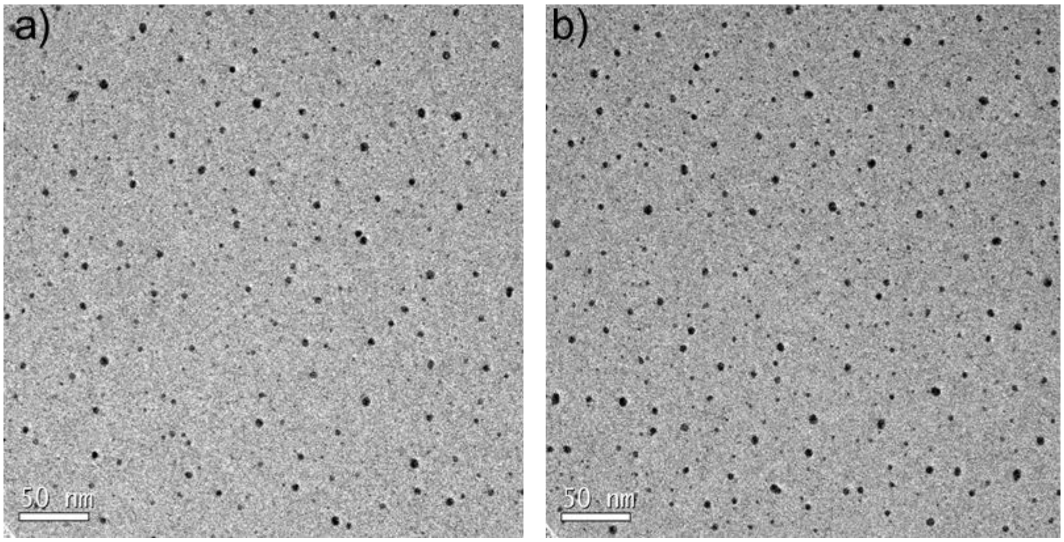

Figure 2.21. TEM images of PNCs in the presence of a) RhB and b) Rh101 dyes.

2.3.A5. Control experiments

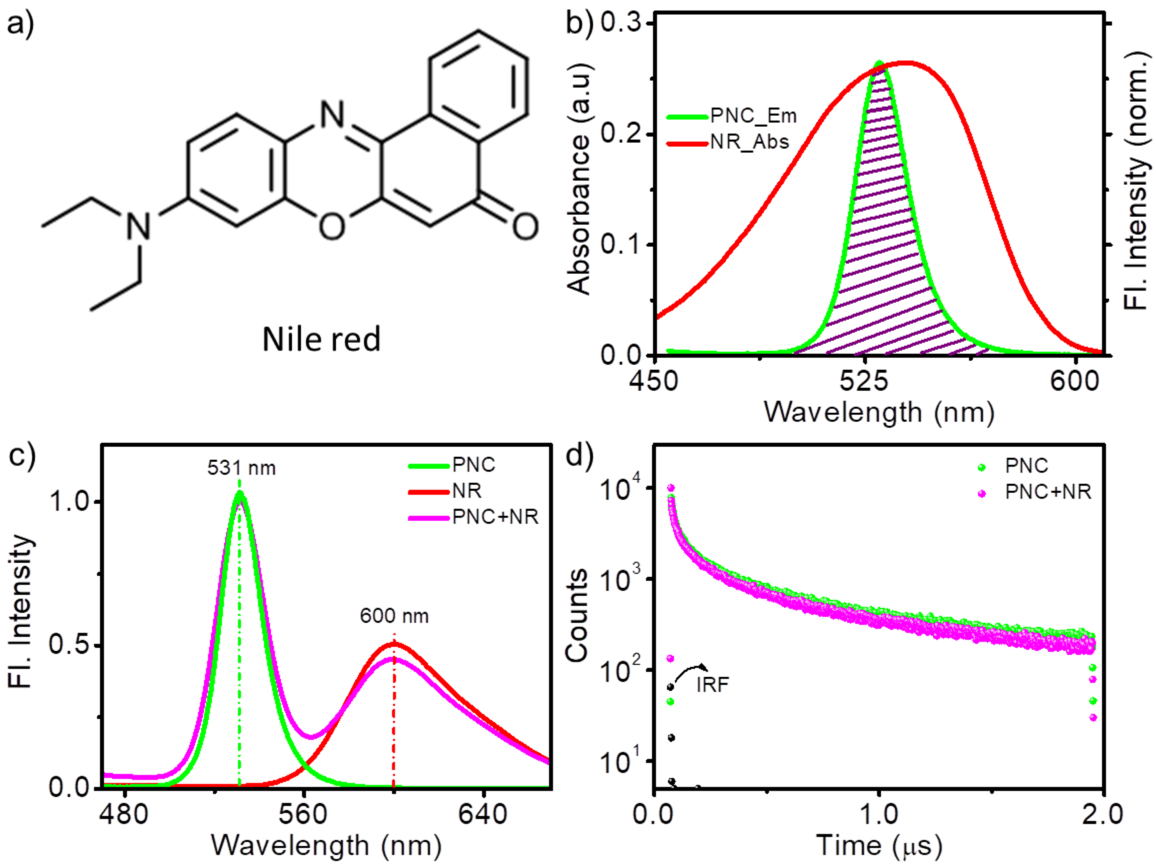

Figure 2.22. a) Chemical structure of nile red. b) Spectral overlap (shaded portion) of the emission spectra of PNCs and absorption spectra of nile red dyes in chloroform (λ_{ex} = 425 nm, l = 10 mm). c) Fluorescence emission spectra of PNC, nile red and their mixture (λ_{ex} = 425 nm) and d) fluorescence decay profile of PNCs in the absence and presence of nile red. The samples were excited with a 410 nm laser and the emission decay was probed at 531 nm.

To further confirm the role of the anchoring group, FRET studies were carried out under identical conditions with nile red (**NR; Figure 2.22a**), which is spectroscopically similar to rhodamines but does not possess any anchoring groups to interact electrostatically with the PNCs. Compared to rhodamines, a better spectral overlap was found between the emission of PNCs and absorption of NR dye due to the complete overlap between PNC emission and dye absorption, (**Figure 2.22b**), and the pair exhibited an overlap integral of 4.04 × 10^{15} M^{-1} cm^{-1} nm^4. Subsequently, FRET studies were carried out by adding NR dye in chloroform to the PNCs dispersed in chloroform (**Figure 2.22c**). On excitation of the mixture at 425 nm, no quenching was observed for the donor emission at 531 nm. Nevertheless, an emission peak corresponding to the NR emission was observed at 600 nm. However, the emission intensity of the NR emission was less compared to the emission on the direct excitation of the dye. These observations indicate that FRET is absent in the PNC/NR pair and the observation of dye emission on excitation at 425 nm, where the dye has negligible absorption, could be due to a simple emission-reabsorption process (photons emitted by PNCs absorbed by NR dyes resulting in NR emission). This was reiterated by the comparison of the fluorescence lifetime profile of PNC alone and PNC/NR mixture (**Figure 2.22d**). As shown in the figure, noticeable changes were absent in the lifetime decay profile of the PNCs in the presence of NR. The emission and FRET properties of PNCs in the absence and presence of RhB/Rh101/NR are summarized in **Figure 2.23**.

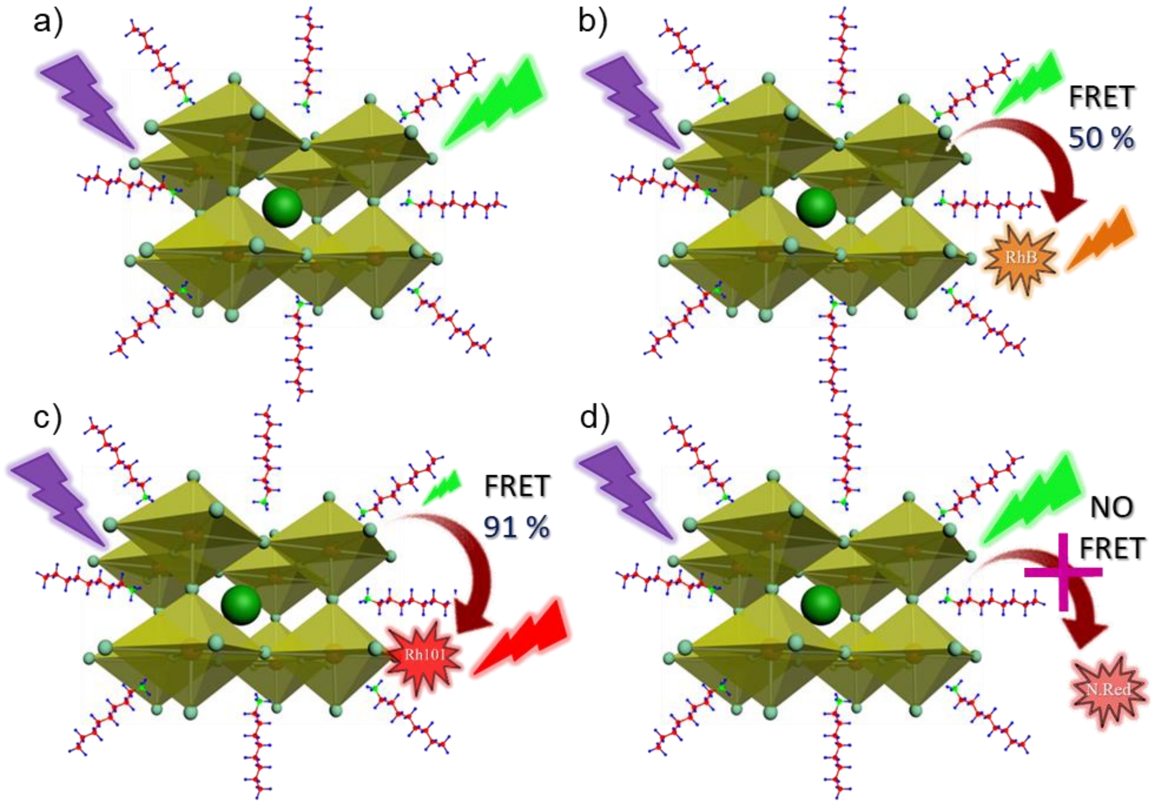

Figure 2.23. Schematic representation of the emission properties and FRET process between PNCs and various dye molecules.

2.3.B. PNCs as energy acceptor

2.3.B1. Synthesis and characterization of PNCs

The energy accepting property of PNCs was studied using polyfluorene (PF) as an energy donor and $CsPbBr_{1.5}I_{1.5}$ based PNCs as an energy acceptor. The $CsPbBr_{1.5}I_{1.5}$ PNCs were synthesized via the hot injection method. Briefly, cesium oleate in 1-octadecene was injected into a solution containing 1-octadecene, $PbBr_2$, PbI_2, oleic acid and oleylamine at 180 °C. The obtained PNCs were washed with toluene and used for further studies. Details of preparation of PNC and samples are provided in the experimental section.

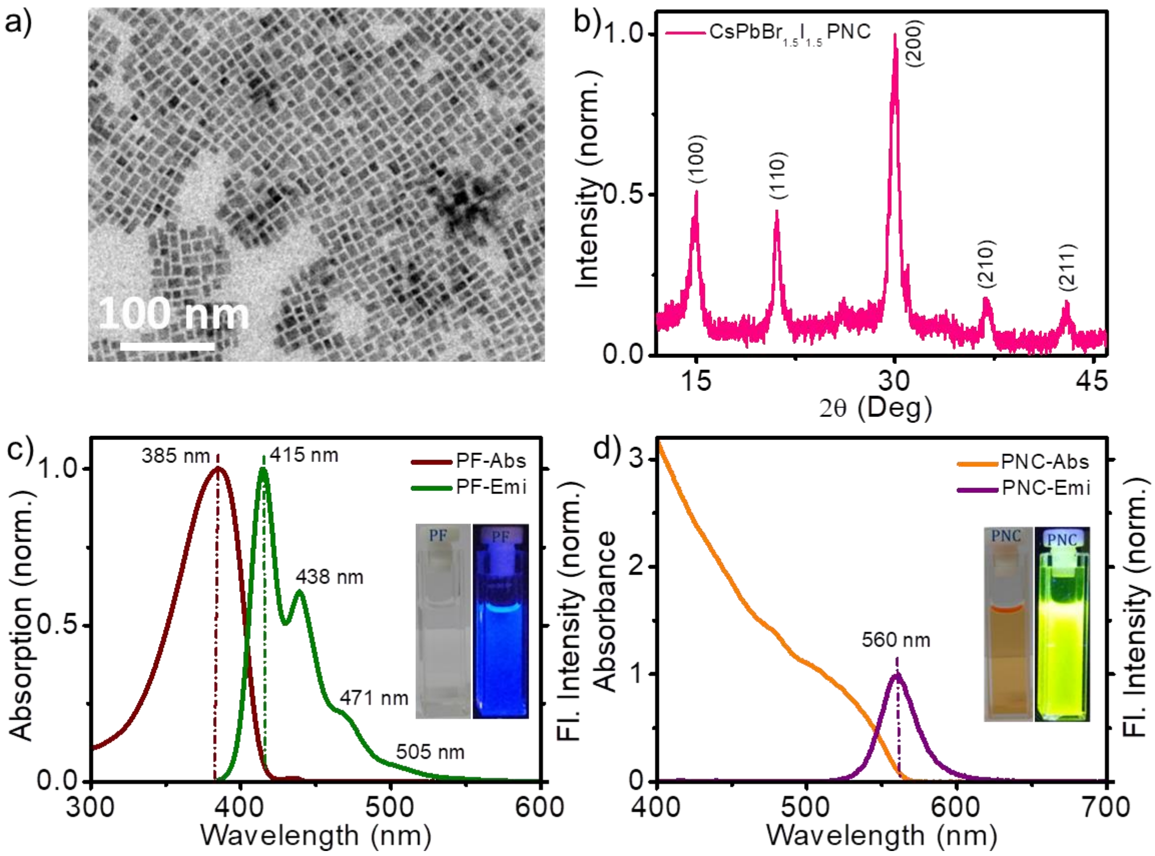

Figure 2.24. a) TEM image of $CsPbBr_{1.5}I_{1.5}$ PNCs showing the nanocrystals are cubic in shape with an average size of 12.8 nm. b) XRD spectrum of $CsPbBr_{1.5}I_{1.5}$ PNCs confirming their phase purity. UV-vis absorption and photoluminescence spectra of c) PF dissolved in toluene and d) PNCs dispersed in toluene. The pale yellow coloured PF under normal light turned into blue emission upon exposure to 365 nm UV light as shown in the inset of Figure 2.24c. The colloidal orange coloured PNCs turned into yellow emission under 365 nm UV light (inset of Figure 2.24d).

The $CsPbBr_{1.5}I_{1.5}$ PNCs were characterized via various microscopic and spectroscopic techniques. The PNCs were cubic in shape with an average edge length of 12.8 nm as confirmed from the TEM image (**Figure 2.24a**). The peaks obtained from the XRD spectrum of PNCs film were similar to the already reported $CsPbBr_{1.5}I_{1.5}$ PNCs[33] and also confirmed the phase purity of nanocrystals (**Figure 2.24b**). The absorption and emission spectra were measured for both PF and PNCs in the solution state (**Figure 2.24c and 2.24d** respectively). The PF polymer dissolved in toluene showed absorption and emission maximum at 385 and 415 nm, respectively. The colour of PF solution was pale yellow and the emission was blue in color upon irradiation with 365 nm as shown in the inset of **Figure 2.24c**. The absorption spectrum of dispersed PNCs in toluene showed a broad excitonic peak and an intense yellow emission maximum at 560 nm with a narrow FWHM of 27 nm (**Figure 2.24d**). The orange coloured nanocrystals exhibited an intense yellow coloured emission on exposure to 365 nm UV light (inset of **Figure 2.24d**). The quantum yield of colloidal PNCs was found to be 64 % by the comparative method using Rh 6G as the standard dye.

2.3.B2. Generation of white light in the solution state

The white light emission was produced by keeping the concentration of blue emitting PF constant and gradually adding yellow emitting PNCs into the polymer. This was done by preparing stock solutions of PF (by dissolving 2 mg in 100 mL toluene) and PNCs (by dispersing 2mg in 5 mL toluene) separately and mixing them as per the requirements. For the steady-state fluorescence measurements, 300 µL of polymer stock solution was diluted to 3 mL with toluene. The emission spectrum was monitored for each addition of 10 µL nanocrystals solution from their stock solution to the 3 mL PF solution (**Figure 2.25a**). PF solution showed bright blue colour fluorescence (λ_{em} = 410 nm) on excitation at 370 nm. On increasing the concentration of PNCs from 0 to 40 µL, the emission intensity of PF was gradually decreased with a concomitant increase in emission of PNCs at 560 nm. The composite (PF: PNC matrix = 1:2.67) emission was turned into a bright white light after the addition of 40 µL PNCs as shown in the inset of **Figure 2.25a**.

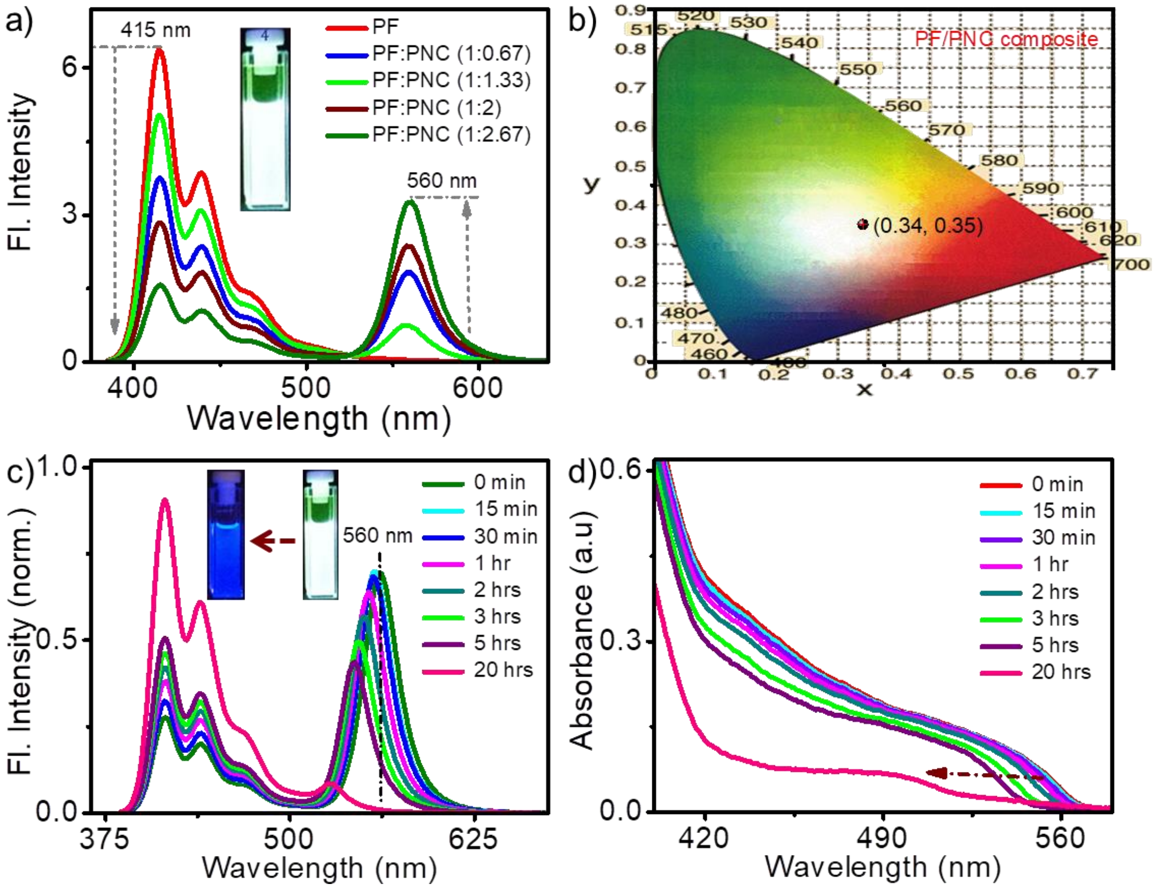

Figure 2.25. a) Steady-state fluorescence spectral changes of PF with increasing the concentration of PNCs. The equivalent ratio between PF and PNC is mentioned in the inset. b) CIE coordinates confirm the white light emission from PF/PNC matrix (1:2.67). Stability studies of white light emission for a period of 20 hours using c) absorption spectra and d) emission spectra (λ_{ex} = 370 nm).

The colour purity of white light emission was obtained from CIE coordinates which provided the values of (0.34, 0.35) corresponding to white light (**Figure 2.25b**). However, the obtained white light emission from PF/PNC was not stable as evidenced from both absorption (**Figure 2.25c)** and emission spectra (**Figure 2.25d)** monitored for 20 hours. The absorption and emission maximum of mixed halide PNCs shifted to the lower wavelength region leading to the disappearance of white emission within a few minutes. This could be explained by considering halogen exchange, a fast process commonly occurs in mixed halide PNCs due to their ionic nature.[34-36] The capping ligands bound with the surface of nanocrystals are highly dynamic and labile in nature.[37,38] This leads to detaching the capping ligands from the surface of nanocrystals in dilute solution providing more surface area to interact with the nearby nanocrystals. Therefore, $CsPbBr_{1.5}I_{1.5}$ PNCs started undergoing rapid halogen exchange to form more stable $CsPbBr_3$ nanocrystals after a period of time which was the reason for the disappearance of white emission. In addition to the blue shift in both absorption and emission maximum of mixed halide PNCs, there was a decrease in their intensities after a period of time. This could be explained as follows: The PNCs started to degrade in dilute solution after the detachment of capping of ligands due to the high surface energy of nanocrystals. The halogen exchange process could enhance thermally activated trap states which lead to decrease PLQY via nonradiative recombination.[38] The degradation and halogen exchange of PNCs increased the fluorescence intensity of PF during a period of time as shown in **Figure 2.25c**.

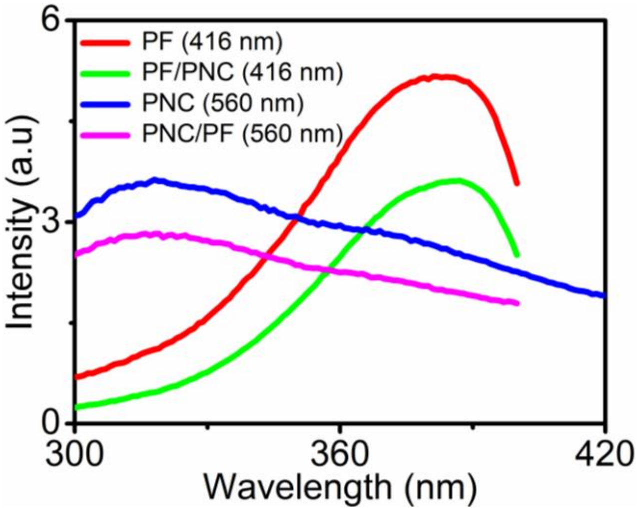

Figure 2.26. Excitation spectra of PF, PNCs and their composite. The collected emission wavelengths are mentioned in the inset of figure.

The obtained white light emission may be due to energy transfer from PF to PNC or direct excitation of both PF and PNC. Therefore, the excitation spectrum of PF/PNC mixture was collected at the emission maximum of PNCs (560 nm). The excitation spectra of PNCs in the presence of PF monitored at λ = 560 nm was similar to the excitation spectrum of PNCs alone monitored at 560 nm (**Figure 2.26**). Moreover, the excitation spectrum intensity of PF was decreased in the presence of PNCs which ruled out the possibility of energy transfer from PF to PNCs. Therefore, the obtained white light emission was a combined emission from PF and PNCs due to direct excitation.

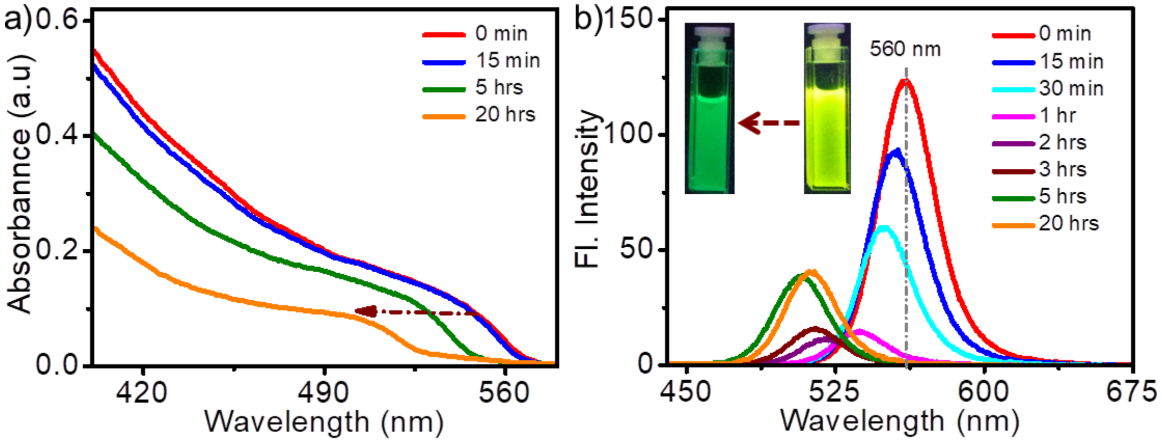

Figure 2.27. a) Absorption and b) Emission spectra of colloidal PNCs alone dispersed in toluene monitored for 20 hours. Change in emission colour of mixed halide PNCs from yellow to more stable green emissive $CsPbBr_3$ PNCs after a period of time is shown in the inset of figure 2.27a.

The spectral changes in both absorption and emission spectra of PNCs in the absence of PF were also monitored for a period of 20 hours (**Figure 2.27a and 2.27b** respectively) to study the role of polymer on the halogen exchange rate. The absorption and emission studies proved that the rate of halogen exchange in PNCs was reduced in the presence of PF. The yellow emissive mixed halide PNCs underwent rapid halogen exchange to form more stable green emissive $CsPbBr_3$ nanocrystals (change in emission colour is shown in the inset of **Figure 2.27b**) in the absence of PF, whereas there, was no such exchange in the presence of PF even after five hours. This may be due to the fact that some of PF polymers bound well onto the surface of nanocrystals via hydrophobic interaction, resulting in the reduction of the rate of halogen exchange.

2.3.B3. Generation of white light in the gel state

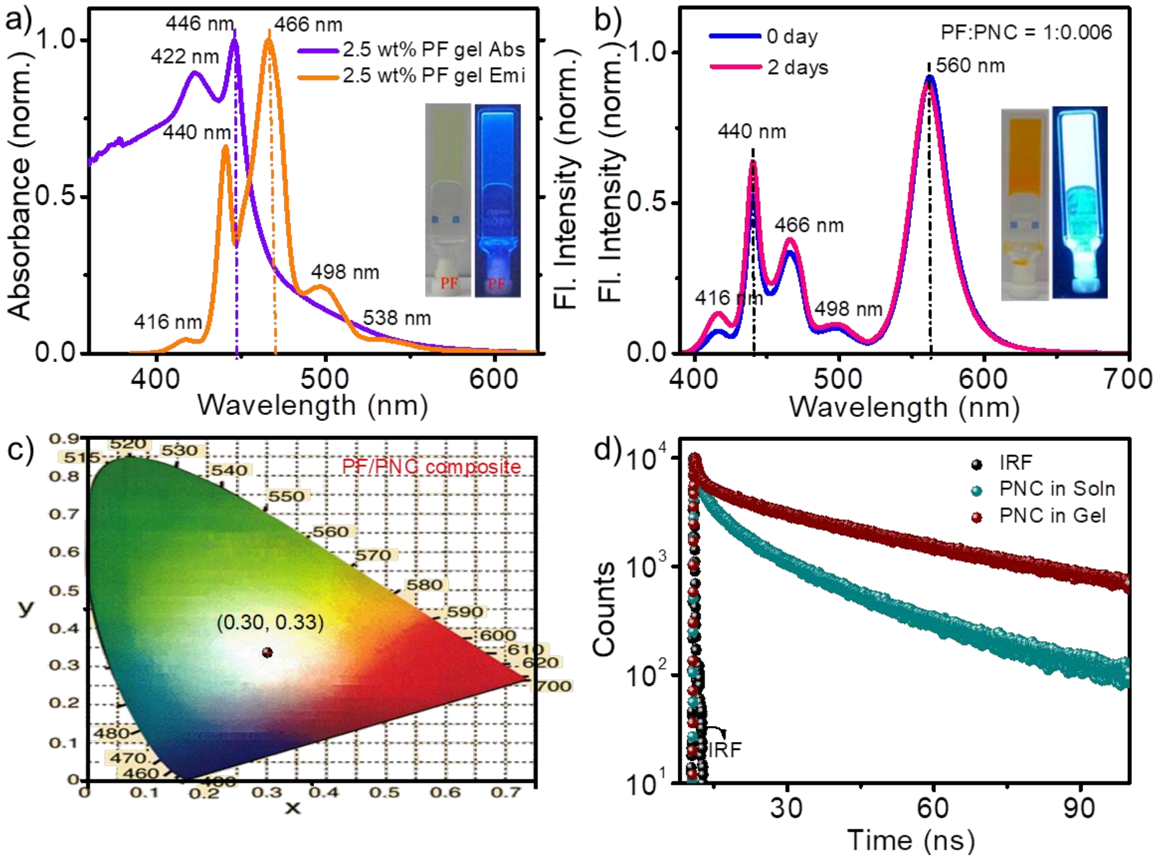

Figure 2.28. a) Absorption and emission spectra of 2.5 wt% PF gel. b) Absorption and emission spectra of PF/PNC gel measured at the initial period and after two days. c) CIE coordinates confirm the white light emission from PF/PNC matrix. d) Fluorescence decay profiles of PNCs dispersed in toluene and in the PF gel matrix. Fluorescence decay profiles were collected at their emission maximum (560 nm). The pale yellow PF gel under room light was changed into bright blue emission as shown in inset of figure 2.28a. The orange coloured PF/PNC gel under room light was changed into bright white emission as shown in inset of figure 2.28b.

Since the halogen exchange has slowed down in the presence of PF, we assumed that increasing the concentration of PF can further reduce it. It is known that PF forms stable gels at high concentration and the confined gel medium was expected to arrest the halogen exchange significantly. For this purpose, 20 µL of PNCs stock solution was added into 2.5 wt% PF dissolved in 300 μL toluene followed by keeping the mixture at -40 °C for 12 hours. Similarly, 2.5 wt% of PF gel without PNCs was also prepared for comparison. The absorption and emission spectra of 2.5 wt% PF gel (**Figure 2.28a**) were red-shifted compared to the same in the solution state (**Figure 2.24c**). This could be attributed to the aggregation of polymer strands in the gel state compared to the molecularly dissolved state in the solution state. However, the absorption and emission spectra of PF gel is different in their peak intensities compared to that in the presence of PNCs (**Figure 2.28b**). The emission maximum of PF gel at 460 nm was shifted to 440 nm in the presence of nanocrystals. This indicates that the PNCs were well bound with polymer molecules leading to reduce the size of PF aggregates and hence the blue shift in the emission maximum of PF gels. Interestingly, the obtained PF/PNCs gel matrix showed a bright white light emission which also found to be stable for more than two days (**Figure 2.28b**). The colour of PF gel was pale yellow in colour which changed into bright blue emission under 365 nm UV light as shown in inset of **Figure 2.28a**. The orange coloured PF/PNC composite was changed into white light emission under 365 nm UV light (inset of **Figure 2.28b**). The CIE coordinates of the PF/PNCs gel matrix (0.30, 0.33) were further confirmed the purity of white colour emission (**Figure 2.28c**). Another important observation was that the emission maximum and FWHM of PNCs both in the colloidal state and gel states were similar. This confirmed the dispersed state of nanocrystals into the polymer gel matrix and also the absence of halogen exchange in mixed halide PNCs.

Interestingly, the lifetime of PNCs in the PF/PNC composite (52 ns) was found to be high compared to that in the monodispersed state (22 ns; **Figure 2.28d**). The fluorescence lifetime of PNCs is generally increased on the reduction of surface defects via better surface ligand passivation.[39,40] Therefore, the observed high lifetime of PNCs in PF gel matrix was assigned to reduced surface defects due to the passivation of nanocrystals surface with capping ligands. In detail, the alkyl part of PF could interact with capping ligands via hydrophobic interactions. Therefore, the presence of PF in the ligand shell stabilizes the nanocrystals by tightening the ligand binding with PNCs which limits the interaction of nanocrystals with the surrounding media. Therefore, the detachment of capping ligands and related defect densities was absent in PNCs dispersed in PF gel matrix resulting in an enhanced lifetime of nanocrystals. The lifetime of PNCs in the absence of PF was also monitored at the initial period and after 20 hours. The lifetime of nanocrystals was decreased from 22 ns to 16 ns after 20 hours (**Figure 2.29**) due to increased concentration of defect densities via detachment of capping ligands.

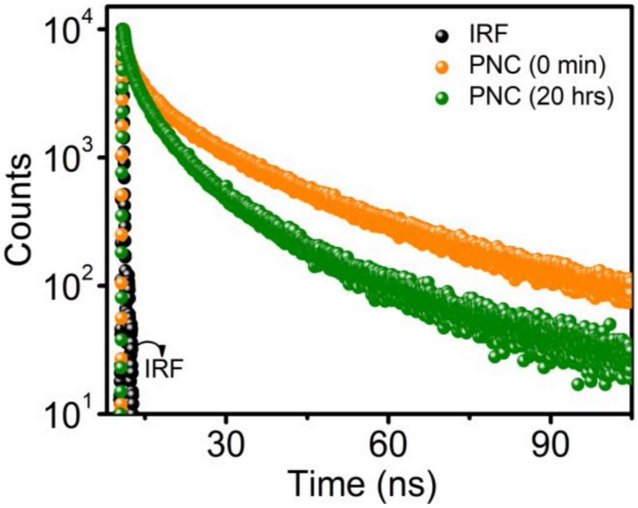

Figure 2.29. Fluorescence lifetime measurement of $CsPbBr_{1.5}I_{1.5}$ PNCs monitored at the initial period and after 20 hours.

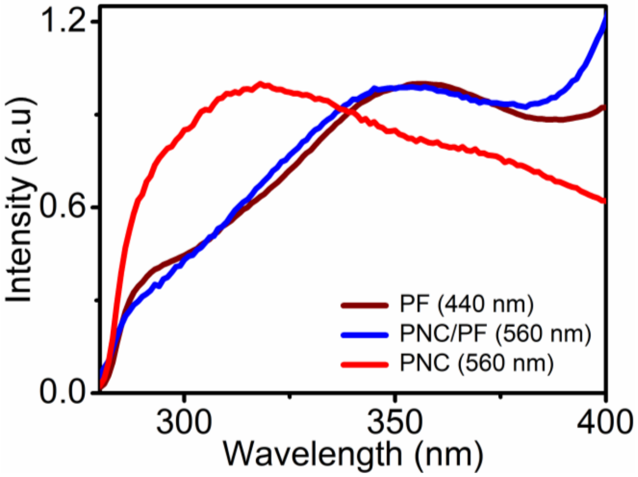

Figure 2.30. Excitation spectra of PNCs in the absence and presence of PF gel collected at their emission maximum (560 nm). The excitation spectrum of PNCs into the PF gel matrix is similar to the excitation spectrum of PF gel confirming the energy transfer from PF polymer to PNCs.

Then the excitation spectrum of PNCs in the absence and presence of PF gel matrix were monitored at their emission maximum (560 nm; **Figure 2.30**). The excitation spectrum of PNC/PF gel matrix recorded at the nanocrystals emission maximum (560 nm) was similar to the excitation spectrum of PF gel. This confirmed energy transfer from PF to PNCs. Therefore, the obtained white light was due to efficient energy transfer from PF to PNCs in PF gel matrix.

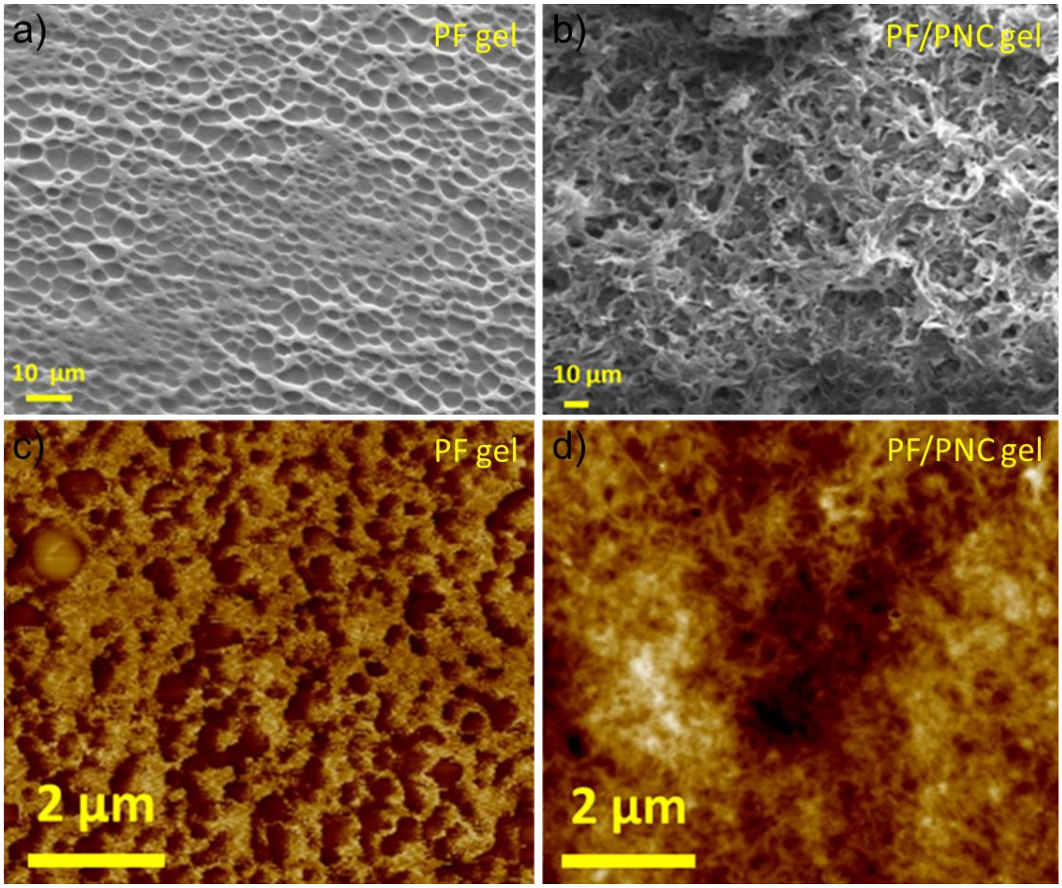

Figure 2.31. SEM image of PF gel in a) Absence and b) Presence of PNCs. c) AFM image of PF gel in the c) Absence and d) Presence of PNCs. The morphology of the PF gel film showed a porous structure which was changed in the presence of nanocrystals.

The interaction of PNCs with PF gel was further studied using SEM and AFM analysis (**Figure 2.31**). The PF gel film showed honey comb like morphology (**Figure**

2.31a & c) which was completely changed into fiber-like morphology in the presence of nanocrystals (**Figure 2.31b & d**) confirming the well distribution of PNCs into the PF gel matrix. The phase purity of PNCs in the polymer gel matrix was studied using XRD spectra. The similar peaks obtained from both the XRD spectra of PNC in the absence and presence of PF gel (**Figure 2.32**) confirmed the phase purity and stability of nanocrystals into the polymer matrix.

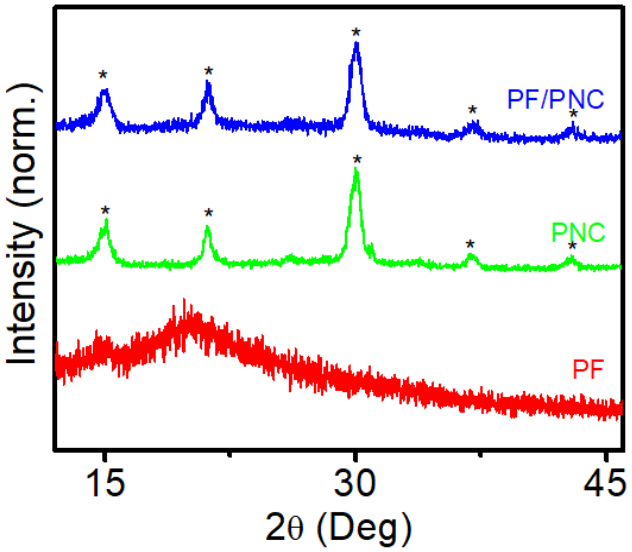

Figure 2.32. XRD spectra of PF film, PNCs in the absence and presence of PF molecules.

2.4. Conclusions

In summary, the application of PNCs as light harvesting antennae for efficient FRET processes was illustrated by using $CH_3NH_3PbBr_3$ PNCs as donor and rhodamine dyes (RhB and Rh101) as acceptors. The interaction between the nanocrystals and dyes were electrostatic in nature, and as a result, the number of binding sites on the acceptor dyes played a crucial role on the FRET efficiency as evident from the significantly higher efficiency for Rh101 with two binding sites than that of RhB with one binding site. As a result of the strong electrostatic interaction, "super-quenching" phenomenon was observed in the presence of Rh101. The importance of the anchoring group was further proved by FRET studies in the presence of an anchoring group free dye, nile red, which exhibited no FRET. Excellent light-harvesting properties and high FRET efficiencies make luminescent PNCs a good candidate as the light absorber in artificial photosynthesis systems. The energy accepting property of PNCs was also studied using blue emitting PF as energy donor and yellow emitting mixed halide $CsPbBr_{1.5}I_{1.5}$ PNCs as energy acceptor. The rate of halogen exchange of mixed halide PNCs was found to be low in the presence of PF. Finally, the halogen exchange of mixed halide PNCs was completely arrested by embedding them into a blue-emitting PF gel matrix. The surface of nanocrystals was well bound with a polymer matrix that resulted in stable white light emission from PF/PNC gel matrix. The white light emission was due to efficient energy transfer from PF to nanocrystals as confirmed excitation spectra. Interestingly, the lifetime of PNCs was increased in the PF matrix due to the arresting of the detachment of capping agents from the surface of nanocrystals by PF. The semiconducting nature of polymer molecules could also promote the PF/PNCs composite not only for fabricating white light-emitting diodes but also to use this composite in various other applications such as catalysis, capacitors, *etc*.

2. 5. Experimental section

2.5.1. Materials

The reagents and chemicals for synthesis were purchased from local suppliers or from Sigma Aldrich, Alfa Aeasar or TCI. Air- and water-sensitive synthetic steps were performed in an argon atmosphere.

^{1}H and ^{13}C NMR spectra were recorded on a 500 MHz Bruker Avance DPX spectrometer. Electronic absorption spectra were recorded on a Shimadzu UV-2600 UV-vis spectrophotometer and the emission spectra were recorded on a SPEX-Fluourolog spectrofluorimeter. Optical properties in solution were measured by using a quartz cuvette with 1 cm path length. For emission studies, right-angle geometry was used. X-ray diffraction studies were carried out on powdered samples with Xeuss Simultaneous 2D WAXs/SAXs using Cu-Kα radiation (λ=1.5418 Å). TEM measurements were carried out using a FEI-TECNAI T30 instrument, with EDAX at an accelerating voltage of 300 kV. Samples for TEM analysis were prepared by drop casting perovskite nanocrystals dispersed in chloroform onto a carbon-coated copper grid at the required concentrations at ambient conditions. The solvent was removed under vacuum. TEM images were obtained without stainstaining. The lifetime studies were carried out using an IBH FluoroCube time-correlated picosecond single-photon counting (TCSPC) system. Samples were excited using a pulsed diode laser (<100 ps pulse duration) at a sample emission wavelength of 410 nm (NanoLED-11) with a repetition rate of 250 kHz.

2.5.2. Synthesis and characterization

2.5.2.1. Synthesis of precursors

Synthesis of methyl- and octylammonium bromides: The precursors, methylammonium bromide (CH_3NH_3Br) and octylammonium bromide ($C_8H_{17}NH_3Br$), were synthesized by reaction of the corresponding amine in water/HBr, using reported procedures.[32] Briefly, for the synthesis of methylammonium bromide, 2.5 mL of 40% methylamine in water (32.2 mM, 1equivalent) was taken in a round-bottom flask, and 8.67 mL of 30% HBr (32.2 mM, 1 equivalent) in glacial acetic acid was added to this at 0 °C. Then the reaction mixture was stirred for about 2 hours, followed by the addition of diethyl ether for the precipitation of methyl ammonium bromide. It was then filtered, washed several times with diethyl ether, and dried under vacuum overnight.

Yield: 98%; ^1H NMR (500 MHz, DMSO, TMS) δ (ppm): 2.34-2.38 (q, 3H), 7.65 (s, 3H); ^{13}C NMR (125 MHz, D_2O) δ (ppm): 24.69.

The same procedure was followed for the synthesis of octylammonium bromide using 1 g of octylamine (7.7 mm, 1 equivalent) and 2.1 mL of 30% HBr (7.7 mm, 1 equivalent) in glacial acetic acid.

Yield: 98%; ^{1}H NMR (500 MHz, $CDCl_3$, TMS) δ (ppm): 0.87-0.89 (t, 3H), 1.26-1.32 (m, 8H), 1.37-1.43 (p, 2H), 1.78-1.84 (p, 2H), 3.00-3.07 (m, 2H), 7.96 (s, 3H); ^{13}C NMR (125 MHz, D_2O) δ (ppm): 13.34, 21.94, 25.50, 26.64, 28.09, 28.14, 30.97, 39.51.

2.5.2.2. Synthesis of $CH_3NH_3PbBr_3$ PNCs

The $CH_3NH_3PbBr_3$ perovskite nanocrystals with octylammonium bromide as the capping agent were synthesized as a suspension in toluene using a procedure reported by Perez-Prieto and co-workers.[26] Briefly, 2 mL of octadecene was heated to 80 °C, and octylammonium bromide (16.8 mg, 0.08 mmol) was added to this solution. Subsequently, methylammonium bromide (13.2 mg, 0.12 mmol dissolved in 100 mL of DMF) and lead (II) bromide (36.7 mg, 0.1 mmol dissolved in 200 mL of DMF) were added. A yellow dispersion was formed and the nanocrystals were immediately precipitated by the addition of acetone. It was then centrifuged at 7000 rpm for 10 min, the supernatant solution was decanted and the residual nanocrystals were dispersed in toluene.

2.5.2.3. Synthesis of $CsPbBr_{1.5}I_{1.5}$ PNCs

The $CsPbBr_{1.5}I_{1.5}$ PNCs were prepared using already reported hot injection method.[33]

Preparation of Cs-oleate: Cs_2CO_3 (0.814g) was loaded into a 100 mL 3-neck flask along with octadecene (40mL) and oleic acid (2.5 mL), dried for 1h at 120 °C, and then heated under N_2 to 150 °C until all Cs_2CO_3 reacted with OA. Since Cs-oleate precipitates out of ODE at room-temperature, it has to be preheated to 100 °C before injection.

Synthesis of PNCs: ODE (5 mL), PbI_2 (0.043 g) and $PbBr_2$ (0.0345g) were loaded into 25 mL 3-neck flask and dried under vacuum for 1h at 120 °C. Dried oleylamine (0.5 mL, OLA) and dried OA (0.5 mL) were injected at 120 °C under N_2. After complete solubilization of a PbX_2 salt, the temperature was raised to 180 °C and Cs-oleate solution (0.4 mL, 0.125 M in ODE, prepared as described above) was quickly injected and, 5s later, the reaction mixture was cooled by the ice-water bath.

2.5.3. Photophysical measurements

2.5.3.1. Sample preparation for PNCs as energy donor studies

PNCs stock solution was prepared by dispersing 2 mg of nanocrystals in 100 mL chloroform ($CHCl_3$) via sonication for 10 minutes. Separately, 1.5×10^{-3} M RhB dye solution was prepared by dissolving 3.6 mg of RhB in 5mL $CHCl_3$. 50 µL of this solution was diluted to 5 mL using chloroform to obtain 15 µM RhB stock solution. 6×10^{-4} M Rh101 dye solution was prepared by dissolving 1.47 mg of Rh101 in 5mL $CHCl_3$. 75 µL of this solution was diluted to 3 mL using $CHCl_3$ to obtain 15 µM Rh101 stock solution. 1.5×10^{-3} M nile red dye solution was prepared by dissolving 2.39 mg of nile red in 5mL $CHCl_3$. 50 µL of this stock solution was diluted to 5 mL using chloroform to obtain 15 µM nile red stock solution.

2.5.3.2. Sample preparation for PNCs as energy acceptor studies

PF stock solution was prepared by dissolving 2 mg of PF in 100 mL toluene via ultra-sonication for 10 minutes. 0.3 mL of this solution was diluted to 3 mL using toluene for energy transfer studies. $CsPbBr_{1.5}I_{1.5}$ PNCs stock solution was prepared by dispersing 2 mg of nanocrystals in 5 mL toluene via ultra-sonication for 5 minutes. 2.5 wt% PF gel was prepared by dissolving 6.6 mg of PF in 300 μL toluene followed by keeping the resultant solution at -40 °C for 12 hours. The PF/PNC composite gel was prepared similar to the preparation of 2.5 wt% PF gel with an additional 20 μL of PNCs solution (2mg PNCs in 1 mL toluene). The weight ratio between PNCs and PF is 1:0.006.

2.6. References

1. https://slideplayer.com/slide/8793883/.
2. C. B. Winiger, S. Li, G. R. Kumar, S. M. Langenegger, R. Haner, *Angew. Chem. Int. Ed*. **2014**, *53*, 13609-13613.
3. R. Ziessel, G. Ulrich, A. Haefele, A. Harriman, *J. Am. Chem. So*c. **2013**, *135*, 11330-11344.
4. P. K. Dutta, R. Varghese, J. Nangreave, S. Lin, H. Yan, Y. Liu, *J. Am. Chem. Soc.* **2011**, *133*, 11985-11993.
5. A. Ajayaghosh, V. K. Praveen, C. Vijayakumar, *Chem. Soc. Rev.* **2008**, *37*, 109-122.
6. A. C. Grimsdale, K. Mullen, *Angew. Chem. Int. Ed.* **2005**, *44*, 5592-5629.
7. S. R. Forrest, *Nature* **2004**, *428*, 911-918.

8. K. Cnops, B. P. Rand, D. Cheyns, B. Verreet, M. A. Empl, P. Heremans, *Nat. Commun*. **2014**, *5*, 1-6.
9. K. Driscoll, J. Fang, N. H. Baker, T. Torres, W. T. Huck, H. J. Snaith, R. H. Friend, *Nano Lett.* **2010**, *10*, 4981-4988.
10. K. Shankar, X. Feng, C. A. Grimes, *ACS Nano* **2009**, *3*, 788-794.
11. J.-H. Yum, B. E. Hardin, S.-J. Moon, E. Baranoff, F. Nuesch, M. D. McGehee, M. Gratzel, M. K. Nazeeruddin, *Angew. Chem. Int. Ed*. **2009**, *48*, 9277-9280.
12. https://en.wikipedia.org/wiki/F%C3%B6rster_resonance_energy_transfer.
13. V. D. Meer, B. W. G. Coker, S. Y. S. Chen. *Resonance Energy Transfer: Theory and Data.* VCH, New York, **1994**.
14. J. R. Lakowicz, *Principles of Fluorescence Spectroscopy*, 2nd Ed. Kluwer, New York, **1999**.
15. D. Zhou, J. D. Piper, C. Abell, D. Klenerman, D.-J. Kang, L. Ying, *Chem. Commun*. **2005**, *38*, 4807-4809.
16. A. R. Clapp, I. L. Medintz, J. M. Mauro, B. R. Fisher, M. G. Bawendi, H. Mattoussi, *J. Am. Chem. Soc*. **2004**, *126*, 301-310.
17. C. Song, Z. Ye, G. Wang, J. Yuan, Y. Guan, *ACS Nano* **2010**, *4*, 5389-5397.
18. C. D. Weerd, L. Gomez, H. Zhang, W. J. Buma, G. Nedelcu, M. V. Kovalenko, T. Gregorkiewicz, *J. Phys. Chem. C* **2016**, *120*, 13310-13315.
19. M. E. F. Bouduban, A. Burgos-Caminal, R. Ossola, J. Teuscher J.-E. Moser, *Chem. Sci.* **2017**, *8*, 4371-4380.
20. H. Huang, L. Polavarapu, J. A Sichert, A. S. Susha, A. S. Urban, A. L. Rogach, *NPG Asia Mater*. **2016**, *8*, e328 (1-15).
21. M. V. Kovalenko, L. Protesescu, M. I. Bodnarchuk, *Science* **2017**, *358*, 745-750.
22. Q. A. Akkerman, G. Rainò, M. V. Kovalenko, L. Manna, *Nat. Mater*. **2018**, *17*, 394-405.
23. V. K. Praveen, S. J. George, R. Varghese, C. Vijayakumar, A. Ajayaghosh, *J. Am. Chem. Soc.* **2006**, *128*, 7542-7550.

24. A. P. H. J. Schenning, E. Peeters, E. W. Meijer, *J. Am. Chem. Soc.* **2000**, *122*, 4489-4495.
25. L. C. Schmidt, A. Pertegas, S. Gonzalez-Carrero, O. Malinkiewicz, S. Agouram, G. M. Espallargas, H. J. Bolink, R. E. Galian, J. Perez-Prieto, *J. Am. Chem. Soc.* **2014**, *136*, 850-853.
26. F. Zhang, H. Zhong, C. Chen, X.-G. Wu, X. Hu, H. Huang, J. Han, B. Zou, Y. Dong, *ACS Nano* **2015**, *9*, 4533-4542.
27. A. Thomas, P. V. Nair, K. G. Thomas, *J. Phys. Chem. C* **2014**, *118*, 3838-3845.
28. T. Wang, V. Chirmanov, W. H. M. Chiu, P. V. Radovanovic, *J. Am. Chem. Soc.* **2013**, *135*, 14520-14523.
29. A. Gopi, S. Lingamoorthy, S. Soman, K. Yoosaf , R. Haridas, S. Das, *J. Phys. Chem. C* **2016**, *46*, 26569-26578.
30. F. Schibilla, L. Stegemann, C. A. Strassert, F. Rizzo, B. J. Ravoo, *Photochem. Photobiol. Sci.* **2016**, *15*, 235-243.
31. A. Pal, S. Srivastava, P. Saini, S. Raina, P. P. Ingole, R. Gupta, S. Sapra, *J. Phys. Chem. C* **2015**, *119*, 22690-22699.
32. G. C. Papavassiliou, G. Pagona, N. Karousis, G. A. Mousdis, I. Koutselas, A. Vassilakopoulou, *J. Mater. Chem.* **2012**, *22*, 8271-8301.
33. L. Protesescu, S. Yakunin, M. I. Bodnarchuk, F. Krieg, R. Caputo, C. H. Hendon, R. X. Yang, A. Walsh, M. V. Kovalenko, *Nano Lett.* **2015**, *15*, 3692-3696.
34. P. Vashishtha, J. E. Halpert, *Chem. Mater*. **2017**, *29*, 5965-5973.
35. C. Eames, J. M. Frost, P. R. Barnes, A. Walsh, M. S. Islam, *Nat. Commun.* **2015**, *6*, 7497.
36. J. M. Azpiroz, E. Mosconi, J. Bisquert, F. D. Angelis, *Energy Environ. Sci*. **2015**, *8*, 2118-2127.
37. P. Liu, W. Chen, W. Wang, B. Xu, D. Wu, J. Hao, W. Cao, F. Fang, Y. Li, Y. Zeng, R. Pan, S. Chen, W. Cao, X. W. Sun, K. Wang, *Chem. Mater.* **2017**, *29*, 5168-5173.

38. X. Li, D. Yu, F. Cao, Y. Gu, Y. Wei, Y. Wu, J. Song, H. Zeng, *Adv. Funct. Mater.* **2016**, *26*, 5903-5912.
39. Y. Wei, X. Deng, Z. Xie, X. Cai, S. Liang, P. A. Ma, Z. Hou, Z. Cheng, J. Lin, *Adv. Funct. Mater.* **2017**, *27*, 1703535-1703542.
40. H. Sun, Z. Yang, M. Wei, W. Sun, X. Li, S. Ye, Y. Zhao, H. Tan, E. L. Kynaston, T. B. Schon, H. Yan, Z. H. Lu, G. A. Ozin, E. H. Sargent, D. S. Seferos, *Adv. Mater.* **2017**, *29*, 1701153-1701161.

Chapter 3

Electron Transfer Properties of Perovskite Nanocrystals

3.1. Abstract

Addressing fundamental photophysical properties of PNCs in combination with other materials calls for exploration, and is expected to further the applications of PNCs in optoelectronic devices. Photoinduced electron transfer (PET) is a fundamental process in natural and artificial photosynthesis. In this chapter, the electron transfer property of PNCs is studied and their application in sensing is explored. For this purpose, hydrophobically capped highly luminescent formamidinium lead bromide ($FAPbBr_3$) PNCs were prepared. When compared with isolated PNCs in a solution, close packed PNCs in a thin film showed longer fluorescence lifetime (ca. 4.2 μs), which was due to hopping or migration of photogenerated excitons among PNCs. Both fluorescence quantum efficiency and lifetime decreased in a PNC thin film doped with fullerene (C_{60}), which was attributed to channeling of exciton migration into electron transfer to C_{60}. Utilizing the electron transfer properties, PNCs were used for the detection of explosives such as dinitro toluene (DNT), trinitro toluene (TNT) and trinitro phenol (TNP, picric acid) in the solution and vapour state. Unlike most fluorescence based sensors, PNCs showed high selectivity and good sensitivity towards TNP, which was attributed to the hydrogen bonding ability and electron accepting strength of TNP.

3.2. Introduction

Electron transfer (ET) is a ubiquitous chemical process, which plays a central role in various crucial events in chemistry and biology.[1,2] The ET process involves the transfer of an electron from a donor molecule (D) to an acceptor molecule (A) without making or breaking any chemical bonds. ET processes occur both thermally and photochemically. The latter is known as photoinduced electron transfer (PET) which takes place following light absorption by the donor followed by the transfer of an excited electron from donor to acceptor.[1] Due to the redox reaction in the excited state, PET results in a charge separated state (**Figure 3.1**). The extra electron presents in the acceptor will return to the donor without the emission of a photon. Nature utilizes this process in the photosynthetic reaction centre to convert solar energy into chemical energy.[3-5] Inspired from the natural photosynthesis, several artificial photosynthetic models capable of imitating these events were developed with an aim of transforming light energy into solar fuels in addition to their applications in various optoelectronic devices.[6-10]

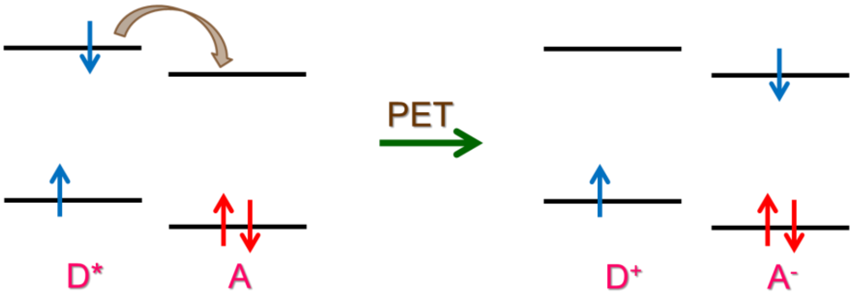

Figure 3.1. Molecular orbital schematic illustration of PET.

PET has been investigated with various donor-acceptor pairs. The commonly used electron donors are organic molecules, nanoparticles, and polymers; quinone, viologen, and fullerene are being used as electron acceptors.[15-17] The study of PET property of nanoparticles with suitable electron acceptors is highly interesting compared to other materials due to the generation and accommodation of multiexcitons in a single nanoparticle by optical excitation.[18,19] In addition to this, the rate of charge carriers recombination after photoexcitation in nanoparticles is much lower compared to organic/polymer materials which could help them efficiently transfer electrons during PET. The excellent PET property of nanoparticles makes them promising candidates for various optoelectronic devices such as solar cells, photodetectors, catalysis, *etc*.[20-24]

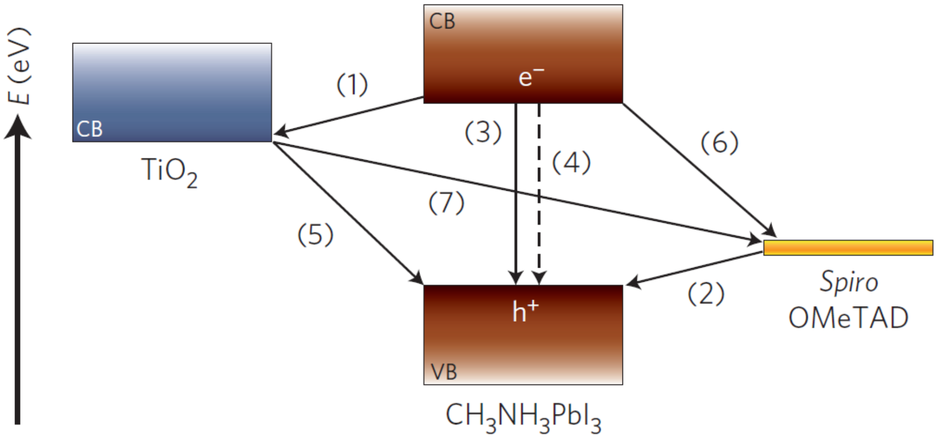

Figure 3.2. Schematic diagram of energy levels and electron transfer processes in an HTM/$CH_3NH_3PbI_3$/TiO_2 cell. The arrows represent (1) electron injection as the primary charge separation step, (2) hole injection as the primary charge separation step, (3) & (4) radiative and non-radiative processes respectively, (5) the back electron transfer at the TiO_2 surface, (6) back charge transfer at the HTM surface and (7) shows charge recombination at the TiO_2/HTM interface (*Adapted from reference 25*).

Recently, electron-transfer studies in perovskite based donor-acceptor systems received great momentum, which is owing to their potential application in solar cell technology. The photoinduced charge transfer processes in hybrid perovskite based solar cells were first investigated by Grätzel and coworkers using time-resolved techniques.[25] They studied the charge transfer dynamics of $CH_3NH_3PbI_3$ film using TiO_2 and Al_2O_3 as electron transport materials and spiro-OMeTAD as a hole-transporting material. The different photophysical processes taken place in this device are schematically represented in **Figure 3.2**. The ultrafast electron and hole injections were taken place from the photoexcited perovskite over similar timescales which reduced the rate of charge carriers (electron and hole) recombination in perovskite after photoexcitation. The rate of charge carriers recombination was found to be slow on TiO_2 film compared to that of Al_2O_3 film. The charge carrier's separation and recombination were also depending on the method of sample preparation.

Sandstorm and coworkers pinpointed the time scale and mechanism of charge transfer from a perovskite material ($CH_3NH_3PbI_3$) to an organic acceptor (PCBM and Spiro-OMeTAD).[26] The corresponding schematic diagram illustrating different photophysical processes is shown in **Figure 3.3**. The rate of hole transfer at $MAPbI_3$/Spiro-OMeTAD interface was found to be the same as its recombination rate. This observation was similar to that in neat $CH_3NH_3PbI_3$ without using Spiro-OMeTAD. The ultrafast recombination was attributed to the presence of highly concentrated dark charges (holes) brought about by unintentional p-type doping of

$MAPbI_3$. On the other hand, the injected electrons from perovskite (hundreds of ps to few ns time scale) to PCBM were recombined immediately with photogenerated and dark holes in $CH_3NH_3PbI_3$ at the same time scale. These studies suggested that the reduction of dark holes concentration in perovskites could help to retard recombination for obtaining high photon conversion efficiency.

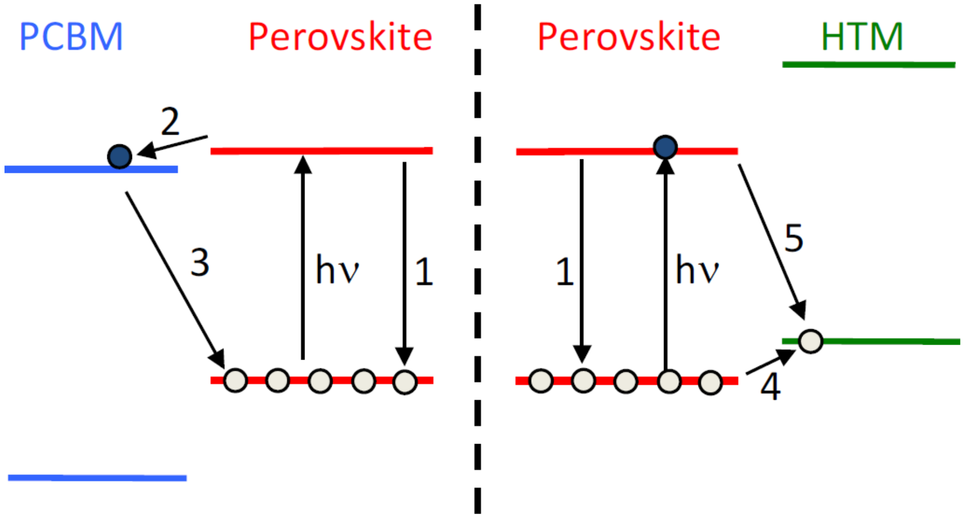

Figure 3.3. Schematic diagram representing the energy levels of $CH_3NH_3PbI_3$ perovskite, Spiro-OMeTAD and PCBM and various photophysical processes, 1: (nongeminate) electron hole recombination, 2: electron injection, 3: interfacial electron hole recombination, 4: hole injection, 5: interfacial electron hole recombination (*Adapted from reference 25*).

Recent studies by the groups of Huang and Sargent showed improved stability and photocurrent response for solar cells based on C_{60}-layered perovskites, which were attributed to passivation of surface defects and removal of grain boundaries in perovskites by C_{60}.[27,28] In detail, the surface defects and grain boundaries were acting as trap states which accelerated the rate of photoexcited electrons recombination leading to the poor photocurrent. The presence of C_{60} molecules onto the surface/grain boundary of perovskite efficiently trapped the excited electrons by arresting their recombination.

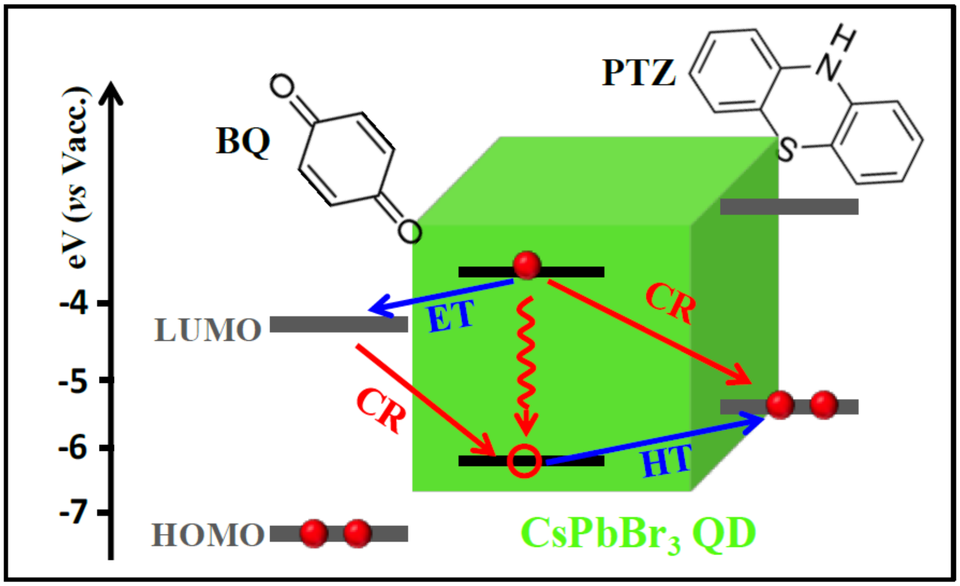

Figure 3.4. Schematic energy level diagram of $CsPbBr_3$ QD, Benzoquinone (BQ) and QD-Phenothiazine (PTZ) complexes and possible charge separation and recombination pathways (*Adapted from reference 29*).

PNCs have also been explored in electron transfer studies with classical electron acceptors such as benzoquinone,[29] phenothiazine,[29] and perylene in the solution state.[30] Lian *et al*. showed that the excitons in $CsPbBr_3$ QDs could be easily dissociated using benzoquinone and phenothiazine as electron and hole acceptors, respectively. The possible separation and recombination of charge carriers were explained using a schematic diagram (**Figure 3.4**). The half-lives for electron transfer from PNCs to benzoquinone and subsequent recombination were found to be 65 ± 5 ps and 2.6 ± 0.4 ns, respectively. Similarly, the hole transfer from PNCs to phenothiazine and subsequent recombination were found to be 49 ± 6 ps and 1.0 ± 0.2 ns, respectively. The efficient interfacial electron and hole transfer property of PNCs makes them suitable for solar cell application.

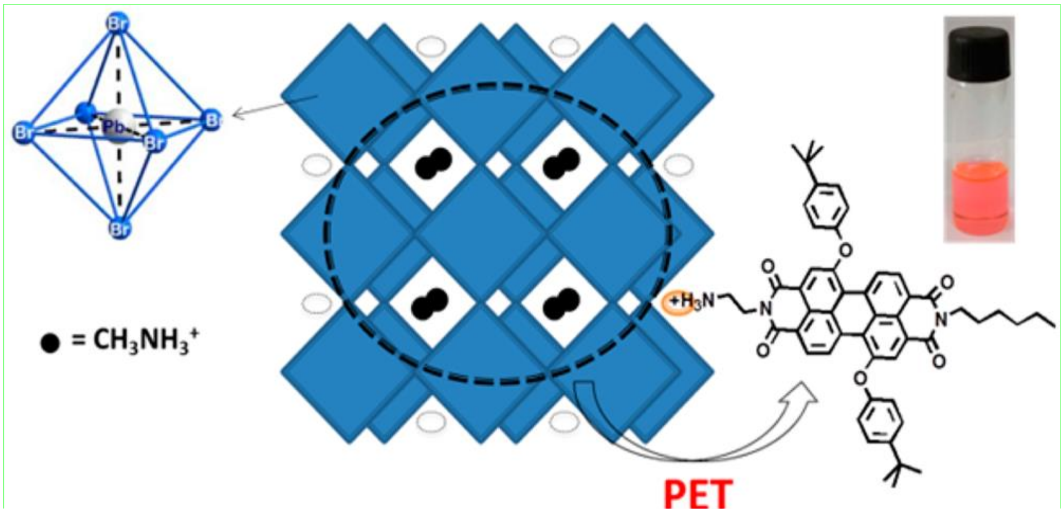

Figure 3.5. Schematic diagram representing PET from $MAPbBr_3$ nanocrystals to electron-deficient perylene diimide based capping ligands (*Adapted from reference 30*).

Li *et al*. have introduced electron deficient organic molecules as capping ligands for studying PET in PNCs.[30] This was achieved by synthesizing $CH_3NH_3PbBr_3$ PNCs functionalized with an electron-accepting organic molecule, perylenetetracarboxylic diimide (PDI), bearing $–NH_3^+$ head group as the capping agent (**Figure 3.5**). The $–NH_3^+$ head group present in organic chromophores strongly interacted with the surface of nanocrystals via electrostatic forces. The photoluminescence of these PNCs was significantly less compared to the corresponding nanocrystals having octylammonium as capping ligands. The efficient fluorescence quenching in the former was attributed to efficient PET from PNCs to the attached PDI molecules.

Though the electron transfer properties of PNCs with various acceptors are studied in the colloidal state, the electron transfer studies in the film state are important for the utilization of these materials in optoelectronic devices. In the present chapter, the electron transfer property of PNCs in the colloidal and film states was studied in detail using C_{60} as the electron acceptor. Further, the electron transfer property of PNCs was utilized in the sensing of explosives.

3.3. Results and discussion

3.3.A. Excitons migration and their harvesting in PNCs

3.3.A1. Synthesis and characterization of PNCs

The $FAPbBr_3$ PNCs were prepared as follows. Octylammonium bromide was dissolved in a mixture of oleic acid and octadecene at 80 °C, which was followed by the addition of FA bromide and lead (II) bromide dissolved in *N*, *N*-dimethylformamide. The addition of acetone to the above reaction mixture precipitated PNCs which were separated by ultracentrifugation. Dry powders were re-dispersed in toluene and used for fluorescence measurements. The peaks obtained from the XRD spectrum of PNCs film showed the cubic nature of the PNCs (**Figure 3.6a**). The absence of peaks other than the peaks corresponding to the cubic phase revealed the material is phase pure.

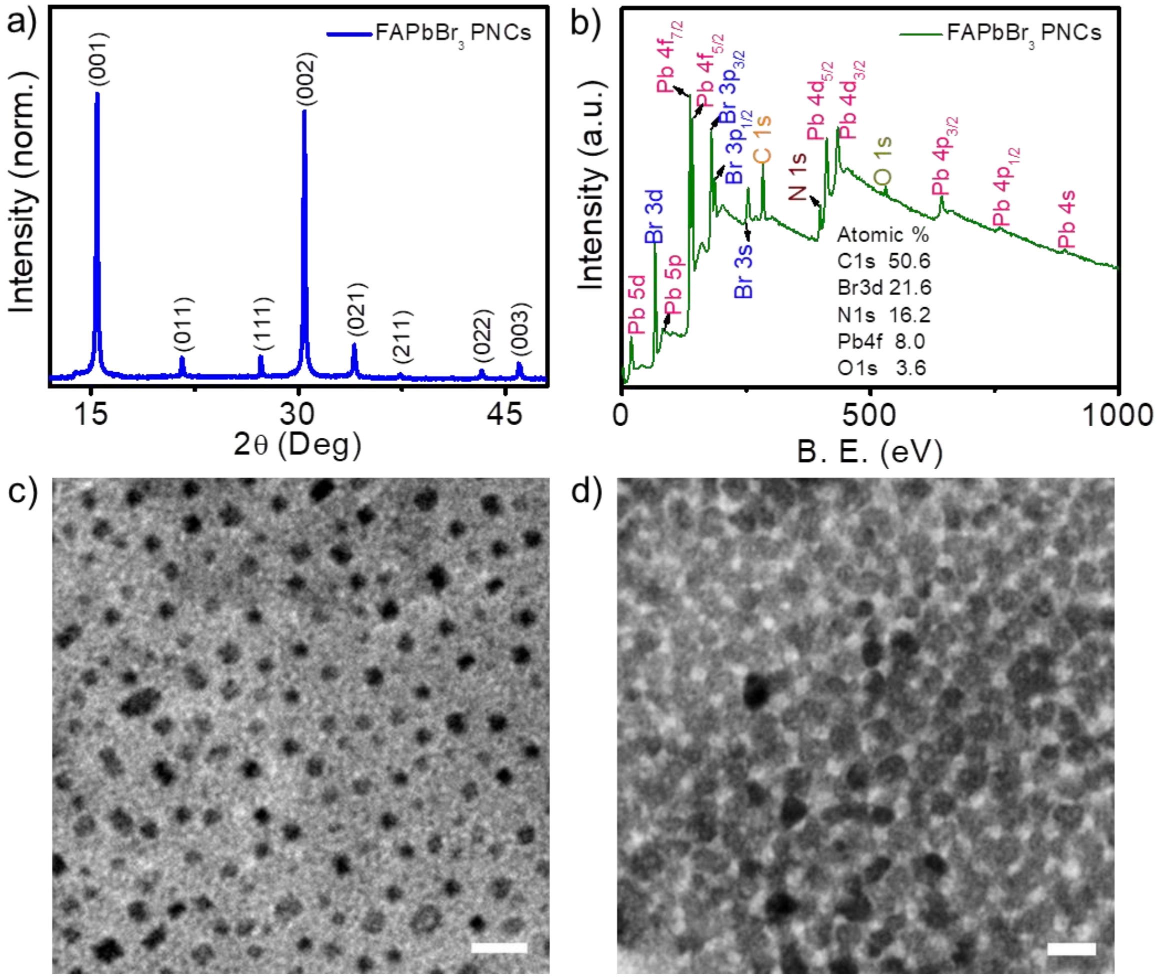

Figure 3.6. a) X-ray diffraction and b) X-ray photoelectron spectrum (XPS) of $FAPbBr_3$ based PNCs film. The samples for XRD and XPS analysis were prepared by drop-casting the colloidal nanocrystals on the glass substrate followed by drying the solvent under an inert atmosphere. TEM images of c) isolated and d) a thin film of PNCs (scale bars: 20 nm). The samples for TEM analysis were prepared by drop-casting the colloidal nanocrystals on carbon coated cu grid followed by drying the solvent under an inert atmosphere.

The phase purity of nanocrystals was further confirmed from XPS analysis (**Figure 3.6b**). XPS spectrum provides chemical state and electronic states of all the elements present in a material. The XPS spectrum of $FAPbBr_3$ PNCs film didn't show any peaks corresponding to impurities. It showed two symmetric peaks of Pb 4f at

136.9 eV and 141.7 eV corresponds to Pb $4f_{7/2}$ and Pb $4f_{5/2}$ levels. The absence of any peak at the lower-binding energy side indicated the absence of metallic lead. The Br 3d peaks were fitted into two peaks centered at 66.8 and 67.6 eV corresponding to the inner and surface Br^{-} ions in PNCs, respectively. The N 1s spectrum had two peaks, indicating the presence of two existing chemical states of the N element. The peak at 398.7 eV was attributed to the presence of the octylammonium capping ligand, while the peak at 400.6 eV originated from formamidinium salt. The lower energy peak at 531.1 eV was corresponding to two nonequivalent O atoms of oleic acid, while the higher energy state peak at 532.7 eV was assigned to two chemically equivalent O atoms from oleate ions. The TEM images of the dilute suspension reveal that the above synthesis provided mostly isolated, spherical NCs with an average diameter of 5 nm (**Figure 3.6c**). Close packing of the PNCs was observed in TEM images of concentrated samples (**Figure 3.6d**).

The colloidal and film states of $FAPbBr_3$ PNCs were yellow in colour with an intense green fluorescence (inset of **Figure 3.7a** and **3.7b** respectively). The absorption and emission spectra of $FAPbBr_3$ PNCs in the solution and film are shown in **Figure 3.7a, b**. In solution, the PNCs absorb light broadly in the UV-visible region with a sharp absorption peak at ca 534 nm. The emission was intense (quantum yield: 72%) and sharp with a narrow FWHM (24 nm). When compared with PNCs in solution phase, the emission band was red-shifted from 541 to 546 nm in the film (**Figure 3.7b**). The red-shift was attributed to energy transfer from smaller to larger crystals in the close-packed film sample. Interestingly, the emission remained intense (quantum yield: 60%) and sharp in the film state, with a spectral FWHM of 25 nm.

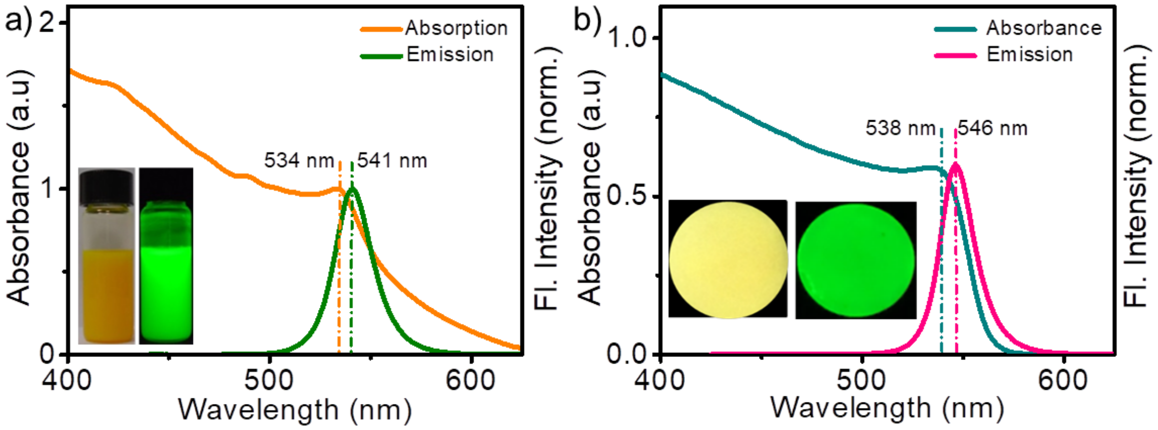

Figure 3.7. Absorption and emission spectra of a) a PNC solution (0.1 mgmL^{-1} in toluene) and b) a PNC thin film. Fluorescence spectra were recorded by exciting the samples at 400 nm. The PNCs dispersed in toluene showed yellow colour which turned into bright green coloured emission upon excitation with UV light as shown in the inset of Figure 3.7a. The same colour was also seen in the film state as shown in the inset of figure 3.7b.

3.3.A2. Electron transfer studies in the solution state

To test electron transfer from $FAPbBr_3$ PNCs, we selected fullerene (C_{60}) as the electron acceptor. Fullerenes, one of the most explored electron acceptors have created an enormous interest in optoelectronics due to their unique behaviour.[32-34] The rigid aromatic structure of fullerenes evokes low reorganization energies during electron transfer reactions and also their extended π-conjugation facilitates effective charge stabilization. The distinctive architectural flexibility and chemical versatility of fullerenes permit modification of their properties. At first, we recorded the fluorescence spectrum of a PNC solution (0.1 mg/mL in toluene) and to which C_{60} (1 mg/mL in toluene) dissolved in toluene was added in 0.5 µM portions. The addition of C_{60} resulted in continuous quenching of the PNC emission, indicating efficient electron transfer from perovskite to C_{60} (**Figure 3.8a**). The initial quenching was remarkably large, and the rate at which C_{60} quenched the emission decreased with the subsequent addition of C_{60}. As the concentration of C_{60} was increased up to 4 µM (equivalent to 2.8 wt% of C_{60} with respect to PNC), the emission of PNCs was quantitatively (ca 98%) quenched (**Figure 3.8a**), which is attributed to efficient

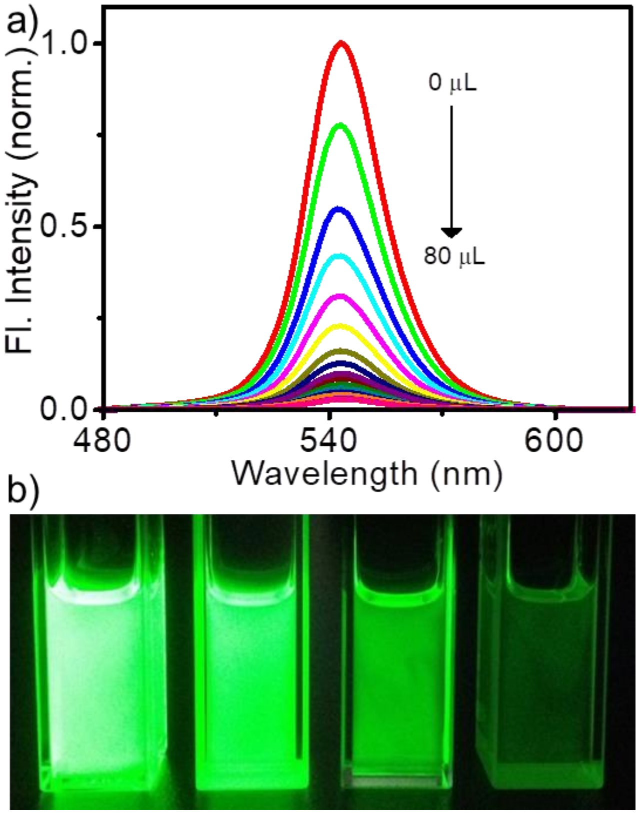

Figure 3.8. a) Fluorescence spectra of a $FAPbBr_3$ PNC solution supplemented with different concentrations (0 to 4 µM) of C_{60} (concentration of $FAPbBr_3$: 0.1 mgmL^{-1}, λ_{ex}=400 nm). b) Photographs of PNC solutions supplemented with different concentrations of C_{60} (from left to right; 0, 0.5, 1.5 and 4 µM).

electron transfer from photoactivated PNC to C_{60}. Visual changes to the emission are clearly seen from the photographs of PNC solutions supplemented with different concentrations (0 to 4 µM) of C_{60} (**Figure 3.8b**). It must be noted that we detected residual fluorescence even at high concentrations of C_{60} (42 wt% of C_{60} with respect to PNC), which suggests that quenching does not follow the theoretical 1:1 ratio.

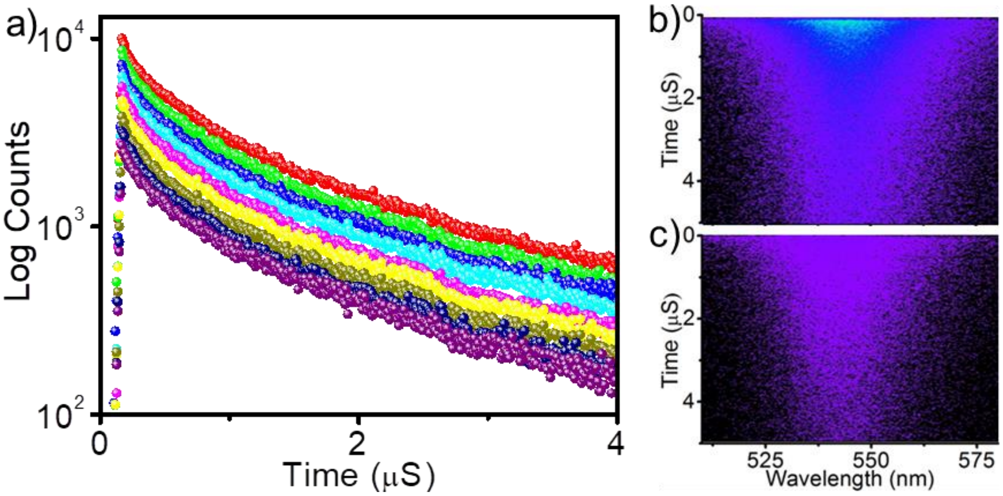

Figure 3.9. a) Fluorescence decay profiles of $FAPbBr_3$ PNCs dissolved in toluene and supplemented with different concentrations of C_{60} (top to bottom: 0 to 4 µM at 0.5 µM). b) Photocount-wavelength decay profiles of b) a PNC solution without C_{60}, and c) a PNC solution with 4 µM C_{60}.

We obtained additional insight into electron transfer from PNC to C_{60} from time-resolved fluorescence data. Fluorescence decay profiles of a solution of PNCs in toluene without or with different amounts of added C_{60} were examined by excitation of the samples with 400 nm fs laser pulses. Interestingly, the fluorescence lifetime of the sample remained essentially intact (1.3 µs) in presence of all (0.5 to 4 µM) concentrations of C_{60} (**Figure 3.9a**); whereas, the number of photons emitted by the sample linearly decreased with increase in the concentration of C_{60}, indicating quenching of photoexcited PNC by C_{60}. Correlation between emitted photons and fluorescence lifetime of PNC is presented in the photocount-wavelength-lifetime 3D images (**Figure 3.9b,c**). The intact fluorescence lifetime, which is accompanied by a monotonous decrease in the number of emitted photons indicates static quenching of the excited state of PNC by C_{60}. In other words, the excited state of PNC is deactivated by electron transfer to C_{60}, whereas residual fluorescence at a given concentration of C_{60} represents PNCs without any adsorbed C_{60}. In other words, a temporal decrease of fluorescence quantum efficiency without any notable change in the fluorescence lifetime, indicates adsorption of C_{60} to the surface of more and more $FAPbBr_3$ PNCs, the surface of which are capped with hydrophobic ligands.

3.3.A3. Electron transfer studies in the film state

To understand the nature of fluorescence quenching by C_{60}, PNC solutions supplemented with different concentrations of C_{60} were processed into thin films by drop-casting, and fluorescence intensities and decay profiles of the films were monitored. We observed a monotonous decrease of both fluorescence lifetime and intensity of PNC films with an increase in the doping density of C_{60} (**Figure 3.10a**), an observation completely different from the C_{60}-independent fluorescence lifetime of samples in the solution phase. The corresponding photocount-wavelength-decay 3D images collected from film samples with and without C_{60} are shown in **Figure 3.10b, c**. The fluorescence lifetime of a pristine PNC film is 4.2 µs, which in presence of 4 μM C_{60} solution was decreased to 210 ns. Interestingly, the concentration of C_{60} needed for quantitative quenching of the excited state of PNC in a film sample was only one- half of that needed for a solution sample (1.4 wt% of C_{60} with respect to PNCs).

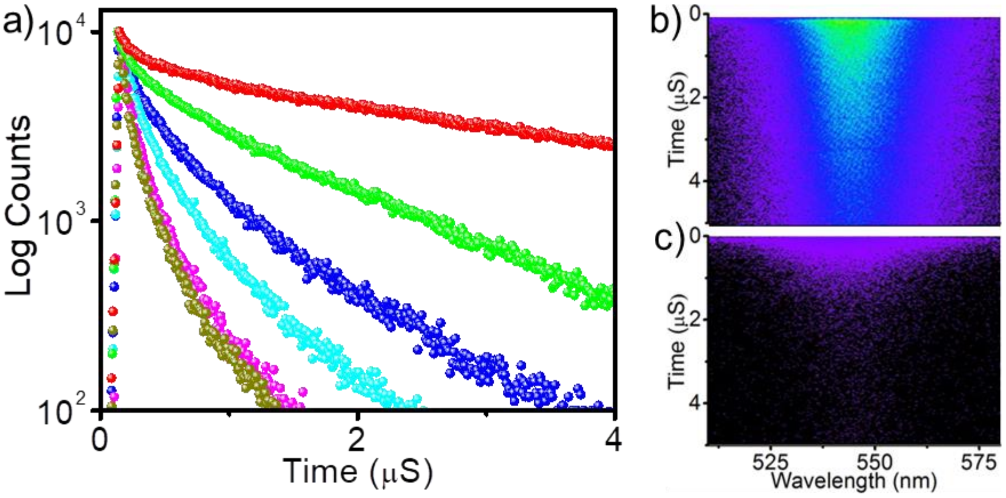

Figure 3.10. Fluorescence decay profiles of $FAPbBr_3$ PNCs a) in thin films prepared from PNC solutions supplemented with different concentrations of C_{60} (top to bottom: 0 to 4 μM at 0.5 μM). Photocount-wavelength decay profile of b) a PNC film without C_{60}, and c) a PNC film with 4 μM C_{60}.

Yet another observation is that the fluorescence lifetime of a PNC film without C_{60} (4.2 μs) was much longer than that of pristine PNC in the solution phase (1.3 μs). The fluorescence lifetime value of PNC films suggests that the electron diffusion length is in the same range as that of solution processed mixed halide perovskites,[35] but longer than that of solution-processed trihalide perovskites.[36] These observations guide us to propose two hypotheses that may have far-reaching implications for perovskite-based electron transfer systems: (i) diffusion or migration of excitons by hopping among

PNCs is probably promoted in close-packed film samples, which lowers the rate of carrier recombination and extends the fluorescence lifetime, and (ii) C_{60} acts as an efficient electron trap that in the film state perturbs exciton migration by acting as an electron scavenger and a center of non-radiative carrier recombination.

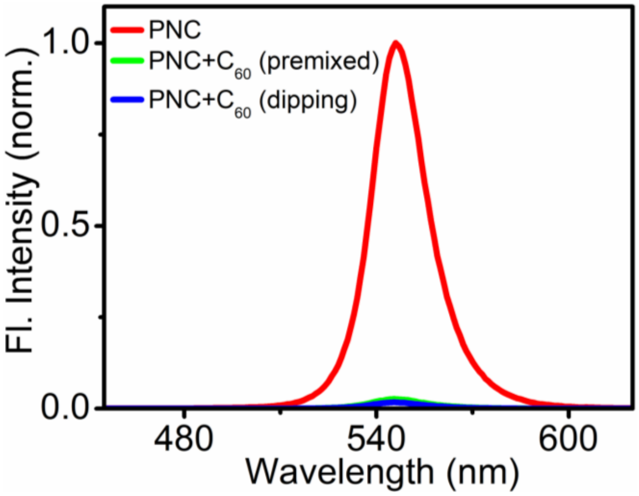

Figure 3.11 Emission spectra of PNC films dipped in 4 µM of C_{60} in toluene.

In order to understand, the mode of sample preparation on the fluorescence quenching, the electron transfer property of PNC film (without mixing C_{60}) after dipping in 4 µM C_{60} solution was also studied. The fluorescence quenching of PNCs by the C_{60} molecules both in the mixing and dipping states were almost the same as shown in **Figure 3.11**. which indicates the uniform distribution of C_{60} molecules onto the PNCs film after dipping. In order to confirm this, TEM images of PNC films with (4 µM) and without C_{60} and after dipping with C_{60} were analyzed. The TEM images showed uniform distribution of C_{60} in the film as shown in **Figure 3.12**.

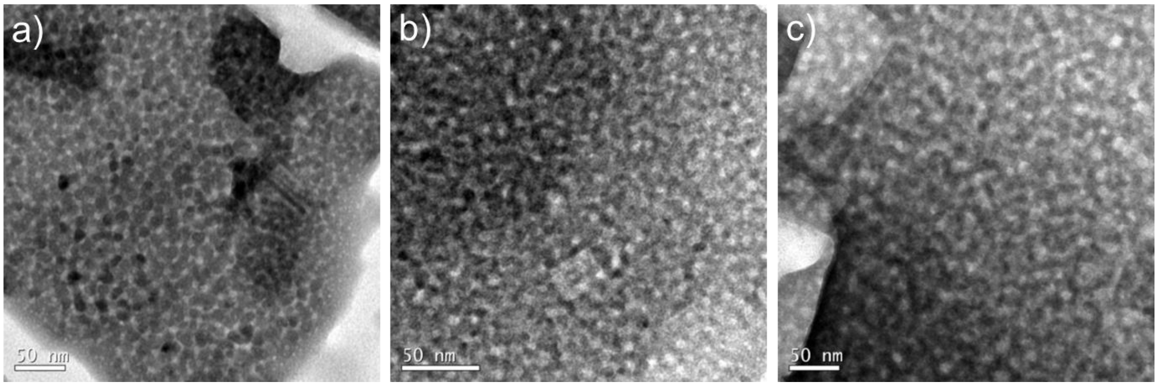

Figure 3.12. TEM images of PNC films a) without and b) with C_{60} doping (4 μM). c) TEM image of PNCs film dipped in 4 μM of C_{60} molecules in toluene.

3.3.A4. Correlation of the key results

We correlate key results in this study with our hypothesis by coining a schematic presentation (**Figure 3.13**) of exciton migration in PNCs and electron transfer to C_{60}. When dissolved in toluene, the capping ligand's octyl chains well-extend into the solvent, rendering PNCs isolated (**Figure 3.13a**). On the other hand, in the film state, the alkyl chains self-assemble by hydrophobic interactions (**Figure 3.13b,c**). Our assumption is that such self-assembly promotes close-packing of PNCs and exciton diffusion in the films state (**Figure 3.13b**). In solution samples, the fluorescence intensity is decreased nearly quantitatively but without any change to the fluorescence lifetime, suggesting that adsorption of even a single C_{60} molecule onto the hydrophobic-capped surface of a PNC leads to static and quantitative quenching of the excited state by electron transfer. Here, efficient trapping of electrons by C_{60} in the PNC-C_{60} composite does not allow us to retrieve any fluorescence from the complex.

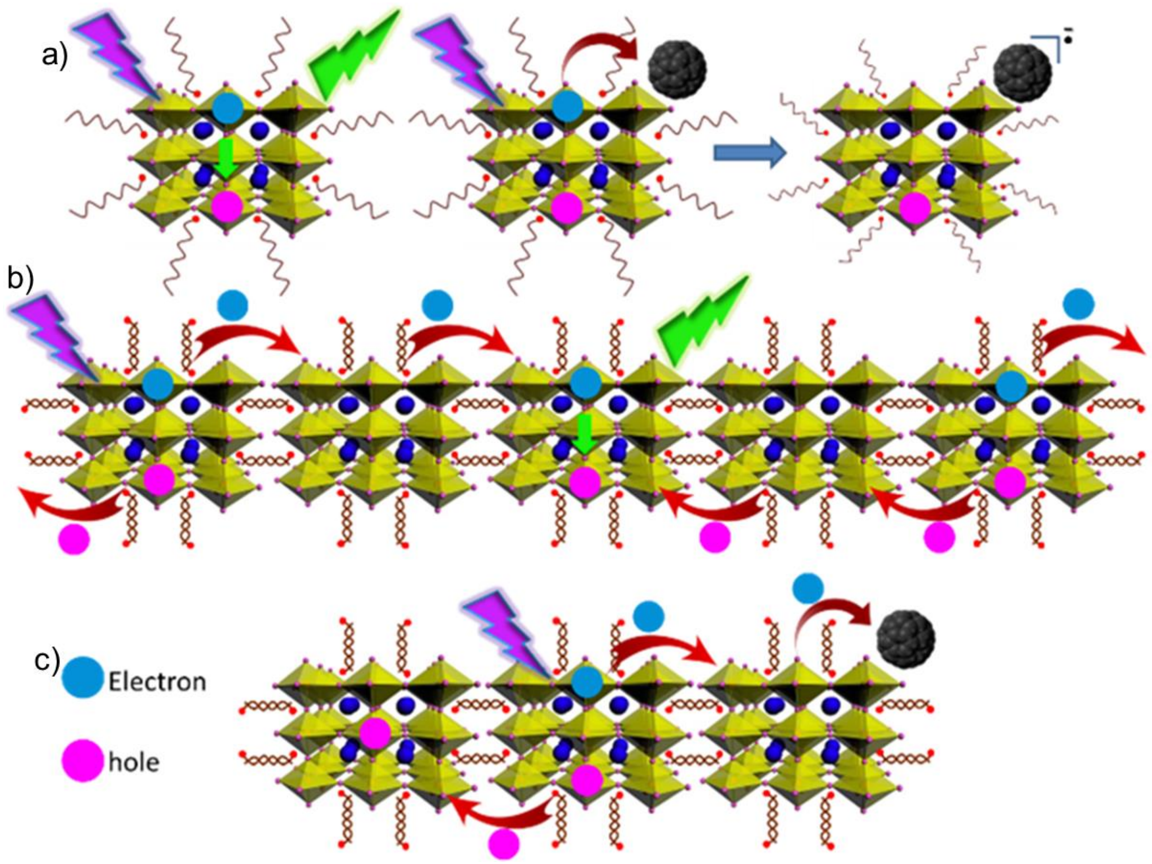

Figure 3.13. Schematic presentation of exciton dynamics in photoactivated $FAPbBr_3$ PNC/fullerene composites: a) fluorescence of PNCs and electron transfer to C_{60} in a solution, b) exciton migration in a PNC film, and c) trapping of migrating exciton by C_{60} doped in a PNC film.

Thus, whatever fluorescence we detect at a given concentration of C_{60} in the PNC-C_{60} mixture is expected to originate from free PNCs, leaving fluorescence lifetime, but not intensity, C_{60}-independent. With the increase in the concentration of C_{60}, more and more PNCs adsorb one or more C_{60}, and the overall fluorescence intensity of the solution decreases. In a film sample, exciton recombination is not limited to the point of a generation because of hole and electron migrations by hopping among closely-packed PNCs, making fluorescence lifetime unusually long when compared with that in a solution where PNCs are isolated. However, when the film is doped with C_{60}, the migrating electrons can be trapped by C_{60}, leading to fluorescence quenching. As the density of doped C_{60} increases, the areas of exciton migration domains shrink, reducing both fluorescence lifetime and intensity. Also, when compared with isolated PNCs, which need at least one C_{60} per PNC for deactivation of the excited state, exciton migration among PNCs suggests only a small number of C_{60} is needed for trapping of electrons activated from a large number of PNCs. Correlation between results and our hypothesis on exciton migration in a $FAPbBr_3$ PNC thin film and fluorescence quenching by electron transfer to C_{60} are presented in **Figure 3.13**.

3.3.B. PNCs as explosive sensor

Nitroaromatics such as 2, 4-dinitrotoluene (DNT), 2,4,6-trinitrotoluene (TNT) and 2,4,6-trinitrophenol (TNP, picric acid) are the most potent explosives used for making lethal weapons. Among the three, the explosive power of TNP is superior to the other two and it is a major component in many unexploded land mines present worldwide. TNP is also widely used in the manufacture of rocket fuels, fireworks, analytical reagents, photographic emulsions, *etc*. and presents in several industrial wastes. It contaminates soil, groundwater, and plant foods, and is dangerous to wildlife and human health because of its biological persistence, and toxicity.[37] Though there are several materials available for the detection of explosives in general,[38-40] surprisingly, less attention has been paid to the selective detection of TNP.[41,42] Most of the reported materials for the detection of nitroaromatic explosives rely on fluorescence signaling, which in turn associated with the PET from the sensor (donor) to the analyte (acceptor).[43,44] Since nitroaromatic explosives are excellent acceptors, they can effectively quench the fluorescence of any donor material resulting in poor selectivity. However, considering the adverse effects of TNP on the environment and living beings, it is important to find new materials for the selective and sensitive detection of TNP. Herein, we explored the use of luminescent PNCs for the selective and sensitive detection of TNP. $CH_3NH_3PbBr_3$ based PNCs were used for this purpose. The synthesis and characterization of the same were explained in **Chapter 2**.

3.3.B1. Selective and sensitive detection of picric acid

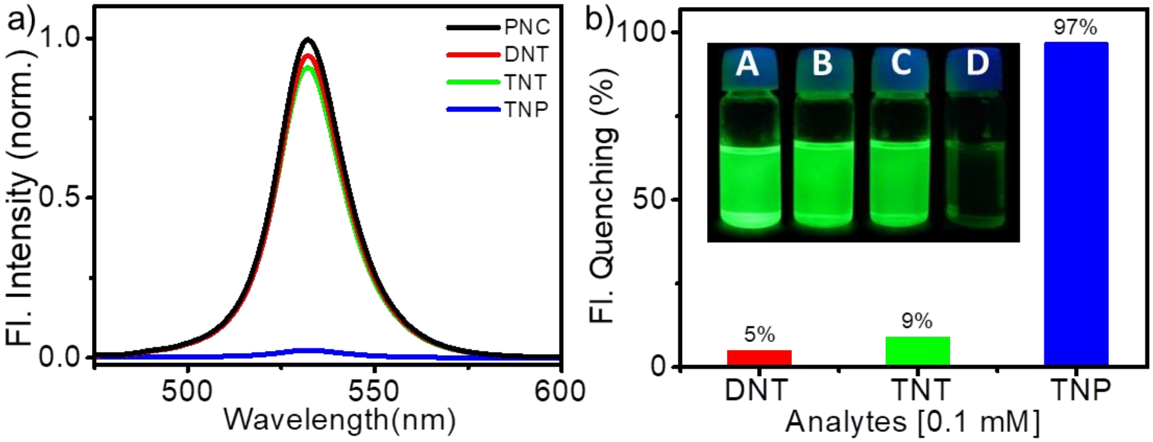

Figure 3.14. a) Fluorescence spectra of PNCs in the absence and presence of DNT, TNT and TNP in toluene (λ_{ex} = 450 nm; l = 10 mm; analyte conc. = 0.1 mM). b) Corresponding fluorescence quenching % at 531 nm. Inset shows the photographs of PNCs alone (A), in the presence of DNT (B), TNT (C) and TNP (D).

The ability of PNCs to sense nitroaromatic explosives was analyzed by adding DNT, TNT, and TNP (50 μL) to the toluene suspension (3 mL) of the former. The solutions of the explosives were prepared in such a way that their concentration will be 0.1 mM in 3 mL of the perovskite suspension. Both DNT and TNT showed no appreciable quenching. On the other hand, TNP showed nearly complete quenching of the perovskite fluorescence almost instantaneously on addition. The emission spectrum of PNCs in the presence of DNT, TNT, and TNP is shown in **Figure 3.14a**. About 5 and 9% fluorescence quenching was seen in the presence of DNT and TNT, respectively. Under identical conditions, TNP exhibited around 97% quenching (**Figure 3.14b**). Photographs of the corresponding solutions under 364 nm UV light is shown in the inset of **Figure 3.14b**.

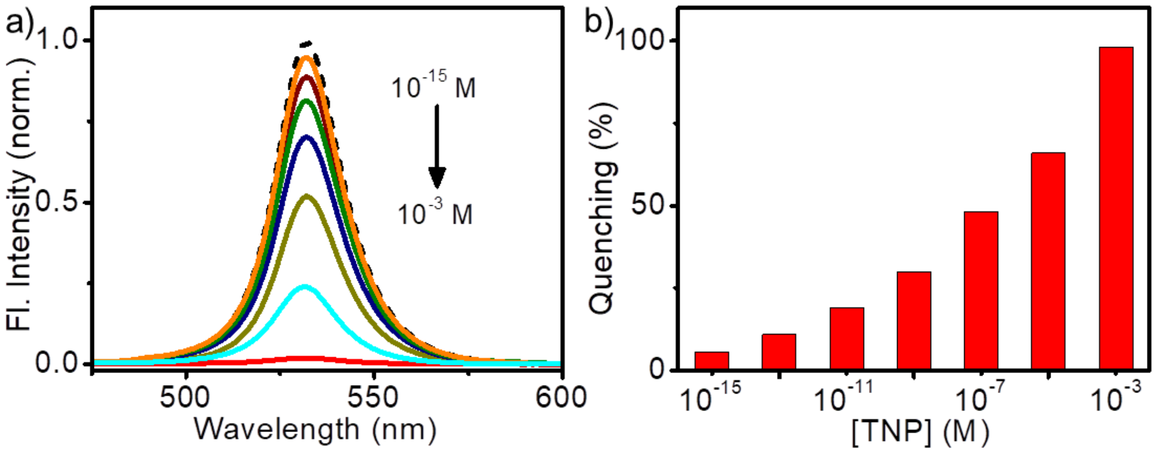

Figure 3.15. a) Fluorescence spectral changes of PNCs in the presence of increasing concentrations of TNP (10^{-3} M to 10^{-15} M). b) Corresponding % quenching of fluorescence versus TNP concentration.

To find the minimum detection limit for TNP, fluorescence quenching studies with different concentrations of TNP (10^{-3} M to 10^{-15} M) was done (**Figure 3.15a and b**). It was seen that noticeable change (~ 6% quenching) in fluorescence was observed even at a concentration as low as femtomolar (10^{-15} M) of TNP. About 30% of quenching was observed in the presence of nM concentrations of TNP. This observation clearly indicates that the PNCs can detect TNP with very high sensitivity.

3.3.B2. Sensing studies in the vapour state

Though the PNCs are capable of detecting TNP with excellent selectivity and high sensitivity in the solution state, it is very important to detect it in the vapour state for practical applications. However, the vapour pressure of TNP (7.48×10^{-7} Torr at 25 °C) is 7 times lesser than that of TNT and 350 times lesser than that of DNT, make it hard to detect in the vapour phase.[45] Nevertheless, the PNCs showed significant fluorescence quenching when exposed to TNP vapour (**Figure 3.16a**). For this experiment, the nanocrystals were coated on a non-fluorescent filter paper strip and kept inside a vial containing saturated vapours of TNP. The fluorescence of the nanocrystals was monitored at different time intervals. About 12% of quenching was observed within 2 minutes of exposure and a maximum of 65% quenching was observed in one hour. Changes in the fluorescence were negligible after one hour. The changes to the nanocrystal fluorescence with time on exposure to TNP vapours are shown in **Figure 3.16a**.

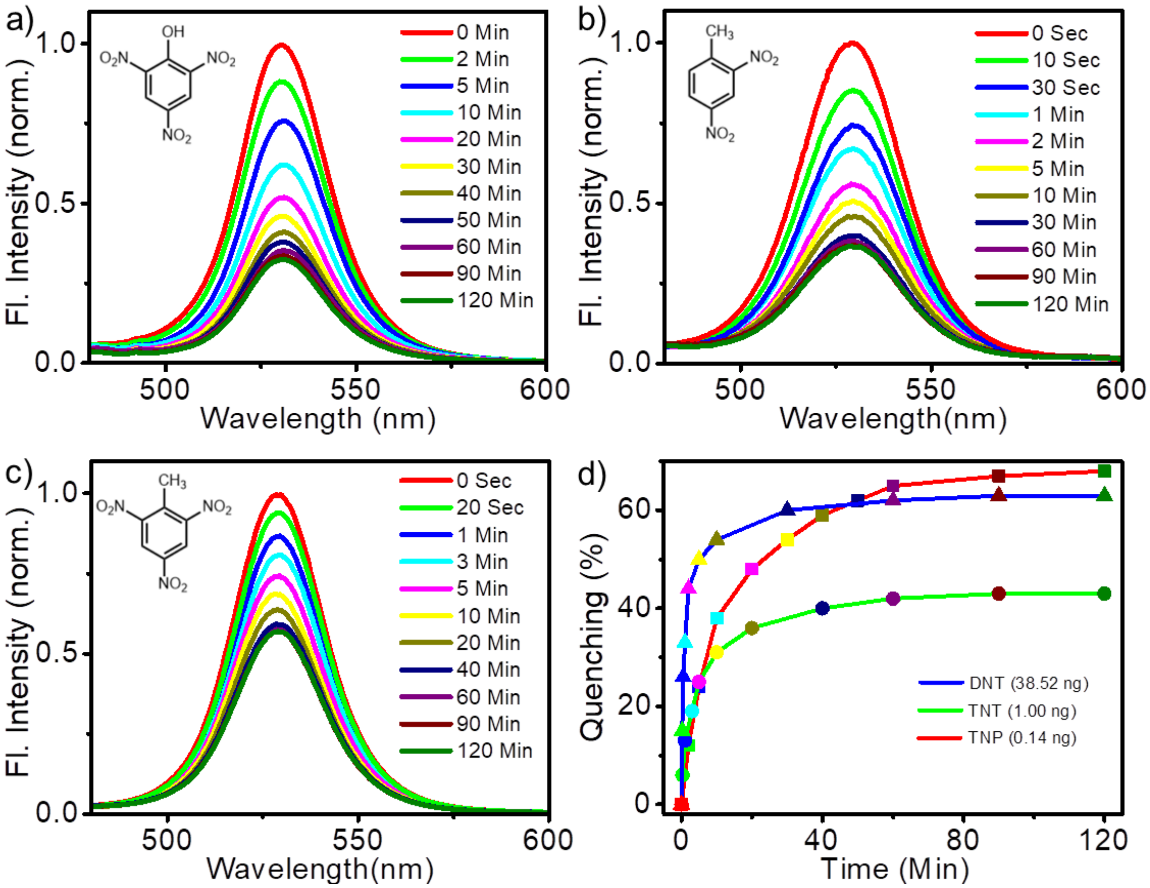

Figure 3.16. Fluorescence spectral changes of PNCs film in the presence of saturated vapours of a) DNT, b) TNT and c) TNP with increasing time. d) Comparison of the corresponding % quenching of fluorescence. The amount of each analyte present in a 15 mL vial at its saturated vapour pressure is shown in Figure 3.16d.

Quenching experiments with DNT and TNT in the vapour phase were also carried out under identical conditions (**Figure 3.16b,c**). The summary of quenching % vs. time for all the explosives is shown in **Figure 3.16d**. The studies revealed that the quenching efficiency followed the order TNP > DNT > TNT, but the selectivity between TNP and DNT was found to be less, which could be correlated to the higher vapour pressure (correspondingly a higher concentration) of the latter. The vapour pressure of TNT (5.50×10^{-6} Torr) and DNT (2.63×10^{-4} Torr) is 1-2 order higher than that of TNP (7.48×10^{-7} Torr). This results in a higher concentration of DNT, and TNT than that of TNP at the saturated vapour pressure (in a 15 mL vial, the saturated vapour pressures of the analytes correspond to 38.52 ng of DNT, 1.00 ng of TNT and 0.14 ng of TNP). Both TNT and DNT showed faster quenching in the initial time probably due to high vapour pressure and reached a plateau region in 15-20 minutes. The plateau formation could be attributed to the equilibrium between the adsorption and desorption processes of the analytes on the film surface. On the other hand, the quenching was slow for TNP at the initial time scale due to low vapour pressure. Similarly, the plateau formation appeared only after 60 minutes. This could be attributed to the presence of the hydroxyl group in TNP, which facilitates the binding of TNP with PNCs through hydrogen bonding. This binding process enhances the adsorption but reduce desorption, and hence delay the equilibrium. Enhanced adsorption through hydrogen bonding also explains the higher quenching efficiency for TNP though it has much lower vapour pressure than that of TNT and DNT.

3.3 B3. Sensing mechanism

Energy levels of the PNCs were calculated from the oxidation potential (obtained using cyclic voltammetry) and optical band-gap (calculated from absorption and emission spectral crossover point). Using these values, the energy levels of PNCs were calculated. The oxidation potential corresponds to the valence band energy, and the addition of the band-gap to it gave the conduction band energy. The HOMO-

LUMO values of TNP, TNT and DNT were obtained from the literature. The energy level diagram (**Figure 3.17**) proves that the electron transfer process from PNCs to the explosive analytes is energetically feasible.

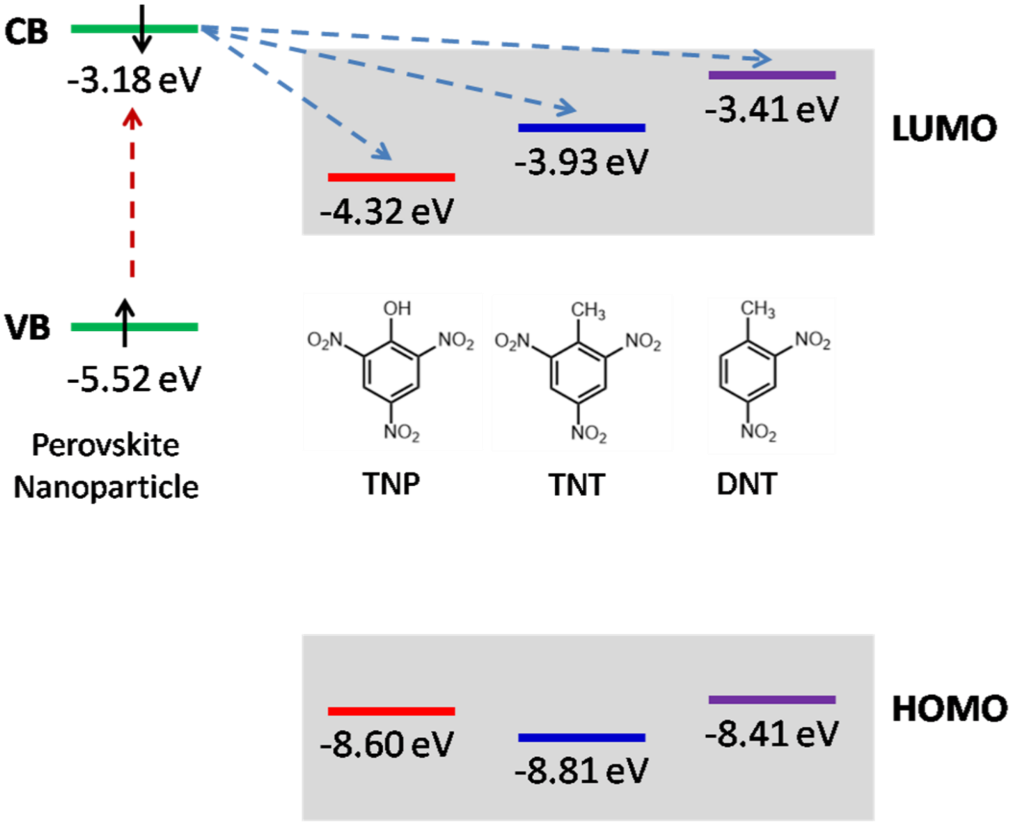

Figure 3.17. Schematic representation of the energy levels of PNCs, TNP, TNT, and DNT.

As mentioned earlier, the distinction between DNT, TNT, and TNP is difficult using fluorescence based sensors because all of them are good electron acceptors and quenches the donor fluorescence efficiently. However, in the present case, high selectivity and sensitivity were observed for the detection of TNP, particularly in the solution state. We anticipated that the hydroxyl group in TNP plays a key role in the overall detection mechanism by interacting with the PNCs through hydrogen bonding. Since such interactions may result in phase distortions to the perovskite structure, we monitored the powder XRD profile of the material in the absence and presence of TNP. The pristine nanocrystals exhibited sharp and intense peaks corresponding to 001 (d = 5.93 Å), 011 (d = 4.20 Å), 002 (d = 2.97 Å), 021 (d = 2.65 Å) planes (**Figure 3.18a**). No change in the XRD profile was seen on the addition of small amounts of TNP. However, at higher concentrations of TNP (~1 mM), new peaks were started appearing in the XRD profile indicating phase distortions to the nanocrystal assembly.

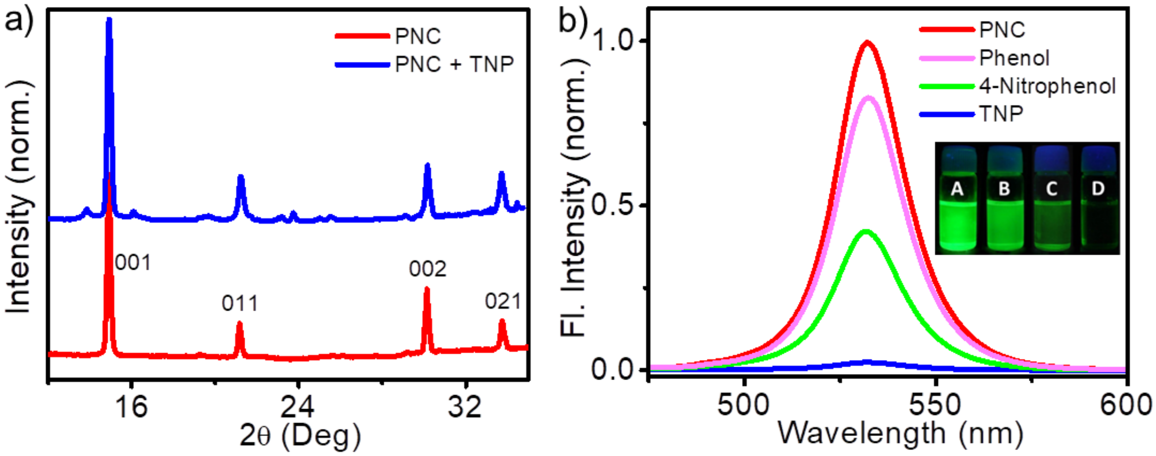

Figure 3.18. a) Powder XRD profile of PNCs in the absence and presence of TNP (b) fluorescence spectra PNCs in the absence and presence of 0.1 mM of phenol, 4-nitrophenol, and TNP in toluene. Photographs of the corresponding solutions under 364 nm UV light is shown in the inset.

In order to get a better insight into the role of hydroxyl on fluorescence quenching, we have selected phenol and 4-nitrophenol, two aromatic compounds with hydroxyl group, as the analytes. As shown in **Figure 3.18b**, 0.1 mM of TNP quenches 97% of the fluorescence. On the other hand, under identical conditions, 4-nitrophenol and phenol can quench up to 54% and 19% of the fluorescence of the nanocrystals (**Figure 3.18b**). Considering the quenching efficiency of the three analytes, it was clear that not only hydroxyl group but also the number of nitro groups on the analyte plays a key role in the quenching mechanism.

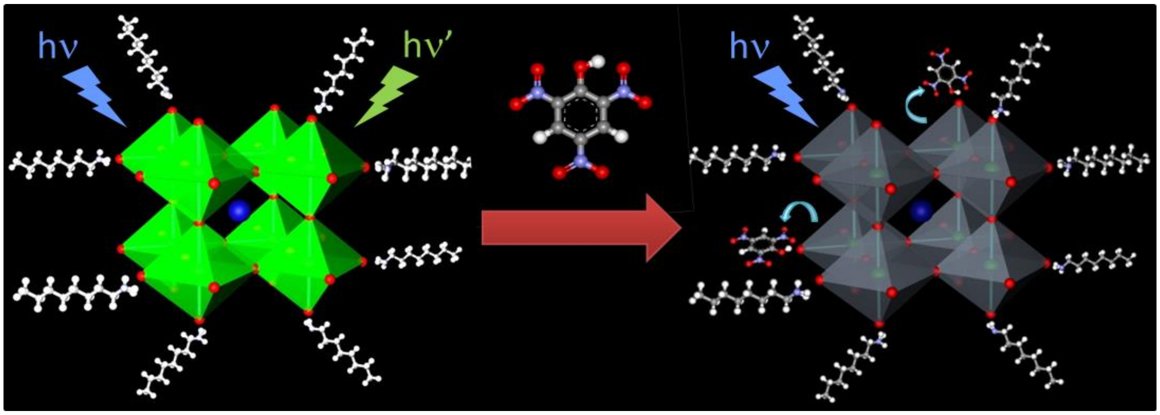

Figure 3.19. Simplified schematic representation of the picric acid sensing mechanism by PNCs.

From the above study, it could be assumed that the hydroxyl group of TNP forms a stable hydrogen bond with PNCs. This interaction could bring the analytes very close to the nanocrystals resulting in fluorescence quenching. Since the exciton diffusion and charge separation is very efficient in perovskite,[35,36] electron transfer could be possible from perovskites to the analytes. This might be acting as the major pathway for the fluorescence quenching. This also explains the higher quenching efficiency for TNP (having three nitro groups, stronger acceptor) when compared to that of nitrophenol (having one nitro group, weaker acceptor). In addition to that, the hydrogen bonding interactions induce some phase distortions, especially at higher concentrations of the analyte, resulting in minor quenching of the fluorescence. This could be attributed to the fluorescence quenching of the nanocrystals in the presence of phenol. Since DNT or TNT doesn't have any hydroxyl groups, there is no driving force for them to come closer to the nanocrystals resulting in poor quenching. This is particularly true in the solution state, where the sensor nanocrystals and analytes move continuously. Based on these observations, the sensing phenomenon could be schematically represented as shown in **Figure 3.19.**

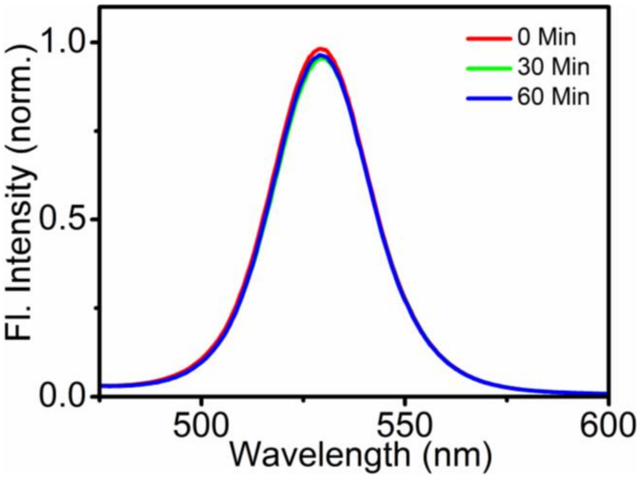

Figure 3.20. Fluorescence spectral changes of PNCs film on exposure to ambient humidity (about 70%) with increasing time.

Since the quenching mechanism of PNCs with TNP involves hydrogen bonding, we have carried out an experiment to study the role of humidity on the fluorescence properties of the former. In this experiment, the PNCs film was exposed to the ambient humidity (about 70%) and measured the fluorescence at different time intervals. As shown in **Figure 3.20**, the change in fluorescence with time was negligible, which indicates humidity has no influence on the quenching of perovskite fluorescence.

3.4. Conclusions

In summary, we have studied in detail the electron transfer properties of PNCs and their application in sensing of explosives. The addition of C_{60} into a solution of hydrophobic-capped PNCs results in the quantitative quenching PNC fluorescence, but without any change to the fluorescence lifetime. Such static quenching of fluorescence is credited to the adsorption of C_{60} molecules onto the hydrophobic surface of NCs and efficient electron transfer from PNC to C_{60}. When compared with pristine PNCs in a solution, their film shows unusually long fluorescence lifetime, indicating hopping or migration of photo-generated excitons among PNCs before radiative recombination. Both fluorescence intensity and lifetime of the PNC film monotonously decreased with an increase in the doping density of C_{60}, which was attributed to channeling of exciton migration into electron transfer to C_{60} molecules, which acted as electron acceptors and centers of non-radiative carrier recombination. Therefore, by analyzing steady-state and time-resolved fluorescence of highly-luminescent PNCs in solution and film states, we successfully detected not only the diffusion of photo-generated excitons but also a restriction of exciton migration by electron transfer to C_{60} molecules doped in the film. Such exciton migration in PNC films and channeling of exciton migration into electron transfer to C_{60} are promising for PNC sensitized solar cells. Luminescent PNCs were also found to be an excellent sensor platform for the detection of TNP with high selectivity and sensitivity. The sensitivity and selectivity of this material were comparable with that of several organic molecules and polymers reported in the literature. Studies revealed that the presence of hydrogen bonding hydroxyl group and nitro groups plays a key role in the detection mechanism. Moreover, the present work illustrates the potential of hybrid perovskites for sensor applications, which is a very important area similar to that of photovoltaics.

3. 5. Experimental section

3.5.1. Materials

The reagents and chemicals for synthesis were purchased from local suppliers or from Sigma Aldrich, Alfa Aeasar or TCI.

The valence band energy levels were measured using cyclic voltammetric technique.

3.5.2. Synthesis of $FAPbBr_3$ PNCs

Precursors of $FAPbBr_3$ PNCs are octylammonium bromide, formamidinium bromide, and lead (II) bromide. In a typical PNC preparation, octylammonium bromide (25.2 mg, 0.12 mmol) was dissolved in a mixture of oleic acid (170 mg, 0.6 mmol) and octadecene (4 mL) by stirring the solution at 80 °C. Subsequently, formamidinium bromide (25.0 mg, 0.20 mmol dissolved in 200 μL of DMF) and lead (II) bromide (73.4 mg, 0.2 mmol dissolved in 250 μl of DMF) were added to the solution of octylammonium bromide. The PNCs were immediately precipitated as a yellow dispersion by the addition of acetone. The mixture was ultra-centrifuged at 7000 rpm for 10 min, and the supernatant was decanted. The residual PNCs from the precipitate were washed repeatedly with acetone and dried in air.

3.5.3. Photophysical measurements:

3.5.3.1. Sample Preparation for excitons migration studies

Stock solutions of $FAPbBr_3$ PNC (1 mg/mL) were prepared by dispersing dried powder of PNC in toluene, which was followed by ultra-sonication for 10 minutes. For solution samples, the stock solution was diluted into 0.1 mg/mL with toluene. In fluorescence quenching experiments, 1 mM solution of C_{60} in toluene was added in 2 to 5 μL portions to PNC solutions. Thin films of PNC were prepared by drop-casting of 100 μL PNC solution (with or without C_{60}) on 10 mM diameter cover glass discs. The samples were dried under a laminar flow of air.

3.5.3.2. Sample Preparation for explosive sensing studies

All the quenching studies in solution state were done in toluene. The PNCs dispersions were prepared in toluene (2 mg in 50 mL) by sonication. Optically matching solutions were prepared for each experiment. The analytes, TNP, DNT, TNT, 4-Nitrophenol, and phenol were also prepared in toluene in varying concentrations. 50 μL of analyte was added to the 3ml of PNCs solution for each measurement. For the vapor state detection, the PNCs dispersed in toluene was drop cast on a non-fluorescent Whatmann filter paper and allowed it for drying in a vacuum desiccator. Then the Filter paper was fixed on a quartz plate and the quartz plate was kept in a well closed vial containing 1g of TNP covered with cotton. The emission of the nanocrystals film was monitored at different time intervals.

3.6. References

1. Electron Transfer in Chemistry, Principles, Theories. Methods and Techniques, ed. V. Balzani, Wiley-VCH, Weinheim, Germany, **2001**, part 1, vol. 1.
2. Electron Transfer in Chemistry, Biological, and Artificial Supramolecular Systems, ed. V. Balzani, Wiley-VCH, Weinheim, Germany, **2001**, part 1, vol. 3.
3. L. Valkunas, J. Chmeliov, G. Trinkunas, C. D. P. Duffy, R. Grondelle, A. V. Ruban, *J. Phys. Chem. B* **2011**, *115*, 9252-9260.
4. J. Deisenhofer, O. Epp, K. Miki, R. Huber, H. Michel, *Nature* **1985**, *318*, 618-624.
5. G. McDermott, S. M. Prince, A. A. Freer, A. M. Hawthornthwaite-Lawless, M. Z. Papiz, R. J. Cogdell, N. W. Isaacs, *Nature* **1995**, *374*, 517-521.
6. C. J. Brabec, N. S. Sariciftci, J. C. Hummelen, Plastic Solar Cells. *Adv. Funct. Mater*. **2001**, *11*, 15-26.
7. S. H. Park, A. Roy, S. Beaupré, S. Cho, N. Coates, J. S. Moon, D. Moses, M. Leclerc, K. Lee, A. J. Heeger, *Nat. Photonics* **2009**, *3*, 297-302.
8. K. M. Haynes, K. C. Kratch, S. D. Stovall, C. O. Obondi, C. R. Thurber, W. J. Youngblood, *ACS Appl. Mater. Interfaces* **2015**, *7*, 16133-16137.
9. A. Bauer, F. Westkamper, S. Grimme, T. Bach, *Nature* **2005**, *436*, 1139-1140.
10. D. Ravelli, D. Dondi, M. Fagnoni, A. Albini, *Chem. Soc. Rev.* **2009**, *38*, 1999-2011.

11. T. P. Yoon, M. A. Ischay, J. Du, *Nat. Chem*. **2010**, *2*, 527-532.
12. J. Xuan, W. J. Xiao, *Angew. Chem., Int. Ed*. **2012**, *51*, 6828-6838.
13. E. Kazuma, J. Jung, H. Ueba, M. Trenary, Y. Kim, *J. Am. Chem. Soc.* **2017**, *139*, 3115-3121.
14. H. Q. Peng, L. Y. Niu, Y. Z. Chen, L. Z. Wu, C. H. Tung, Q. Z. Yang, *Chem. Rev*. **2015**, *115*, 7502-7542.
15. N. S. Sariciftci, L. Smilowitz, A. J. Heeger, F. Wudl, *Science* **1992**, *258*, 1474-1476.
16. M. Natali, S. Campagna, F. Scandola, *Chem. Soc. Rev*. **2014**, *43*, 4005-4018.
17. T. Fiala, L. Ludvikova, D. Heger, J. Svec, T. Slanina, L. Vetrakova, M. Babiak, M. Necas, P. Kulhanek, P. Klan, V. Sindelar, *J. Am. Chem. Soc*. **2017**, *139*, 2597-2603.
18. A. O. El-Ballouli, E. Alarousu, A. Usman, J. Pan, O. M. Bakr, O. F. Mohammed, *ACS Photonics* **2014**, *1*, 285-292.
19. L. A. Padilha, J. T. Stewart, R. L. Sandberg, W. K. Bae, W.-K. Koh, J. M. Pietryga, V. I. Klimov, *Acc. Chem. Res*. **2013**, *6*, 1261-1269.
20. C. Ratanatawanate, A. Chyao, K. J. Balkus, *J. Am. Chem. Soc.* **2011**, *133*, 3492-3497.
21. X. Yu, Y. Li, X. Hu, D. Zhang, Y. Tao, Z. Liu, Y. He, M. A. Haque, Z. Liu, T. Wu, Q. J. Wang, *Nat. Commun*. **2018**, *9*, 4299.
22. H. Zhu, Y. Yang, T. Lian, *Acc. Chem. Res*. **2013**, *46*, 1270-1279.
23. Y. Yang, W. Rodríguez-Córdoba, T. Lian, *Nano Lett.* **2012**, *12*, 4235-4241.
24. J. Huang, Z. Huang, Y. Yang, H. Zhu, T. Lian, *J. Am. Chem. Soc.* **2010**, *132*, 4858-4864.
25. A. Marchioro, J. Teuscher, D. Friedrich, M. Kunst, R. Krol, T. Moehl, M. Gratzel, J.-E. Moser, *Nat. Photonics* **2014**, *508*, 250-255.

26. C. S. Ponseca, Jr., E. M. Hutter, P. Piatkowski, B. Cohen, T. Pascher, A. Douhal, A. Yartsev, V. Sundstrçm, T. J. Savenije, *J. Am. Chem. Soc.* **2015**, *137,* 16043-16048.
27. Y. Shao, Z. Xiao, C. Bi, Y. Yuan, J. Huang, *Nat. Commun.* **2014**, *5*, 5784.
28. J. Xu, A. Buin, A. H. Ip, W. Li, O. Voznyy, R. Comin, M. Yuan, S. Jeon, Z. Ning, J. J. McDowell, P. Kanjanaboos, J.-P. Sun, X. Lan, L. N. Quan, D. H. Kim, I. G. Hill, P. Maksymovych, E. H. Sargent, *Nat. Commun.* **2015**, *6*, 7081.
29. K. Wu, G. Liang, Q. Shang, Y. Ren, D. Kong, T. Lian, *J. Am. Chem. Soc*. **2015**, *137,* 12792-12795.
30. J. H. Bang, P. V. Kamat, *ACS Nano* **2011**, *5,* 9421-9427.
31. Z. Xu, M. Cotlet, *Angew. Chem. Int. Ed.* **2011**, *50,* 6079-6083.
32. M. H. Stewart, A. L. Huston, A. M. Scott, E. Oh, W. R. Algar, J. R. Deschamps, K. Susumu, V. Jain, D. E. Prasuhn, J. B. Canosa, P. E. Dawson, I. L. Medintz, *ACS Nano* **2013**, *7,* 9489-9505.
33. R. Zhu, C. Gao, T. Sun, L. Shen, D. Sun, X. Li, *Langmuir* **2016**, *32,* 3294-3299.
34. G. H. Ahmed, J. Liu, M. R. Parida, B. Murali, R. Bose, N. M. AlYami, M. N. Hedhili, W. Peng, J. Pan, T. M. D. Besong, O. M. Bakr, O. F. Mohammed, *J. Phys. Chem. Lett.* **2016**, *7,* 3913-3919.
35. S. D. Stranks, G. E. Eperon, G. Grancini, C. Menelaou, M. J. P. Alcocer, T. Leijtens, L. M. Herz, A. Petrozza, H. J. Snaith, *Science* **2013**, *342*, 341-344.
36. G. Xing, N. Mathews, S. Sun, S. S. Lim, Y. M. Lam, M. Gratzel, S. Mhaisalkar, T. C. Sum, *Science* **2013**, *342,* 344-347.
37. J. F. Wyman, M. P. Serve, D. W. Hobson, L. H. Lee, D. E. Uddin, *J. Toxicol. Environ. Health, Part A* **1992**, *37,* 313-327.
38. A. Rose, Z. Zhu, C. F. Madigan, T. M. Swager, V. Bulovic, *Nature* **2005**, *434*, 876-879.
39. S. J. Toal, W. C. Trogler, *J. Mater. Chem*. **2006**, *16,* 2871-2883.

40. C. Vijayakumar, G. Tobin, W. Schmitt, M.-J. Kim, M. Takeuchi, *Chem. Commun*. **2010**, *46*, 874-876.
41. B. Gole, S. Shanmugaraju, A. K. Bar, P. S. Mukherjee, *Chem. Commun*. **2011**, *47*, 10046-10048.
42. V. Vij, V. Bhalla, M. Kumar, *ACS Appl. Mater. Interfaces* **2013**, *5*, 5373-5380.
43. J.-S. Yang, T. M. Swager, *J. Am. Chem. Soc.* **1998**, *120*, 11864-11873.
44. T. Naddo, Y. Che, W. Zhang, K. Balakrishnan, X. Yang, M. Yen, J. Zhao, J. S. Moore, L. Zang, *J. Am. Chem. Soc.* **2007**, *129*, 6978-6979.
45. H. Ostmark, S. Wallin, H. G. Ang, *Propellants, Explos. Pyrotech.* **2012**, *37*, 12-23.

Chapter 4

Perovskite Nanocrystal/Squaraine Dye Conjugate: Development of Visibly Opaque and NIR Transmitting Material

4.1. Abstract

Visibly opaque and near-infrared transmitting (VONIRT) materials play a crucial role in forensic detection, security imaging, night-vision photography, and biomedical applications. In this work, the development of such material using alpha-formamidinium lead iodide based perovskite nanocrystals (PNCs) and squaraine (SQ) dyes is described. It is achieved by gradually increasing the size of PNCs followed by attaching them with a novel low bandgap SQ dye as capping ligand. The acid group present in the SQ dye efficiently interacts with the surface of the nanocrystals via non-covalent interactions. Incorporation of SQ dyes onto PNCs yields composite films with uniform transmittance of below 2% in the visible region (380-740 nm) and above 60% in the NIR region, the prime requisites for VONIRT materials. Further, the addition of SQ dyes imparts better moisture stability and high film quality to the nanocrystals. Opaqueness in the visible region and excellent NIR transparency of the nanocomposite make them useful as a security material and for NIR photography application.

4.2. Introduction

The study of the NIR spectral region is an interesting topic because it extends the visualization of physical phenomena beyond the visible spectral region.[1] In this context, NIR photography is a powerful technique in different situations to gain better results which could not be seen by the human eyes or obtained by photographing the visible light spectrum. It is widely used in various applications such as night vision, to find out hidden structures and texts, document examination, gunshot residue documentation, locating blood vessels under the skin, *etc*.[2,3] A normal camera contains a silicon based detector, which could be modified into NIR camera by just replacing NIR reflecting filter with a visibly opaque, NIR transmitting filter.[4] The materials such as metal oxides, chalcogenide glasses, germanium, and silicon semiconductors have been used as the NIR transmitting materials.[5-7] However, these materials are expensive, brittle in nature, and require high temperature processing conditions.

The low-cost, black coloured organic small molecules and polymers could also absorb light in the entire visible region,[8-11] but still have several problems in developing NIR transmitting filters. In polymers, it is difficult to retain the same range of optical absorption in the entire visible region due to the change in the degree of polymerization in batch-to-batch synthesis. Many of the polymers also have very poor solution processability. On the other hand, organic small molecules suffer from the sharp recovery of transmittance in the NIR region due to their aggregation property, which hinders their real-world applications.

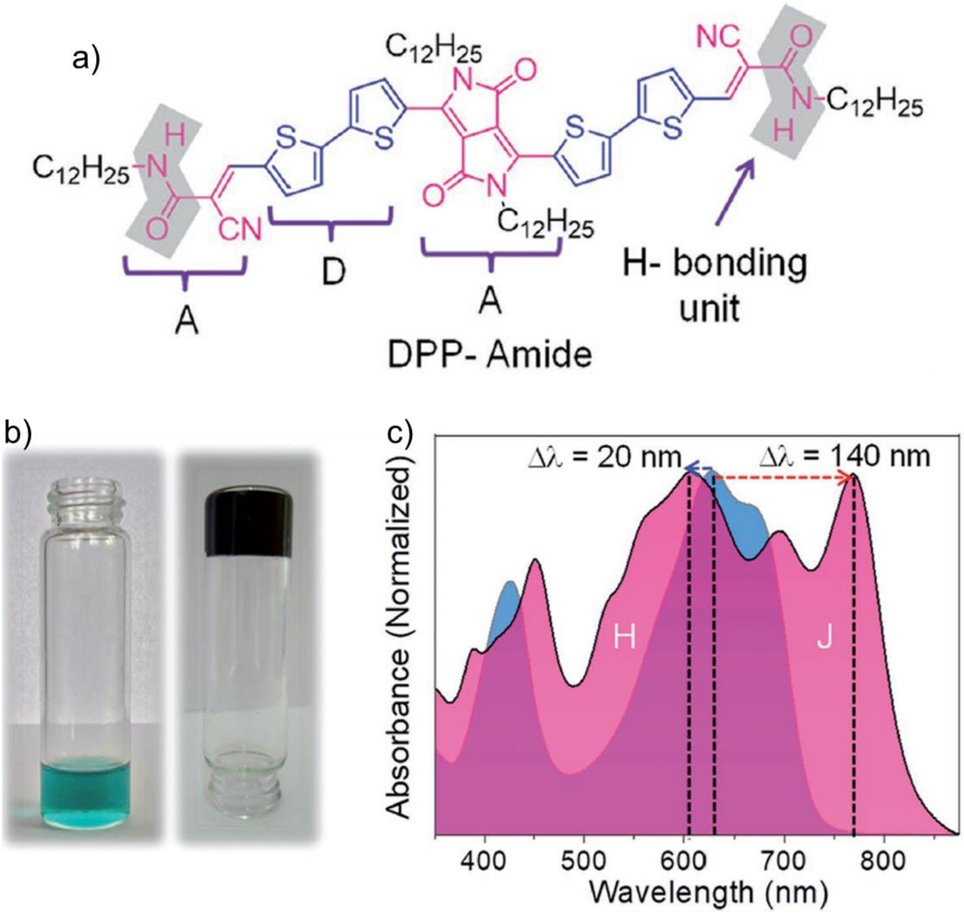

Figure 4.1. a) Chemical structure of DPP-Amide based organic molecule. b) Photograph of the molecule in solution (chloroform) and gel (toluene) states. c) Normalized absorption spectra of DPP-Amide in the monomeric and aggregated states (*Adapted from reference 12*).

Recently, Ajayaghosh and his group developed a novel supramolecular black dye from a diketopyrrolopyrrole (DPP) based organogelator for security and forensic applications.[12] The chemical structure of the synthesized DPP-Amide based organic molecule is shown in **Figure 4.1a**. In solution state, DPP-Amide monomer exhibited a deep green colour (**Figure 4.1b**) with a broad absorption in the visible region (**Figure 4.1c**) due to charge transfer from donor to acceptor moiety. Interestingly, it formed a black coloured organogel (**Figure 4.1b**) in toluene due to H-bonding and π-stacking. The gel showed a broad coverage of absorption from 300-800 nm (**Figure 4.1c**) due to the simultaneous formation of both H- and J-type aggregates. A free-standing, visibly opaque, NIR-transmitting elastomeric black filter was developed by embedding 0.15 wt% of nanoscopic molecular aggregates of DPP-Amide into a poly(dimethylsiloxane) matrix. Finally, the potential use of this filter for NIR photography, security, and forensic-related applications was demonstrated.

Hybrid perovskite materials are well known, efficient photoactive material used in solar cells due to their excellent optoelectronic properties.[13-15] Two dominant properties of perovskite materials such as broader light absorption in the entire visible region and high absorption coefficients are suitable for developing visibly opaque, NIR transmitting filter. Among different hybrid perovskite materials, bulk α-$FAPbI_3$ perovskite material is highly appropriate for this purpose due to its uniform absorption in 400-800 nm region.[16-18] However, this material undergoes a rapid phase transition under ambient conditions which restricts its applications. Nevertheless, it is reported that this problem could be solved by preparing this material in the nanocrystal form.[19,20] The presence of capping ligands in nanocrystals provide phase retention property and environmental stability to them.

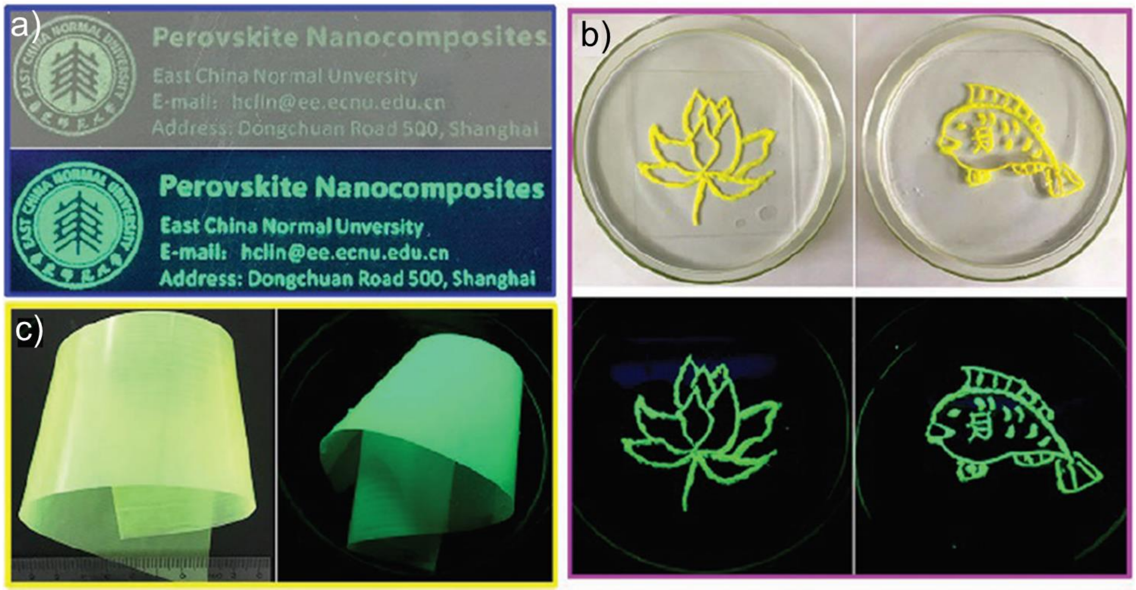

Figure 4.2. Photographs of a) the screen printed sample, b) artworks and c) flexible polyethylene terephthalate (PET) film developed from $CH_3NH_3PbBr_3$ PNC/SSDC composite. All samples were immersed in water before taking photographs to show their stability (*Adapted from reference 21*).

PNCs have been widely used in various security applications due to their excellent photoluminescent quantum yield, tunable bandgap emission and narrow full width at maximum.[21-25] For example, Wang *et al*.[21] developed a simple strategy for the preparation of PNCs-based composite via blending $CH_3NH_3PbBr_3$ nanocrystals with different silicone resins, silicone sealant Dow cornings 937 (SSDC) or phenyl methyl silicone resin (PMSR). Then, the composite was used for screen printing, painting pictures, and flexible coatings as illustrated in **Figure 4.2**. The obtained composite after drying showed excellent PLQY (62%) and unprecedented stability against water, heat and UV exposure. This composite was also used as paints or phosphors for the fabrication of green and white light LEDs.

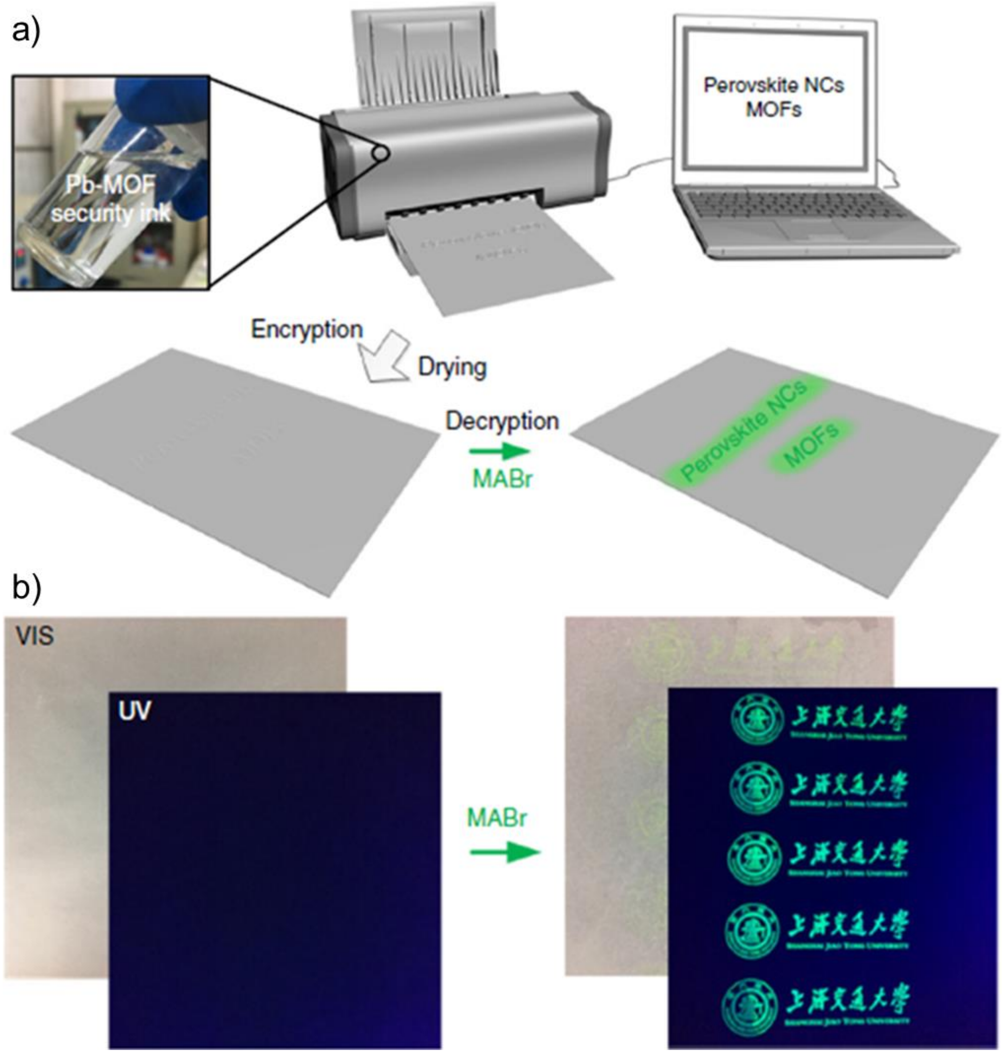

Figure 4.3. a) Schematic illustrations of the patterning, information encryption, and decryption process of the $CH_3NH_3PbBr_3$ PNCs-MOF platform. b) Digital images of the printed logo of Shanghai Jiao Tong University on a commercial parchment paper before and after MABr loading under ambient light and a 365 nm UV lamp (*Adapted from reference 25*).

Zhang *et al.*[25] described a method to store and protect confidential information using 'invisible' lead-based metal-organic frameworks (Pb-MOFs). A colourless and stable precursor solution of Pb-MOF was used as the security ink to print various patterns by an inkjet printer (**Figure 4.3**). The 'invisible' pattern became 'visible' under both normal and UV light after treating with CH_3NH_3Br quaternary salt. The visibility of the pattern was due to the formation of highly luminescent $CH_3NH_3PbBr_3$ nanocrystals by the reaction of Pb-MOF with quaternary salt. The luminescence of PNCs could again be quenched to return the original Pb-MOF state after treating the patterns with a polar solvent, methanol. The reversible on/off switching of the luminescence signal for multiple information encryption and decryption processes were also realized.

Though the PNCs are found to be promising for various security applications, their use for NIR photography is not yet explored. In the present chapter, α-$HC(NH_2)_2PbI_3$ based PNCs were synthesized for developing visibly opaque NIR transmitting filters for NIR photography application. In order to obtain NIR transmitting filter, the size of PNCs was gradually increased via washing the nanocrystals with toluene/ACN mixture to improve their absorption in the longer wavelength region (575-740 nm). Then, a low bandgap squaraine dye molecules were introduced onto the surface of nanocrystals not only to enhance the absorption characteristics in the lower energy region (longer wavelength) but also to provide better environmental stability and solution processability to the nanocrystals. Finally, the visibly opaque NIR transmitting filter obtained from α-$HC(NH_2)_2PbI_3$ PNCs/SQ dye composite was used for the security and NIR photography applications.

4.3. Results and discussion

4.3.1. Synthesis and characterization of PNCs

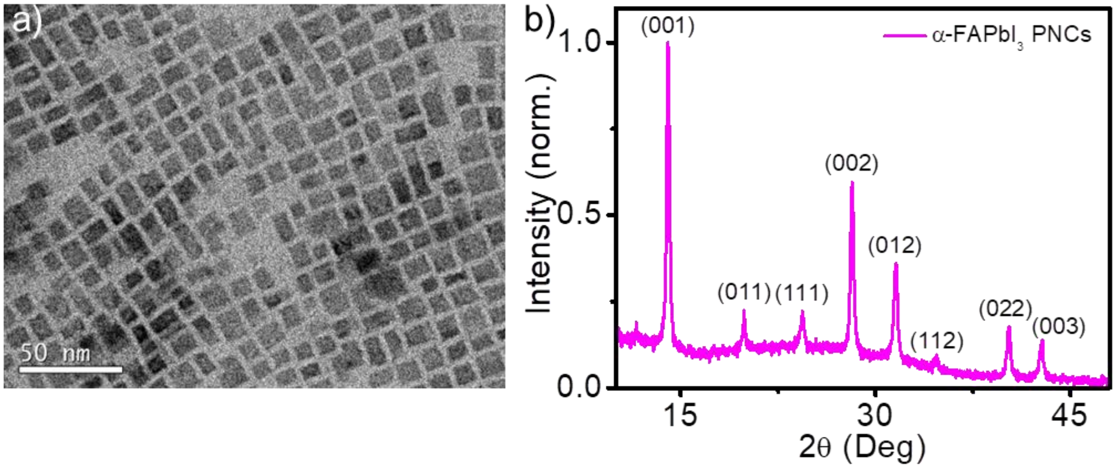

Figure 4.4. a) TEM image of α-FAPbI$_3$ PNCs. b) XRD spectrum of PNCs films coated on a glass substrate.

The α-FAPbI$_3$ PNCs were synthesized via the hot injection method.[19] Briefly, formamidium oleate in 1-octadecene was injected into a solution containing 1-octadecene, PbI$_2$, oleic acid and oleylamine at 80 °C. The obtained PNCs were filtered, washed with toluene, and used for further studies. Details of the preparation of PNCs and samples are provided in the experimental section. The obtained nanocrystals were well characterized using various analytical techniques. For TEM measurements, the PNCs dispersed in toluene were drop cast onto a carbon coated copper grid and dried under vacuum. The TEM analysis showed the PNCs were having a rectangular shape (**Figure 4.4a**) with an average edge length of 9.8 nm. For XRD measurement, the nanocrystals dispersed in toluene were drop cast onto a glass substrate and dried at ambient temperature. The XRD spectrum displayed diffraction peaks corresponding to (001), (011), (111), (002), (012), (112), (022) and (003) planes (**Figure 4.4b**), which indicate a cubic structure of the nanocrystals.[20] Well-defined and sharp peaks in the XRD spectrum proved the material was highly crystalline in nature. Further, the absence of peaks corresponding to any chemical (eg. PbI_2) or phase (δ-$FAPbI_3$) impurities implies the nanocrystals have excellent phase purity.

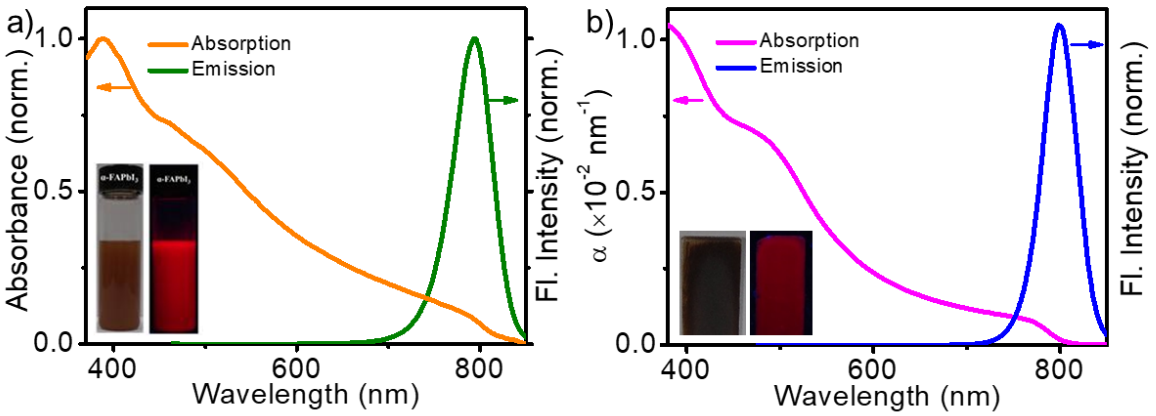

Figure 4.5. UV-vis absorption and emission spectra of PNCs in a) toluene solution and b) film coated on a quartz plate. Corresponding photographs of the solution and film under room light (left) and 365 nm UV light (right) are shown in the inset.

The absorption and emission spectra of PNCs dispersed in toluene are shown in **Figure 4.5a**. The absorption spectrum is broad and covers the UV, visible, and partially the NIR region (300-840 nm). They showed a sharp emission in the NIR region with a maximum at 794 nm. **Figure 4.5b** shows the absorption of PNCs in the film state in terms of the absorption coefficient, which was derived from the corresponding transmittance and reflectance spectra, followed by normalization with the film thickness. Details of the calculation are given in the experimental section. Compared to the solution state, 5 nm red-shift was observed in the emission maximum in film state (**Figure 4.5b**), which could be attributed to the energy transfer from smaller to larger sized PNCs.[26,27] The photographs of the nanocrystals in colloidal solution and film taken under daylight and 365 nm UV light are shown in the insets of **Figure 4.5 a,b**.

4.3.2. Tuning the size of PNCs

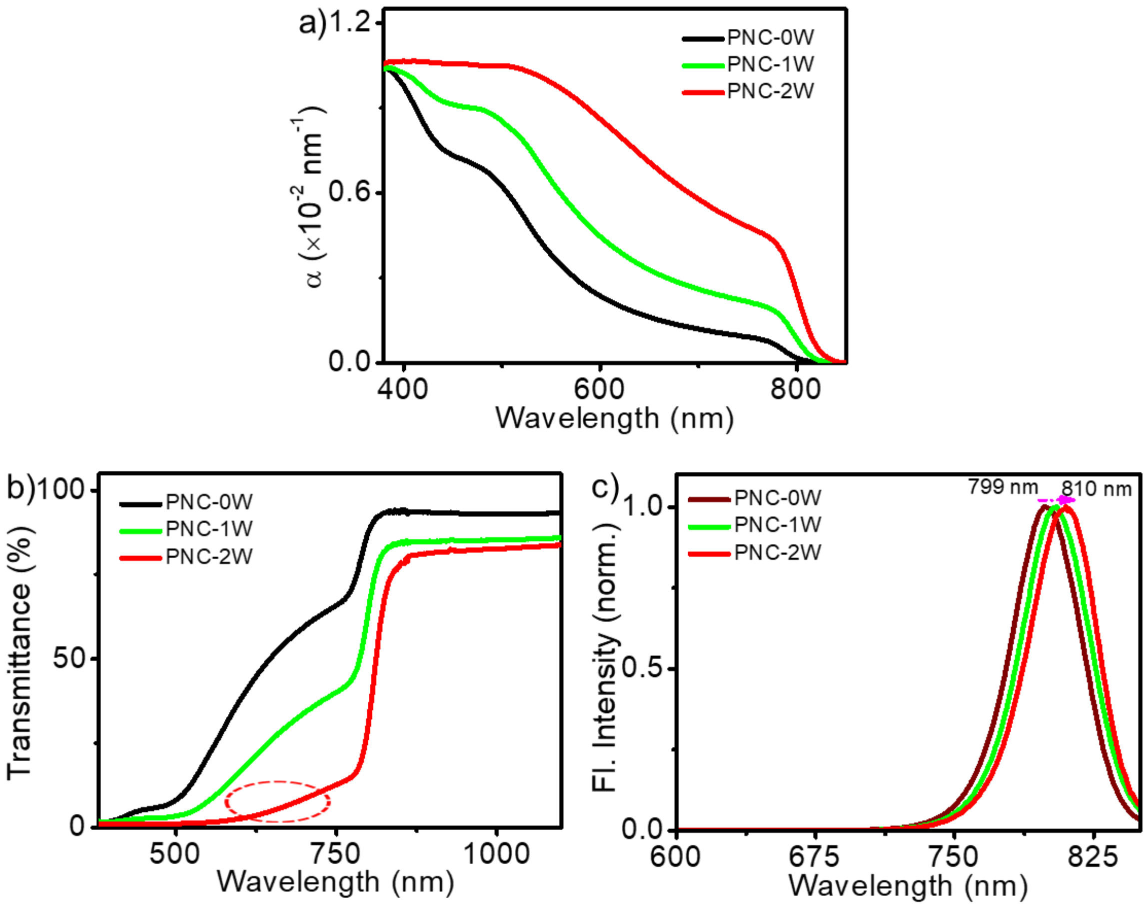

Figure 4.6. a) Absorption, b) Transmittance, and c) Emission spectra for 0, 1, and 2 times washed colloidal PNCs (named as PNC-0W, PNC-1W, and PNC-2W, respectively) film on quartz substrates drop cast from a

toluene dispersion. The red dotted circle indicates the visible region with >2% transmittance. The thicknesses of the films are as follows: PNC-0W: 395 nm, PNC-1W: 400 nm, PNC-2W: 410 nm.

Film prepared from as-synthesized PNCs had a low absorption (**Figure 4.6a**, black line) and hence high transmittance (**Figure 4.6b**, black line) in the longer wavelengths of the visible region (575-740 nm). The reduced absorption at higher wavelengths was expected as the density of states in this region is low (discrete energy levels) due to the quantum confinement effect.[28] As mentioned earlier, the primary condition for VONIRT materials is that they should have uniform transmittance of <2% in the visible region (380-740 nm) and >60% transmittance in the NIR region. Reducing the quantum confinement effect by increasing the size of the nanocrystals is one way to improve the absorbance at longer wavelengths, which can be done by controlled washing. In this work, the synthesized PNCs were washed with a 3:1 toluene/acetonitrile solvent mixture to increase their size. As a result, there was an increase in absorption intensity (decrease in transmittance) in the longer wavelength region (**Figure 4.6a**). It was also associated with a slight red-shift in the excitonic absorption peak. These observations could be attributed to the reduction of bandgap as well as an increase in the density of states in the low energy transition with an increase in the size of nanocrystals. The increased size of nanocrystals further reduced the percentage of visible light transmitting through the PNCs film (**Figure 4.6b**). The emission maximum of PNCs film was also red shifted due to the reduced bandgap of nanocrystals during washing (**Figure 4.6c**). The effect of washing on the size of PNCs was visualized from TEM analysis (**Figure 4.7**). The average size of PNCs was changed from 9.8 nm in the pristine sample (PNC-0W) to 38 nm in one-time washed sample (PNC-1W), and 70 nm in two-times washed sample (PNC-2W).

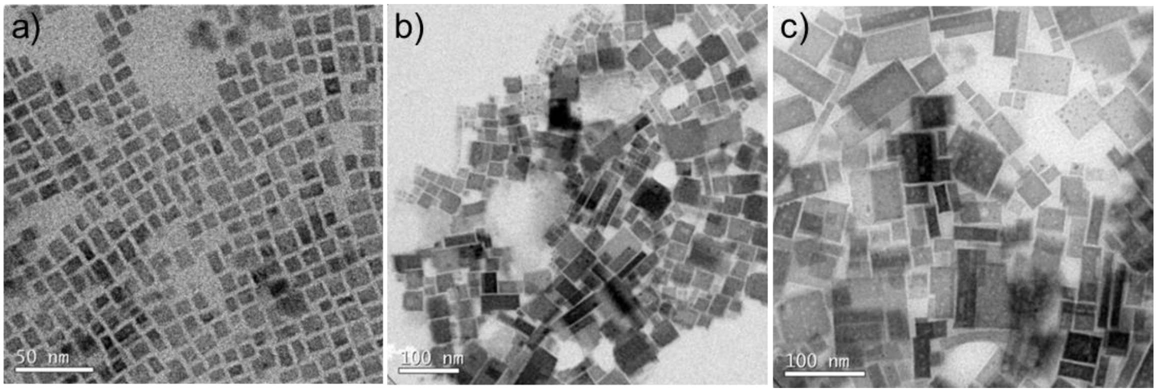

Figure 4.7. a-c) TEM images of PNC-0W, PNC-1W, and PNC-2W samples (from left to right). The size of PNCs is gradually increasing with increasing washing cycles.

The increase in the size of nanocrystals during washing could be explained through the following mechanism.[29,30] The binding of capping ligands such as oleate and oleylammonium ions with the surface of PNCs are highly dynamic and labile in nature. During washing, some of the capping ligands may detach from the surface of nanocrystals creating an iodide-poor environment. The nanocrystal facets with open sites (after detachment of capping ligands) are prone to recombine with nearby nanocrystals due to high ion mobility, thus reconstruction occurs to give larger PNCs. In other words, the iodide ions present onto the surface of one nanocrystal interacts with the iodide vacancies present in nearby nanocrystals to form larger PNCs, which is schematically represented in **Figure 4.8**.

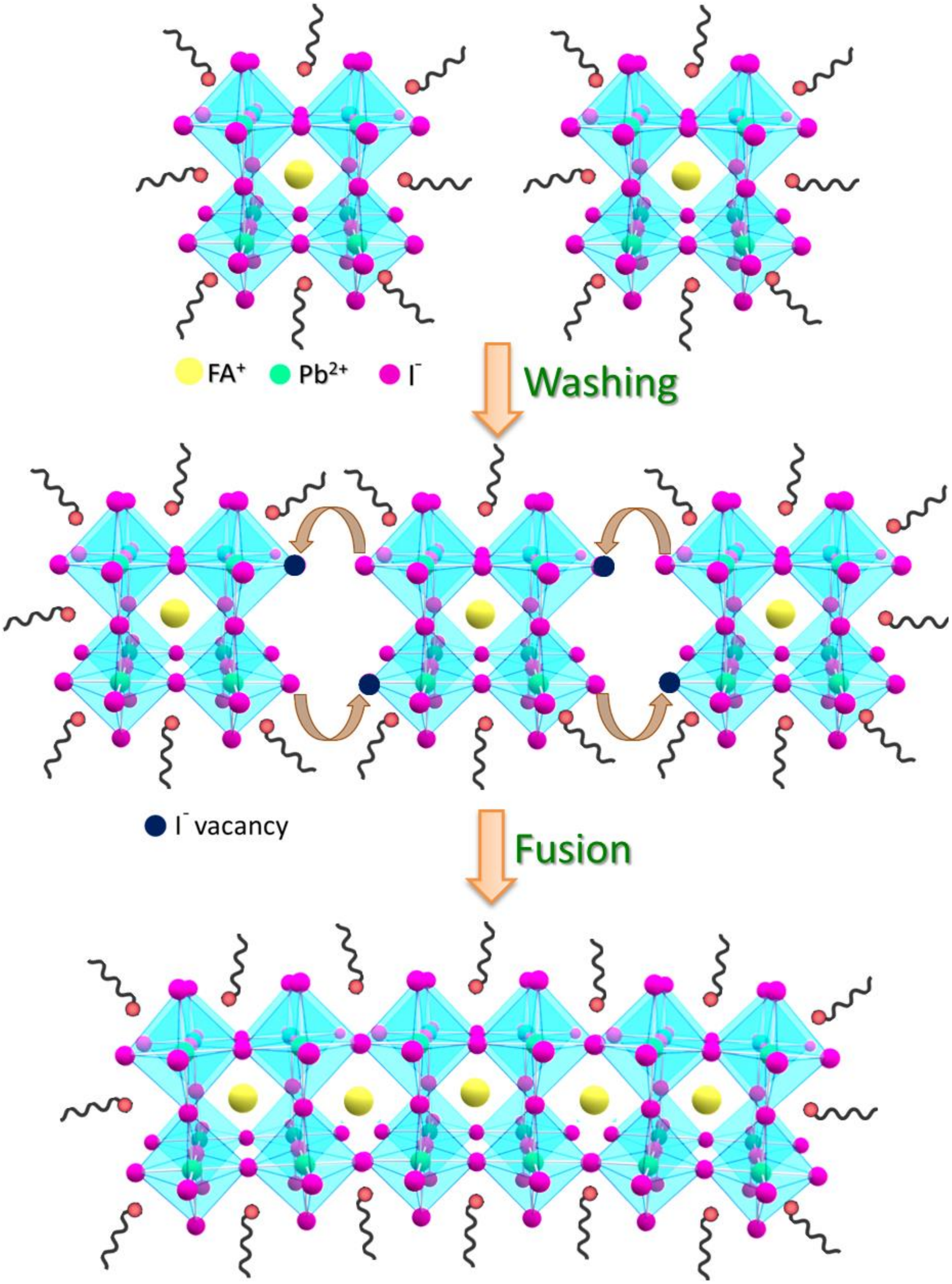

Figure 4.8. Schematic diagram illustrating the change in the size of nanocrystals on washing.

4.3.3. Development of visibly opaque NIR transmitting filter

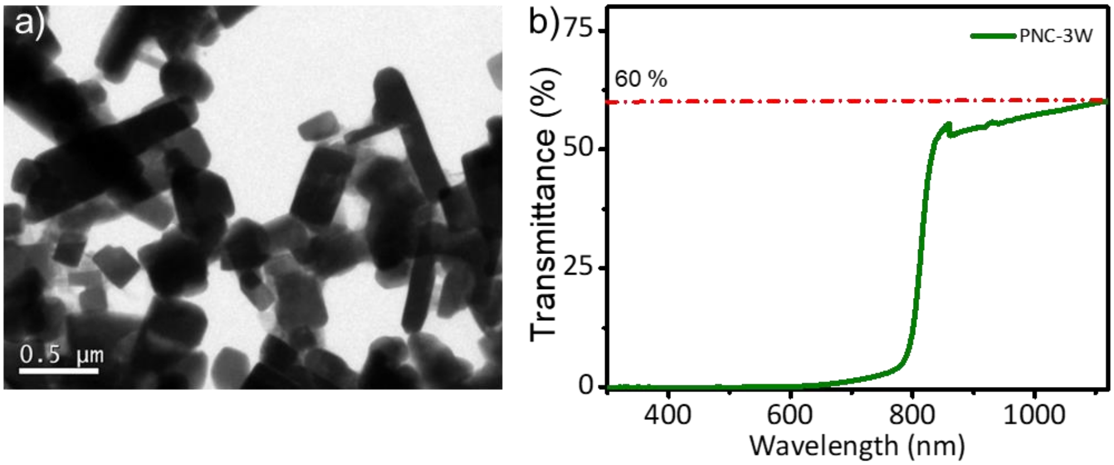

Figure 4.9. a) TEM image and b) transmittance spectrum of three-times washed PNCs (PNC-3W). TEM image shows the formation of larger sized nanocrystals than that of PNC-2W. The transmittance in the NIR region is lower than 60% due to the scattering of light by the larger sized nanocrystals.

The main condition for developing visibly opaque NIR transmitting filter is that the filter should have the transmittance below 2% in the visible region and above 60% recovery in the NIR region. PNC-0W showed a transmittance of 65% at 740 nm, which was reduced to 12% in PNC-2W. The transmittance of PNC-2W in the 575-740 nm region was between 2% and 12% (indicated by the red dotted circle in **Figure 4.6b**), which is still not suitable for making VONIRT filters. We tried to address this problem by further increasing the size of nanocrystals through washing. The transmittance of three-times washed PNCs (PNC-3W) was below 2% in the visible region, but the recovery of transmittance in the NIR region was lower than 60% due to the scattering of light by the larger size of the nanocrystals (**Figure 4.9**). It must be noted that the absorption and transmittance are not complementary, particularly at higher wavelengths, which may be considered as unusual. This anomaly was created by scattering; a part of the light was lost due to scattering from the film samples owing to its inhomogeneous nature. This effect is more evident in the film of PNC-2W than that of PNC-0W due to the increase in the size of the nanocrystals. However, this scattering is not apparent in the absorption spectrum because the method used for calculating the absorption coefficient has taken reflectance (due to scattering) also into consideration. Details of the calculation of the absorption coefficient are explained in experimental section.

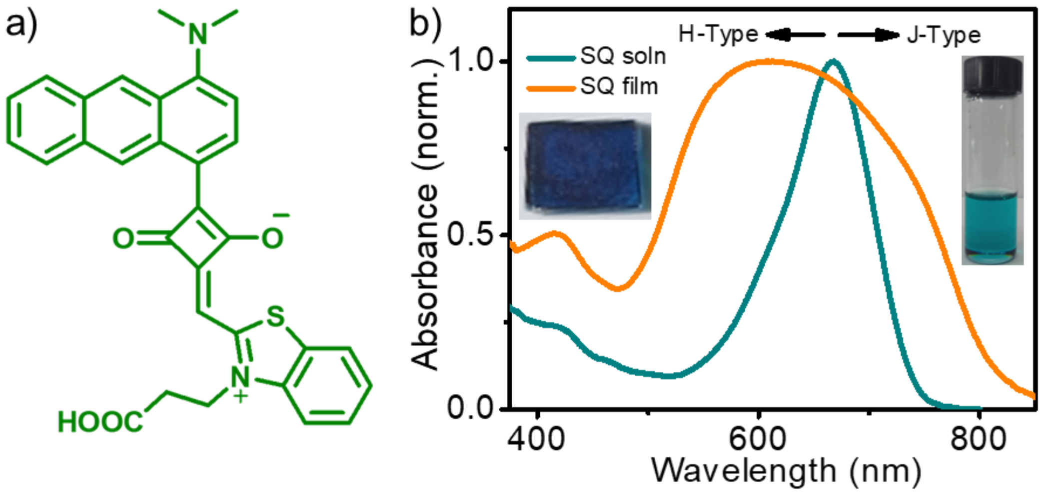

Figure 4.10. a) Chemical structure of the SQ dye. b) Absorption spectra of the SQ dye in solution (solvent: toluene) and film state (drop cast from toluene solution). Photographs of the solution (right) and film (left) samples under room light are shown in the inset.

The transmittance of PNC-2W in the 575-740 nm region was in the range of 2-12%, which is not suitable for making VONIRT filters. To address this issue, a novel low bandgap SQ dye with an acid anchoring group was selected to bind with the surface of PNCs. The chemical structure of SQ dye is shown in **Figure 4.10a**, and the synthesis details are given in the experimental section. The main reasons for the selection of this particular SQ dye are i) the presence of an acid group that can efficiently interact with the surface of nanocrystals to form a stable composite, ii) intense absorption in the 570-750 nm range (**Figure 4.10b**), which could augment the absorbance of PNCs in this region. The absorption spectra of the dye in toluene and in film state drop cast from toluene solution are shown in **Figure 4.10b**. The corresponding photographs are shown in the inset. The absorption spectrum of the film was broadened compared to that in solution due to the formation of both H-type and J-type aggregates (respectively absorbs in the blue and red sides of the solution state absorption spectrum).[31] To make the PNC/SQ dye composite, about 1.2 wt% of SQ dye was mixed with PNC-2W dispersed in toluene via sonication. The resulting

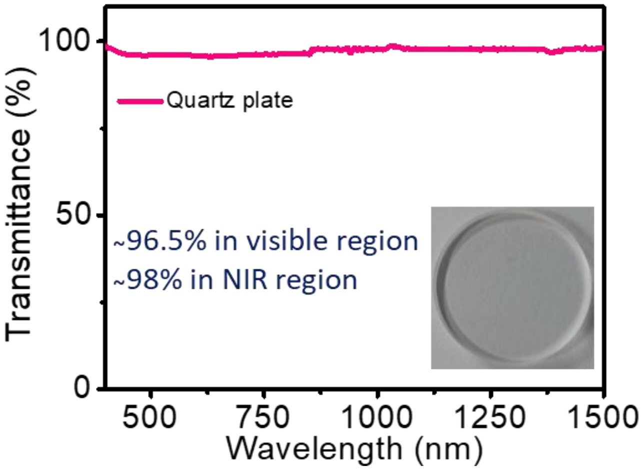

Figure 4.11. Transmittance spectrum of a typical quartz plate used for experiments. It shows ~96.5 % and ~98 % transmittances in the visible and NIR regions, respectively.

homogeneous solution was drop cast onto a quartz plate, which is transparent to the visible and infrared wavelengths (**Figure 4.11**).

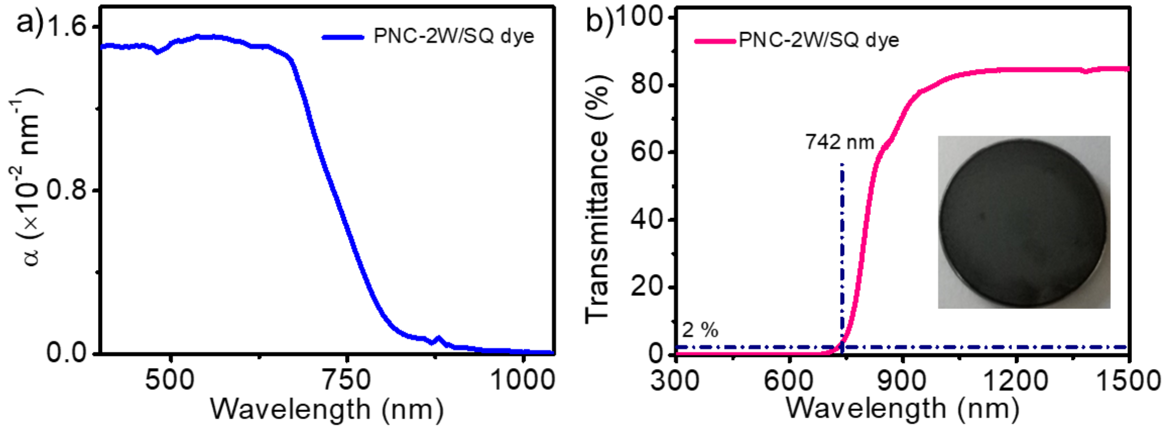

Figure 4.12. a) Absorbance and b) Transmittance spectra of PNC/SQ composite (1.2 wt% of SQ dye with respect to PNCs) based film (film thickness: 425 nm). A photograph of the film is shown in the inset.

The composite film showed excellent absorption in the entire visible region (**Figure 4.12a**). Since the added SQ dye has intense absorption in the 570-750 nm range, it brought down the transmittance of the film below 2% up to 742 nm covering the whole visible region (**Figure 4.12b**). More importantly, the transmittance was above 80% in the NIR region with a sharp recovery after 742 nm. The photograph of the PNC/SQ dye composite film is shown in the inset of **Figure 4.12b**, which is black in color due to the complete absorption of the visible wavelengths. In this context, it must be noted that PNC-0W was not suitable for making composite with SQ dye. Due to the high concentration of capping ligands in PNC-0W, it was difficult for the SQ dye to efficiently interact with the surface of the PNCs. Also, a large quantity of SQ dye was required, which led to the segregation of dye molecules resulting in the loss of homogeneity of the composite.

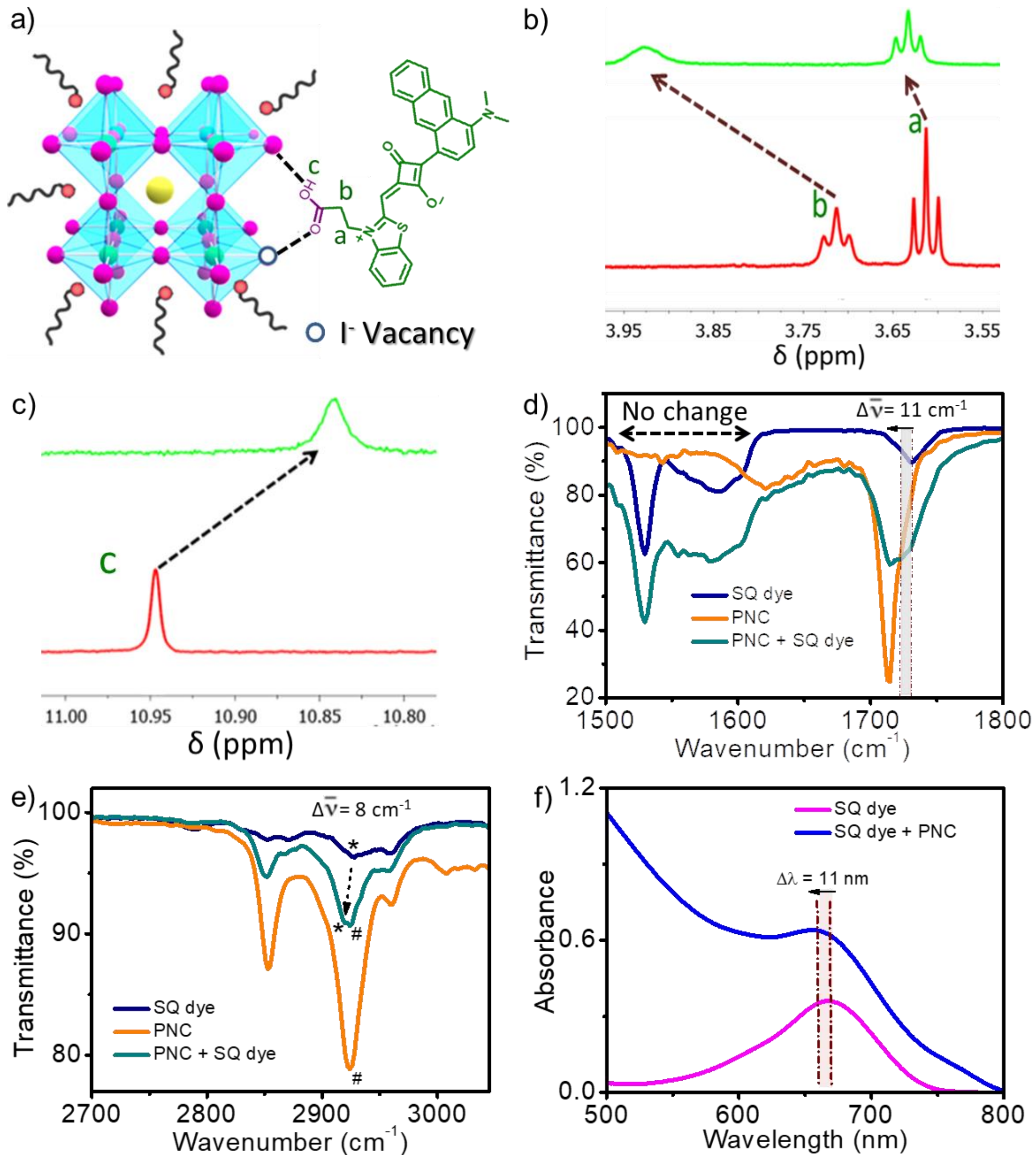

Figure 4.13. a) Simplified schematic diagram of a PNC bound with SQ dye. ^{1}H NMR spectra of SQ dyes (0.05 mM) measured in deuterated benzene in the absence (red) and presence (green) of PNCs showing the regions

corresponding to the b) alkyl and c) carboxylic acid protons. IR spectra of powdered SQ dyes in the absence (blue) and presence (green) of PNCs in the regions corresponding to the stretching of d) carbonyl moiety in the acid group and e) hydroxyl group. f) Comparison of the absorption of SQ dye in the absence (magenta) and presence (blue) of PNCs in toluene.

It is an established fact that capping ligands containing carboxylic acid groups bind with PNCs either through the carboxylic acid or the corresponding carboxylate group depending on the nature of the molecules and the reaction conditions. In the present work, the SQ dyes were introduced at room temperature after the synthesis of PNCs, dispersed in toluene. Since the conversion of carboxylic acid in SQ dyes to the corresponding carboxylate is not feasible in a non-polar medium like toluene, the binding must happen through the acid groups. This interaction could be explained through Lewis acids and bases theory[32-34] and hydrogen bonding.[35] The SQ dye acts as a Lewis base, donates a pair of electrons (lone pair of electrons on the oxygen atom in carbonyl group) to the I^- ion vacancy (under-coordinated Pb^{2+} ions) on the perovskite surface, which acts as a Lewis acid and accept the pair of electrons. In addition to that, the hydroxyl group of acid forms hydrogen bonding with the halide ions present in the surface of PNCs. A schematic diagram illustrating the binding of SQ dye with PNC is shown in **Figure 4.13a**. The ^1H NMR and IR analysis of the composite have confirmed this mode of binding. The ^1H NMR of SQ dye dissolved in deuterated benzene in the absence and presence of PNCs were shown in **Figure 4.13b,c**. The interaction of the carbonyl group has induced the de-shielding of the nearest protons due to its increased electron accepting capability after binding. As a result, the alkyl protons near the acid group (δ = 3.60-3.70 ppm) were shifted downfield (δ = 3.64-3.95 ppm) in the presence of nanocrystals. The iodide-anions present in PNCs bind with the hydroxyl groups by $O\text{-}H\cdots I^-$ hydrogen bonding. Due to this, the electron density on H ions increases, and hence the hydroxyl group proton (δ = 10.95 ppm) was shifted upfield (δ = 10.83 ppm) in the presence of PNCs. The IR spectra were recorded for SQ dye in the absence and presence of nanocrystals (**Figure 4.13d,e**). The carbonyl stretching frequency of the acid group was shifted to a lower frequency by 11 cm^{-1} in the presence of PNCs. The interaction of the carbonyl group with the surface of nanocrystals reduces the bond strength, which leads to a reduction of its stretching frequency. The presence of hydrogen bonding was difficult to explain with IR spectra as the -C-H stretching frequencies of PNCs overlap with that of the hydroxyl group. However, it was still evident that the hydroxyl stretching was shifted to a lower frequency by 8 cm^{-1} in the presence of PNCs. The interaction of the hydroxyl group with the surface of PNCs reduces the bond strength, which leads to a reduction in stretching frequency. Usually, squaraine groups do not show -C=O stretching vibrations due to the resonance-stabilized zwitterionic form of cyclobutene moiety.[36] A new peak corresponding to the -C=O stretching would be formed around 1,675 cm^{-1} if the negative charge (O^- ion) or carbonyl group on the squaraine group interacts with PNCs. However, there was no peak in that region, indicating the absence of the direct interaction of squaraine moiety with PNCs. The blue shift of 11 nm in the absorption maximum of SQ dye in the presence of PNC was another evidence for the interaction between them (**Figure 4.13f**). The observation of only a small shift is as expected because the carboxylic acid group binding with PNCs is not conjugated with the chromophore part of the SQ dye.

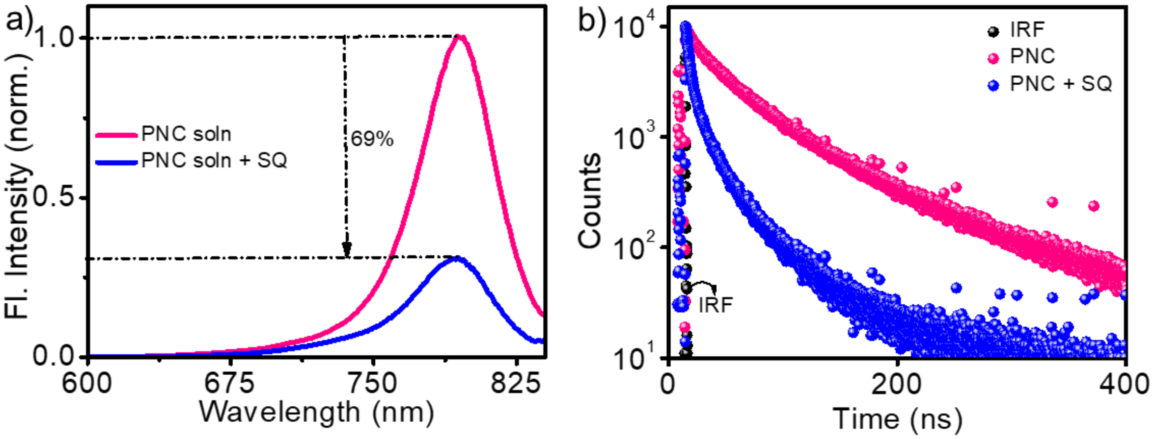

Figure 4.14. Fluorescence a) emission and b) lifetime spectra of PNCs dispersed in toluene in the absence and presence of SQ dye.

The fluorescence emission and lifetime spectra of PNCs (solution and film states) showed significant quenching in the presence of SQ dyes (**Figures 4.14** and **4.15**), probably due to efficient electron transfer from the former to the latter in close proximity. Samples were excited at 375 nm using a xenon lamp for fluorescence measurement. 378 nm laser source was used for fluorescence decay measurement. Observation of significant quenching of fluorescence (69% in the solution state and 93% in the film state) and decrease in fluorescence lifetime (67% in the solution state and 87% in the film state) of PNCs in the presence of SQ dye is probably due to the electron transfer from PNCs to SQ dyes.

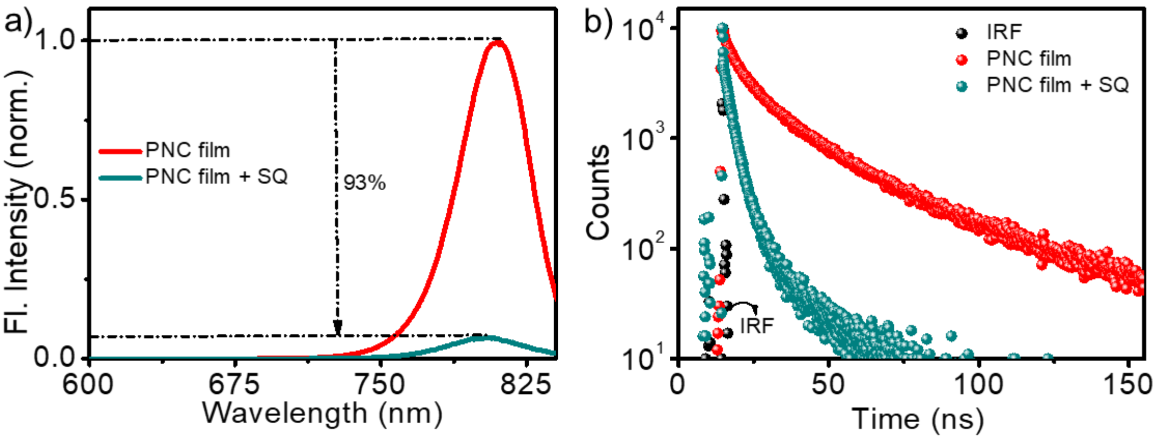

Figure 4.15. Fluorescence a) emission and b) lifetime spectra of PNC films drop-cast on a quartz plate in the absence and presence of SQ dye. Toluene dispersions were used for making films.

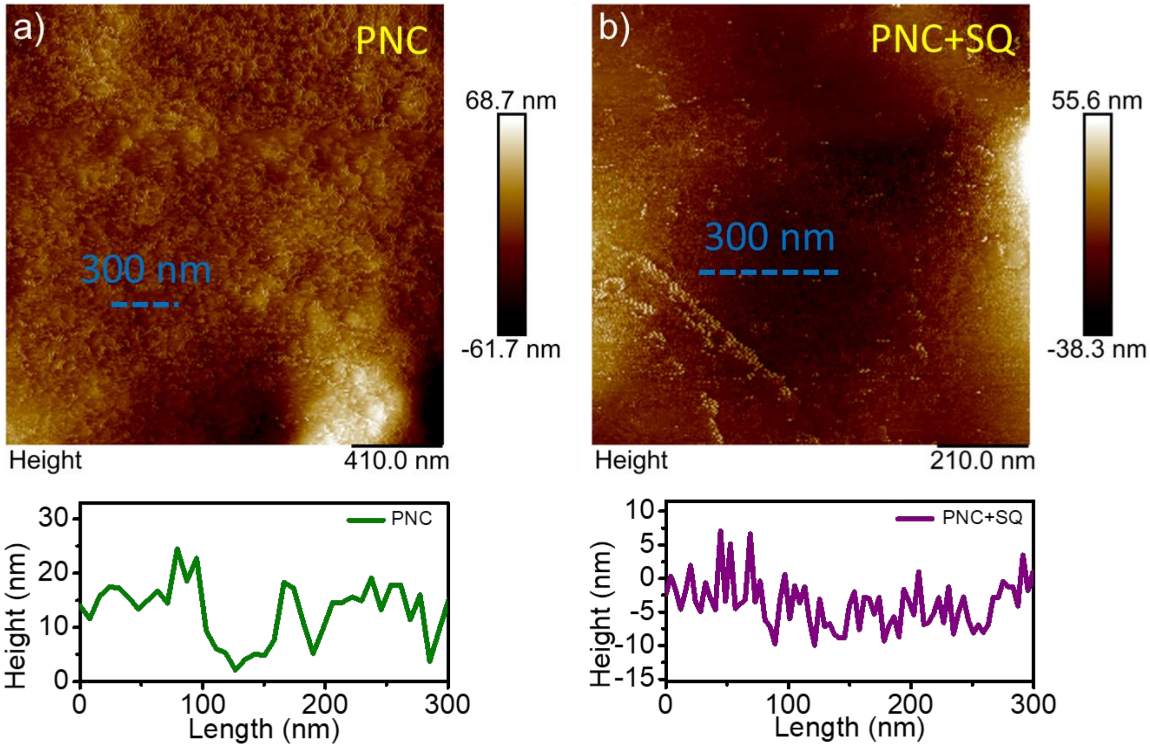

Figure 4.16. AFM images of PNC films coated on the quartz plate in the a) absence and b) presence of SQ dyes. The height profiles corresponding to a selected 300 nm long area from the respective images are shown below.

The presence of SQ dye improved the smoothness of PNCs/SQ composite film compared to oleylammonium/oleate based capping ligands as evident from AFM and SEM analysis (**Figure 4.16 & 4.17**). Since this improvement was uniform throughout the film, it could be assumed that the SQ dyes have a uniform distribution in the composite.

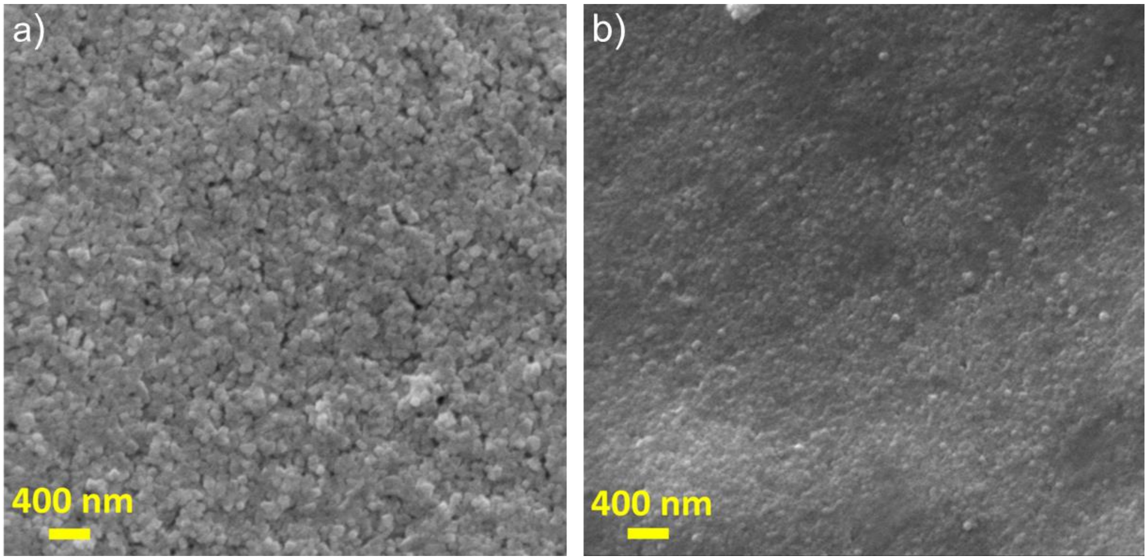

Figure 4.17. SEM images of PNC films coated on quartz plates in the a) absence and b) presence of SQ dyes.

The transmittance spectrum of the composite measured at three different positions of the film was similar (**Figure 4.18**), which further proved the uniformity. This observation is relevant from the application point of view also because it is necessary that the absorption/transmittance of the composite film should be uniform for practical uses. Due to the uniform distribution and the strong binding of hydrophobic SQ dyes, the environmental stability of the nanocrystals was improved. The composite was found to be stable even in the presence of water for several hours (**Figure 4.19**).

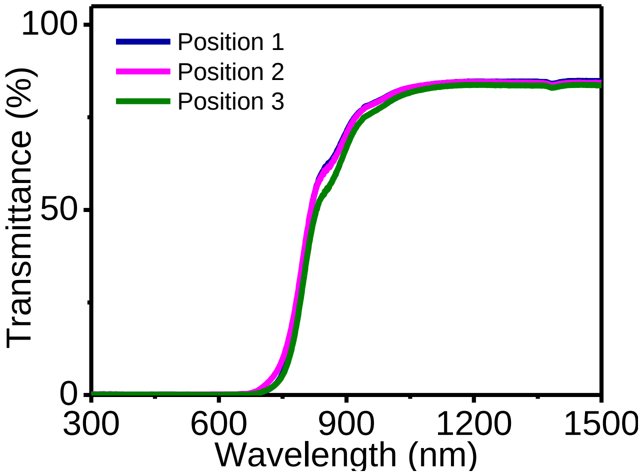

Figure 4.18. Transmittance spectra of PNC-2W/SQ dye composite based filter monitored at three different positions.

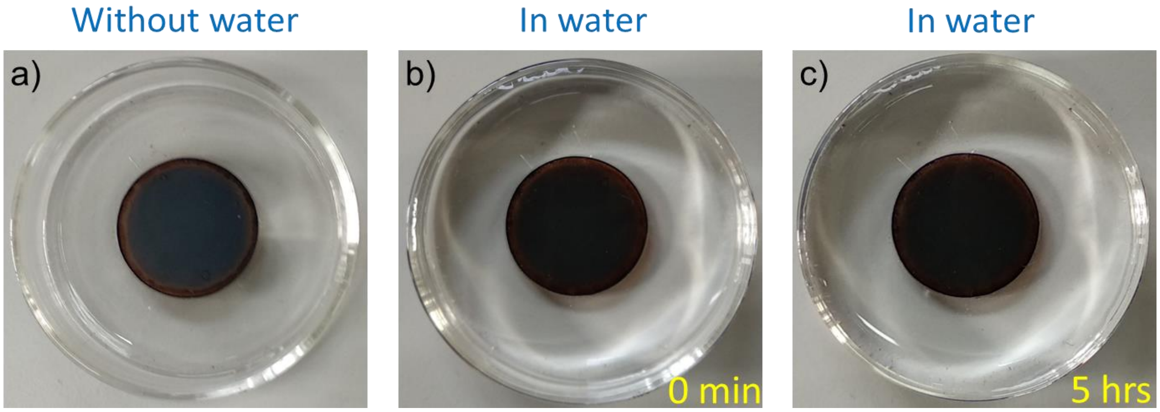

Figure 4.19. a) Photographs of PNC-2W/SQ dye composite film under various conditions: a) ambient atmosphere, b) immediately after immersed in water and c) 5 hours after immersed in water.

4.3.4. Security and NIR photography applications

Figure 4.20. Photographs of the word "NIIST" under various conditions: a) imaged with a normal camera, b) covered with the VONIRT filter made from the PNC/SQ dye composite and imaged with a normal camera, c) covered with the VONIRT and imaged with a NIR reflector removed camera, d) the letter "N" covered with NIR reflector and photographed with a normal camera, e) the letter "N" covered with an NIR reflector, and the entire word covered with the VONIRT filter and imaged with a NIR reflector removed camera.

To study the use of the composite film as a VONIRT material/filter for security and NIR photography applications, the following experiments were conducted. The word "NIIST" printed on a paper was photographed with a normal camera (**Figure 4.20a**). When this word was covered with the composite filter, it became invisible to the normal camera (**Figure 4.20b**). On the other hand, the word "NIIST" was visible through a camera in which the NIR reflector was removed under a NIR source (**Figure 4.20c**; an IR lamp was used as the NIR source). Subsequently, the letter "N" in "NIIST" was covered with a NIR reflector as shown in **Figure 4.20d** (photographed using normal camera). When this word was photographed using the NIR reflector removed camera, the letter "N" became invisible (**Figure 4.20e**). These experiments proved that the composite could be used as a security material to make writings/barcodes invisible to the human eye but visible to a modified camera.

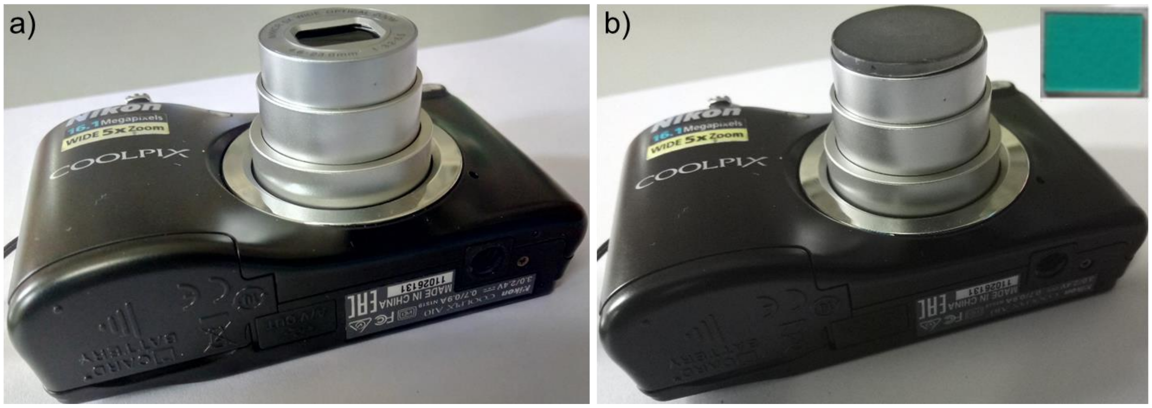

Figure 4.21. Photographs of the a) normal digital camera (sensitive to the visible wavelengths) and b) modified camera in which the NIR reflector is removed (shown in the inset) and the PNC/SQ dye composite filter is attached to the zoom lens (sensitive to the NIR wavelengths).

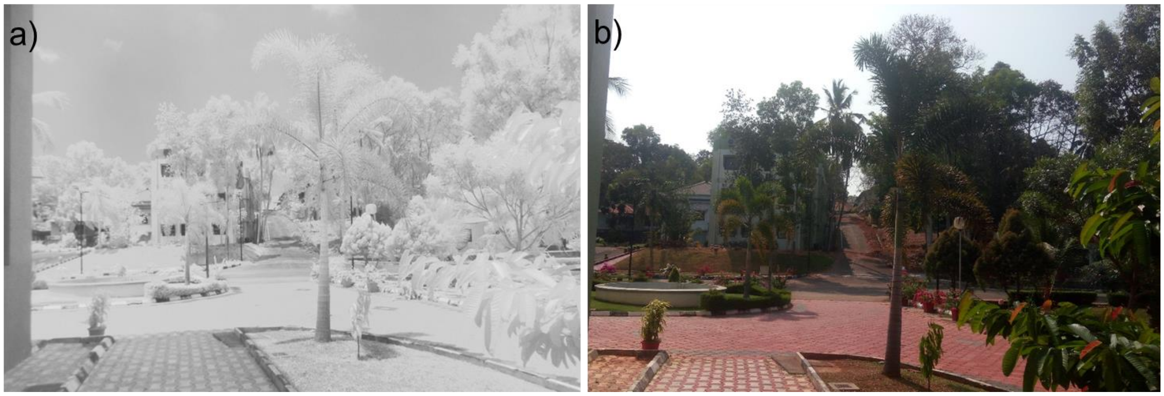

Figure 4.22. Photographs taken with a) normal camera and b) camera equipped with the VONIRT filter (NIR source: sunlight).

To check the potential of the composite for the NIR photography application, the filter was fixed onto the zoom lens of a NIR reflector removed camera (**Figure 4.21**). Photographs were taken with this modified camera (**Figure 4.22a**) and compared with that taken with a normal camera (**Figure 4.22b**). The picture taken with the modified camera was apparent and had similar features to that taken with the normal camera proving the potential of the filter for NIR photography. More photographs proving the capability of the composite for NIR and night vision photography are shown in **Figures 4.23-4.27**.

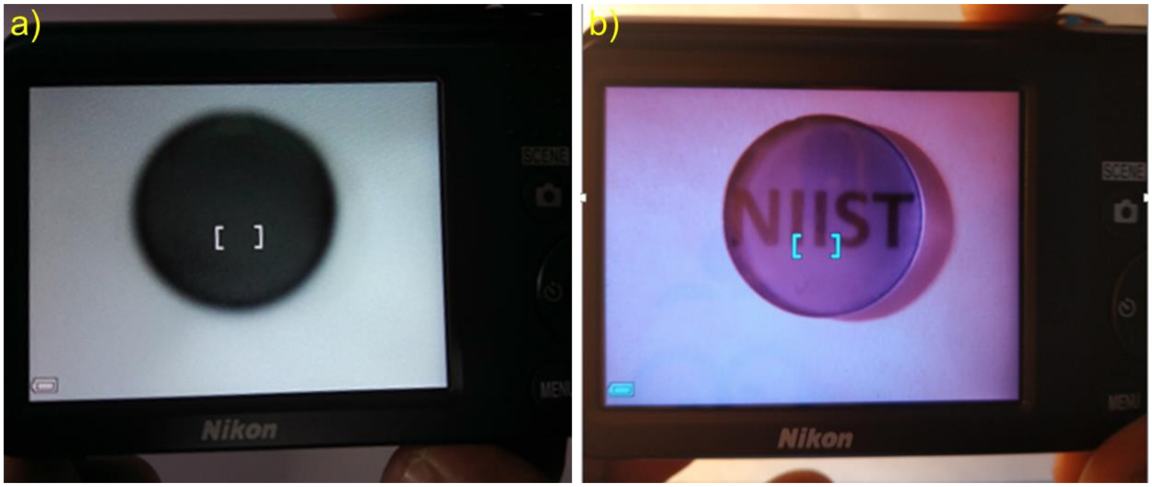

Figure 4.23. Photographs of the word 'NIIST' in a white paper cover with the PNC/SQ dye composite filter is a) invisible to the normal camera but b) visible to the modified NIR camera (NIR source: IR lamp).

Figure 4.24. Photograph of an outdoor area imaged with the modified NIR camera (NIR source: Sunlight).

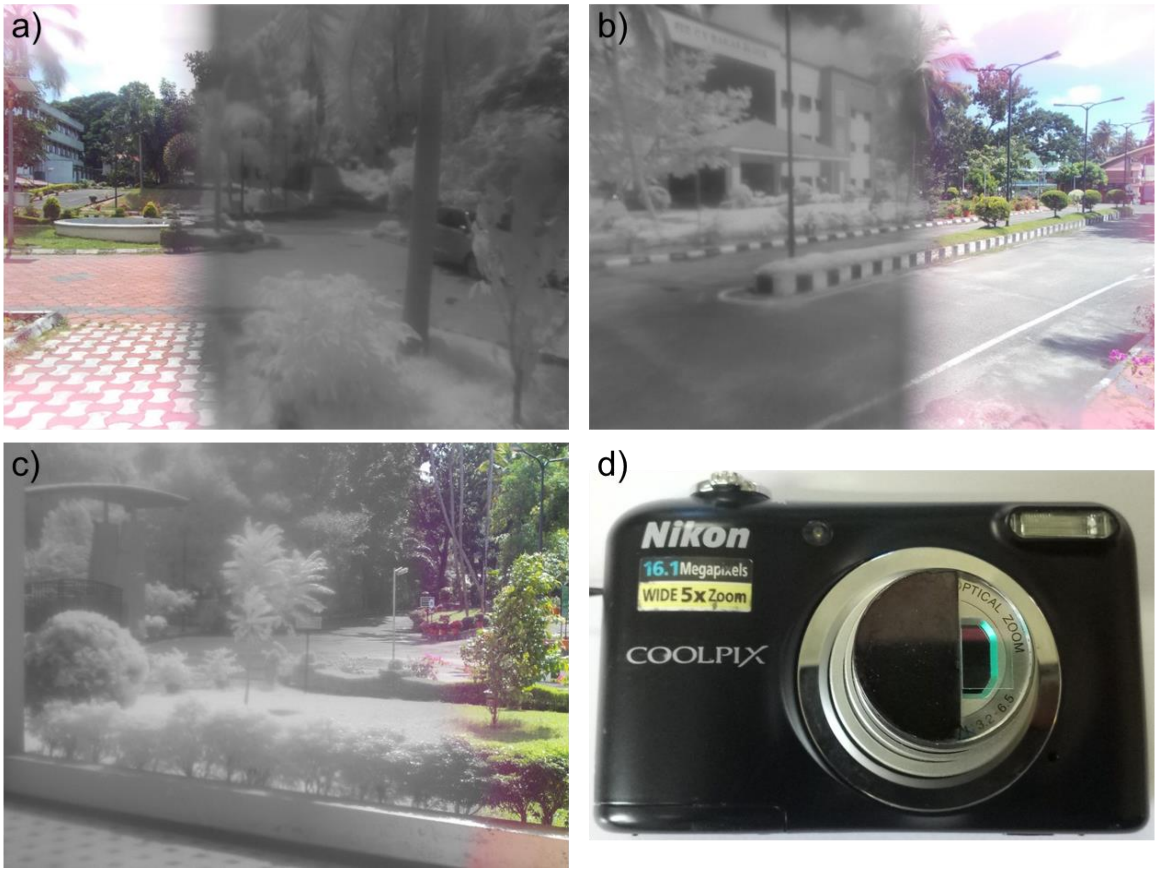

Figure 4.25. a), b) and c) Photographs of outdoor areas imaged with the modified camera in which the zoom lens is partly covered with the NIR reflector and partly with the VONIRT filter (NIR source: Sunlight). d) Photo of the camera used. Since the effective focal length of the camera is different for the NIR reflector and VONIRT filter filters, the obtained pictures have less quality.

Figure 4.26. Photograph of a research diary taken in night using the modified NIR camera (NIR source: IR lamp).

Figure 4.27. Photograph of a vacuum oven taken in night using the modified NIR camera (NIR source: IR lamp).

4.4. Conclusions

In conclusion, alpha-formamidinium lead iodide based PNCs were prepared by a two-step hot injection method. The size of the nanocrystals was gradually increased via washing them with a toluene/acetonitrile solvent mixture to obtain the visibly opaque and NIR transmitting property. Though the two-times washed nanocrystals showed remarkable improvements in opaqueness in the visible region and NIR transmitting property, it could not meet the conditions for a VONIRT material. To address this issue, a novel low bandgap SQ dye was incorporated with the nanocrystals as capping ligands. As a result, composite films achieved uniform transmittance of below 2% in the visible region (380-740 nm) and above 60% in the NIR region, making them suitable for developing VONIRT materials/filters. The acid group present in SQ dyes strongly interacted with the surface of PNCs, which enhanced the environmental stability of the composite as well as the film quality. This cost-effective and easy-to-prepare composite was found to be suitable as a security material to hide sensitive data and for NIR photography.

4.5. Experimental section

4.5.1. Materials

The reagents and chemicals for synthesis were purchased from local suppliers or from Sigma Aldrich, Alfa Aeasar or TCI. Air- and water-sensitive synthetic steps were performed in an argon atmosphere.

The absorption/reflectance/transmittance spectra were recorded on a Perkin Elmer Lambda 950 UV-vis/NIR spectrophotometer. Atomic force microscopy images were recorded under ambient conditions using a NTEGRA (NT-MDT) operating with a use tapping mode regime. Micro fabricated thin cantilever tips (NSG 10) with a resonance frequency of 299 kHz and a spring constant of 20-80 N m^{-1} were used. The absorption (A) spectra of PNC and PNC/SQ dye composite films were obtained from the corresponding transmittance (T) and reflectance (R) spectra using the relation, A = -log[T/(1-R)].[37] Subsequently, it was converted into the corresponding absorption coefficients (α) using the formula, α = 2.303 A/t, where t is the thickness of films.[38]

4.5.2. Synthesis and characterization of squaraine (SQ) dye:

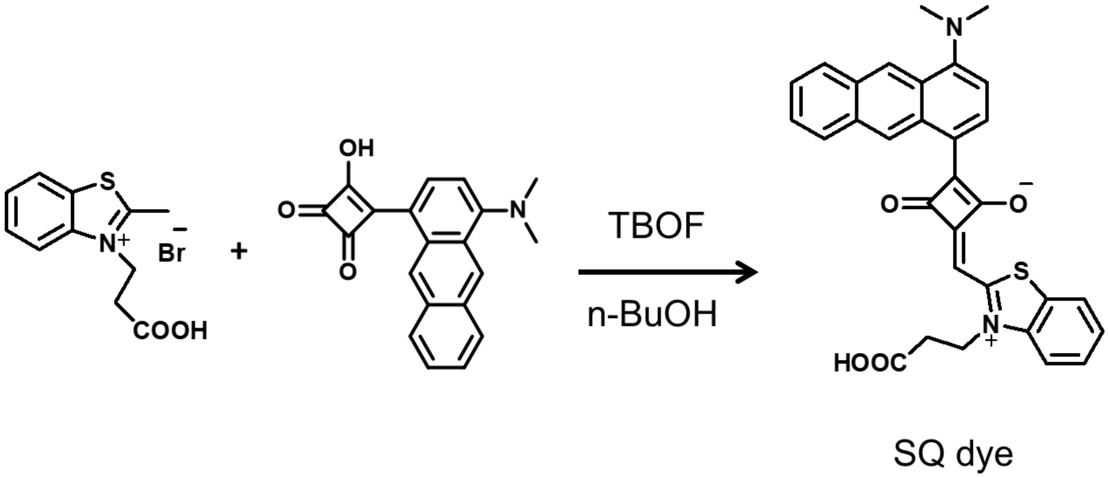

Scheme 4.1. Synthesis of SQ dye under study.

3-[4-(*N*,*N*-dimethylamino)anthracene]-4-hydroxycyclobutene-1,2-dione (42 mg, 0.13 mmol) and 3-carboxyethyl-2-methylbenzothiazolium bromide (40 mg, 0.13

mmol) were added to a solvent mixture containing 10 mL n-butanol and 1 mL tributylorthoformate (TBOF) in a 100 mL round bottom flask and heated for 3 h at 60-70 °C (**Scheme 4.1**). The solvent was removed under reduced pressure and the product was precipitated by adding hexane and it was purified by column chromatography over silica gel (100-200 mesh) using 10% MeOH/$CHCl_3$ mixtures as eluent to give the solid product (25 mg, 37%). Mp 215-220 °C (decomp.); ^{1}H-NMR (300 MHz, $CD_3OD/CDCl_3$ (1:1)): δ 2.88 (2H, t, $-CH_2-CO-$), 3.06 (6H, s, $-NCH_3$), 3.19 (2H, t, $+NCH_2-$), 6.7-9.9 (13H, m, aromatic, vinylic); (HRMS-FAB) Mol. wt. calcd. for $C_{31}H_{24}N_2O_4S$ (MH+) 520.59; Found 521.48.

4.5.3. Synthesis of *α*-FAPbI$_3$ PNCs:

The PNCs were synthesized using an already reported hot injection method.[19]

4.5.3.1. Synthesis of formamidinium oleate precursor:

Formamidinium acetate (FA-acetate, 0.521 g, 5 mmol), 1-octadecene (16 mL, vacuum-dried at 120 °C), and oleic acid (11.3 mmol, 4 mL) were added to a 50 mL round-bottom flask. The mixture was degassed for 10 min at RT and then heated under a nitrogen atmosphere to 130 °C, which yielded a clear solution. This solution was dried for 30 min at 50 °C under vacuum yielding FA-oleate as the pure product. FA-oleate was heated to 100 °C under nitrogen just before the next step because it often precipitates when stored at room temperature.

4.5.3.2. Synthesis of PNCs

PbI_2 (0.086 g, 0.187 mmol) and 1-octadecene (5 mL) were added to a 25 mL round-bottom flask, dried for 1 h at 120 °C, and mixed with oleic acid (1 mL, vacuum-dried at 120 °C) and oleylamine (0.5 mL, vacuum-dried at 120 °C). When PbI_2 was fully dissolved and the mixture was cooled to 80 °C, the preheated FA-oleate precursor (2 mL, yielding a molar ratio FA: Pb = 2.7) was injected. After 10-60 s of stirring, the solution was cooled to RT in a water bath. The crude solution was centrifuged for 5 min at 12000 rpm, the supernatant solution was discarded, and the precipitate was redispersed in toluene. The nanocrystals were finally washed with toluene for further studies.

4.5.4. Sample preparation for PNCs/SQ dye filter

100 µL 3:1 toluene:acetonitrile mixture was used for each washing of the nanocrystals (40 mg). PNC/SQ dye composite consisting of 1.2 wt% of the former was prepared by adding 60 µL of squaraine dye solution (1mg in 1 mL toluene) into PNCs solution (5mg in 1 mL toluene) followed by ultra-sonication for 5 minutes. 100 µL of PNC/SQ dye composite was drop cast onto a quartz substrate followed by drying under ambient atmosphere to obtain visibly opaque NIR transmitting filter.

4.5.5. Conversion of a Normal Camera to NIR Camera

A normal digital camera or DSLR camera can be converted into an NIR camera by replacing the inbuilt NIR reflector and attaching the VONIRT filter on to the top of the zoom lens. In detail, a normal camera contains Si-based detector chips, which are sensitive up to 1100 nm. In order to match the appearance of photos to the human visual sensation, the NIR part of the radiation was blocked before reaching the detector by the NIR reflector. If this reflector is removed, the incident radiation containing NIR radiation (sunlight or an IR lamp as the source) will also reach the detector. If a VONIRT filter is attached to the camera, only NIR radiation (740-1100 nm) will reach the detector, and the camera can be used as NIR camera. In the present work, Nikon Coolpix A10 16.1 MP Digital Camera (sensor: CCD, which is capable of detecting both visible and NIR region.) was used as normal and NIR camera by following the above procedure. White balancing is done in pictures taken with the NIR camera.

4.6. References

1. K. Mangold, J. A. Shaw, M. Vollmer, *Eur. J. Phys*. **2013**, *34*, 51-71.
2. Infrared Photography, http://www.crime-scene-investigator.net/Infrared_Photography_research_paper.pdf (accessed: January **2017**).
3. R&D and industrial applications for Near Infrared (NIR) cameras, http://support.flir.com/appstories/AppStories/R&D/Near_Infrared_(NIR)_cameras_EN.pdf (accessed: January **2017**).
4. D. Sandidge, “Digital Infrared Photography,” Wiley (**2009**).
5. X. Zhang, B. Bureau, P. Lucas, C. Boussard-Pledel, J. Lucas, *Chem. Eur. J.* **2008**, *14*, 432-442.
6. B. J. Eggleton, B. Luther-Davies, K. Richardson, *Nat. Photonics* **2011**, *5*, 141-148.
7. A. Llordes, G. Garcia, J. Gazquez, D. J. Milliron, *Nature* **2013**, *500*, 323-326.

8. J. J. Griebel, S. Namnabat, E. T. Kim, R. Himmelhuber, D. H. Moronta, W. J. Chung, A. G. Simmonds, K. J. Kim, J. van der Laan, N. A. Nguyen, E. L. Dereniak, M. E. Mackay, K. Char, R. S. Glass, R. A. Norwood, J. Pyun, *Adv. Mater.* **2014**, *26*, 3014-3018.
9. L. E. Anderson, T. S. Kleine, Y. Zhang, D. D. Phan, S. Namnabat, E. A. LaVilla, K. M. Konopka, L. Ruiz Diaz, M. S. Manchester, J. Schwiegerling, R. S. Glass, M. E. Mackay, K. Char, R. A. Norwood, J. Pyun, *ACS Macro Lett.* **2017**, *6*, 500-504.
10. X. Liu, Y. Sun, L. A. Perez, W. Wen, M. F. Toney, A. J. Heeger, G. C. Bazan, *J. Am. Chem. Soc.* **2012**, *134*, 20609-20612.
11. S. Ghosh, X. Q. Li, V. Stepanenko, F. Wurthner, *Chem. Eur. J.* **2008**, *4*, 11343-11357.
12. S. Ghosh, S. Cherumukkil, C. H. Suresh, A. Ajayaghosh *Adv. Mater.* **2017**, *29*, 1703783 (1-8).
13. Y. Zhao, K. Zhu, *Chem. Soc. Rev.* **2016**, *45*, 655-689.
14. B. Saparov, D. B. Mitzi, *Chem. Rev.* **2016**, *116*, 4558-4596.
15. J. S. Manser, J. A. Christians, P. V. Kamat, *Chem. Rev.* **2016**, *21*, 12956-13008.
16. Y. Zhou, J. Kwun, H. F. Garces, S. Pang, N. P. Padture, *Chem. Commun.* **2016**, *52*, 7273-7275.
17. G. E. Eperon, S. D. Stranks, C. Menelaou, M. B. Johnston, L. M. Herz, H. J. Snaith, *Energy Environ. Sci.* **2014**, *7*, 982-988.
18. A. Binek, F. C. Hanusch, P. Docampo, T. Bein, *J. Phys. Chem. Lett.* **2015**, *6*, 1249-1253.
19. L. Protesescu, S. Yakunin, S. Kumar, J. Bär, F. Bertolotti, N. Masciocchi, A. Guagliardi, M. Grotevent, I. Shorubalko, M. I. Bodnarchuk, C.-J. Shih, M. V. Kovalenko, *ACS Nano* **2017**, *11*, 3119-3134.

20. P. Papagiorgis, A. Manoli, L. Protesescu, C. Achilleos, M. Violaris, K. Nicolaides, T. Trypiniotis, M. I. Bodnarchuk, M. V. Kovalenko, A. Othonos, G. Itskos, *ACS Photonics* **2018**, *5*, 907-917.
21. H. Wang, H. Lin, X. Piao, P. Tian, M. Fang, X. An, C. Luo, R. Qi, Y. Chena, H. Peng, *J. Mater. Chem. C* **2017**, *5*, 12044-12049.
22. X. Yu, L. Wu, H. Hu, M. Chen, Y. Tan, D. Yang, Q. Pan, Q. Zhong, T. Supasai, Q. Zhang, *Langmuir* **2018**, *34*, 10363-10370.
23. A. Pan, J. Wang, M. J. Jurow, M. Jia, Y. Liu, Y. Wu, Y. Zhang, L. He, Y. Liu, *Chem. Mater.* **2018**, *30*, 2771-2780.
24. H. Wang, W. Yao, Q. Tian, M. Li, B.Tian, L. Liu, Z. Wu, W. Wu *Adv. Mater. Technol.* **2018**, *3*, 1800150 (1-8).
25. C. Zhang, B. Wang, W. Li, S. Huang, L. Kong, Z. Li, L. Li, *Nat. Commun.* **2017**, *8*, 1138.
26. C. Weerd, L. Gomez, H. Zhang, W. J. Buma, G. Nedelcu, M. V. Kovalenko, T. Gregorkiewicz, *J. Phys. Chem. C* **2016**, *120*, 13310-13315.
27. M. E. F. Bouduban, A. Burgos-Caminal, R. Ossola, J. Teuscher, J.-E. Moser, *Chem. Sci.* **2017**, *8*, 4371-4380.
28. L. Polavarapu, B. Nickel, J. Feldmann, A. S. Urban, *Adv. Energy Mater.* **2017**, *7*, 1700267.
29. P. Liu, W. Chen, W. Wang, B. Xu, D. Wu, J. Hao, W. Cao, F. Fang, Y. Li, Y. Zeng, R. Pan, S. Chen, W. Cao, X. W. Sun, K. Wang, *Chem. Mater.* **2017**, *29*, 5168-5173.
30. A. Pan, J. Wang, M. J. Jurow, M. Jia, Y. Liu, Y. Wu, Y. Zhang, L. He, Y. Liu, *Chem. Mater.* **2018**, *30*, 2771-2780.
31. G. Miguel, M. Ziółek, M. Zitnan, J. A. Organero, S. S. Pandey, S. Hayase, A. Douhal, *J. Phys. Chem. C* **2012**, *17*, 9379-9389.
32. P.-L. Qin, G. Yang, Z.-W. Ren, S. H. Cheung, S. K. So, L. Chen, J. Hao, J. Hou, G. Li, *Adv. Mater.* **2018**, *30*, 1706126.

33. R. Fu, Y. Zhao, Q. Li, W. Zhou, D. Yu, Q. Zhao, *Chem. Commun*. **2017**, *53*, 1829-1831.
34. N. K. Noel, A. Abate, S. D. Stranks, E. S. Parrott, V. M. Burlakov, A. Goriely, H. J. Snaith, *ACS Nano* **2014**, *8*, 9815-9821.
35. X. Li, M. I. Dar, C. Yi, J. Luo, M. Tschumi, S. M. Zakeeruddin, M. K. Nazeeruddin, H. Han, M. Grätzel, *Nat. Chem.* **2015**, *7*, 703.
36. Z. Wang, A. Pradhan, M. A. kamarudin, M. Pandey, S. S. Pandey, P. Zhang, C. H. Ng, A. S. M. Tripathi, T. Ma, S. Hayase, *ACS Appl. Mater. Interfaces* **2019**, *11*, 10012.
37. Y. Yang, M. Yang, K. Zhu, J. C. Johnson, J. J. Berry, J. V. D. Lagemaat, M. C. Beard, *Nat. Commun*. **2016**, *7*, 12613.
38. Y. Li, W. Yan, Y. Li, S. Wang, W. Wang, Z. Bian, L. Xiao, Q. Gong, *Sci. Rep.* **2015**, *5*, 14485.

Chapter 5

Perovskite Nanocrystals based Memristor Devices: Chemically Induced Control of Operational Parameters

5.1. Abstract

Resistive switching based non-volatile random access memory devices are promising due to their simple device structure, excellent performance, and low power consumption. In this chapter, we report the use of PNCs for resistive random access memories (ReRAMs). The PNCs have a general formula of $CH_3NH_3PbBr_{3-x}Cl_x$*, where* $x = 0$*, ~0.5 and ~1.0, and the devices were fabricated with a simple configuration consisting of FTO/PNC/Ag. The resistive memory devices showed excellent bipolar and bistable switching behaviour with small on-off voltage (from 2V to 0.5V). Surprisingly, the write-erase voltages of the devices reduced with the chloride content in the nanocrystals, while the on/off ratio, retention, and endurance of the devices got enhanced. This showed the possibility to control the operational parameters of resistive switching based memory devices through chemical modifications. A plausible mechanism was also proposed to explain the observations.*

5.2. Introduction

Memory devices are major components in the field of information technology (IT) and the fast growth of this area needs memory devices with high storage density and speed. Flash memories, dynamic random access memories (DRAMs), and hard-disk drives (HDDs) are the three leading memory device technologies.[1,2] Silicon-based flash memories which have an architecture consisting of a metal-oxide-semiconducting field-effect transistor with a floating gate are commonly used in recent years. They are low-cost devices with nonvolatile characteristics and high storage density. However, they have the disadvantages of low write-erase speeds (0.1-1 ms), high voltage (>10 V) for writing the data, and a limited number of rewrite cycles (10^6). Though DRAMs possess the advantages of a large number of write-erase cycles and high operation speed, they are highly volatile in nature and have to be refreshed frequently. HDDs, on the other hand, have the ability to store more data and many write-erase cycles but they show a very slow response.

To address the issues associated with the existing technologies, random access memory devices (RAMs) were introduced. RAMs are hardware devices that can be accessed randomly; that is, any byte of memory can be accessed without touching the preceding bytes. In other words, information can be accessed randomly instead of sequentially like it is on a CD or hard drive and hence the access times are much faster. RAM is widely used in servers, PCs, tablets, smartphones, and other electronic devices. Ferroelectric, phase-change, magnetic, and resistive are the four different types of RAMs. Ferroelectric and magnetic RAMs have issues pertaining to their sizes, while phase-change RAMs require high power for the phase transition between the amorphous and crystalline phases. On the other hand, resistive random access memories (ReRAMs) emerge as a promising candidate for memristors, neuromorphic computing and logic-in-memory applications due to their smaller size, simple device architecture, minimum power consumption, low switching voltage, scalability, high operation speed (ns), long data retention, endurance, and low-cost fabrication.[3-9] More importantly, they exhibit non-volatile characteristics as the stored data could be maintained even if the devices are in the off-state. Therefore, they can potentially overcome all the technical difficulties observed in conventional devices.

In ReRAMs, the active layer (insulator/semiconductor) is sandwiched between two conducting electrodes as shown in **Figure 5.1a**. This simple device architecture enables easy stacking of ReRAMs into a passive crossbar array with a small size of $4F^2$ (F is the minimum size of a device). The size of the crossbar array could be further decreased to $4F^2/n$ within vertically stacked three-dimensional (3-D) buildings (n is the number of stacking layer in crossbar array).[10] The basic principle of ReRAMs is resistive switching (RS), which implicates that the memory devices could be easily switched into two resistant states such as low resistance state (LRS/ON state) and high resistance state (HRS/OFF state) under applied voltages to store the data. The RS is generally caused by the formation and rupture of filaments or charge trapping by the defects. The current flows uniformly throughout the device in the OFF (HRS) state which is restricted to a local region (via conducting filament) with low resistance in the ON (LRS) state.[11] The switching event from OFF state to ON state is known as set process and the corresponding voltage is represented by V_{set}. In contrast, the switching event from ON state to OFF state is known as the reset process and the corresponding voltage is represented by V_{reset}.

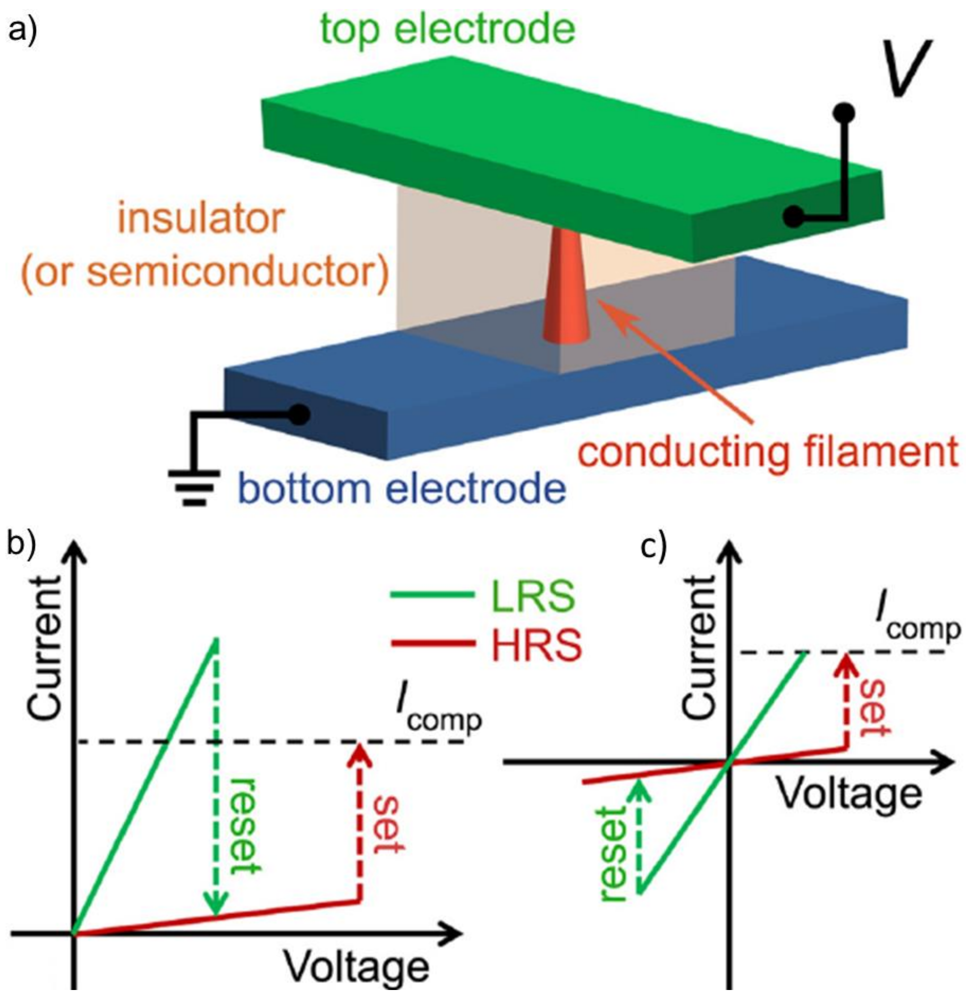

Figure 5.1. a) Schematic illustration of a ReRAM in which the active layer, insulating or semiconducting material is sandwiched between two conducting electrodes. Typical current-voltage (*I*-*V*) curves representing b) unipolar and c) bipolar switching behaviour of memory devices. compliance current (I_{comp}) is applied to avoid the permanent breakdown of the devices during the SET process (*Adapted from reference* 2).

There are two types of switching modes in ReRAMs, *viz.*, unipolar and bipolar switching. In unipolar switching, the set and reset processes occur at the same electrical polarity, whereas, in the latter case, the set and reset processes occur at opposite electrical polarities as shown in **Figure 5.1b** and **5.1c**, respectively.

The first experimental observation of RS was demonstrated by Hickmott in 1962.[12] He observed large negative differential resistance in different anodic oxide films which include SiO_2, Ta_2O_5, Al_2O_3, TiO_2, and ZrO_2. Later, various materials were found to show resistive switching exhibiting varying switching mechanisms.[13-15] Since the late 1990s, interest in RS saw a gradual rise due to the search on finding an alternative to Si-based flash memories. Zhuang *et al.* demonstrated the first ReRAMs for practical application.[16] A 64-bit ReRAM array was fabricated using $Pr_{0.7}Ca_{0.3}MnO_3$ as the active material which showed excellent performance with low switching voltage (< 5 V), a large memory window ($>10^3$), and high operation speed (10 ns). Organic materials were also found to be suitable as the active layer in ReRAMs.[17] The world’s leading ReRAM was introduced by Baek’s team in 2004 where they used binary transition-metal-oxide as the active material.[18] These devices demonstrated the operation at a low voltage (< 3 V), low current (2 mA), 10^6 times of set/reset cycles, and 10^{12} reading cycles. Recent reports show enhanced significance of ReRAMs as the physical realization of the fourth fundamental passive circuit element named memristor,[19] and also been suggested for their application in new fields including unconventional computing[20] and logic devices.[21]

Semiconductors such as metal oxides, perovskite oxides, organic and two-dimensional materials are widely used in ReRAMs. In particular, inorganic perovskite materials are highly promising candidates in ReRAM application due to their unique properties such as semiconducting, ferroelectric, dielectric, and light-sensitive properties.[22-24] However, high temperature processability and brittle, rigid structures are the major drawbacks of these materials. Organic-inorganic hybrid perovskite materials could also be used as the active layer in ReRAM application considering their unique current-voltage hysteresis arising from defects and fast ion migration. The switching mechanism in perovskite materials is the formation and rupturing of conducting filaments formed by halide ion vacancies. The organic cation interacts with the halide ions present in inorganic octahedra via hydrogen bonding. The molecular ion rotation in perovskites under the electric field reduces the H-bonding strength which leads to the migration of halide ions (or halide vacancies) easily to form a conductive filament. However, hybrid perovskites are not explored for memory device applications so far except for some scanty reports.

Wang *et al*. have fabricated bulk hybrid perovskite materials based ReRAMs with a simple device architecture consisting of FTO/$CH_3NH_3PbI_{3-x}Cl_x$/Au (**Figure 5.2**).[25] The thickness of the active layer was around 2.5 μm to avoid the pin-hole in the active layer. The *I-V* characteristics of the device showed a bipolar RS behavior with low operational switching voltages (SET voltage = 0.8 V, RESET voltage = -0.6 V). The devices also showed stable endurance (>100 times), long retention time (>10^4 s) and high temperature stability.

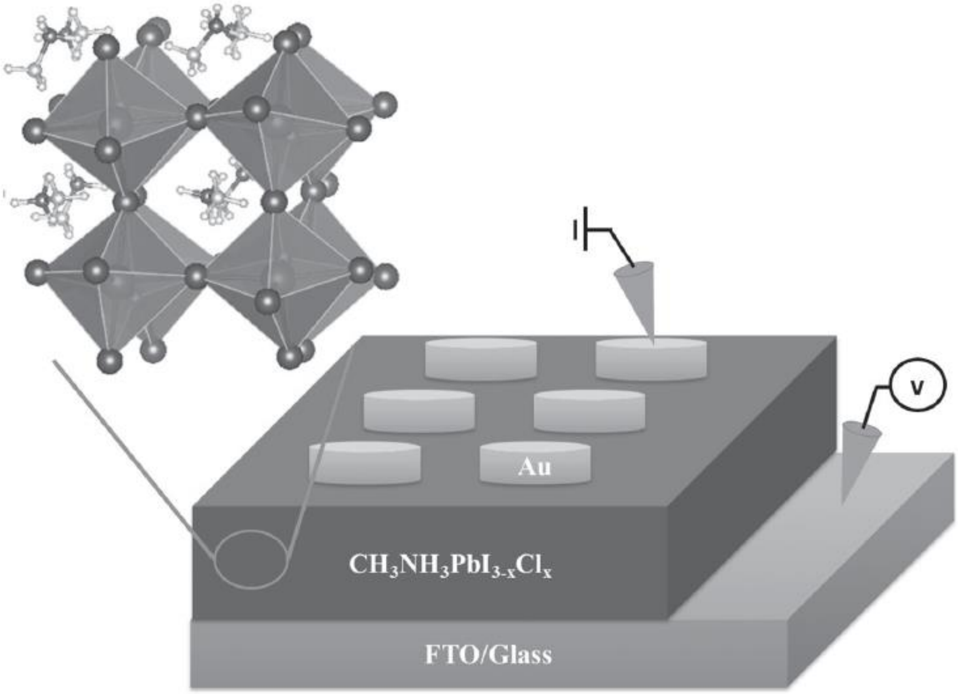

Figure 5.2. Schematic illustration of the Au/$CH_3NH_3PbI_{3-x}Cl_x$/FTO memory device structure (*Adapted from reference 25*).

Lee *et al*. fabricated flexible nonvolatile memory devices using $CH_3NH_3PbI_3$ perovskite material as the active layer.[26] A typical *I-V* curve of the memory device is shown in **Figure 5.3** (left side). The devices showed an operational voltage of around 0.7 V with long retention time (10^4 s) and better endurance properties. The devices performed uniform and reliable programmable memory operations even under tensile and compressive bent states. The migration of iodide vacancies (**Figure 5.3**, right side) and their conductive filaments formation under the electric field was found to be the major reasons for the RS mechanism.

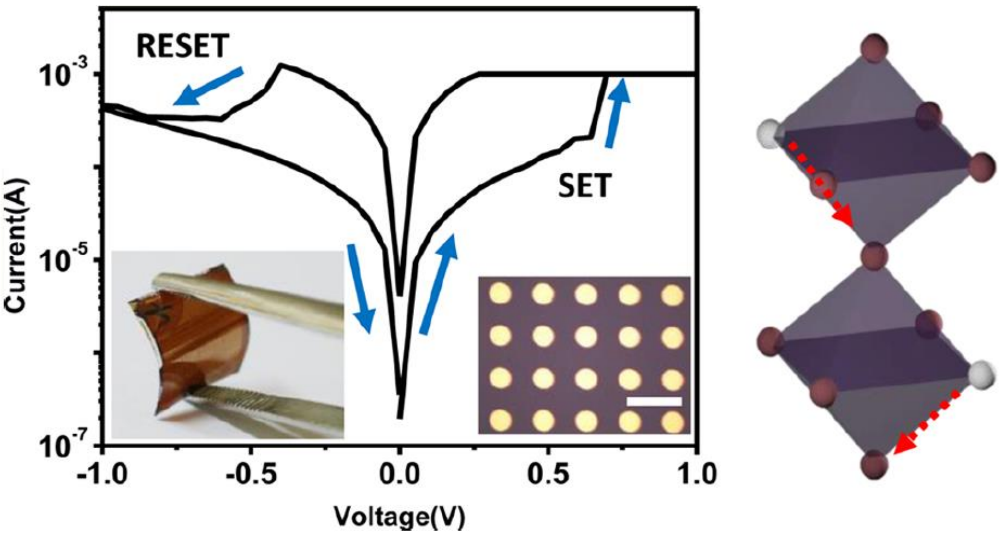

Figure 5.3. Left: The *I-V* curve showing the bipolar resistive switching property of FTO/$CH_3NH_3PbI_3$/Ag device. Inset shows photographs of the flexible memory device. The top view image of the device is also shown in the inset of Figure 5.3a. Right side: Schematic representation of the iodide vacancy migration in perovskite material (*Adapted from reference 26*).

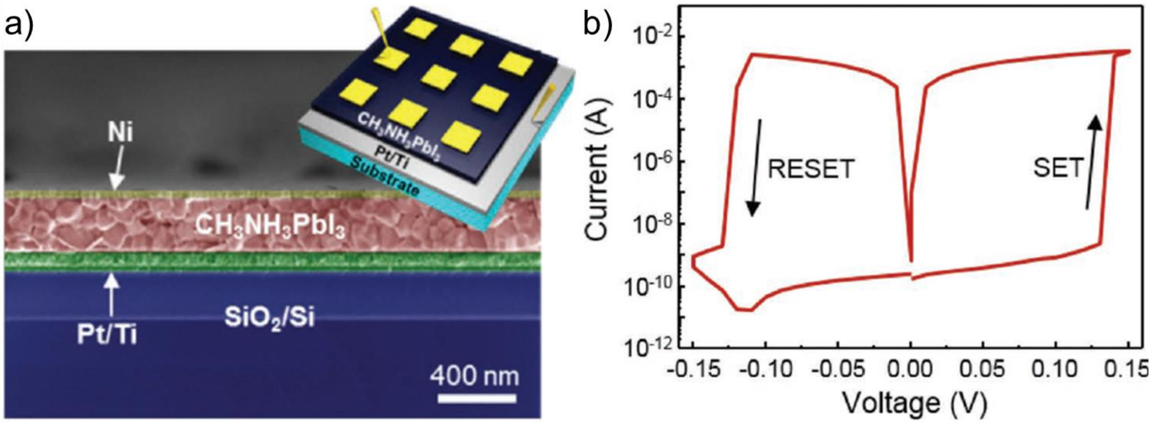

Figure 5.4. a) Cross-sectional SEM image of a memory device having a device structure, Substrate/Pt/$CH_3NH_3PbI_3$/Ni. The inset shows the schematic representation of the device. b) The *I-V* curve showing the bipolar resistive switching property of the device (*Adapted from reference 27*).

Jang and coworkers observed a multilevel resistive switching behavior in perovskite based memory devices having the architecture of Ag/$CH_3NH_3PbI_3$/Pt.[27] The cross-sectional SEM image of the device showed uniform and pinhole-free $CH_3NH_3PbI_3$ films (**Figure 5.4a).** A typical *I-V* curve of the memory device is shown in **Figure 5.4b**. The devices showed electroforming-free resistive switching with a low SET voltage (0.13 V) and high ON/OFF ratios (10^6). The devices also showed four-level storage capabilities due to their excellent properties. The high performance of the devices was attributed to the energetically favourable migration of iodide vacancies.

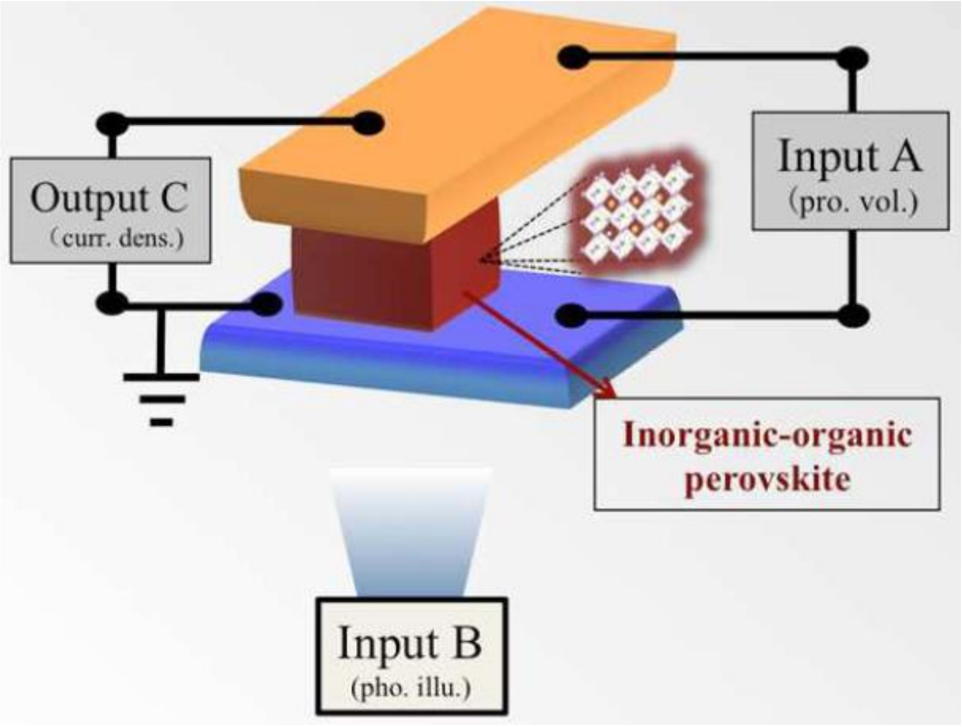

Figure 5.5. Schematic diagram of the light illumination induced $CH_3NH_3PbI_3$ based logic OR gate (*Adapted from reference 28*).

Sun *et al.* used $CH_3NH_3PbI_3$ as the active material for memory devices coupled with photoresponsive performance.[28] A schematic diagram of the device is shown in **Figure 5.5**. Due to the different photoresponse of two resistance states, logic OR gate could be constructed with this device by using electric field and light illumination as the input sources. The studies proved that this material is also suitable for different applications such as logic circuits, optical quantum information and optical digital computation for beneficial supplementation of the von Neumann architecture, or even for computing beyond it.

The above mentioned reports describe the use of hybrid perovskites in the bulk form that is inherently unstable under ambient conditions due to their interaction with moisture. In order to address this issue, we have selected hybrid perovskite material in the nanocrystal form consisting of octylammonium halides as the capping agent. The presence of a long alkyl chain based capping agent provides the materials with excellent air and moisture stability, and also good processability from common organic solvents. The PNCs used in the present study have a general formula of $CH_3NH_3PbBr_{3-x}Cl_x$, where x = 0 (PNC1), 0.46 (PNC2), and 1.03 (PNC3). The most explored $CH_3NH_3PbI_3$ based perovskites were not used because of their lower stability when compared to that of the corresponding bromide/chloride based perovskites even in the nanocrystal state. The memory devices were fabricated with a simple configuration consisting of FTO/PNC/Ag. The non-volatile resistive memory devices showed excellent bipolar and bistable switching behavior with small on-off voltage. Surprisingly, the write-erase voltages of the devices reduced with the increase in the chloride content of the nanocrystals (PNC1: 2.66 V; PNC2: 1.04 V; and PNC3: 0.53 V), while the on/off ratio, retention, and endurance of devices were enhanced. Hence this work opens up an excellent route to control the operational parameters of resistive switching based memory devices through chemical modifications.

5.3. Results and discussion

5.3.1. Synthesis and characterization of PNCs

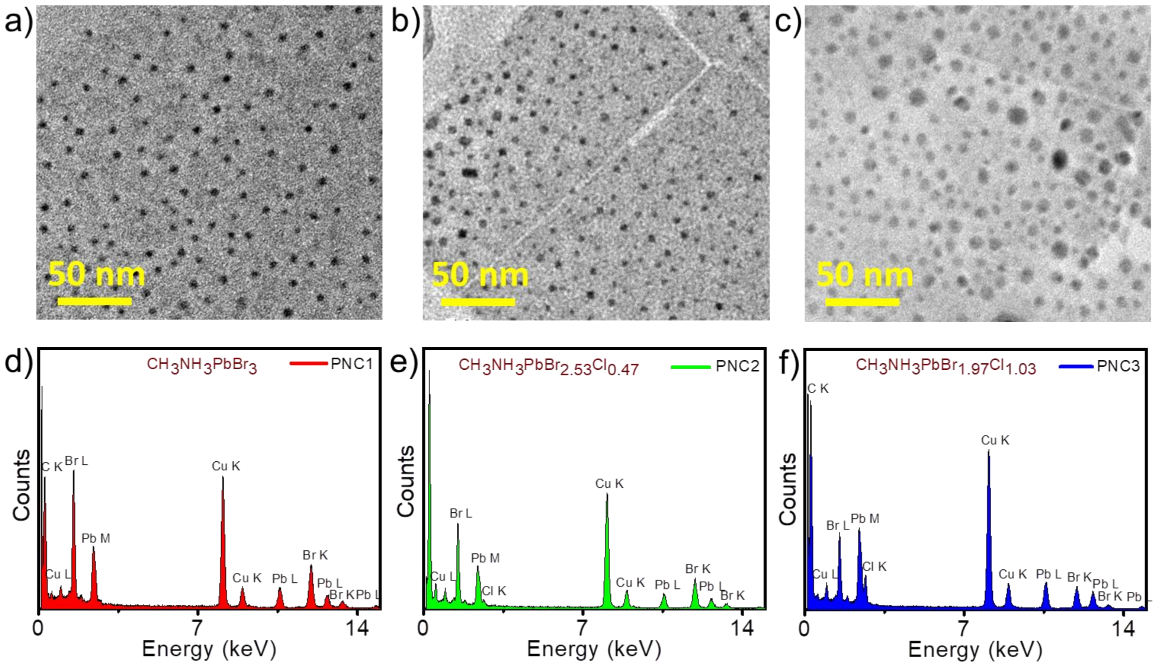

Figure 5.6. HR-TEM images of a) PNC1, b) PNC2 and c) PNC3 on a carbon coated copper grid, drop-cast from toluene suspension. Elemental analysis of d) PNC1, e) PNC2 and f) PNC3 by energy dispersive X-ray (EDX) method.

The PNCs of three different compositions (PNC1-3) were prepared by the method mentioned in **Chapter 2** with some modifications.[29] They were characterized by TEM, UV-visible absorption and fluorescence spectroscopy, X-ray diffraction spectroscopy, and cyclic voltammetric measurements. The size and shape of the nanocrystals were studied by TEM analysis (**Figure 5.6a-c**). It showed spherical nanocrystals of an average diameter of about 6 nm with relatively uniform dispersion. The halogen (chloride and bromide) compositions of PNCs were obtained from EDX measurements using TEM (**Figure 5.6d-f**). It revealed the compositions of the nanocrystals as $CH_3NH_3PbBr_3$ (PNC1), $CH_3NH_3PbBr_{2.54}Cl_{0.46}$ (PNC2), and $CH_3NH_3PbBr_{1.97}Cl_{1.03}$ (PNC3).

5.3.2. Photophysical characterization

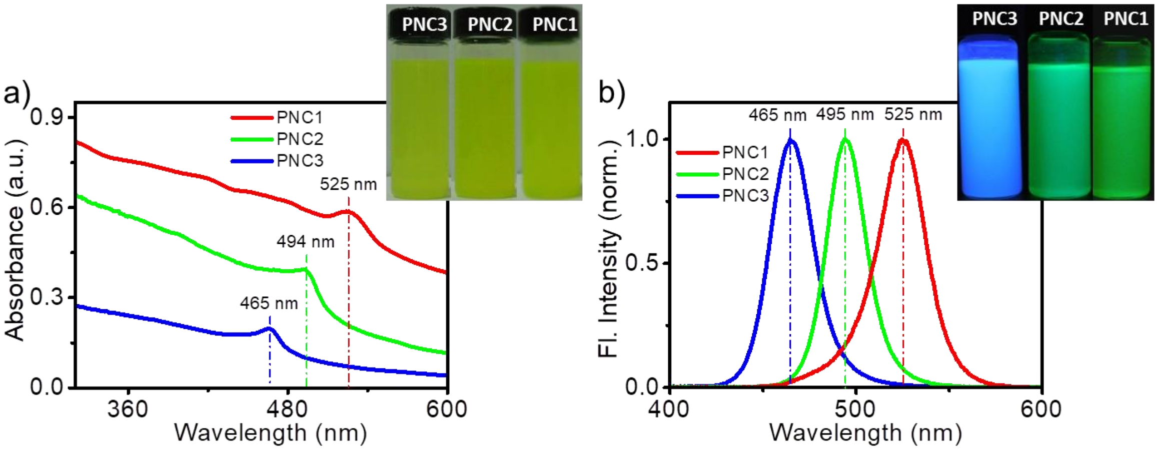

Figure 5.7. a) Absorption and b) emission spectra of PNCs dispersed in toluene. Photographs of the nanocrystals under normal and UV light are shown in the inset of figure 5.7a and 5.7b, respectively.

The absorption and emission spectra of the nanocrystals were measured both in the colloidal and film states (**Figure 5.7** and **5.8**). The toluene suspension of nanocrystals showed strong absorption in the UV-vis region with a maximum corresponding to the excitonic absorption, which was close to the onset of absorption spectrum (**Figure 5.7a**). However, a contribution from scattering was seen in the absorption spectrum. The emission spectra of PNCs showed a sharp peak with a narrow FWHM (**Figure 5.7b**). A very small Stoke's shift for all the PNCs indicates that the emission was directly originating from excitonic recombination. The nanocrystals suspension was yellow in color under day light and emitted bright green (PNC1), cyanish green (PNC2), and cyan (PNC3) fluorescence on excitation with UV (365 nm). The absorption and emission maximum of all the PNCs were shown in **Figures 5.7a** and **b** respectively.

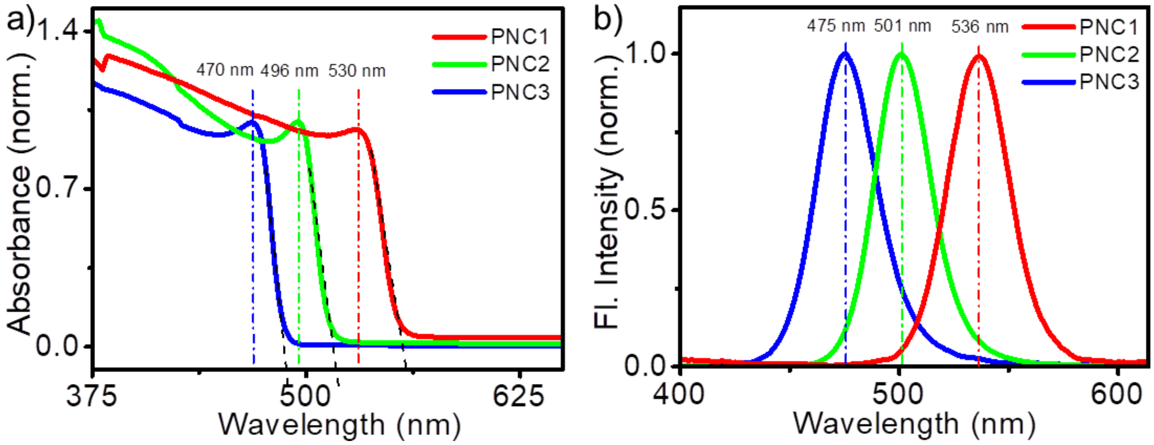

Figure 5.8. a) Absorption (derived from diffuse reflectance spectra using Kubelka–Munk method), and b) emission spectrum of the nanocrystals (PNC1, PNC2 & PNC3) in the film state spin-cast from toluene suspension.

Similarly, the PNCs films exhibited strong absorption in the UV-vis region with a maximum corresponding to the excitonic absorption, which was close to the onset of the absorption spectrum (**Figure 5.8a**). The fluorescence emission was intense in the visible region with a narrow FWHM (**Figure 5.8b**). The nanocrystals with no chloride content (PNC1) exhibited an absorption maximum at 530 nm, whereas the emission maximum was at 536 nm. On doping with chloride ions, both absorption and emission maximum was shifted to blue region. The absorption maximum of PNC2 and PNC3 was at 496 and 470 nm, respectively. Similarly, the emission maximum was shifted to 501 and 475 nm for PNC2 and PNC3, respectively. Blue shift in the absorption and emission maximum from PNC1 to PNC3 indicates the increase in bandgap with the increase in chloride content in the nanocrystal structure.

5.3.3. Bandgap calculation

The bandgap of the PNCs was calculated from the diffuse reflectance spectra using the Kubelka-Munk method (**Figure 5.9**).[30,31] The band gap was found to be 2.27 eV for PNC1, 2.45 eV for PNC2, and 2.60 eV for PNC3 respectively. The valence band (VB) was calculated using squarewave voltammetry (**Figure 5.10a-c**). 0.1 M tetrabutyl-ammonium hexafluorophosphate ($TBAPF_6$) in acetonitrile was used as supporting electrolyte, glassy carbon as a working electrode, platinum wire as counter electrode, and Ag/AgCl electrode as a reference electrode. The reference electrode was calibrated using ferrocene/ferrocenium (Fc/Fc^+) redox couple as an external standard at a scan rate of 100 mV/s. The PNCs dispersed in toluene were drop cast onto the working electrode and the solvent was dried under vacuum. Conduction band (CB) energy level was calculated by the addition of bandgap with valence band energy. The resulting values of VB and CB are summarized in **Figure 5.10d**.

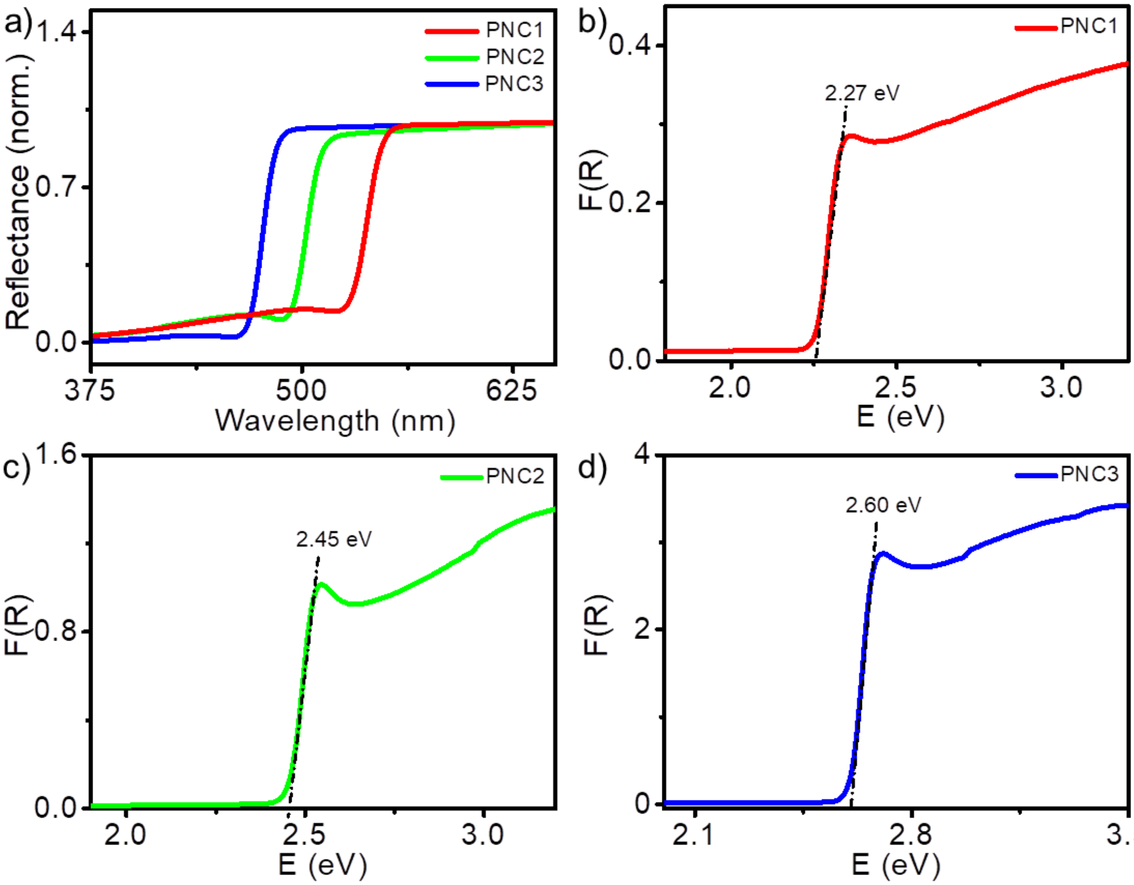

Figure 5.9. Diffuse reflectance spectra of PNCs (PNC1-3). Kubelka-Munk spectra for the PNCs (PNC1-3) revealing optical band gaps of 2.27, 2.45 and 2.60 eV respectively.

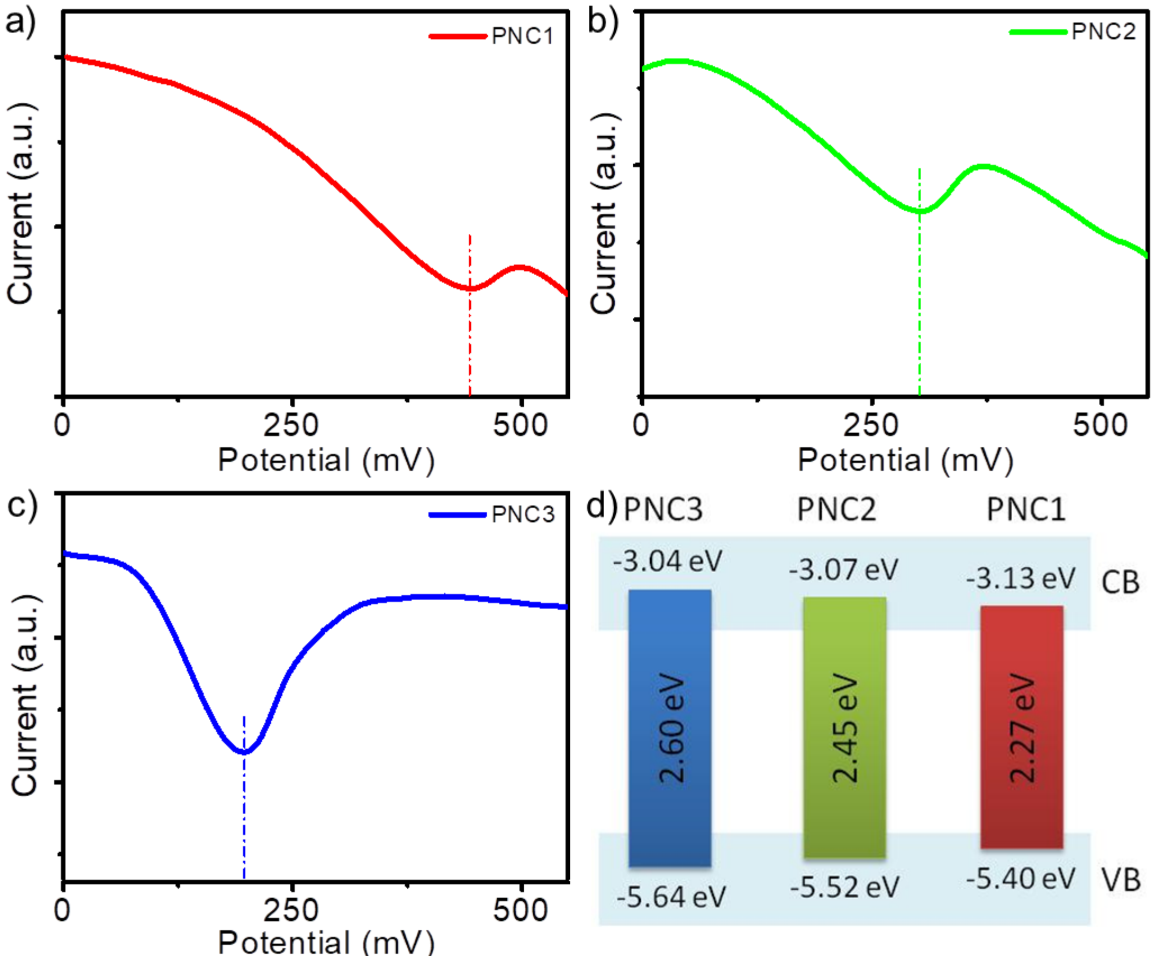

Figure 5.10. Squarewave voltammograms of a) PNC1, b) PNC2 and c) PNC3 PNCs. d) valence band (VB) and conduction band (CB) energy levels of the nanocrystals.

5.3.4. Memory device characterization

Resistive memory devices were made using the PNCs as the active layer. The toluene suspension of the nanocrystals was probe-sonicated and spin-coated on FTO substrates, yielding a uniform, smooth layer of ≈200 nm thickness. After vacuum drying the film, 200 nm thick silver was thermally evaporated on the perovskite layer using a shadow mask, to form FTO/PNC/Ag devices. **Figure 5.11a** shows the representative cross-sectional scanning electron microscope image of a device. The area of the individual devices was 1 mm^2.

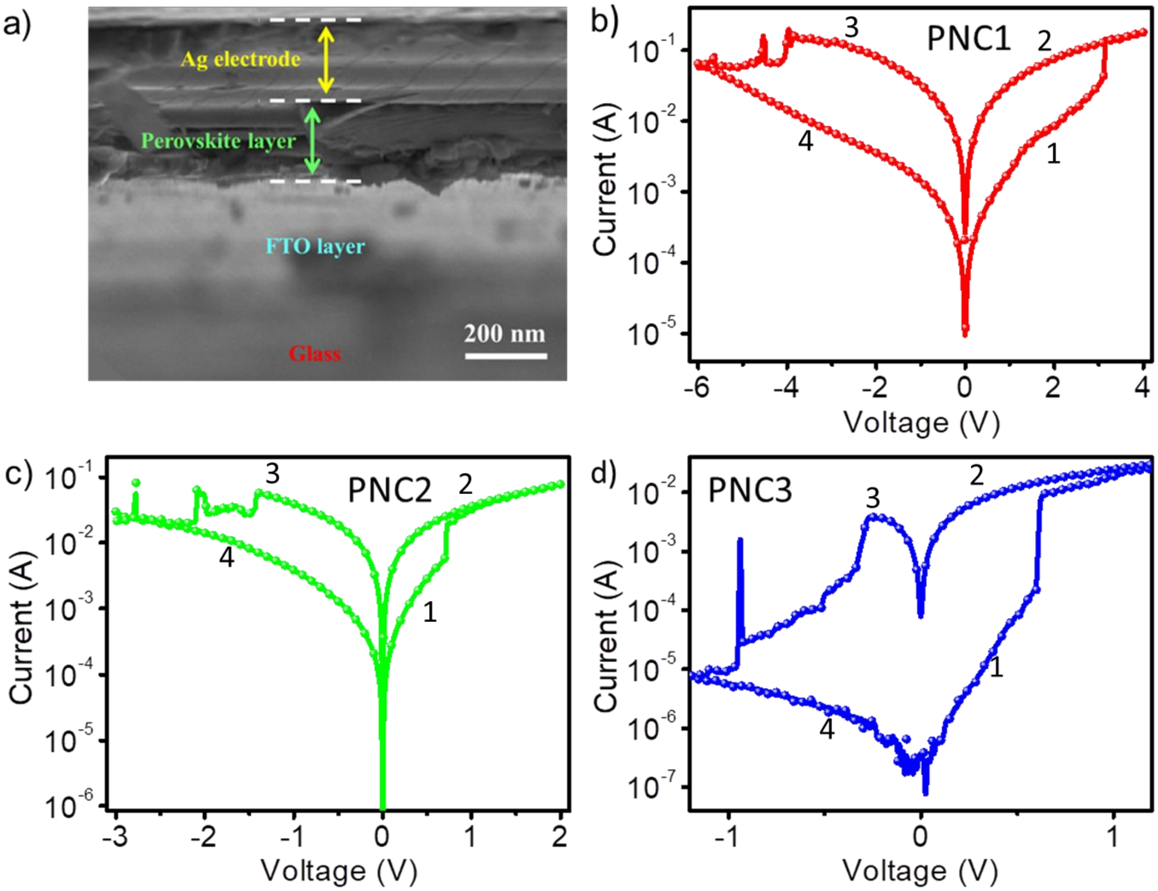

Figure 5.11. a) Cross-sectional scanning electron microscope image of the PNC1 device. Typical bipolar resistive switching behavior of devices comprising a) PNC1, b) PNC2, and c) PNC3 as the active switching media.

As the bias voltage was increased, the devices that were initially at a high resistance state (HRS) were turned on to a low resistance state (LRS) indicating the occurrence of the set process. After this transition, the LRS state remained until a negative reverse bias voltage was applied, where the device switched back to its HRS state, corresponding to the reset process. The set and reset processes in the device occur at opposite bias polarities, which indicate that the device has bipolar resistive switching characteristics, which was consistently observed in the fabricated devices. For instance, the PNC1 device was initially in the off-state with its intrinsic high resistance state of ≈1 kΩ. During the voltage sweep, it switched abruptly to the on-state at 3.08 V (i.e.) at a low resistance state with 25 Ω resistance. The device switched back to the high resistance state around -3.10 V. This bipolar switching behavior of the PNCs device was repeated for several cycles to analyze the reproducibility of the memory performance. The *I-V* characteristics of the devices with PNC2 as the active layer exhibited a much higher off-state resistance of 1.2 MΩ and on-state resistance of 60 Ω. Similarly, PNC3 exhibited an off-state resistance of 2.5 MΩ and on-state resistance of 80 Ω. The typical *I-V* characteristics of ReRAM devices with PNCs are shown in **Figure 5.11b-d**.

The reliability of the memory devices was investigated by plotting the Weibull distributions of the set and reset voltages of devices, as shown in **Figure 5.12a,c,e**. The Weibull slopes of the set and reset processes for PNC1-3 were found to be gradually increasing, indicating that the reliability of the devices was increasing with an increase in the chloride content in the perovskite nanostructure. **Figure 5.12b,d,f** shows the reproducible switching behavior of the devices to a set-reset voltage pulse sequence applied to the devices. The peaks of pulses were chosen to be larger than the average set and reset voltages measured for the respective samples. The endurance

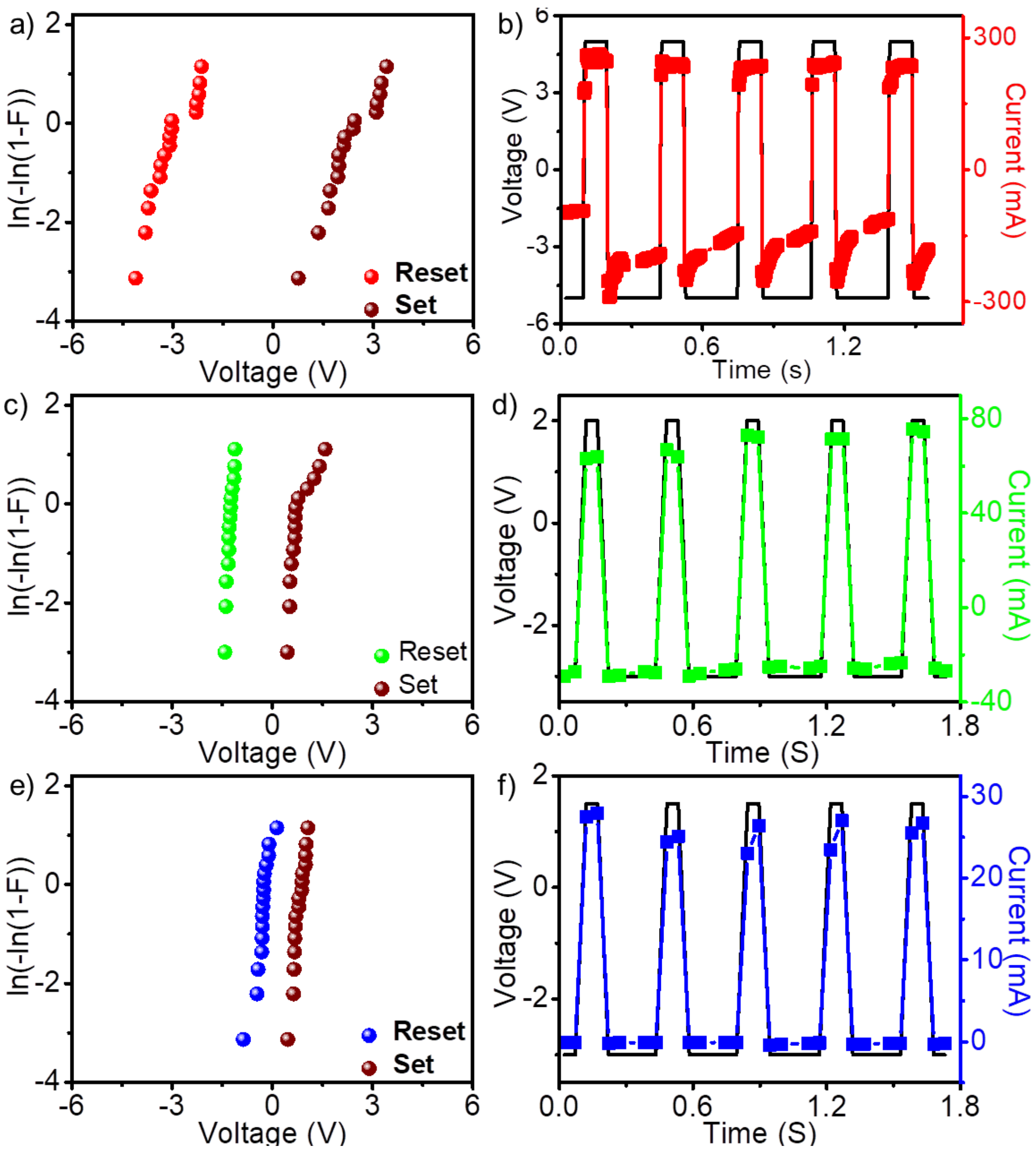

Figure 5.12. The Weibull distributions of the set and reset voltages of devices with a) PNC1, c) PNC2, and e) PNC3 as the active media (plotted using the switching data of 15 devices). The response of ReRAM devices to the set-reset voltage pulses; b) PNC1, d) PNC2, and f) PNC3.

upto to 250 cycles have been measured, showing consistent switching in the devices. An immediate observation from the Weibull distributions was that the set and reset voltages are tunable with chloride content in the material. The average values of the set and reset voltages of devices as a function of its chloride content were plotted in **Figure 5.13**.

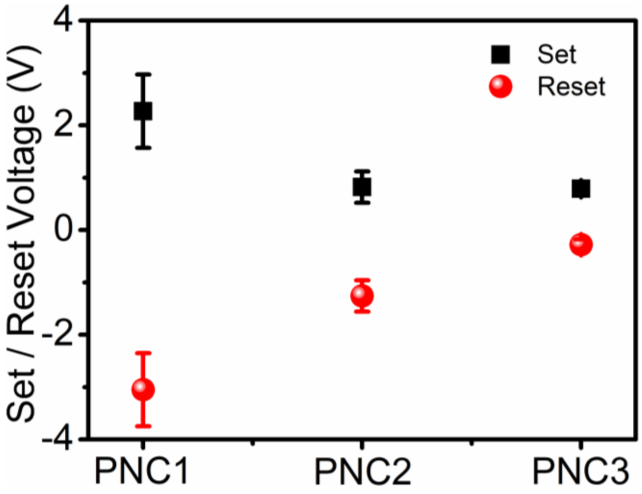

Figure 5.13. The average set and reset voltages of the devices comprising the PNCs, as a function of the chlorine content.

5.3.5. Resistive switching mechanism

The analysis of resistance switching characteristics in **Figure 5.11 b-d** shows that the off-state resistance was increasing (and thus the off-current is reducing) with the chloride content in the PNCs. This was expected from the fact that the bandgap of these nanocrystals increases with an increase in its chloride content. Thus, the off-current, which was initially Ohmic will be lower for larger bandgap (E_g) materials due to the fact that the free carrier density depends on $e^{-Eg/kT}$. Space charge limited current (SCLC) region was not observed once the device was set on, indicating that the switching involves a large number of defects/ions leading to the conductive path formation.

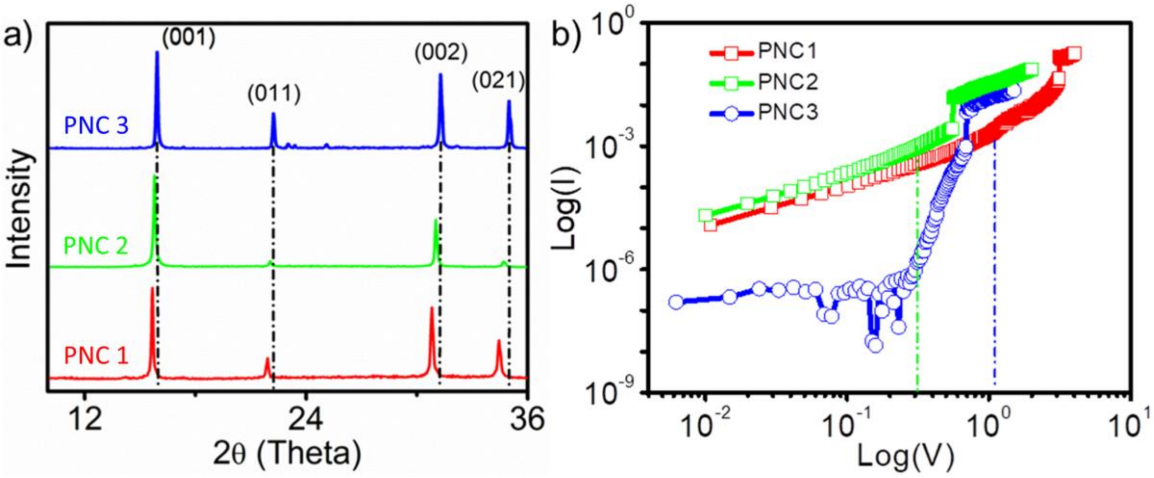

Figure 5.14. a) X-ray diffraction profiles of the PNCs. b) log(*I*)-log(*V*) plot of the devices from the off-state until the set process.

In order to get a better insight into the switching mechanism by understanding the microstructure of the nanocrystals and the effect of doping on the microstructure, X-ray diffraction (XRD) studies were carried out (**Figure 5.14a**). PNC1 showed the typical diffraction of a cubic structure with sharp and intense peaks corresponding to the planes 001 (d = 5.93 Å), 011 (d = 4.20 Å), 002 (d = 2.97 Å), and 021 (d = 2.65 Å). Distortion of the cubic structure was seen on the incorporation of chloride ions as evident from the decrease in the d-spacing values of all planes. For instance, the d-spacing of 001 planes was found to be 5.87 and 5.82 Å for PNC2 and PNC3, respectively. This could be attributed to the size mismatch of halogen ions.[25] The metal-halogen bond is expected to shorten when larger bromide ions were replaced with smaller chloride ions. The shortening of the bond length results in lattice shrinkage which in turn distorts the cubic structure as evident from the XRD analysis. The deviation in bond length has significant effects on the perovskite properties as it is highly correlated with the metal-halogen bond length. This explains the change in absorption and emission properties and increases in the bandgap of the nanocrystals on doping with chloride ions as shown in **Figure 5.8**.

As a consequence of such a lattice shrinkage, one would expect a larger switching voltage if the switching was due to the conductive filament formation. On the contrary, the larger bandgap samples have smaller switching voltages as shown in **Figure 5.13**. This means that there are alternative paths for the electronic conduction through the nanocrystal film, such as surface defects and the grain boundaries between the nanocrystals. Solution processed perovskites are abundant in surface defects particularly consisting of mixed halides due to size mismatch,[25] which paves the route for the electronic conduction through SCLC mechanism. In the PNCs reported here, replacement of Br^- by Cl^- will introduce defects in the core structure and the surface. **Figure 5.14b** shows the log(*I*) versus log(*V*) plot of the devices from the off-state until the set process. The characteristic of the PNC1 device shows a transition from Ohmic conduction to SCLC at around 1 V, whereas PNC2 has the transition at 0.2 V. Interestingly, PNC3 does not show a transition from Ohmic to SCLC conduction, instead exhibiting a strong increase in current with voltage related to the Poole–Frenkel conduction. It indicates that the defect density is increasing with the Cl^- content in the nanocrystal. The increase in defects leading to an early set/reset process in the device as shown in **Figure 5.12**.

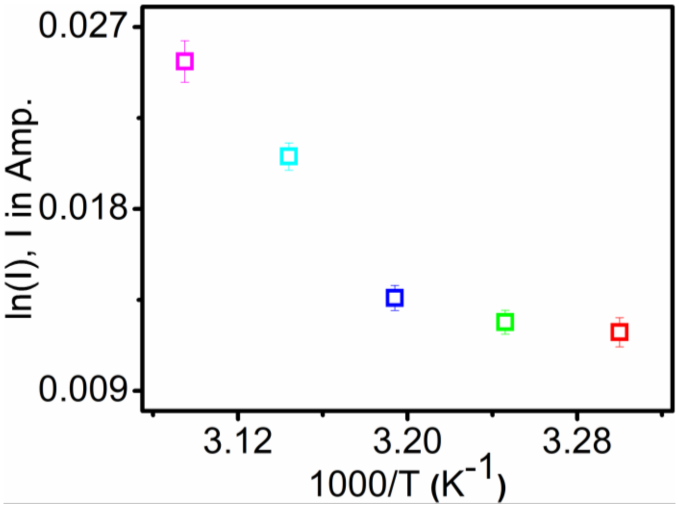

Figure 5.15. Arrhenius plot of the on-current of the PNC1 device as a function of 1/T.

The current through the PNC1 device after the set process (on-current), as a function of temperature was measured. It was observed that the on-current increases with an increase in temperature, which indicates that the charge transport after the set process is a thermal activation process or a hopping mechanism that obeys the Arrhenius behavior. **Figure 5.15** shows the Arrhenius plot of the on-current as a function of 1/T. The activation energy of the electron hopping in this case is estimated to be 55.38 meV, which is nearly twice the thermal energy of an electron at room temperature. This shows that the set process induces defects in the active material.

5.3.6. Endurance and retention studies

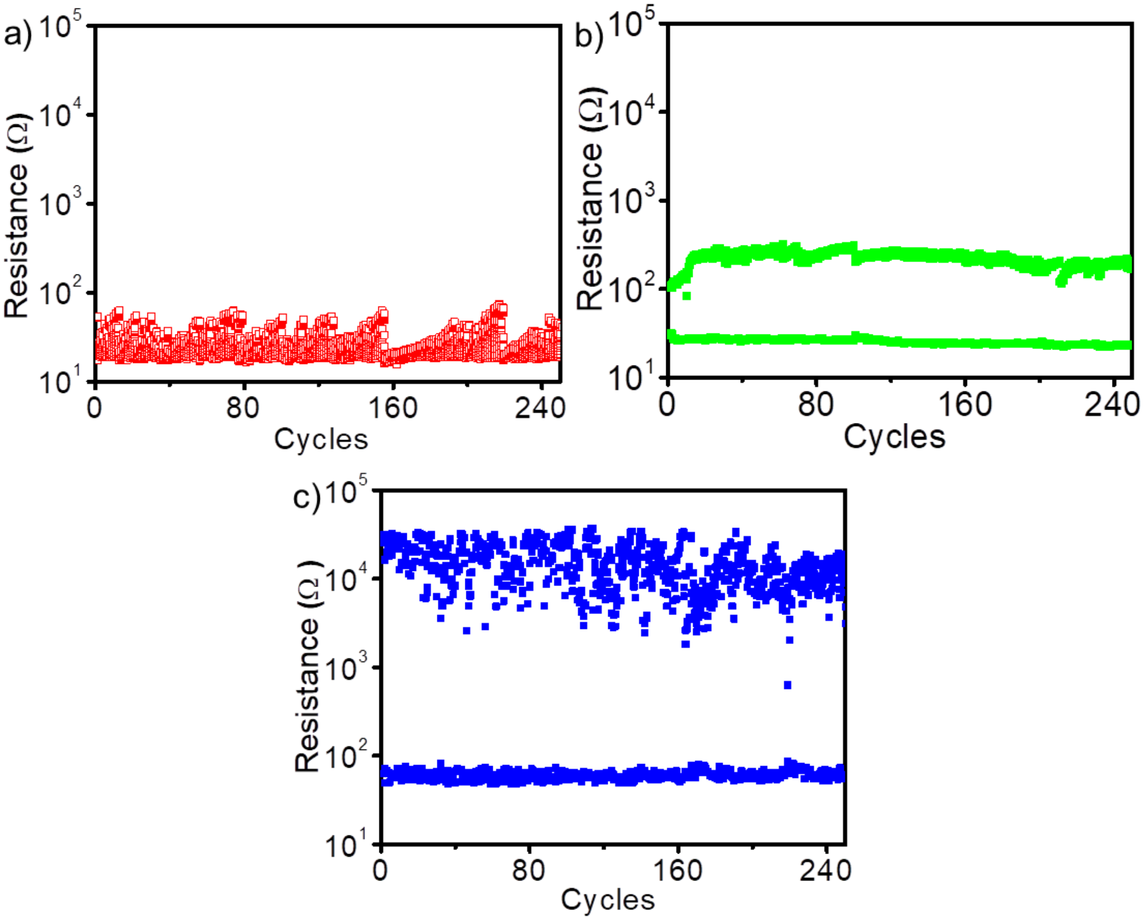

Figure 5.16. The endurance of devices measured for 250 cycles; a) PNC1, b) PNC2, and c) PNC3.

The endurance performances of devices have been tested for 250 cycles of write-erase processes. **Figure 5.16a-c** shows the results of the endurance test in terms of their off- and on-state resistances. The device comprising PNC1 as the active medium exhibits the lowest on-off ratio, whereas, the performance was improving upon increasing the chloride content in the nanocrystals. This can be understood as follows: the off-state resistance of the device was decided by the SCLC transport, together with the intrinsic conductivity of the nanocrystals. The on-state resistance was dictated by halide vacancies, the density of which increases with increasing Cl^- content in the nanocrystals. For these reasons, the on-off ratios of three samples were enhanced in the order of 2, 10, and 500 for PNC1, PNC2, and PNC3 samples.

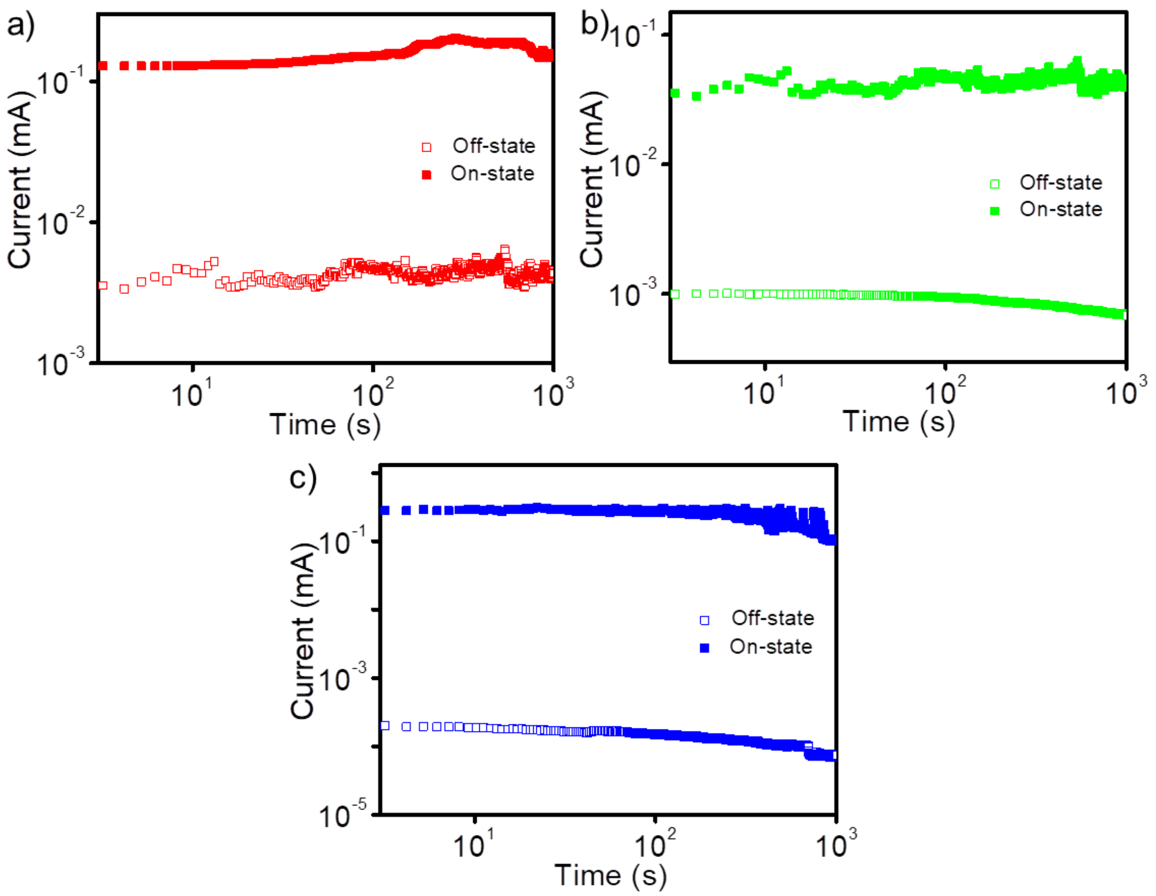

Figure 5.17. The retention properties of a) PNC1, b) PNC2, and c) PNC3 devices. The off-states were measured at 0.5 V, whereas, the on-states were measured at 5, 3, and 1 V for PNC1, PNC2, and PNC3, respectively.

Figure 5.17 shows the retention properties of the devices comprising of PNC1, PNC2, and PNC3 as the active layers, measured for 1000 s. Since the set voltages vary for devices with different active layers, the on-states were measured at 5, 3, and

1 V for PNC1, PNC2, and PNC3, respectively. On the other hand, the off-state measurements were done at 0.5 V. No considerable degradation was observed in the devices in the programmed states after 1000 s, showing the stability of the devices. The devices were also found to be stable even after six months indicating excellent stability of the material (**Figure 5.18**).

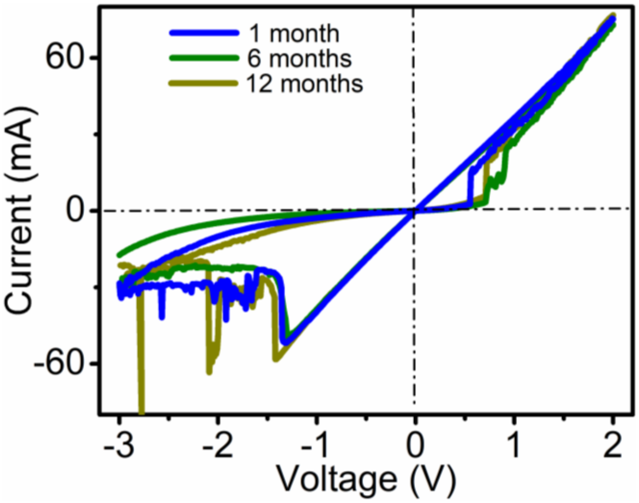

Figure 5.18. *I-V* characteristics of PNC2 device measured after one month, six months, and twelve months.

In one of the recent reports on hybrid perovskites, it was mentioned that moisture (or water) initiates the decomposition of perovskite materials into iodide containing volatile species (methylammonium iodide and hydrogen iodide).[32] Subsequently, these iodine containing volatile species interact with Ag resulting in the formation of AgI. In the case of our materials, as we mentioned above, they are highly resistant to moisture/water and hence the chance of HBr or HCl generation and the subsequent formation of AgBr or AgCl is negligible. In order to prove this, we have measured the

I-*V* characteristics of PNC2 based device after one month, six months, and twelve months (**Figure 5.18**). No notable change in the *I*-*V* characteristics essentially shows that the Ag contact in the FTO/PNC/Ag device is not reacting with Br/Cl in the interface. This analysis also confirmed the time dependent stability of the devices.

It has been already established that inorganic oxide perovskite materials hold a lot of promise for memory application as they show excellent switching behaviors at low voltages. But poor processability and the need of harsh conditions for fabrication is a disadvantage. The performance of the organic-inorganic hybrid perovskites presented in this work is on a par with the switching properties of the conventional inorganic oxide perovskites. These materials also possess a great advantage of solution processability at ambient conditions, which make them highly promising for developing high-performance low-cost memory devices for practical applications. Moreover, these materials exhibited a very interesting feature of programming the operational parameters such as write-erase voltage, on/off ratio, retention, and endurance through simple chemical modifications. This is a unique finding from both fundamental and technology viewpoints and may open up a new path for tuning device physics of memory devices through materials chemistry. It could be assumed that further improvements in the device parameters could be possible in these materials by varying metal, organic, halide, and/or the capping agent of the basic perovskite nanocrystals structure.

5.4. Conclusions

In summary, we have demonstrated that organic-inorganic hybrid PNCs are excellent material for resistive random access memory devices with bipolar and bistable switching behavior at low operating voltages. Further, we have proved that the switching properties could be controlled by the doping of chloride ions to the basic perovskite structure. The obtained results reveal that the PNCs could meet the criteria of a switching layer for non-volatile memory devices, which not only exhibit impressive resistive switching behavior at low operating voltage but also has the advantage of low temperature processability.

5.5. Experimental section

5.5.1. Materials

The reagents and chemicals for synthesis were purchased from local suppliers or from Sigma Aldrich, Alfa Aeasar or TCI. Air- and water-sensitive synthetic steps were performed in an argon atmosphere.

The current-voltage (*I*-*V*) characteristics were measured using a Cascade Microtech four-probe station connected to Agilent B1500A parametric analyzer, and the endurance data were measured with Agilent B2912A source measurement units.

5.5.2. Fabrication of memory devices

The PNCs stock solution (10mg/mL) was prepared by dispersing the nanocrystals in toluene via probe-sonication for 10 minutes. Subsequently, it was spin-coated on a

FTO substrate at 2000 rpm for 60s. The spin-coating was repeated for two more times to obtain a thickness of around 200 nm. After vacuum drying the film, 200 nm thick silver was thermally evaporated on to the perovskite layer using a shadow mask to form FTO/PNC/Ag devices.

5.5.3. Synthesis of PNCs

PNC1**:** 2 mL of octadecene was heated to 80 °C, and the capping agent octylammonium bromide (16.8 mg, 0.08 mmole) was added. $PbBr_2$ (36.7 mg, 0.1 mmole) dissolved in 200 μL of DMF and methylammonium bromide (9.0 mg, 0.08 mmole) dissolved in 100 μL of DMF were added to this solution separately. A yellow dispersion was formed and the nanocrystals were immediately precipitated by the addition of acetone. The solution was centrifuged at 7000 rpm for 10 min, the supernatant solution was decanted and the residue was dried under vacuum yielding the nanocrystals.

PNC2**:** PNC2 was prepared by following the above procedure using 2 mL of octadecene, octylammonium bromide (29.4 mg, 0.14 mmole), $PbCl_2$ (13.9 mg, 0.05 mmole) dissolved in 500 μL of DMF, and methylammonium bromide (23.5 mg, 0.21 mmole) dissolved in 100 μL of DMF.

PNC3: The same procedure was followed with octylammonium bromide (16.8 mg, 0.08 mmole) and methylammonium bromide (13.4 mg, 0.12 mmole). Other reagents were the same as above.

5.6. References

1. International Technology Roadmap for Semiconductors (**2011**) Edition. http://www.itrs.net/ Links/2011ITRS/Home2011.htm.
2. G. W. Burr, B. N, Kurdi, J. C. Scott, C. H, Lam, K. Gopalakrishnan, R. S. Shenoy, *IBM J. Res. Dev*. **2008**, *52*, 449-464.
3. F. Pan, S. Gao, C. Chen, C. Song, F. Zeng, *Mater. Sci. Eng. R* **2014**, *83*, 1-59.
4. C. Ho, C. L. Hsu, C. C. Chen, J. T. Liu, C.-S. Wu, C.-C. Huang, C. Hu, F. L. Yang, *IEDM Tech. Dig*. **2010**, *10*, 436-439.
5. Y. Yang, J. Ouyang, L. Ma, C. W. Chu, R. J. Tseng, *Adv. Funct. Mater*. **2006**, *16*, 1001-1014.
6. J. Ouyang, C. W. Chu, C. Szmanda, L. Ma, Y. Yang, *Nat. Mater*. **2004**, *3*, 918-922.
7. L. P. Ma, J. Liu, Y. Yang, *Appl. Phys. Lett*. **2002**, *80*, 2997-2999.
8. A. C. Torrezan, J. P. Strachan, G. Medeiros-Ribeiro, R. S. Williams, *Nanotechnology* **2011**, *22*, 485203(1-7).
9. J. Ouyang, *J. Mater. Chem. C* **2015**, *3*, 7243-7261.
10. S. Song, B. Cho, T. W. Kim, Y. Ji, M. Jo, G. Wang, M. Choe, Y. H. Kahng, H. Hwang, T. Lee, *Adv. Mater.* **2010**, *22*, 5048-5052.
11. R. Waser, R. Dittmann, G. Staikov, K. Szot, *Adv. Mater*. **2009**, *21*, 2632-2663.
12. T. W. Hickmott, *J. Appl. Phys*. **1962**, *33*, 2669-2682.
13. J. F. Gibbons, W. E. Beadle, *Solid-State Electron*. **1964**, *7*, 785-797.
14. J. G. Simmons, R. R. Verderber, *Proc. R. Soc. A* **1967**, *301*, 77-102.
15. G. Dearnaley, A. M. Stoneham, D. V. Morgan, *Rep. Progr. Phys.* **1970**, *33*, 1129-1191.
16. W. W. Zhuang, W. Pan, B. D. Ulrich, J. J. Lee, L. Stecker, A. Burmaster, D. R. Evans, S. T. Hsu, M. Tajiri, A. Shimaoka, K. Inoue, T. Naka, N. Awaya, K.

Sakiyama, Y. Wang, S. Q. Liu, N. J. Wu, A. Iganatiev, *IEDM Tech. Dig.* **2002**, 193.

17. L. P. Ma, J. Liu, Y. Yang, *Appl. Phys. Lett.* **2002**, *80*, 2997-2999.
18. I. G. Baek, M. S. Lee, S. Seo, M. J. Lee, D. H. Seo, D. S. Suh, J. C. Park, S. O. Park, H. S. Kim, I. K. Yoo, U. I. Chung, J. T. Moon, *IEDM Tech. Dig.* **2004**, 587.
19. D. B. Strukov, G. S. Snider, D. R. Stewart, R. S. Williams, *Nature* **2008**, *453*, 80-83.
20. S. H. Jo, T. Chang, I. Ebong, B. B. Bhadviya, P. Mazumder, W. Lu, *Nano Lett*. **2010**, *10*, 1297-1301.
21. J. Borghetti, G. S. Snider, P. J. Kuekes, J. J. Yang, D. R. Stewart, R. S. Williams, *Nature* **2010**, *464*, 873-876.
22. G. Chen, C. Song, C. Chen, S. Gao, F. Zeng, F. Pan, *Adv. Mater*. **2012**, *24*, 3515-3520.
23. S. Gao, C. Song, C. Chen, F. Zeng, F. Pan, *J. Phys. Chem. C* **2012**, *116*, 17955-17959.
24. X. Zhu, W. Su, Y. Liu, B. Hu, L. Pan, W. Lu, J. Zhang, R.-W. Li, *Adv. Mater*. **2012**, *24*, 3941-3946.
25. E. J. Yoo, M. Lyu, J.-H. Yun, C. J. Kang, Y. J. Choi, L. Wang, *Adv. Mater.* **2015**, *27*, 6170-6175.
26. C. Gu, J.-S. Lee, *ACS Nano* **2016**, *10*, 5413-5418.
27. J. Choi, S. Park, J. Lee, K. Hong, D.-H. Kim, C. W. Moon, G. D. Park, J. Suh, J. Hwang, S. Y. Kim, H. S. Jung, N.-G. Park, S. Han, K. T. Nam, H. W. Jang, *Adv. Mater*. **2016**, *28*, 6562-6567.
28. G. Lin, Y. Lin, R. Cui, H. Huang, X. Guo, C. Li, J. Dong, X. Guoce, B. Sun, *J. Mater. Chem. C* **2015**, *3*, 10793-10798.
29. L. C. Schmidt, A. Pertegás, S. González-Carrero, O. Malinkiewicz, S. Agouram, G. M. Espallargas, H. J. Bolink, R. E. Galian, J. Pérez-Prieto, *J. Am. Chem. Soc*. **2014**, *136*, 850-853.

30. F. Hao, C. C. Stoumpos, R. P. H. Chang, M. G. Kanatzidis, *J. Am. Chem. Soc.* **2014**, *136*, 8094-8099.
31. T. Baikie, N. S. Barrow, Y. Fang, P. J. Keenan, P. R. Slater, R. O. Piltz, M. Gutmann, S. G. Mhaisalkar, T. J. White, *J. Mater. Chem. A* **2015**, *3*, 9298-9307.
32. Y. Kato, L. K. Ono, M. V. Lee, S. Wang, S. R. Raga, Y. Qi, *Adv. Mater. Interfaces* **2015**, *2*, 1500195 (1-6).

Chapter 6

α- and δ-$FAPbI_3$ Perovskite Nanocrystals: Phase Effect on Memristor Characteristics

6.1. Abstract

Formamidinium lead triiodide ($FAPbI_3$) is an important material among numerous hybrid perovskites due to their superior optoelectronic properties. It is crystallized either as a yellow hexagonal non-perovskite phase (δ-$FAPbI_3$) or a black cubic perovskite phase (α-$FAPbI_3$) depending on preparation temperature. In this chapter, we have studied memristor characteristics of δ- and α-$FAPbI_3$ in nanocrystals form. The ReRAM devices fabricated from α-$FAPbI_3$ as an active layer showed a remarkable switching property with an operating set voltage of around 2 V. Interestingly, this is in contrast to the bulk α-$FAPbI_3$ perovskite, which is not capable of exhibiting resistive switching due to the difficulty in rupturing filaments formed by iodide vacancies. Our studies revealed that the presence of capping ligands plays a key role in the switching of PNCs. Interestingly, the memristors fabricated from δ-$FAPbI_3$ nanocrystals showed a 4-fold enhanced on/off ratio (~10^5) compared to that of α-form (10). We found that individual hexagonal nanocrystals of δ-$FAPbI_3$ self-assemble to form nanorods which are parallelly orientated on the FTO substrate. The δ-$FAPbI_3$ nanocrystals are one-dimensional in nature. As a result, the intrinsic conductivity (off current) was decreased resulting in high on/off ratio for δ-$FAPbI_3$.

6.2. Introduction

Formamidinium lead iodide, $HC(NH_2)_2PbI_3$ ($FAPbI_3$), based perovskite material is found to be a superior alternative to the most studied $MAPbI_3$ perovskite in several aspects due to smaller bandgap, broader light absorption, high thermal stability, longer charge carriers lifetime, and good photostability.[1-3] This material is crystallized either as a yellow hexagonal non-perovskite phase (δ-$FAPbI_3$) with an indirect bandgap of 2.48 eV or a black cubic perovskite phase (α-$FAPbI_3$) with a direct bandgap of ~1.45 eV depending on heat-treatment temperature.[4,5] The α-$FAPbI_3$ is having a three-dimensional (3D) structure formed by the corner sharing of PbI_6^{4-} octahedra in all directions (**Figure 6.1a**). On the other hand, the δ-form is having a one-dimensional (1D) structure formed by the face sharing of PbI_6^{4-} octahedra in one direction (**Figure 6.1b**). Though the former is considered as a promising material for several optoelectronic devices, it undergoes a phase transition to form δ-$FAPbI_3$ under ambient conditions in the presence of moisture, limiting its applications. Literature reports suggest that the bond angle between Pb-I-Pb (180 °C) is reduced in the presence of moisture resulting in the formation of air stable low dimensional δ-form (**Figure 6.1c**). The δ-$FAPbI_3$ material can return back to α-$FAPbI_3$ perovskite on heating at above 170 °C.[6,7] In the present chapter, we studied the memristor properties of both forms of $FAPbI_3$ in the nanocrystal form.

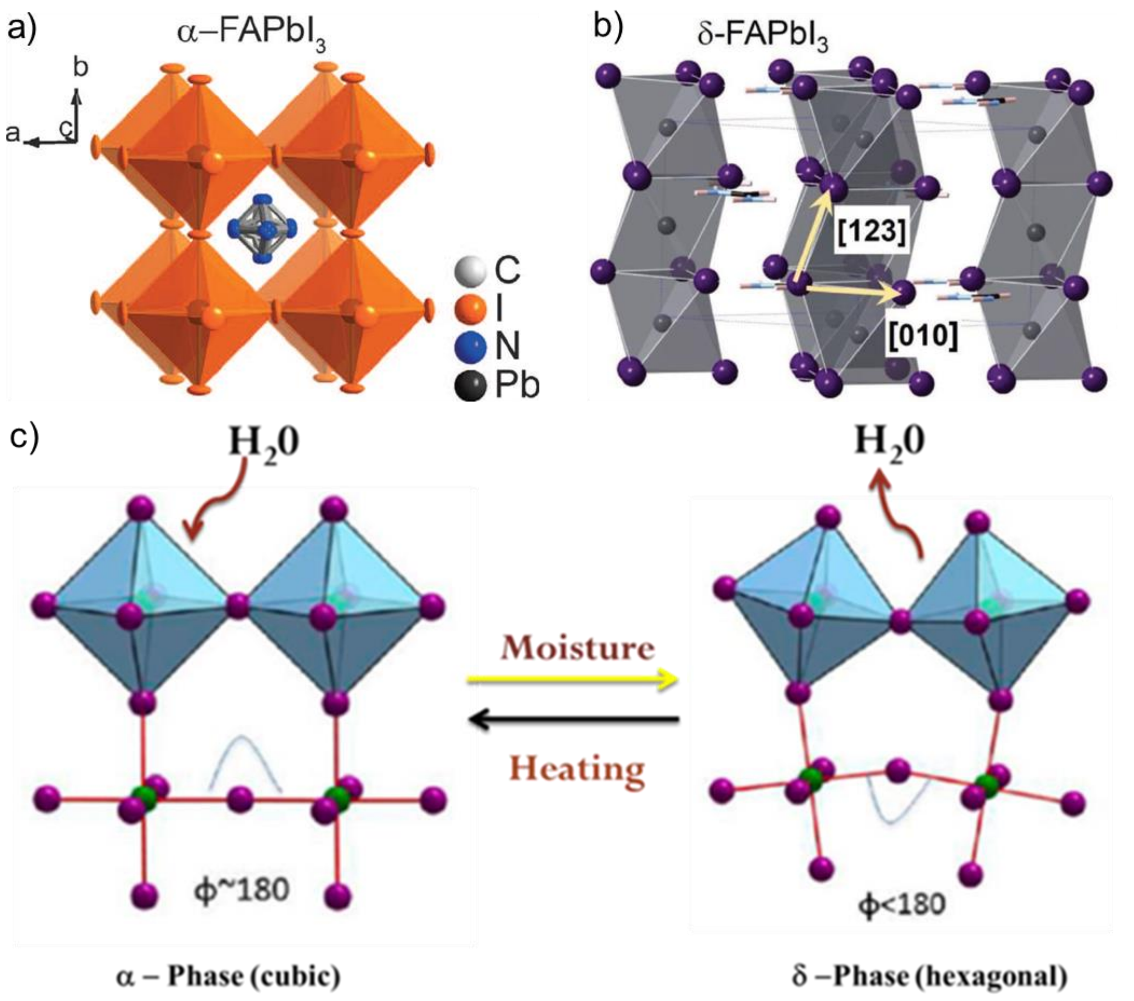

Figure 6.1. a) Crystal structure of three-dimensional cubic *α*-FAPbI$_3$ (showing orientational disorder of the FA molecules). b) Crystal structure of one-dimensional *δ*-FAPbI$_3$. c) Schematic diagram representing phase transition of FAPbI$_3$. (*Adapted from reference 6 & 7*).

In this context, it is important to consider the report by Park *et al.* on the memristor behavior of bulk *α*-FAPbI$_3$ perovskite.[7] This material was found to be inactive in memristor devices due to the difficulties in rupturing of conducting filaments formed by the iodide vacancies (V_I). Density Functional Theory (DFT) calculations revealed that the electronic states of V_I are overlapped with the conduction band and diffused through the entire conduction band. As a result, two V_I interact through the conduction band and the interaction energy does not decrease as the physical distance increases. Therefore, the formed iodide vacancies filaments at the set process are very difficult to rupture during the reset process. Moreover, as mentioned above, this material undergoes a rapid phase transition from α- to δ-form under ambient conditions.

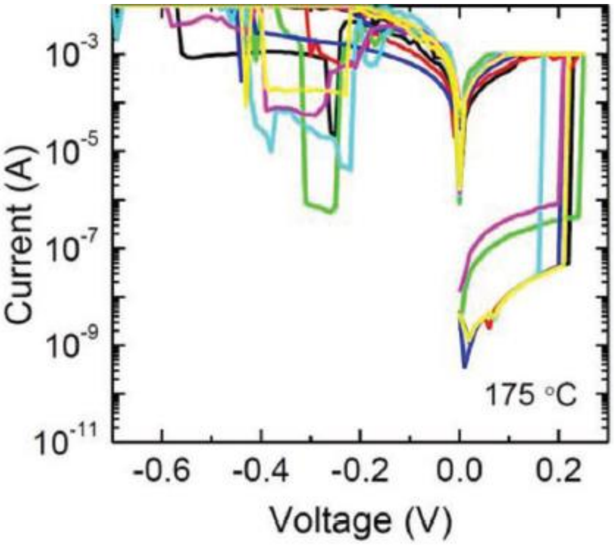

Figure 6.2. First sweep of *I–V* curves measured for seven memory devices (each cell shows different color in *I–V* curve) containing α-FAPbI$_3$ bulk perovskite as the active layer (*Adapted from reference* 7).

Recent reports suggest that the phase retention of the black phase could be achieved in the nanocrystal form. This could be attributed to the presence of capping ligands on the nanocrystal surface, which provides moisture tolerance.[8,9] In this chapter, air stable α- and δ-FAPbI$_3$ nanocrystals were prepared via the hot injection method and studied the phase effect on the memristors characteristics. It should be noted that δ-$FAPbI_3$ is not explored for any applications in any form due to their low dimensionality and insulating nature. The memristors fabricated using a thin layer of α-$FAPbI_3$ nanocrystals showed reproducible and reliable bipolar resistive switching properties, which is contrary to the observation in the corresponding bulk material.[7] It also showed good electrical characteristics such as low voltage operation, long data retention, and good endurance. Based on the detailed studies, we suggest that the switching mechanism is assisted by the rupturing and forming of V_I filaments. Interestingly, the memristors fabricated from δ-$FAPbI_3$ nanocrystals showed better on/off ratio compared to the α-form due to their orientation towards the electrode and low-dimensionality.

6.3. Results and discussion

6.3.A1. Synthesis and characterization of α-$FAPbI_3$ PNCs

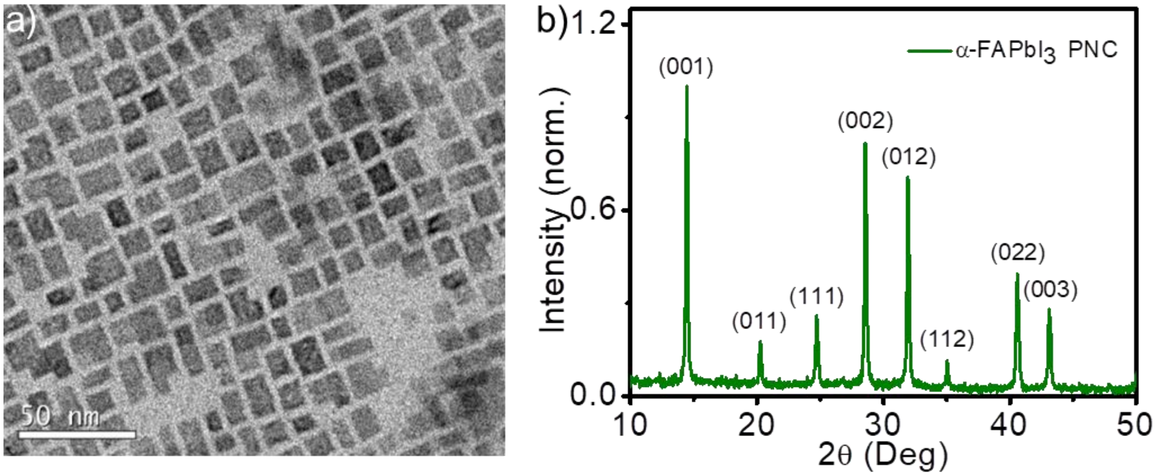

Figure 6.3. a) TEM image of α-$FAPbI_3$ PNCs drop cast from a toluene solution onto the carbon coated Cu grid. b) The XRD pattern of the PNC film coated on a glass substrate.

The α-$FAPbI_3$ PNCs were prepared by a hot injection method reported in the literature and mentioned in **Chapter 4** with some modifications. Details of which are explained in the experimental section. Briefly, formamidium iodide in DMF-oleic acid mixture was injected into a solution containing 1-octadecene, PbI_2, oleic acid, and oleylamine at 80 °C. The obtained PNCs were washed twice with toluene and characterized using TEM, XRD, UV-visible absorption, fluorescence, and lifetime spectroscopy techniques. For TEM measurements, the PNCs dispersed in toluene were drop cast onto a carbon coated copper grid and dried the solvent under vacuum. TEM analysis showed the nanocrystals were rectangular in shape with an average edge length of 9.3 nm (**Figure 6.3a**). XRD analysis showed peaks corresponding to (001), (011), (111), (002), (012), (112), (022) and (003) planes (**Figure 6.3b**) indicating the cubic structure of the nanocrystals.[8] The XRD spectrum also confirmed the absence of any chemical (eg. PbI_2) or phase (δ-$FAPbI_3$) impurities in the material.

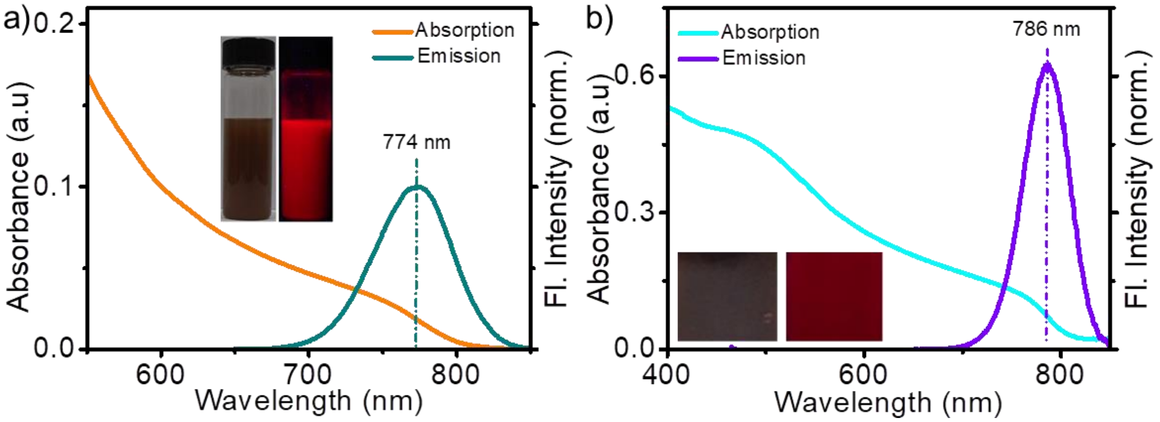

Figure 6.4. UV-vis absorption and emission spectra of α-$FAPbI_3$ PNCs a) dispersed in toluene and b) in film state. Corresponding photographs under room light (left) and UV light (right) are shown in the inset of figure 6.4a

and 6.4b. The PNCs film was obtained by drop casting the colloidal nanocrystals in toluene onto a quartz substrate followed by drying under ambient conditions.

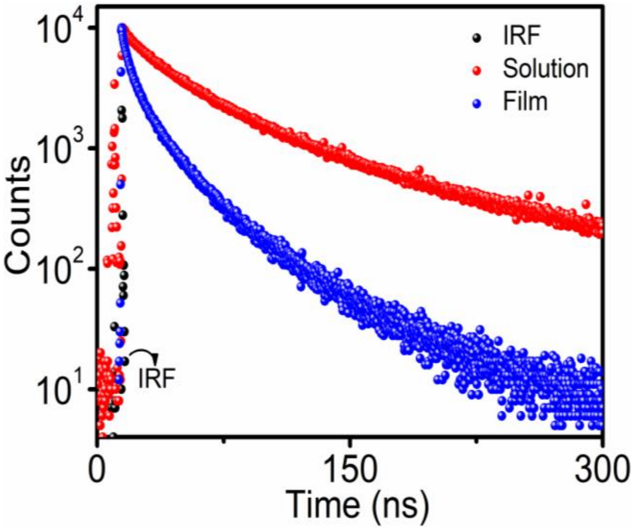

Figure 6.5. Fluorescence decay profiles of α-FAPbI$_3$ PNCs in colloidal (red) and film (blue) states collected at their respective emission maximum (774 nm for the colloidal solution and 786 nm for the film).

The absorption spectrum of both colloidal and film samples showed broad coverage across the UV and visible region (300-800 nm; **Figure 6.4a** and **6.4b**, respectively). The latter was derived from the corresponding reflectance spectra using the Kubelka-Munk function. The calculated bandgap from the absorption was 1.54 eV. The emission spectra of dispersed PNCs in toluene showed a maximum at 774 nm with a narrow FWHM (27 nm). About 12 nm red shift was observed for the emission maximum in the film state (**Figure 6.4b**), which could be attributed to an energy transfer from smaller to larger nanocrystals.[10] The quantum yield in the colloidal state was found to be 54% by the relative method using nile red as the standard. The lifetimes of the colloidal and film states were found to be 67 and 18 ns, respectively

(**Figure 6.5**). The reduced lifetime in the film state further confirmed the energy transfer from smaller to larger PNCs.

6.3.A2. Characterization of memory device

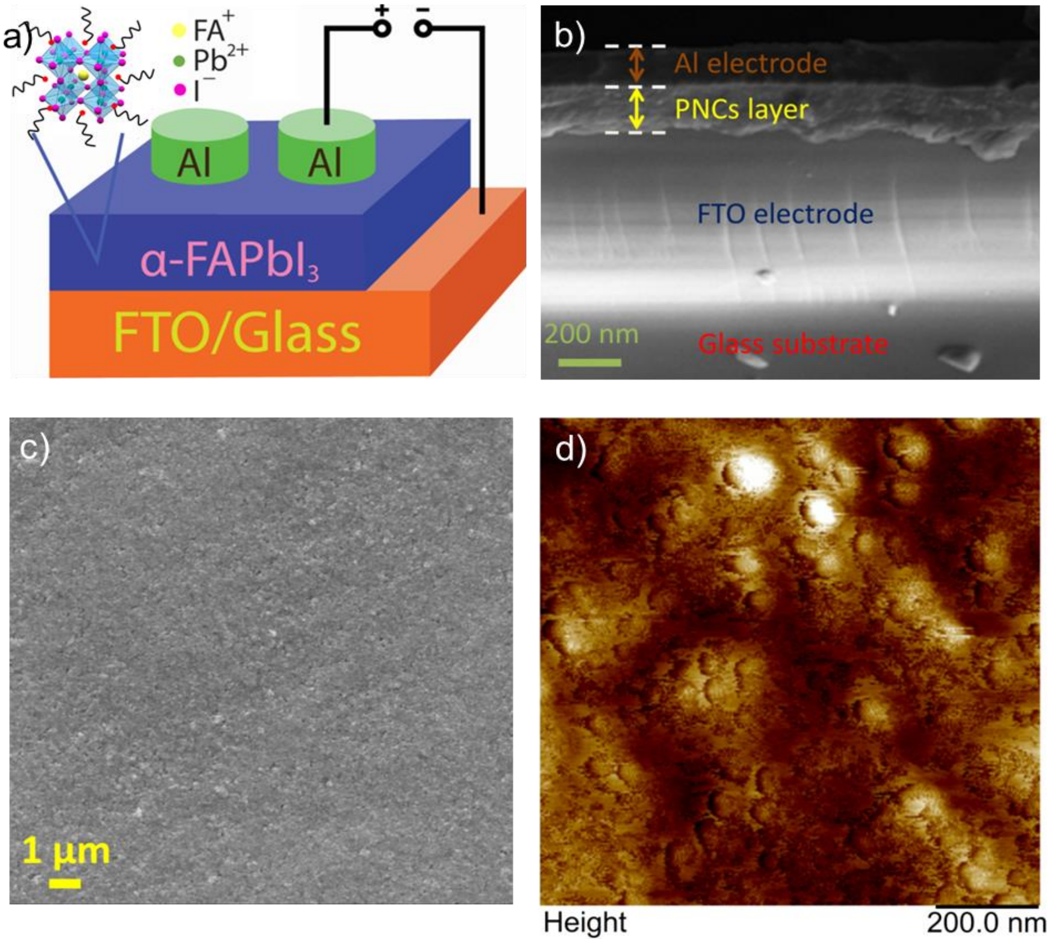

Figure 6.6. a) Schematic diagram and b) Cross-sectional SEM image of the memory device fabricated from *α*-FAPbI$_3$ based PNCs. c) SEM and d) AFM images of *α*-FAPbI$_3$ PNCs film on the FTO substrate.

The memory devices were fabricated using PNCs as the active layer. The nanocrystals were dispersed in toluene via probe sonication for 30 minutes and spin coated on the FTO glass substrate to get a uniform and smooth film with a thickness of around 200 nm. After drying the film at ambient conditions, 200 nm thick Al layer was thermally evaporated onto the film to obtain memory devices with a structure of FTO/PNC/Al. The area of an individual device was 1 mm^2. The schematic representation of the device is shown in **Figure 6.6a** and the cross-sectional SEM image of the device is shown in **Figure 6.6b**. The uniformity of the PNC film on the FTO substrate was evident from the SEM image. The smoothness of the film and absence of pinholes in it were further confirmed from topological SEM and AFM analysis (**Figure 6.6c** and **d**).

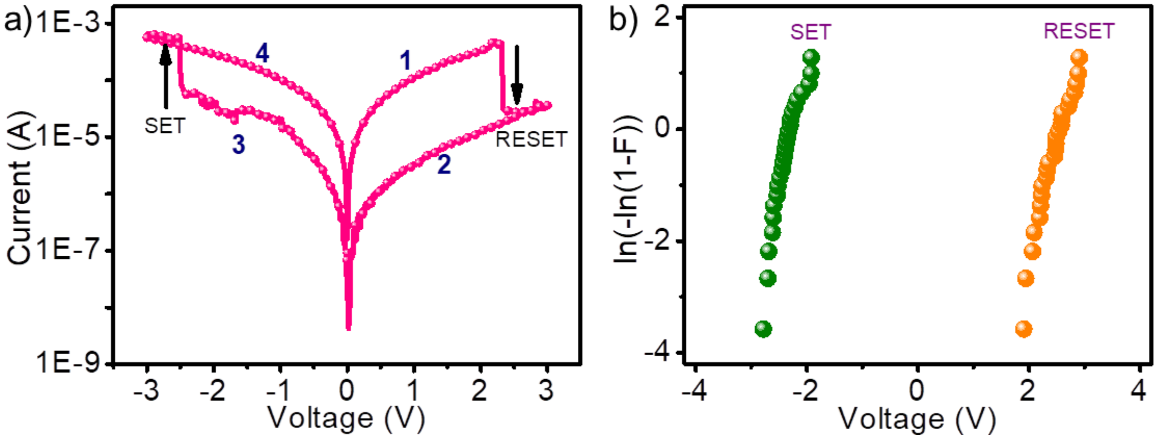

Figure 6.7. a) Representative *I-V* characteristics of the memory device. b) The Weibull distributions of the set and reset voltages obtained from 25 devices.

The *I-V* sweeping of the memristor is shown in **Figure 6.7a**. As the bias voltage was increased to 2.3 V, the device that was initially at the low resistance state (LRS) was switched to the high resistance state (HRS, reset process). The device remained in the HRS until a negative reverse bias voltage was applied. The switching back to the

LRS was observed at -2.4 V (set process). The set and reset processes occur at opposite bias polarities indicating the bipolar resistive switching behavior of the device. The reliability of the devices was confirmed from Weibull distributions of the set and reset voltages measured from 25 devices (**Figure 6.7b**).

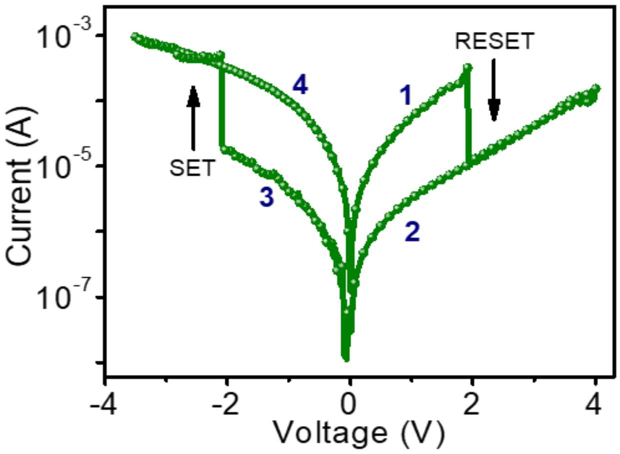

Figure 6.8. Typical current-voltage (*I-V*) characteristics of a memory device with larger voltage sweeps to check unipolar switching behaviour.

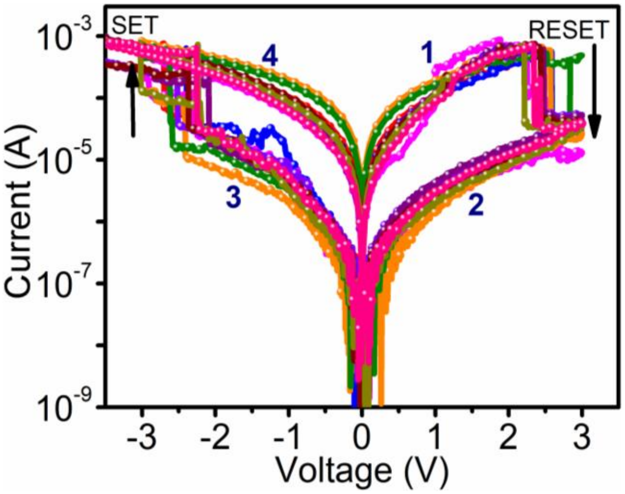

Figure 6.9. The bipolar resistive switching properties of a single memory device measured for ten cycles.

The devices were also tested with larger voltage sweeps, but no unipolar switching behavior was observed (**Figure 6.8**). This bipolar switching behavior was repeated for several cycles to confirm the reproducibility (**Figure 6.9**).

6.3.A3. Resistive switching mechanism

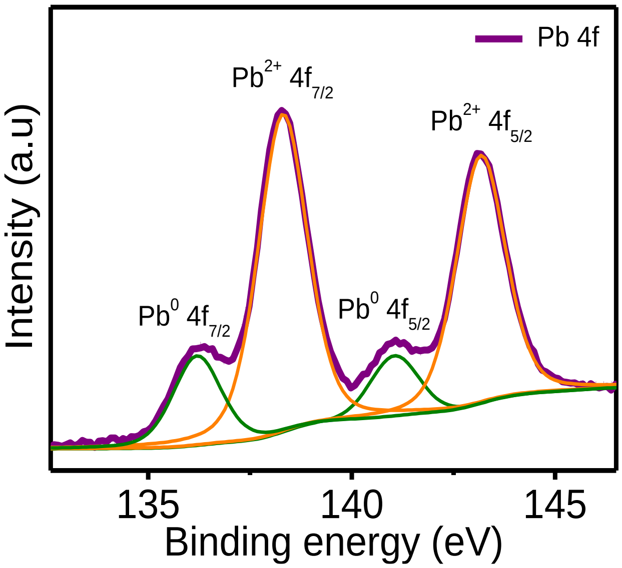

Figure 6.10. Pb 4f XPS spectra of α-FAPbI$_3$ nanocrystals film on the FTO substrate.

The device was initially in the LRS instead of HRS, which is contrary to the observation in most of the bulk perovskite based memory devices.[11-16] This observation implies that the PNCs do not need any electroforming process, and the conducting path is already available without any externally applied voltage. To get a plausible explanation for this observation, X-Ray photoelectron spectroscopy (XPS) analysis of the PNC film was carried out. The XPS spectrum of Pb 4f showed two intense peaks at 138.2 and 143.2 eV corresponding to Pb^{2+} and two low-intense peaks at 136.3 and 141.1 eV, indicating the presence of metallic Pb (**Figure 6.10**). During purification of PNCs, V_I may be generated due to the partial detachment of capping ligands.[17-19] These vacancies can trigger a redox reaction reducing the interstitial Pb^{2+} to metallic Pb. This process is known as 'valence change'[20] and is responsible for observing XPS peaks corresponding to the metallic Pb. An underlying implication of this observation confirms the presence of V_I in the PNC film. In other words, the observed peaks in XPS indicate not only the presence of metallic Pb but also the V_I, which is attributed to the initial LRS of the device. Though metallic Pb is present in the film, the formation and rupturing of conducting channels are exclusively caused by V_I because Pb is difficult to move. During the reset process, the self-formed conducting channels are broken due to the movement of V_I to the bottom electrode. A schematic diagram illustrating set and reset processes are shown in **Figure 6.11**.

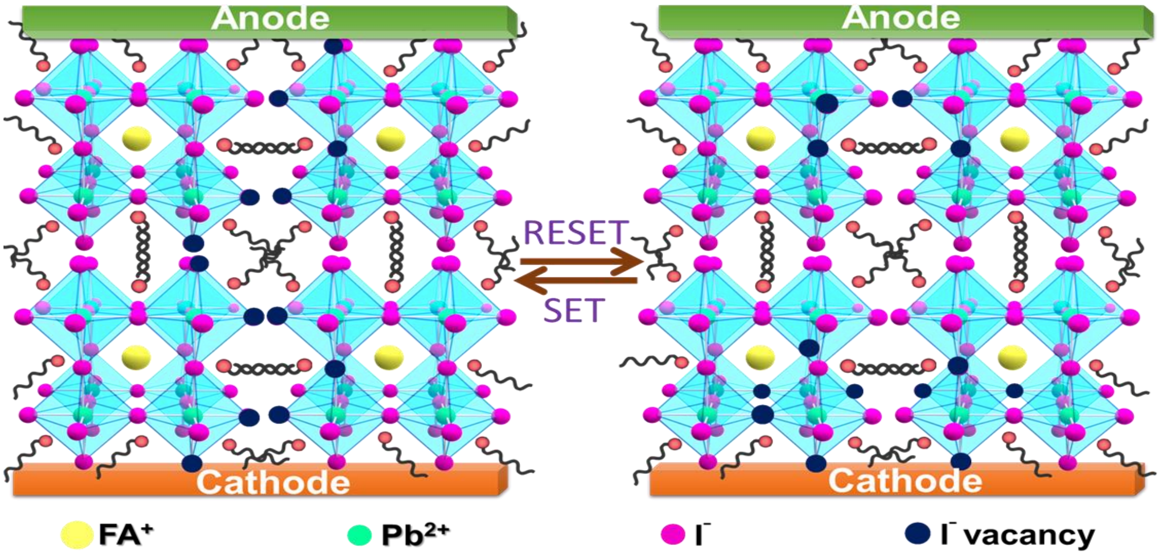

Figure 6.11. Simplified schematic representation of the 'set' and 'reset' processes in the memory devices.

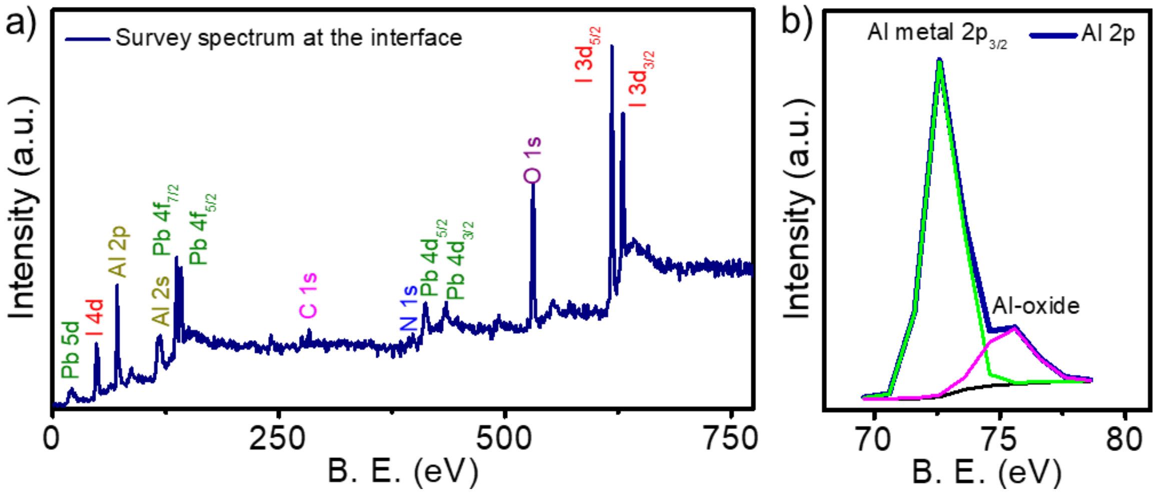

Figure 6.12. a) In-depth XPS survey spectrum of a PNCs based memory device monitored at the interface between PNC layer and aluminum electrode. b) High resolution XPS profile of Al 2p which shows the presence of AlOx at the interface.

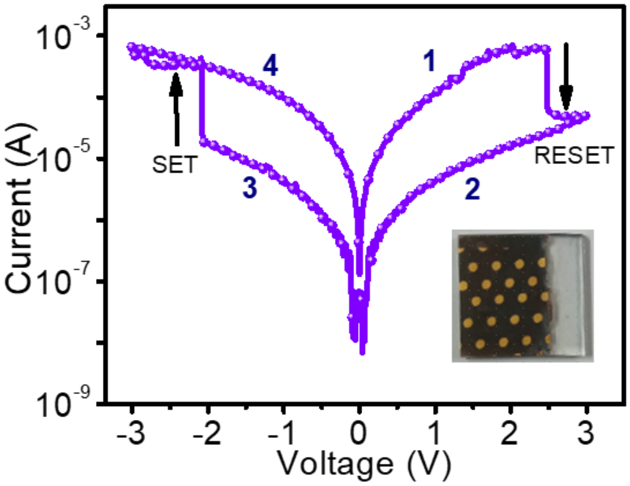

Figure 6.13. Typical current-voltage (*I*-*V*) characteristics of a memory device with a structure of FTO/PNCs/Au.

Since aluminum was used as the top electrode, arguably, there is one more possibility for switching; aluminum is known for the interfacial oxidation (**Figure 6.12**) and has been reported to be one reason for resistive switching.[21,22] In this type of switching, the device will be in ON state initially and go to OFF state on applying the electric field. To rule out the possibility of the aluminum electrode contribution to resistive switching, memory devices with gold as the top electrode was fabricated and characterized (device structure: FTO/PNCs/Au). The typical *I*-*V* characteristics of such a device is shown in **Figure 6.13**, which was similar to that of the aluminum-based devices. This observation confirmed that the aluminum electrode has no role in the resistive switching property of PNCs.

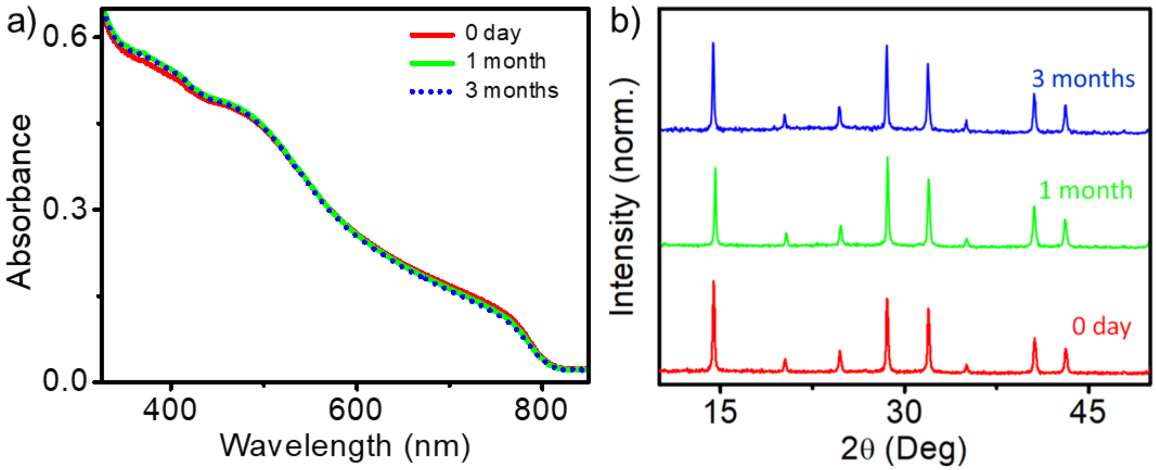

Figure 6.14. a) Absorption and b) XRD spectra of PNCs taken at different time intervals kept under ambient conditions. The changes were negligible, which indicates excellent phase retention behaviour of the PNCs.

Another aspect to rule out is the possibility of the origin of memory effect due to the phase change between perovskite/ nonperovskite phases. Certain perovskites in the bulk form known to exhibit switching between perovskite/ non-perovskite phases and are used to develop memory devices.[23] However, the perovskite material used in the present case is in the form of nanocrystals with hydrophobic capping ligands.

They are highly stable and do not undergo phase changes, as evident from the absorption and XRD spectra (**Figure 6.14**). To prove there is no phase change during the switching of the device from LRS to HRS, we have analyzed the XPS profile of the material in the HRS state (**Figure 6.15**). The XPS profile remained exactly similar to that of the LRS state, which excluded the possibility of phase change based resistive switching mechanism.

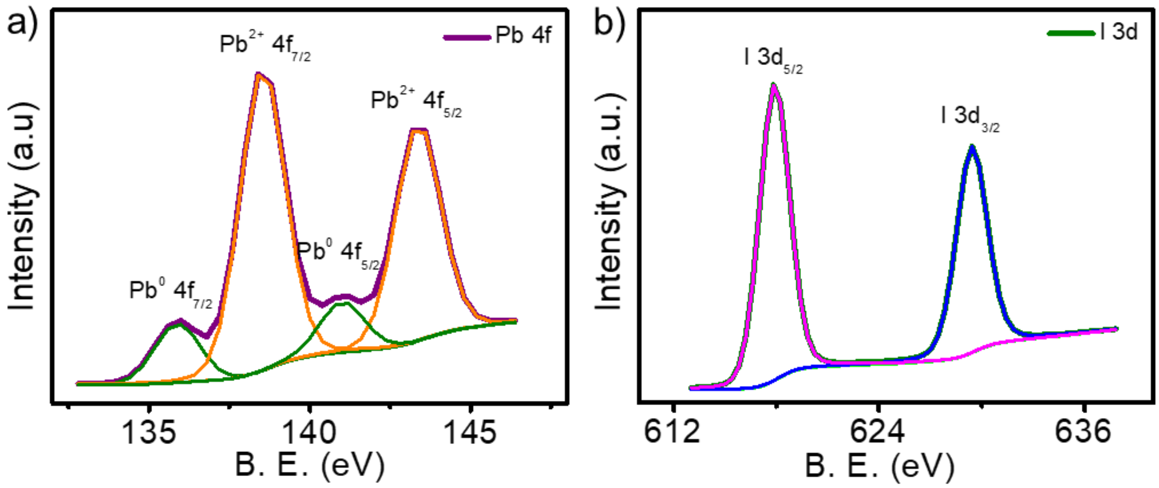

Figure 6.15. XPS profile of PNCs corresponding to a) Pb 4f and b) I 3d measured in the HRS (off state). Absence of both peak shift and formation of new peaks when compared to that of the LRS state confirmed that no change in crystallinity or phase of the nanocrystals occurs during the switching from LRS to HRS state.

The conduction mechanism was investigated by plotting natural logarithmic *I-V* plots corresponding to the SET and RESET processes (**Figure 6.16**). In the SET process, the slopes of HRS at low (green line) and high (blue line) electric fields were different. The slope of ~1 at the low electric field indicates Ohmic conduction. On the other hand, the slope of ~2.7 observed at a high electric field indicates space charge limited current (SCLC) conduction with some contributions from the Poole-Frenkel

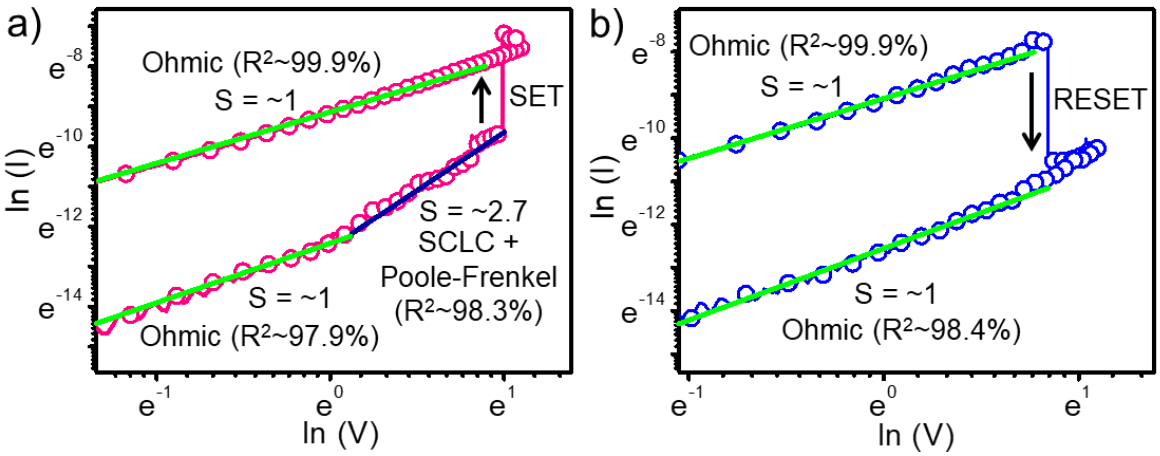

Figure 6.16. Natural logarithmic *I-V* plots corresponding to the a) SET and b) RESET processes of a typical memory device. The slopes of the plots and the conduction mechanisms are indicated inside the graphs. The R^2 values are shown in the inset.

conduction mechanism. Poole-Frenkel charge injection is a trap-assisted conduction mechanism, where the electrons get emitted from traps into the conduction band of the dielectric by thermal excitation. The linear relationship between ln(J/E) and $E^{1/2}$, where J is current density and E is the electric field, is a proof for this mechanism (**Figure 6.17**). This situation remains the same until the applied reverse voltage reaches near -2.4 V, where the SET process occurs. At this point, the current abruptly increased, and the slope changed into Ohmic (green line), resulting in the formation of conducting channels. In the RESET process, the slope of LRS (green line) represents Ohmic conduction, which is in agreement with the LRS mechanism in the SET process. When the applied voltage is near 2.3 V, a sudden decrease in current occurs, and the device switches to HRS due to the disruption of conducting channels, again following Ohmic conduction. This analysis revealed the involved conduction mechanisms are Ohmic, SCLC, and Poole-Frenkel. All of them comes under the bulk-limited conduction mechanisms, which depend on the electrical properties of the dielectric (PNC film) itself and rules out the contribution from electrode assisted interface switching mechanism.[19,24,25]

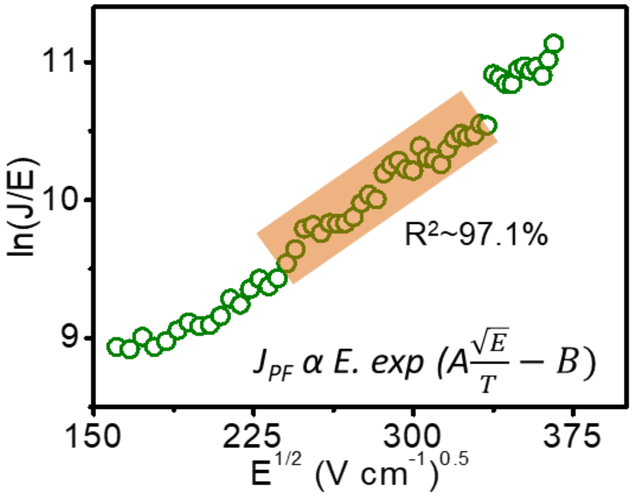

Figure 6.17. Plot of ln(J/E) vs $E^{1/2}$ of the memory devices in an area within the SCLC region shown in Figure 6.16a. The proposed mechanism happens in the highlighted regions. A linear relationship between ln(J/E) and $E^{1/2}$ confirms the Poole-Frenkel conduction mechanism.

6.3.A4. Endurance and retention studies

To demonstrate the potential of the material as a rewritable resistive switching memory device, write-read-erase-read cycling tests (endurance) were carried out. In this experiment, DC voltage pulses were applied consecutively to evaluate the electrical stability at V_{SET} = -3 V and V_{RESET} = 3 V. The reading voltage of the device

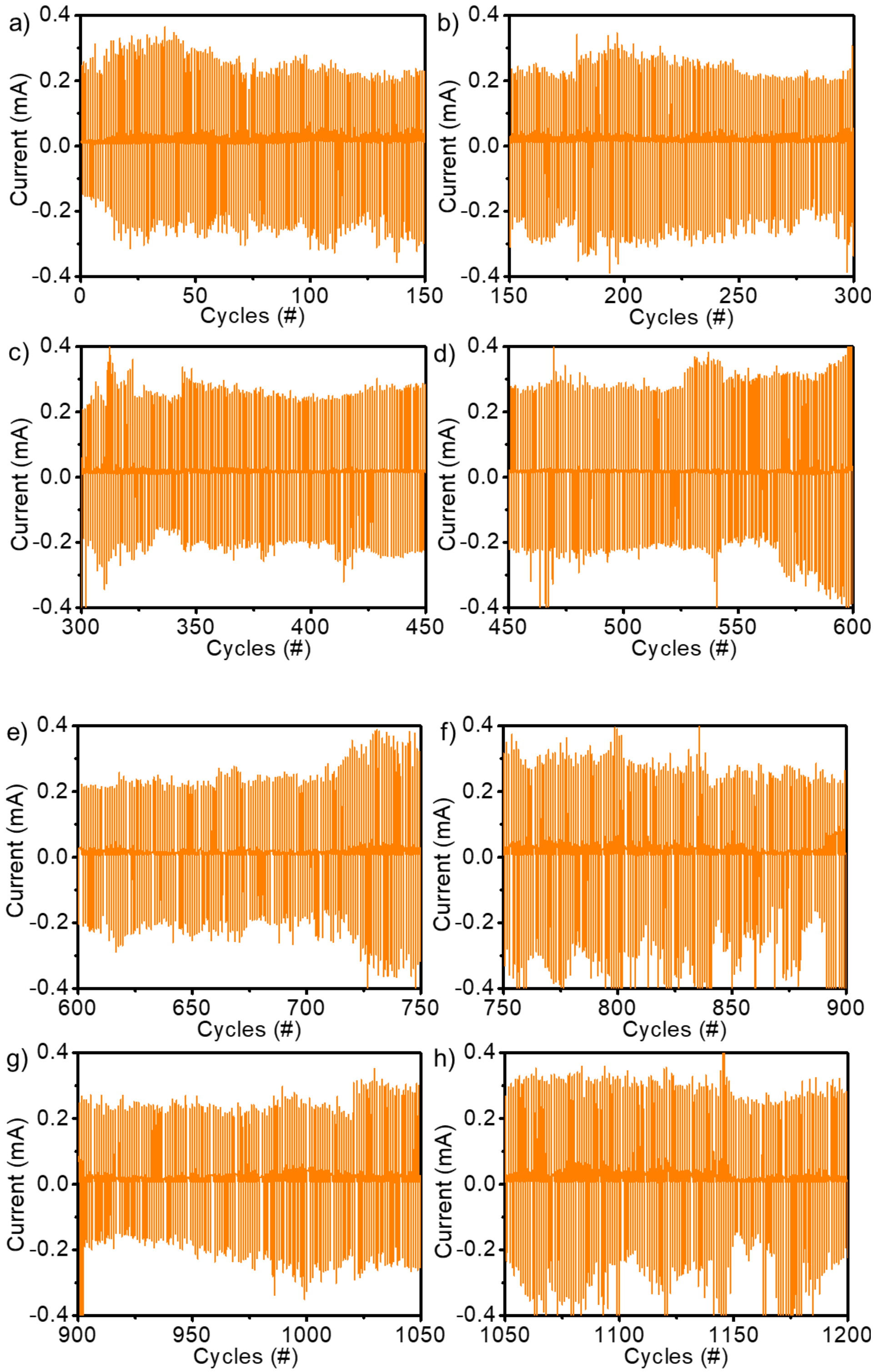

Figure 6.18. Endurance cycling measurements of the device at pulse voltages of -3, 1, and 3V respectively for 1,200 cycles. The graphs are shown in eight windows for clarity, but the measurement data is continuous.

was fixed at 1 V. The endurance was tested for 1,200 cycles (**Figure 6.18**), and the device exhibited stable switching throughout the experiment. First 75 cycles of the endurance analysis is shown in **Figure 6.19a**. The retention performance of the device at room temperature was measured for 1,000 s (**Figure 6.19b**). The on and off-states were measured at 1 V. There was no considerable degradation to the materials in the device in the programmed states even after 1,000 s. The on/off ratio of the devices was found to be 20.

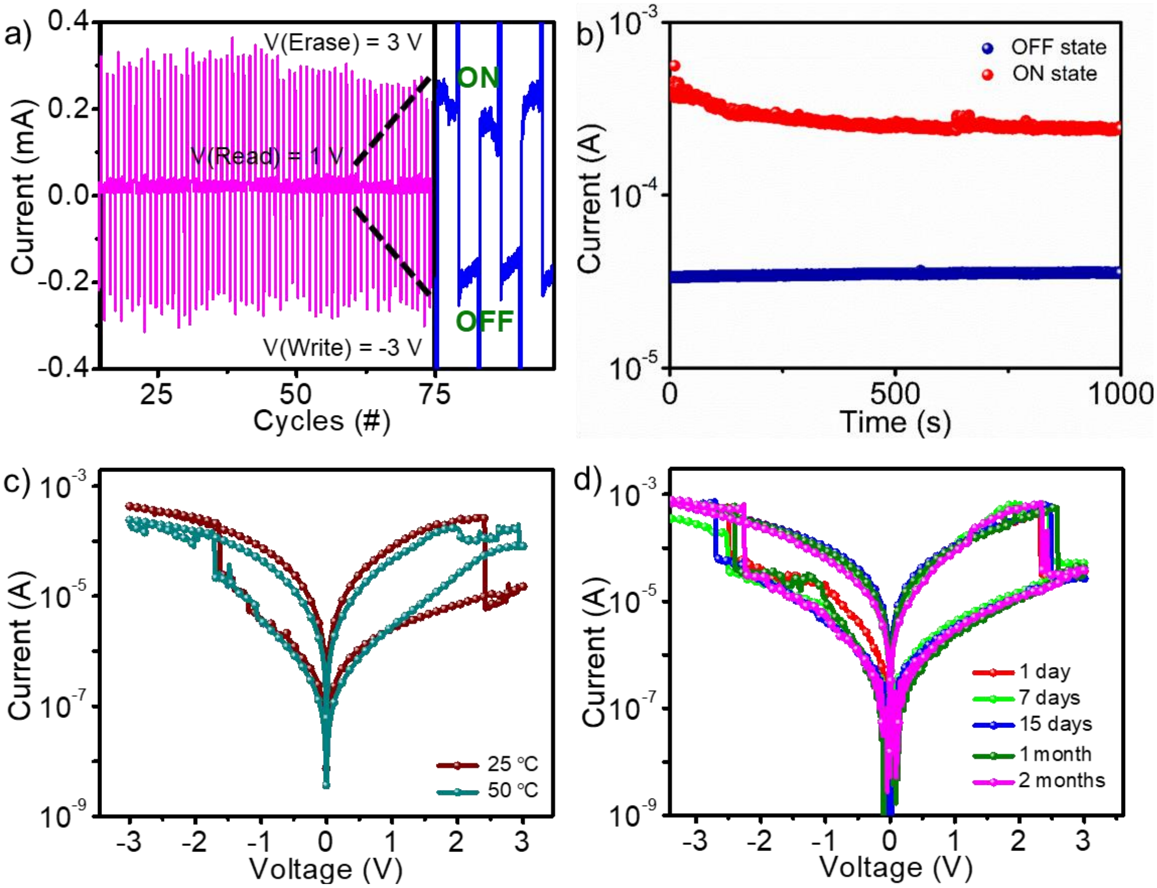

Figure 6.19. a) 75 cycles of the endurance analysis of the devices (writing voltage: -3V, erasing voltage: 3 V, reading voltage: 1 V). Zoomed area of three cycles shown on the right side. b) LRS and HRS as a function of

retention time measured at 1 V. The current-voltage characteristics of a memory device measured at different c) temperatures and d) time.

The stability of the device was monitored at two different temperatures (25 °C and 50 °C) (**Figure 6.19c**). It is observed that the LRS to HRS transition occurs at a slightly earlier voltage, and the off current after setting to HRS is larger at elevated temperatures. This observation indicates that the initial LRS is due to the aggregation of mobile hopping sites, where the temperature assists the diffusion of the iodide vacancies. For any practical applications, devices should be stable for an extended period. Most of the hybrid lead halide perovskite materials are unstable under ambient conditions and require an inert atmosphere for the fabrication and storage of devices. Metal oxides were used as the protective layer for the long-term stability of methylammonium/ cesium lead halide perovskites based memory devices.[26] On the other hand, the PNCs used in this work are highly stable for several months without using any external layer. As a result, they showed similar resistive switching properties even after two months (**Figure 6.19d**).

6.3.A5. Reason for resistive switching in α-$FAPbI_3$ PNCs

As mentioned earlier, α-$FAPbI_3$ perovskite in the bulk form was inactive in the ReRAM devices due to the difficulty in the rupturing of conducting channels formed by V_I.[7] On the other hand, PNCs exhibited excellent resistive switching behavior. A significant difference between the bulk and nanocrystal forms is the presence of capping ligands in the latter. The large bandgap, electronically inactive capping ligands such as oleylammonium and oleate ions used in the present case attached to the surface, could act as an energy barrier between the adjacent nanocrystals (**Figure 6.20**). In other words, the capping ligands reduce the overlapping of energy levels between the neighboring nanocrystals.[27-31] Consequently, though it is difficult to calculate, it could be assumed that the interaction energy between the V_I present in adjacent PNCs will be lowered. As a result, it was possible to rupture the V_I channels formed during the reset process resulting in ReRAM characteristics.

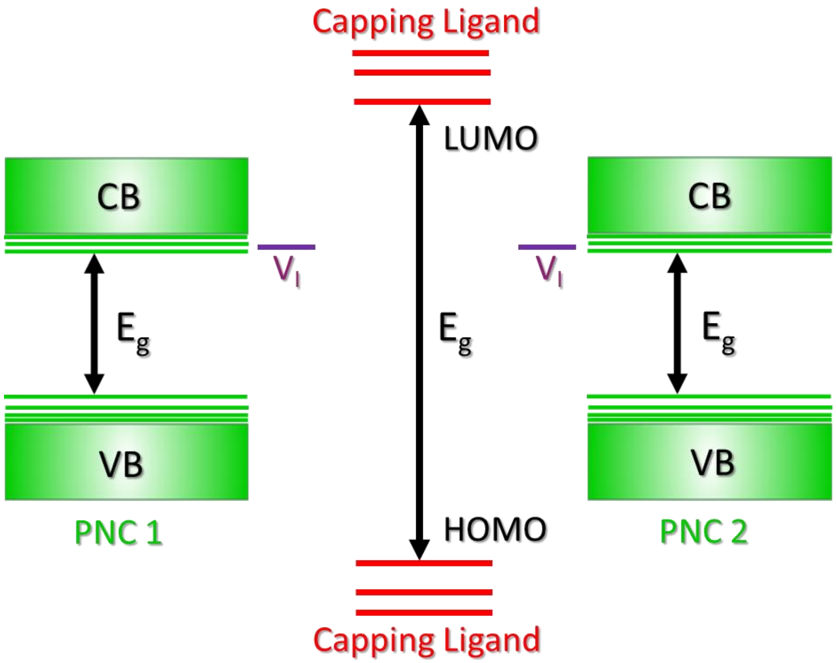

Figure 6.20. Simplified schematic diagram showing the capping ligands acting as an energy barrier between two neighbouring PNCs.

The switching parameters are excellent and on par with many of the hybrid perovskites with a comparable device architecture (**Table 6.1**). The α-FAPbI$_3$ PNCs based devices showed outstanding resistive switching properties compared to bulk perovskites with a comparable device architecture, particularly in terms of endurance and retention properties. Though our device showed low on/off ratio, it could be improved by the incorporation of an insulator layer in the device structure. In addition to that, contrary to the bulk state, the nanocrystal form of α-FAPbI$_3$ has excellent phase retention behavior and high moisture tolerance making them suitable for real-world applications.

Table 6.1. Comparison of the resistive switching properties of α-FAPbI$_3$ PNCs based memory devices (this work) with other PNCs and bulk perovskite devices with a similar device architecture (electrode-perovskite layer-electrode).

S. No	Device structure	Set voltage (V)	Reset voltage (V)	Endurance (cycles)	Retention (time, s)	On/off ratio	Ref
1	FTO/$CH_3NH_3PbBr_{1.97}Cl_{1.03}$ PNCs/Ag (Our previous work)	+0.7	-0.5	250	1000	10^3	32
2	p$^+$-Si/Bulk $MAPbI_3$/Al	-3.15	2.21	200	10000	10^3	33
3	FTO/Bulk $MAPbI_3$/Al	-1.2	1.2	100	-	3.5	34
4	FTO/Bulk $MAPbI_3$/Al	+2.5	-1.4	1000	-	20	35
5	ITO/Bulk $MAPbI_3$/Al	+4.7	-1.3	-	-	100	36
6	ITO/Bulk $CsBi_3I_{10}$/Al	-1.7	0.9	150	10000	1000	37
7	FTO/α-$FAPbI_3$ PNCs/Al	-2.4	+2.3	1200	1000	20	(This work)

6.3.B. δ-FAPbI$_3$ NCs based ReRAM

We have studied the memristor behavior of δ-FAPbI$_3$ based nanocrystals in the following sections of this chapter. The synthesized phase pure hexagonal δ-FAPbI$_3$ NCs possess excellent colloidal stability as in the case of α-FAPbI$_3$ PNCs. However, they undergo self-assembly in the film state resulting in the formation of nanorods (NRs). The NRs were used as the active material for the memory device fabrication. The devices showed excellent resistive switching properties. Due to the low dark current (off state) of the material, higher On/Off ratio (~10^5) observed, which was 4-fold higher than the corresponding α-FAPbI$_3$ PNCs based devices.

6.3.B1. Synthesis and characterization of δ-FAPbI$_3$ NCs

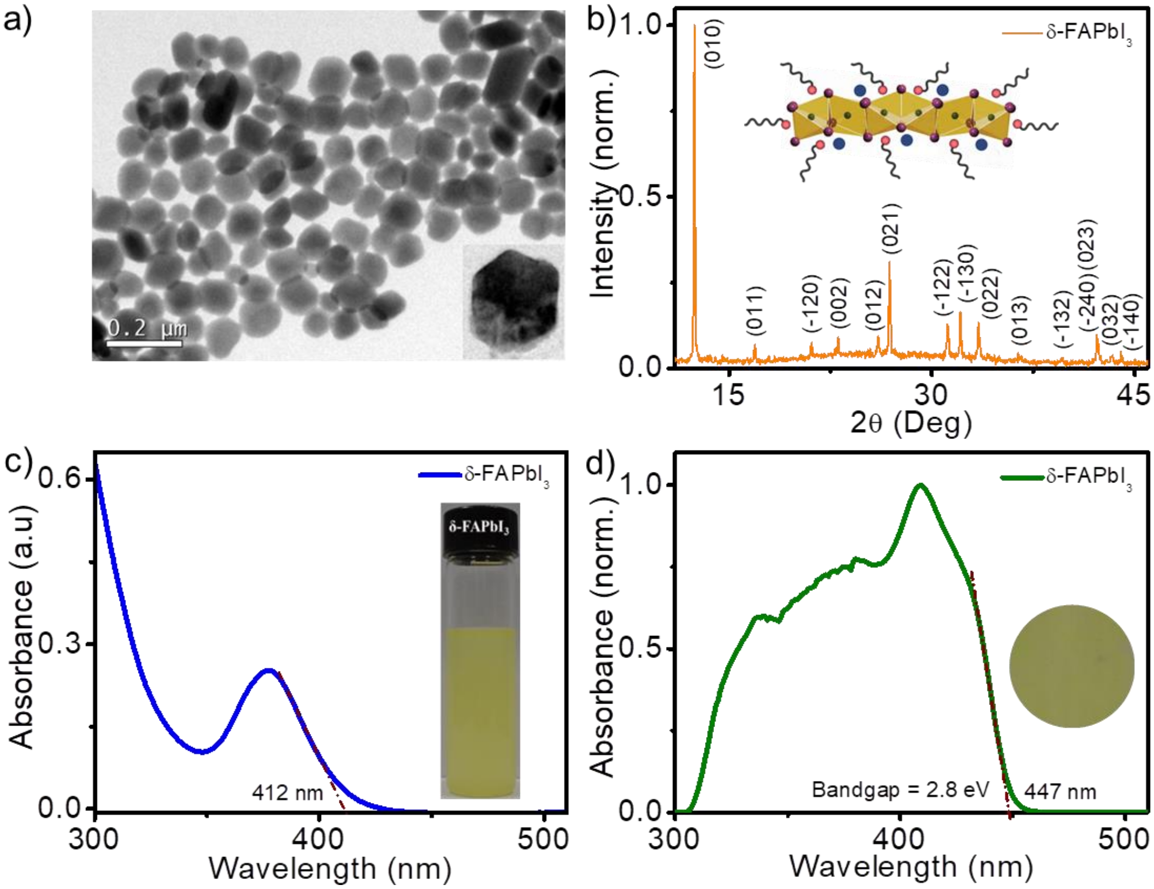

Figure 6.21. a) TEM image of δ-FAPbI$_3$ NCs (average size is 80 nm). The sample was drop cast from toluene onto a carbon coated Cu grid. The inset shows a TEM image of a single NC showing hexagonal structure. b)

XRD spectrum of NCs film. The absorption spectrum of NCs c) dispersed in toluene and d) as film on quartz plate. The corresponding photographs are shown in the insets.

The δ-FAPbI$_3$ NCs were prepared by a hot injection method mentioned in **Chapter 4** with some modifications. Details of which are explained in the experimental section. Briefly, formamidium iodide in DMF-oleic acid mixture was injected into a solution containing 1-octadecene, PbI$_2$, oleic acid and oleylamine at 150 °C. The obtained NCs were characterized by TEM, SEM, XRD, and UV-visible absorption spectroscopy. For TEM measurements, the NCs dispersed in toluene were drop cast onto a carbon coated copper grid and dried the solvent under vacuum. The TEM image showed that the NCs are hexagonal in shape with an average size of 80 nm (**Figure 6.21a**). The peaks obtained from the XRD spectrum (**Figure 6.21b**) of NCs film are identical with their corresponding bulk materials further confirming the hexagonal structure of the NCs.[38] The XRD analysis also showed the chemical and phase purity of NCs (absence of impurities such as PbI$_2$ and α-FAPbI$_3$, respectively). The absorption spectrum of δ-FAPbI$_3$ NCs dispersed in toluene showed absorption up to 425 nm (**Figure 6.21c**), which was blue-shifted when compared to α-FAPbI$_3$ PNCs (**Figure 6.4a**) due to their low dimensionality. The NCs were pale yellow in colour and highly dispersible in toluene due to the presence of capping ligands (inset of **Figure 6.21c)**. The absorption spectrum of NCs film (**Figure 6.21d**) was derived from its reflectance spectrum using the Kubelka-Munk function. The bandgap obtained from the film state absorption was 2.80 eV. The absorption spectrum of the film was 35 nm red-shifted compared to that in the dispersed state which could be attributed to the electronic coupling between the nanocrystals in the film state. The NCs did not show any emission both in the solution and solid-state due to their indirect bandgap nature.[39]

6.3.B2. Self-assembly property of δ-FAPbI$_3$ NCs

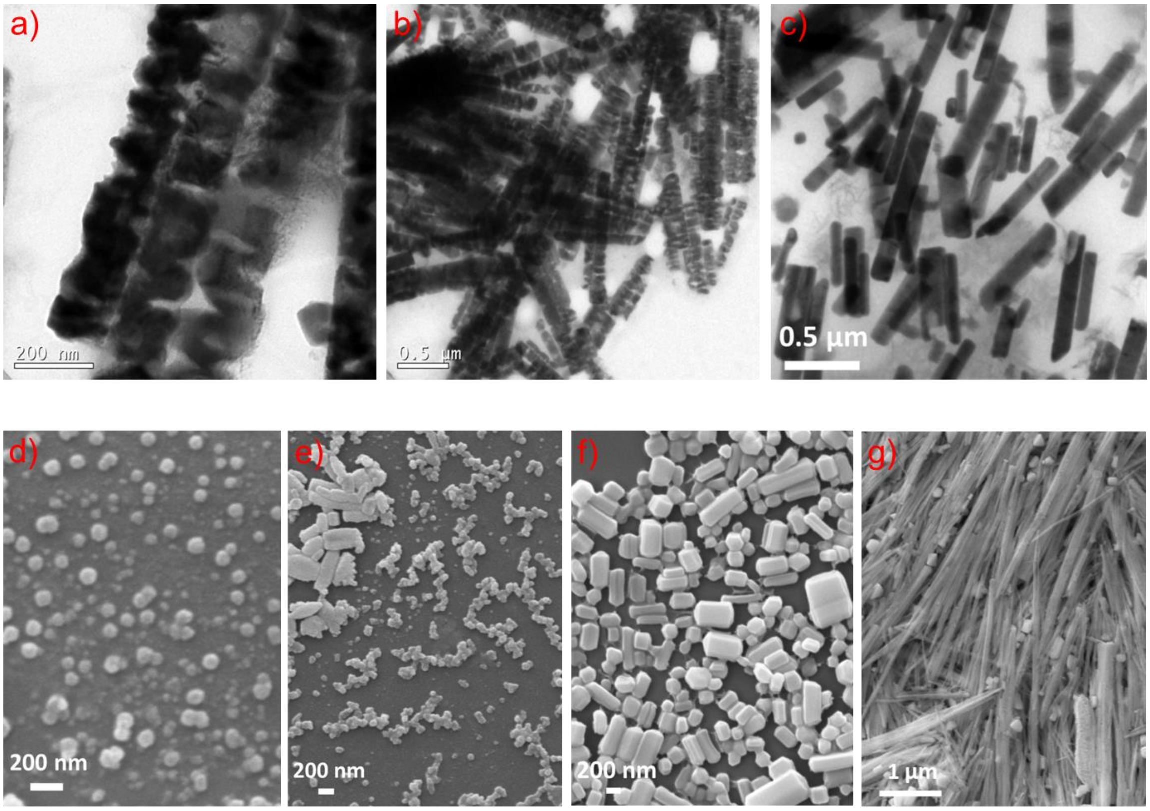

Figure 6.22. a-c) TEM image showing the self-assembly of monodispersed δ-FAPbI$_3$ nanocrystals into nanorods. d-g) The corresponding SEM images.

The NCs were monodispersed in the colloidal state which started to self-assemble in the film state. The self-assembly process of δ-FAPbI$_3$ NCs consists of several hierarchical steps. To elucidate the formation process of NRs, the evolution of the growth reaction at different stages was monitored using HRTEM and SEM (**Figure 6.22**). For this studies, δ-FAPbI$_3$ PNCs dispersed in toluene was drop-cast onto an FTO substrate for SEM analysis and onto a Cu grid for TEM analysis followed by drying the solvent under ambient condition. The NCs were hexagonal in shape at low concentrations (**Figure 6.21a**). With increasing concentration, spontaneous orientation and organization of individual NCs was observed along one direction resulting in NRs (**Figure 6.22**).

The driving force for the spontaneous alignment and fusion of δ-FAPbI$_3$ NCs is believed to be due to the interaction energy between the NC after the partial displacement of capping ligands.[40,41] It is known that ligands are intrinsically mobile and susceptible to detachment from NC surfaces. The solvent efficiently detached the surface ligands, and hence the NCs ultimately fuse together via bare-surface contact to form NRs. Recent report suggests that the binding energy of OAm onto the PNCs surface is much stronger than that of OA. Therefore, OA ligand detaches relatively more easily from the surface of nanocrystals than OAm ligand during the washing period, yielding one directional growth of nanocrystals to form NRs. A 35 nm red shift in the absorption spectrum of δ-FAPbI$_3$ NCs film compared to their colloidal state further confirmed the fusion of monodispersed individual NCs into NRs.

6.3.B3. Characterization of memory device

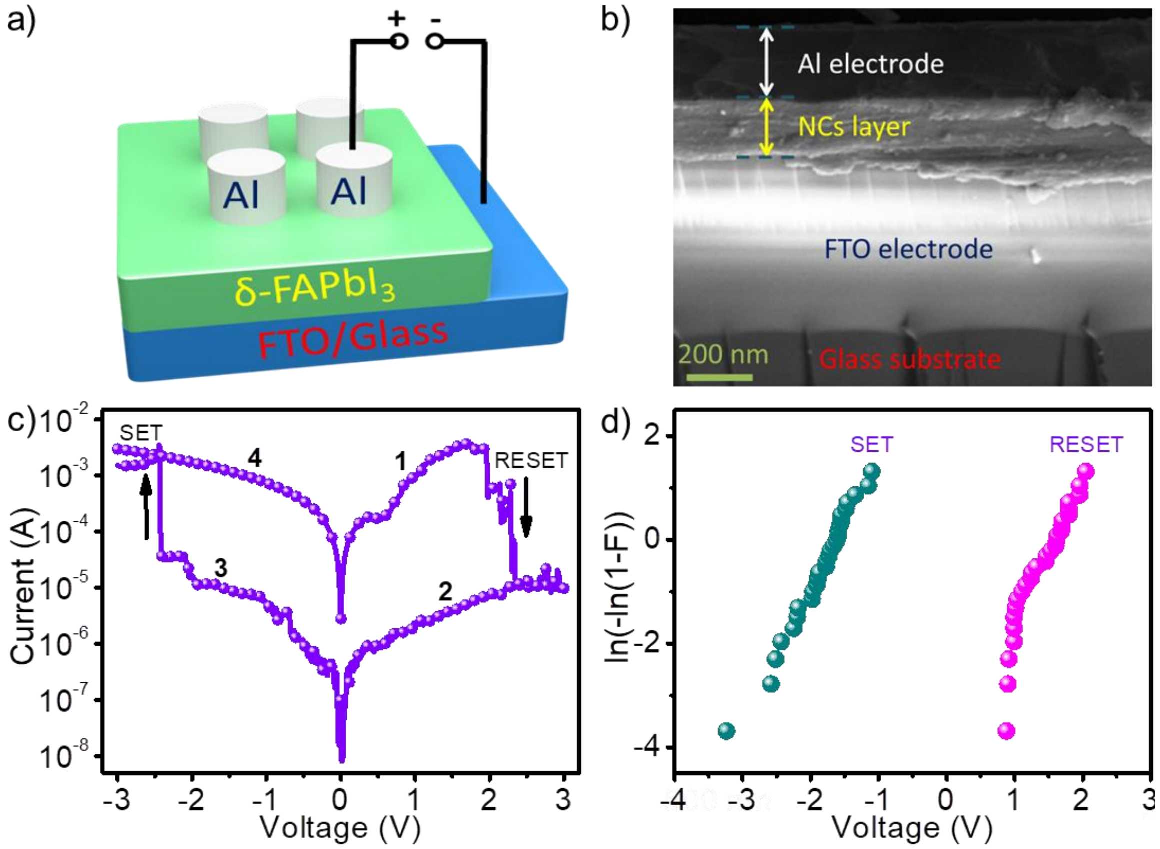

Figure 6.23. a) Schematic representation of δ-FAPbI$_3$ NRs based memory device. b) Cross-sectional SEM image of the FTO/NRs/Al memory device. c) Typical bipolar resistive switching behavior of devices comprising NRs as the switching active media and d) The Weibull distributions of the set and reset voltages measured for 25 devices.

The memory devices were fabricated using δ-FAPbI$_3$ NRs as the active layer. The nanocrystals were dispersed in toluene via probe sonication for 30 minutes and spin coated on the FTO glass substrate to get a uniform and smooth film with a thickness of around 200 nm. After drying the film at ambient conditions, 200 nm thick Al layer was thermally evaporated on to the film to obtain FTO/NRs/Al devices. The area of an individual device was 1 mm^2. The schematic illustration and the cross-sectional SEM image of a memory device are shown in **Figures 6.23a** and **6.23b**, respectively. The electrical characteristics of NRs based ReRAMs were first examined. The characteristic electrical switching of the memory device is shown in **Figure 6.23c**. The *I*-*V* characteristic of the memory device (**Figure 6.23c**) was obtained by applying the bias voltages in the ranges of -3V → 0V → 3V → 0V → -3V onto the Al electrode and grounding the FTO electrode. Initially, the devices were at the LRS which was then turned into the HRS with increasing the bias voltage indicating the occurrence of RESET process. The devices remain in the HRS until a negative reverse bias voltage was applied and then returned to the LRS on applying a reverse bias voltage (SET process). The SET and RESET processes of the devices occur at opposite bias polarities under applied bias voltages indicating the bipolar resistive switching behavior of the devices. The reliability of the memory devices was investigated by plotting the Weibull distributions of the set and reset voltages measured for 25 devices (**Figure 6.23d**) which indicates the reliability of the NRs.

6.3.B4. Resistive switching mechanism

The resistive switching mechanism of memory devices can be explained through the vacancy defect conductive filaments formation. The devices were initially in the LRS, which means that the NRs don’t need any forming process and the conducting filament was already formed in the NRs film without any externally applied voltage as observed in α-$FAPbI_3$ PNCs based ReRAM. Therefore, the conducting filaments initially formed by the iodide vacancies are responsible for the initial LRS. The presence of iodide vacancies are confirmed from the presence of metallic lead in δ-$FAPbI_3$ NRs (**Figure 6.24**). The self-formed conducting filament is ruptured due to the movement of iodide vacancies to the bottom electrode and heat generated by the current flow (HRS).

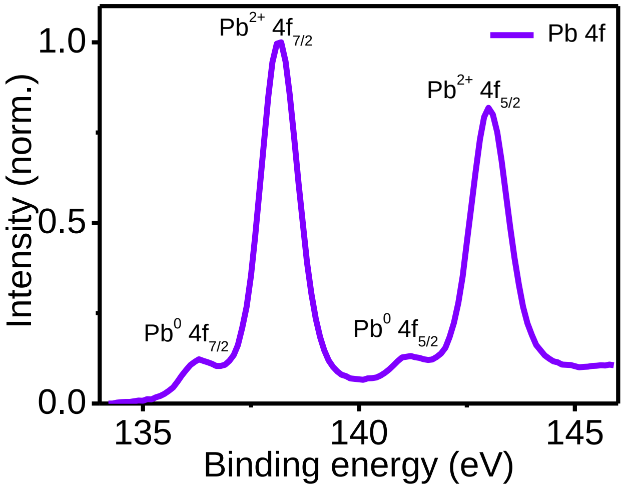

Figure 6.24. Pb 4f XPS spectra of δ-$FAPbI_3$ nanocrystals film on the FTO substrate.

The conduction mechanism was investigated by plotting natural logarithmic *I*-*V* plots corresponding to the SET and RESET processes (**Figure 6.25**). In the SET process, the slopes of HRS at low (green line) and high (blue line) electric fields were different: Ohmic conduction at low electric field and SCLC conduction with some contributions from the Poole-Frenkel conduction at a high electric field. The linear relationship between $\ln(J/E)$ and $E^{1/2}$ is a proof for Poole-Frenkel conduction (**Figure**

6.26). This situation remains the same until the applied voltage reaches near -2.5 V, where the SET process occurs. At this point, the current abruptly increased, and the slope changed into Ohmic (green line), resulting in the formation of conducting channels. In the RESET process, the slope of LRS (green line) represents Ohmic conduction, which is in agreement with the LRS mechanism in the SET process. When the applied voltage is near 1.9 V, a sudden decrease in current occurs, and the device switches to HRS due to the disruption of conducting channels, again following Ohmic conduction. This analysis revealed that the involved conduction mechanisms are Ohmic, SCLC, and Poole-Frenkel. All of them come under the bulk-limited conduction mechanisms, which depend on the electrical properties of the dielectric (NRs film) itself.

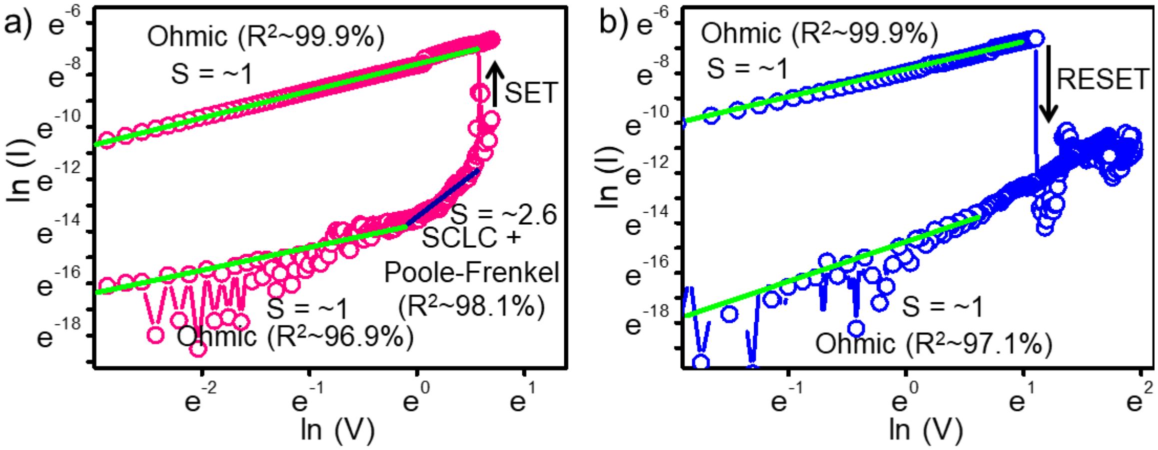

Figure 6.25. Natural logarithmic *I-V* plots corresponding to the a) SET and b) RESET processes of a typical memory device. The slopes of the plots and the conduction mechanisms are indicated inside the graphs. The R^2 values are shown in the inset.

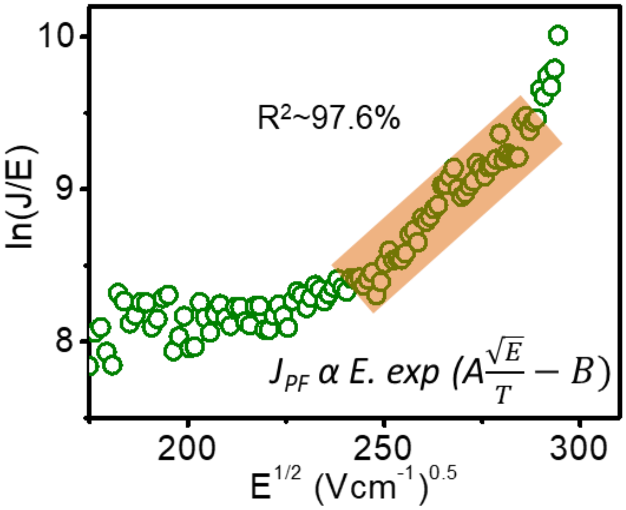

Figure 6.26. Plot of ln(J/E) vs $E^{1/2}$ of the memory devices in an area within the SCLC region shown in Figure 6.25a. The proposed mechanism happens in the highlighted regions.

6.3.B5. Endurance and retention studies

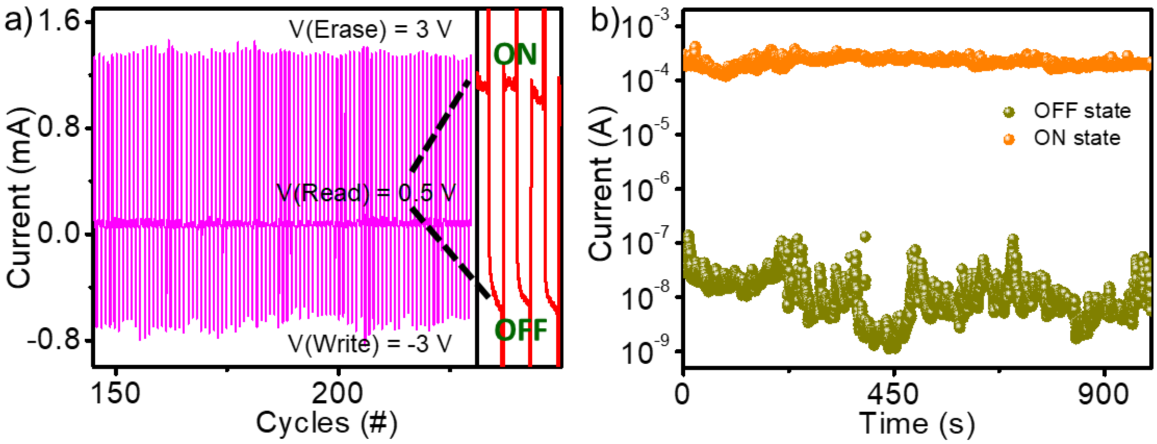

Figure 6.27. a) 250 cycles of the endurance analysis of the devices (writing voltage: -3V, erasing voltage: 3 V, reading voltage: 0.5 V). Zoomed area of three cycles is shown on the right side. b) The retention properties of the devices where the off and on states were measured at 1 V.

The 250 cycles of write-read-erase processes (**Figure 6.27a**) were carried out to demonstrate the potential of FTO/NRs/Al device for practical applications. In this experiment, consecutive DC voltage pulses were applied to evaluate the electrical stability under V_{SET} = -3 V and V_{RESET} = -3 V. The reading voltage of the device was fixed at 0.5 V and the devices exhibited stable resistive switching even after 250 cycles. The retention performance of the device at room temperature measured for 1000s is shown in **Figure 6.27b**. The on-state and off-states were measured at 1 V. There was no considerable degradation of the materials in the devices in the programmed states even after 1000 s. The on/off ratio of the devices was found to be ~10^5. The minimum current detection of the used instrument was 10^{-8}-10^{-9} A, otherwise the on/off ratio would be higher than 10^5. The high on/off ratio of the current device compared to α-$FAPbI_3$ PNCs based memristor was attributed to the low off-state current (dark current) of δ-$FAPbI_3$ NRs.

In order to find out the reason for the low off-state current of NRs, the orientation of NRs onto the FTO substrate was monitored using SEM analysis. The cross-sectional SEM image of NRs coated onto the FTO substrate confirmed their parallel orientation to the FTO substrate (**Figure 6.28a**). The thickness of NRs film was somewhat high compared to the memory device for the better clarity of their orientation. The SEM image of NRs film morphology in the memory device (**Figure 6.28b**) and its zoomed image (**Figure 6.28c**) further confirmed the parallel orientation of NRs towards the FTO substrate. The NRs are also one dimensional in nature. Therefore, the orientation of NRs and their low dimensionality must be the reason for low off-state current.

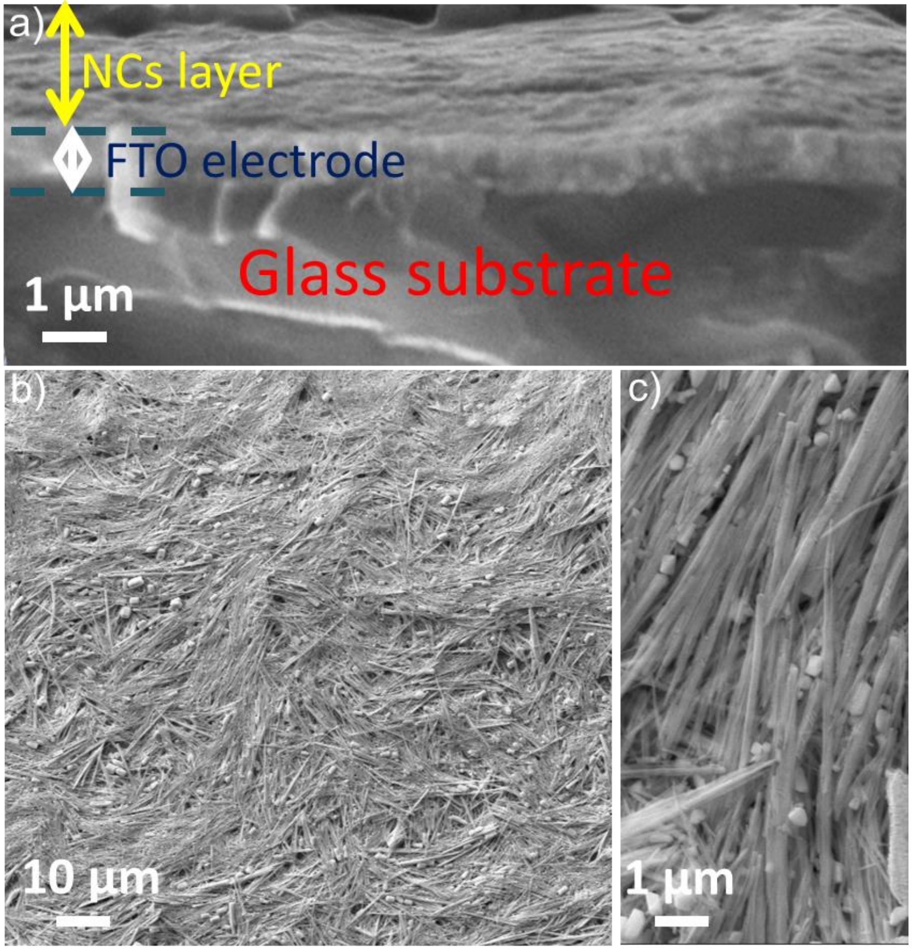

Figure 6.28. a) Cross-sectional SEM image of δ-FAPbI$_3$ NRs coated onto the FTO substrate. b) The SEM topography image of δ-FAPbI$_3$ NRs film in the memory device and c) the corresponding zoomed image.

The long-term stability of the devices is also important for practical applications. However, the stability of most of the above-mentioned devices was not studied. The NRs used in the present work showed an excellent environmental stability as evident from the comparison of the XRD profiles of one-year old sample with that of a freshly prepared one (**Figure 6.29**). The δ-FAPbI$_3$ NCs are formed through face sharing of PbI_6^{4-} octahedras which must be the reason for high stability of δ-FAPbI$_3$ NRs. As a result, the current devices were found to be stable even after extended period of time (**Figure 6.30**).

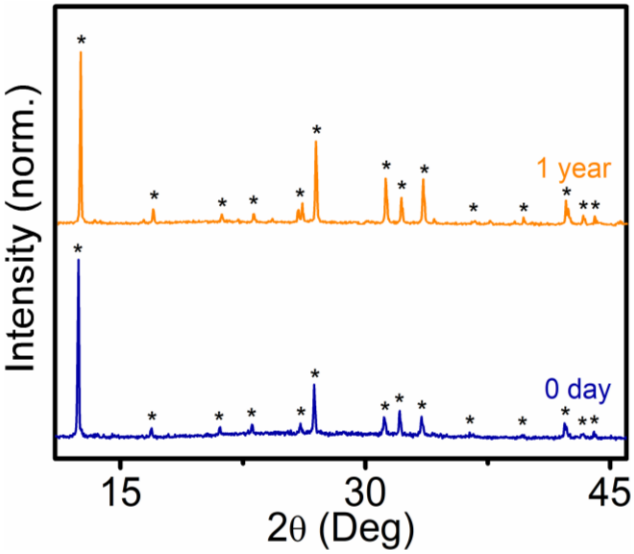

Figure 6.29. Comparison of the XRD profiles of one-year old δ-$FAPbI_3$ NRs sample with that of a freshly prepared one.

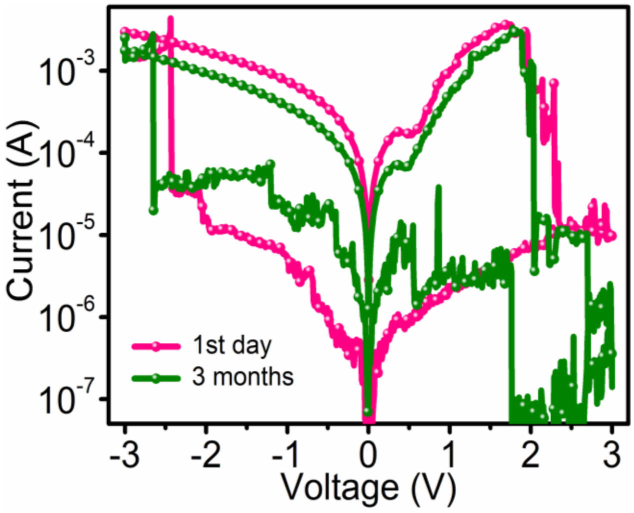

Figure 6.30. Typical *I-V* characteristics of δ-$FAPbI_3$ NRs based memristors measured on the first day and after three months. The NRs showed almost similar switching properties even after 3 months.

Finally, the resistive switching property of black phase α-$FAPbI_3$ PNCs was compared with that of yellow phase δ-$FAPbI_3$ NRs. Both materials possess good environmental stability and solution processability due to the presence of hydrophobic capping ligands which provided long-term stability to the devices too. Both devices showed almost similar performances in terms of operation voltage, switching mechanism, retention, and endurance performance. However, δ-$FAPbI_3$ NRs based devices showed better on/off ratio (4-fold higher) compared to the α-form due to the parallel orientation of NRs towards FTO substrate and their low dimensionality. The detailed studies proved that δ-$FAPbI_3$ NRs based memristor is the best one due to their high on/off ratio which would be helpful to store a large quantity of information.

6.4. Conclusions

In conclusion, the phase effect on the memristor characteristics of $FAPbI_3$ NCs was studied in detail. Black phase α-$FAPbI_3$ PNCs were prepared by a single step hot injection method using hydrophobic oleylamine as the capping agent. Unlike bulk α-$FAPbI_3$ perovskite materials, the memory devices fabricated using the nanocrystals showed bipolar resistive switching properties. This was attributed to the low interaction energy between iodide vacancies and the resulting rupture filaments formed by these iodide vacancies during the RESET process. The yellow phase δ-$FAPbI_3$ NRs were prepared from the self-assembly of their corresponding individual NCs for the ReRAM application. The δ-$FAPbI_3$ NRs based memory devices showed low resistive switching voltages, good endurance, and retention properties similar to α-$FAPbI_3$ PNCs. However, the later one showed a high on/off ratio due to its low dark current which was attributed to the parallel orientation of NRs with respect to the FTO substrate and low dimensionality of δ-form.

6.5. Experimental section

6.5.1. Synthesis of α-$FAPbI_3$ PNCs

87 mg of PbI_2 (0.187 mmol) was added into 5 mL of 1-octadecene taken in a 20 mL Schlenk tube and heated to 150 °C for about 15 minutes under vacuum. 0.35 mL of oleylamine and 0.7 mL of oleic acid were injected one by one into the above mixture under nitrogen atmosphere. Then, the mixture was left until the complete solubilization of lead iodide. After that, 80 mg of formamidinium iodide (0.465 mmol) dissolved in 100 µL of DMF and 0.8 mL oleic acid was quickly injected into the lead iodide solution at 80 °C. Finally, the PNCs were centrifuged at 12,000 rpm for 5 minutes. The obtained PNCs were washed twice with toluene and finally dispersed in toluene for further studies.

6.5.2. Synthesis of δ-$FAPbI_3$ nanocrystals

5 mL of 1-octadecene was heated to 150 °C under vacuum and 87 mg of PbI_2 (0.187 mmol) was added to it. Then, 0.8 mL of oleic acid and 0.35 mL of oleylamine were added to 1-octadecene separately in an inert atmosphere and heated the mixture until complete solubilization of lead iodide. Formamidinium iodide (58.3 mg, 0.339

m.mol) dissolved in 100 µL of DMF and 0.8 mL of oleic acid was injected into the solution resulting in the precipitation of NCs. Finally, the obtained NCs were separated by centrifugation at 12,000 rpm for 10 minutes and washed thrice with toluene.

6.5.3. Fabrication of memory devices

The α-$FAPbI_3$ PNCs stock solution (10mg/mL) was prepared by dispersing the nanocrystals in toluene via probe-sonication for 10 minutes. Subsequently, the solution was spin-coated onto a FTO substrate at 2000 rpm for 60s. The spin-coating was repeated for three more times to obtain a thickness of around 200 nm. After vacuum drying the film, 200 nm thick aluminium was thermally evaporated on the perovskite layer using a shadow mask to form FTO/α-$FAPbI_3$ PNCs/Al devices. Same procedure was used for δ-$FAPbI_3$ NCs also.

6.6. References

1. G. E. Eperon, S. D. Stranks, C. Menelaou, M. B. Johnston, L. M. Herz, H. J. Snaith, *Energy Environ. Sci.* **2014**, *7*, 982-988.
2. N. Pellet, P. Gao, G. Gregori, T. Y. Yang, M. K. Nazeeruddin, J. Maier, M. Grätzel, *Angew. Chem., Int. Ed*. **2014**, *53*, 3151-3157.
3. J.-W. Lee, S. H. Lee, H.-S. Ko, J. Kwon, J. H. Park, S. M. Kang, N. Ahn, M. Choi, J. K. Kim, N.-G. Park, *J. Mater. Chem. A* **2015**, *3*, 9179-9186.
4. Y. Zhou, J. Kwun, H. F. Garces, S. Pang, N. P. Padture, *Chem. Commun*. **2016**, *52*, 7273-7275.

5. A. Binek, F. C. Hanusch, P. Docampo, T. Bein, *J. Phys. Chem. Lett*. **2015**, *6*, 1249-1253.
6. O. Nazarenko, S. Yakunin, V. Morad, I. Cherniukh, M. V. Kovalenko, *NPG Asia Mater*. **2017**, *9*, e373.
7. J.-M. Yang, S.-G. Kim, J.-Y. Seo, C. Cuhadar, D.-Y. Son, D. Lee, N.-G. Park, *Adv. Electron. Mater*. **2018**, *4*, 1800190 (1-9).
8. L. Protesescu, S. Yakunin, S. Kumar, J. Bär, F. Bertolotti, N. Masciocchi, A. Guagliardi, M. Grotevent, I. Shorubalko, M. I. Bodnarchuk, C.-J. Shih, M. V. Kovalenko, *ACS Nano* **2017**, *11*, 3119-3134.
9. P. Papagiorgis, A. Manoli, L. Protesescu, C. Achilleos, M. Violaris, K. Nicolaides, T. Trypiniotis, M. I. Bodnarchuk, M. V. Kovalenko, A. Othonos, G. Itskos, *ACS Photonics* **2018**, *5*, 907-917.
10. C. D. Weerd, L. Gomez, H. Zhang, W. J. Buma, G. Nedelcu, M. V. Kovalenko, T. Gregorkiewicz, *J. Phys. Chem. C* **2016**, *120*, 13310-13315.
11. J. Choi, S. Park, J. Lee, K. Hong, D.-H. Kim, C. W. Moon, G. D. Park, J. Suh, J. Hwang, S. Y. Kim, H. S. Jung, N.-G. Park, S. Han, K. T. Nam, H. W. Jang, *Adv. Mater*. **2016**, *28*, 6562-6567.
12. K. Yan, B. Chen, H. Hu, S. Chen, B. Dong, X. Gao, X. Xiao, J. Zhou, D. Zou, *Adv. Electron. Mater*. **2016**, *2*, 1600160.
13. J.-Y. Chen, Y.-C. Chiu, Y.-T. Li, C.-C. Chueh, W.-C. Chen, *Adv. Mater*. **2017**, *29*, 1702217.
14. J.-Y. Seo, J. Choi, H.-S. Kim, J. Kim, J.-M. Yang, C. Cuhadar, J. S. Han, S.-J. Kim, D. Lee, H. W. Jang, N.-G. Park, *Nanoscale* **2017**, *9*, 15278-15285.
15. Z. Hong, J. Zhao, K. Huang, B. Cheng, Y. Xiaoa, S. Lei, *J. Mater. Chem. C* **2019**, *7*, 4259-4266.
16. F. Zhou, Y. Liu, X. Shen, M. Wang, F. Yuan, Y. Chai, *Adv. Funct. Mater*. **2018**, *28*, 1800080.

17. Q. A. Akkerman, G. Rainò, M. V. Kovalenko, L. Manna, *Nat. Mater*. **2018**, *17*, 394-405.
18. P. Liu, W. Chen, W. Wang, B. Xu, D. Wu, J. Hao, W. Cao, F. Fang, Y. Li, Y. Zeng, R. Pan, S. Chen, W. Cao, X. W. Sun, K. Wang, *Chem. Mater*. **2017**, *29*, 5168-5173.
19. A. Pan, J. Wang, M. J. Jurow, M. Jia, Y. Liu, Y. Wu, Y. Zhang, L. He, Y. Liu, *Chem. Mater*. **2018**, *30*, 2771-2780.
20. J.-M. Yang, E.-S. Choi, S.-Y. Kim, J.-H. Kim, J.-H. Park, N.-G. Park, *Nanoscale* **2019**, *11*, 6453-6461.
21. S. Z. Rahaman, S. Maikap, *Nanoscale Res. Lett*. **2013**, *8*:509.
22. V. J. Manjunath, A. Rush, A. Barua, R. Jha, *Solid State Electron. Lett*. **2019**, *1*, 52-57.
23. C. Zou, J. Zheng, C. Chang, A. Majumdar, L. Y. Lin, *Adv. Optical Mater*. **2019**, *7*, 1900558.
24. F.-C. Chiu, *Adv. Mater. Sci. Eng*. **2014**, 578168.
25. D. J. Kim, Y. J. Tak, W.-G. Kim, J. K. Kim, J. H. Kim, H. J. Kim, *Adv. Mater. Interfaces* **2017**, *4*, 1601035.
26. Y. Wu, Y. Wei, Y. Huang, F. Cao, D. Yu, X. Li, H. Zeng, *Nano Research* **2017**, *10*, 1584-1594.
27. A. J. Knight, L. M. Herz, *Energy Environ. Sci*. **2020**, *13*, 2024-2026.
28. S. G. Motti, F. Krieg, A. J. Ramadan, J. B. Patel, H. J. Snaith, M. V. Kovalenko, M. B. Johnston, Laura M. Herz, *Adv. Funct.Mater.* **2020**, *30*, 1909904.
29. E. T. Vickers, E. E. Enlow, W. G. Delmas, A. C. DiBenedetto, A. H. Chowdhury, B. Bahrami, B. W. Dreskin, T. A. Graham, I. N. Hernandez, S. A. Carter, S. Ghosh, Q. Qiao, J. Z. Zhang, *ACS Energy Lett*. **2020**, *5*, 817-825.
30. J. Dai, J. Xi, L. Li, J. Zhao, Y. Shi, W. Zhang, C. Ran, B. Jiao, X. Hou, X. Duan, *et al*. *Angew. Chem., Int. Ed*. **2018**, *57*, 5754-5758.

31. E. T. Vickers, T. A. Graham, A. H. Chowdhury, B. Bahrami, B. W. Dreskin, S. Lindley, S. B. Naghadeh, Q. Qiao, J. Z. Zhang, *ACS Energy Lett*. **2018**, *3*, 2931-2939.
32. C. Muthu, S. Agarwal, A. Vijayan, P. Hazra, K. B. Jinesh, V. C. Nair, *Adv. Mater. Interfaces* **2016**, *3*, 1600092.
33. D. J. Kim, Y. J. Tak, W.-G. Kim, J. K. Kim, J. H. Kim, H. J. Kim, *Adv. Mater. Interfaces* **2017**, *4*, 1601035.
34. Y. Ren, V. Milo, Z. Wang, H. Xu, D. Ielmini, X. Zhao, Y. Liu, *Adv.Theory Simul*. **2018**, *1*, 1700035.
35. Y. Ren, H. Ma, W. Wang, Z. Wang, H. Xu, X. Zhao, W. Liu, J. Ma, Y. Liu, *Adv. Mater. Technol.* **2019**, *4*, 1800238.
36. G. T. S. How, N. A. Talik, B. K. Yap, H. Nakajima, S. Tunmee, B. T. Goh, *Appl. Surf. Sci*. **2019**, *473*, 194-202.
37. Z. Xiong, W. Hu, Y. She, Q. Lin, L. Hu, X. Tang, K. Sun, *ACS Appl. Mater. Interfaces* **2019**, *11*, 30037-30044.
38. Z. Li, M. Yang, J.-S. Park, S.-H. Wei, J. J. Berry, K. Zhu, *Chem. Mater*. **2016**, *28*, 284-292.
39. G. P. Li, H. Wang, Z. F. Zhu, Y. J. Chang, T. Zhang, Z. H. Song, Y. Jiang, *Chem. Commun.* **2016**, *52*, 11296-11299.
40. J. K. Sun, S. Huang, X. Z. Liu, Q. Xu, Q. H. Zhang, W. J. Jiang, D. J. Xue, J. C. Xu, J. Y. Ma, J. Ding, Q. Q. Ge, L. Gu, X. H. Fang, H. Z. Zhong, J. S. Hu, L. J. Wan, *J. Am. Chem. Soc.* **2018**, *140*, 11705-11715.
41. J. Liu, K. Song, Y. Shin, X. Liu, J. Chen, K. X. Yao, J. Pan, C. Yang, J. Yin, L.-J. Xu, H. Yang, A. M. El-Zohry, B. Xin, S. Mitra, M. N. Hedhili, I. S. Roqan, O. F. Mohammed, Y. Han, O. M. Bakr, *Chem. Mater*. **2019**, *31*, 6642-6649.

LIST OF PUBLICATIONS

1. Luminescent Hybrid Perovskite Nanoparticles as a New Platform for Selective Detection of 2,4,6-Trinitrophenol; **Chinnadurai Muthu,** Sunena R. Nagamma and Vijayakumar C. Nair*; *RSC Adv.* **2014***, 4,* 55908-55911.

2. Hybrid Perovskite Nanoparticles for High-Performance Resistive Random Access Memory Devices: Control of Operational Parameters through Chloride Doping; **Chinnadurai Muthu,** Shivani Agarwal, Anuja Vijayan, Preetam Hazra, Kochupurackal B. Jinesh, and Vijayakumar C. Nair*; *Adv. Mater. Interfaces* **2016***, 3,* 1600092 (1-6).

3. Quantum Confinement Effects in Organic Lead Tribromide Perovskite Nanoparticles; Prashant Kumar, **Chinnadurai Muthu,** Vijayakumar C. Nair, and K. S. Narayan*; *J. Phys. Chem. C* **2016***, 120,* 18333-18339.

4. Channeling Exciton Migration into Electron Transfer in Formamidinium Lead Bromide Perovskite Nanocrystal/Fullerene Composites; Vijayakumar C. Nair,* **Chinnadurai Muthu,** Andrey L. Rogach, Reiko Kohara, and Vasudevanpillai Biju*; *Angew. Chem. Int. Ed.* **2017***, 56,* 1214-1218 (Highlighted as Hot Paper & Frontispiece).

5. $CH_3NH_3PbBr_3$ Perovskite Nanocrystals as Efficient Light Harvesting Antenna for Fluorescence Resonance Energy Transfer; **Chinnadurai Muthu,** Anuja Vijayan, and Vijayakumar C. Nair*; *Chem. Asian J*. **2017**, *12*, 988-995.

6. Zero-Dimensional Methylammonium Bismuth Iodide-based Lead-Free Perovskite Capacitor; Johnpaul K. Pious, M. L. Lekshmi, **Chinnadurai Muthu,** R. B. Rakhi*, and Vijayakumar C. Nair*; *ACS Omega*, **2017**, *2*, 5798-5802.

7. A Zero-Dimensional Lead-Free Hybrid Perovskite-Like Material with a Quantum-Well Structure; Johnpaul K. Pious, Ankita Katre, **Chinnadurai Muthu,** Sudip Chakraborty, Swathi Krishna, and Vijayakumar C. Nair*; *Chem. Mater.* **2019**, *31*, 1941-1945.

8. Photoinduced Photoluminescence Enhancement in Self-Assembled Clusters of Formamidinium Lead Bromide Perovskite Nanocrystals; Sushant Ghimire, Vijayakumar C. Nair*, **Chinnadurai Muthu**, Martin Vacha, Vasudevanpillai Biju*; *Nanoscale* **2019**, *11*, 9335-9340 (Inside Front Cover Page).

9. Bismuth based Zero-Dimensional Perovskite-Like Material: Effect of Benzylammonium on Dielectric Confinement and Photoconductivity; Johnpaul K. Pious, **Chinnadurai Muthu,** Selgiya Dani, Akinori Saeki, and Vijayakumar C. Nair*; *Chem. Mater.* **2020**, *32*, 2647-2652.

10. Anisotropic Photoconductivity and Long-Lived Charge Carriers in Bismuth-Based One-Dimensional Perovskite with Type-IIa Band Alignment; Johnpaul K. Pious, Manasa G. B, **Chinnadurai Muthu**, Nayana Krishna, Ryosuke Nishikubo, Akinori Saeki, Sudip Chakraborty, and Vijayakumar C. Nair*; *J. Phys. Chem. Lett*. **2020**, *11*, 6757-6762.

11. Formamidinium Lead Iodide Perovskite Nanocrystal/Squaraine Dye Composite based Visibly Opaque and Near-Infrared Transmitting Material; **Chinnadurai Muthu,** Johnpaul K. Pious, Parambatheri S. Seethal, Nayana Krishna, and C. Vijayakumar*; *Adv. Opt. Mater*. **2020**, https://doi.org/10.1002/adom.202001130.

12. Resistive Switching in Formamidinium Lead Iodide Perovskite Nanocrystals: A Contradiction to the Bulk Form; **Chinnadurai Muthu,** A. N. Resmi, Johnpaul K. Pious, G. Dayal, Nayana Krishna, K. B. Jinesh*, and C. Vijayakumar*; *J. Mater. Chem. C* **2020**, DOI: https://doi.org/10.1039/D0TC03275A.

13. Cesium Lead Halide Perovskite Nanocrystals/ Polyfluorene Organogel Composite for Stable White Light Emission by Supressing Halide Ions Migration; **Chinnadurai Muthu**, Johnpaul K. Pious, Tino Thankachan, Nayana Krishna, and C. Vijayakumar* (Manuscript to be communicated).

14. Delta Formamidinium Lead Iodide based Nanorods: Effect of Orientation on Resistive Switching Property; **Chinnadurai Muthu**, A. N. Resmi, Johnpaul K. Pious, G. Dayal, Shyam Sunder, K. B. Jinesh*, and C. Vijayakumar* (Manuscript to be communicated).

PAPERS/POSTERS PRESENTED IN CONFERENCE

1. ‘Luminescent Perovskite Nanoparticles as a Light Harvesting Antenna for Efficient Fluorescence Resonance Energy Transfer’; **Chinnadurai Muthu** and Vijayakumar C. Nair* presented a **poster** in the ‘International Symposium on Photonics Applications and Nanomaterials’, Hotel Residency Tower, Trivandrum, Kerala, during October 28–30, **2015.** (**Achievement: Best Poster Award**).

2. ‘Hybrid Perovskite Nanoparticles for High-Performance Resistive Random Access Memory Devices: Control of Operational Parameters through Chloride Doping’; **Chinnadurai Muthu** and Vijayakumar C. Nair* presented a **poster** in the ‘Discussion Meeting on Hybrid Perovskite Materials HyPe-2017’ at S. N. Bose National Centre for Basic Sciences, Kolkata, West Bengal, India during 14, 15th December **2017.**

3. ‘Luminescent Formamidinium Lead Iodide Perovskite: Stabilization of α-Phase in the Nanocrystal Form’; **Chinnadurai Muthu** and Vijayakumar C. Nair*, presented a **poster** in the ‘National Conference on Luminescence and Applications’, CSIR-NIIST, Trivandrum, Kerala, February 14-16, **2018.**

4. ‘Nanocrystals to Nanorod Transformation in δ-$FAPbI_3$ Perovskite: Study of Self-Assembly and Resistive Switching Memory Device Application’; **Chinnadurai Muthu** and Vijayakumar C. Nair,* presented a **oral** in ‘National Conference Emerging Trends in Science, Technology & Application of Electron Microscope (STAEM-2018)’ at CSIR-NIIST, Trivandrum, Kerala, December 19-21, **2018.**

5. ‘Yellow Phase δ-$FAPbI_3$ Nanorods – An Insignificant Material Renovates into Valuable Resistive Switching Memory Device’; **Chinnadurai Muthu** and Vijayakumar C. Nair*, presented a **poster** in ‘31st KERALA SCIENCE CONGRESS’ at Fatima Mata National College, Kollam, Kerala, India during 2-3 February **2019.** (**Achievement: Best Poster Award**).

6. ‘Formamidinium Lead Iodide Perovskite Nanocrystals: Development of Visibly Opaque NIR Transmitting Filters’; **Chinnadurai Muthu** and Vijayakumar C. Nair,* presented a **poster** in ‘National Seminar on Advanced Functional Materials for Analytical, Energy, Environmental and Biomedical Applications (NSAFM)’ in University of Kerala, Thiruvananthapuram, India during March 25-27, **2018.** (**Achievement: Best Poster Award**).